Dipl.-Ing. William Perret

Welding Simulation of Complex Automotive Welded Assembly - Possibilities and Limits of the Application of Analytical Temperature Field Solutions

BAM-Dissertationsreihe · Band 108
Berlin 2013

Die vorliegende Arbeit entstand an der BAM Bundesanstalt für Materialforschung und -prüfung.

Impressum

Welding Simulation of Complex Automotive Welded Assembly - Possibilities and Limits of the Application of Analytical Temperature Field Solutions

2013

Herausgeber:
BAM Bundesanstalt für Materialforschung und -prüfung
Unter den Eichen 87
12205 Berlin
Telefon: +49 30 8104-0
Telefax: +49 30 8112029
E-Mail: info@bam.de
Internet: www.bam.de

Layout: BAM-Referat Z.8

ISSN 1613-4249
ISBN 978-3-9815944-0-9

Welding Simulation of Complex Automotive Welded Assembly - Possibilities and Limits of the Application of Analytical Temperature Field Solutions

Vorgelegt von

Dipl.-Ing.

William Perret

aus Hyères-les-Palmiers

Von der Fakultät V – Verkehrs- und Maschinensysteme

der Technischen Universität Berlin

zur Erlangung des akademischen Grades

Doktor der Ingenieurwissenschaften

Dr.-Ing.

genehmigte Dissertation

Promotionsausschuss:

Vorsitzender:	Prof. Dr.-Ing. Rainer Stark
Berichter:	Prof. Dr.-Ing. Michael Rethmeier
Berichter:	Prof. Dr.-Ing. Vasily Ploshikhin

Tag der wissenschaftlichen Aussprachen: 31. Mai 2013

Berlin 2013

D83

DANKSAGUNG

Mit der Fertigstellung dieser Dissertation ist es nun Zeit, einer Reihe von Personen zu danken, die mich in diesem Lebensabschnitt begleitet und unterstützt haben.

Besonderer Dank gilt dabei meinem Doktorvater Prof. Dr.-Ing. Michael Rethmeier für die Begleitung meiner Promotion. Er ermöglichte es mir, mich fachlich und persönlich weiterzuentwickeln, um somit optimal auf meine berufliche Zukunft vorbereitet zu sein. Für die bereitwillige Übernahme des Zweitgutachtens danke ich Prof. Dr.-Ing. Vasily Ploshikhin. Prof. Dr.-Ing. Rainer Stark danke ich für die Übernahme des Vorsitzes des Promotionsausschusses.

Des Weiteren gilt mein Dank meinem Arbeitsgruppenleiter Dr. Christopher Schwenk für seine Unterstützung und die vielen fachlichen Diskussionen.

Besonderer Dank gilt meinem Kollegen und Büronachbarn Dr. Andreas Pittner, der mir durch unzählige fachliche Diskussionen wichtige Impulse gab, die maßgeblich zum Gelingen meiner Doktorarbeit beigetragen haben. Bedanken möchte ich mich auch bei Raphael Thater und Max Biegler für die Durchführung von Experimenten und Berechnungen.

Mein Dank gilt auch den weiteren Kollegen der Fachgruppe 5.5 "Sicherheit gefügter Bauteile" für ihre Unterstützung. Hervorheben möchte ich hier insbesondere Thomas Michael und Stefan Brunow für ihre MIG/MAG Expertise und Marco Lammers für seinen fachlichen und experimentellen Beistand beim Thema Laserstrahlschweißen. Den weiteren Kollegen der Fachgruppe 5.5 danke für ihre konstruktive und freundschaftliche Zusammenarbeit und so manch lustige Begebenheit.

Diese Arbeit entstand in Kooperation mit der Audi AG. Mein Dank gilt an dieser Stelle Dr. Klaus Koglin und Dr. Markus Bauer für das Vertrauen, das sie in mich gesetzt haben und für die finanzielle Unterstützung. Insbesondere möchte ich mich weiterhin bei Dr. Uwe Alber für seine Unterstützung in Neckarsulm bedanken.

Zuletzt danke ich meinen Eltern, die immer an mich geglaubt haben und mir das Studium erst ermöglicht haben.

Meiner Frau Birgit danke ich für ihre Geduld und ihre Unterstützung während dieser langen und schweren Reise und vor allem für Ihre Liebe.

DANKE.

Diese Arbeit ist meinem Sohn Rémy gewidmet, mein schönstes Weihnachtsgeschenk, der mein Leben und meine Doktorarbeit ganz schön auf den Kopf gestellt hat.

ABSTRACT

Before the development of computational science, heat conduction problems were mainly solved by analytical techniques. Analytical solutions are exact solutions of differential equations; the investigated physical phenomena, for instance the temperature, are solved locally for one single point independently of the rest of the investigated structure resulting in extremely short computational times. These analytical solutions are however only valid for some simple geometries and boundary conditions making their applications for complex industrial geometries directly not possible. Numerical techniques, such as the Finite Element Method, enable overcoming this problem. However, the numerical simulation of the structural heat effect of welding for complex and large assemblies requires high computational effort and time. Therefore, the wide application of welding simulation in industry is not established, yet.

The aim of this study is to combine the advantages of analytical and numerical simulation methods to accelerate the calibration of the thermal model of structure welding simulation. This is done firstly by calibrating automatically the simulation model with a fast analytical temperature field solution and secondly by solving the welding simulation problem numerically with the analytically calibrated input parameters. In order to achieve this goal, the analytical solution of the heat conduction problem for a point source moving in an infinite solid was extended and validated against reference models until a solution for a volumetric heat source moving on a thin small sheet with several arbitrary curved welding paths was found. The potential of this analytical solution by means of computational time was subsequently demonstrated on a semi-industrial geometry with large dimensions and several curved welds.

The combined method was then transferred to an industrial assembly welded with four parallel welds. For this joint geometry, it was possible to apply the extended analytical solution. The calibration of the simulation model was done automatically against experimental data by combining the extended fast analytical solution with a global optimisation algorithm. For this calibration, more than 3000 direct simulations were required which run in less computational time than one corresponding single numerical simulation. The results of the numerical simulation executed with the analytically calibrated input parameters matched the experimental data within a scatter band of ± 10 %. The limit of the combined method is shown for an industrial assembly welded with eight overlap welds. For this joint geometry, a conventional numerical approach was applied, since no analytical solution was actually available. The final simulation results matched the experimental data within a scatter band of ± 10 %.

The results of this work provide a comprehensive method to accelerate the calibration of the thermal model of the structure welding simulation of complex and large welded assemblies, even though within limitation. In the future, the implementation of this method in a welding simulation tool accessible to a typical industrial user still has to be done.

Table of content

1 Introduction

With the continuous improvement of the computing power in the last decades, the application of virtual methods gains importance in a wide range of industrial sectors. In engineering fields, the finite-element-method (FEM), the finite-difference-method (FDM), the finite-volume-method (FVM) or the boundary-element-method (BEM) are the four major numerical methods to simulate the behaviour of loaded complex structures under different boundary conditions like external loads. In 2002, the German Federal Ministry of Education and Research ("Bundesministerium für Bildung und Forschung BMBF" in German) already recognised that a virtualisation of the automotive process chain is of major importance to guarantee the continuous increase of the competitiveness of German automotive suppliers [1]. Today, some simulation tools are completely integrated in the Product Development Process (Produktentstehungsprozess, PEP, in German) in the production planning of various Original Equipment Manufacturers (OEM), e.g. for crash test, forming or casting simulation. For the simulation of joining processes and particularly for the welding simulation, the industrial demand (particularly in the automotive industry) is high. As recently observed by Babu [2], however, the industrial implementation of welding simulation is still not established yet. Two main aspects are mainly responsible for this statement. Firstly, the entire workflow to run a structure welding simulation for a complex and large welded assembly with a standard numerical method is time-consuming. Secondly, the lack of software solutions adapted to the industrial requirements for welding simulation by means of computational time and user-friendly software interface has also hindered its wider industrial application.

These two aspects have been focused on in the following Ph.D. thesis to improve the application of welding simulation for complex welding assemblies in the automotive industry. In order to achieve a reduction of the entire welding simulation workflow, a combined method between fast analytical temperature field simulation methods and conventional numerical methods is investigated. Since the conventional well-known analytical temperature field solutions in the literature are not valid for complex industrial geometries but only for simple geometries like infinite thick plates for instance, several extensions of these analytical expressions are firstly proposed and validated against referred numerical results. The combined technique between the corresponding validated analytical temperature field solutions with a conventional numerical approach is then tested to simulate the welding induced temperature field of two real simple test cases called the simplified geometry "parallel weld" and "overlap weld". Finally, the possibilities and limits of the proposed combined method are investigated by simulating two industrial large and complex welding assemblies, a wheelhouse made of steel and a crossbeam in aluminium, covering a wide range of possible industrial applications of welding simulation.

2 State of the Art

2.1 Welding simulation

A welding process is composed of several different non-linear physical phenomena, which have an influence on the final properties of the welded joint. Their consideration in one simulation model is unrealistic for two main reasons: Firstly, the mathematical description of all these acting phenomena with their respective coupling is extremely difficult. Secondly, the computational time of such a model would be unacceptable with the available computational resources. To decrease the model's complexity, simplifications and assumptions are taken into consideration depending on the focus and the respective required accuracy of the investigated problem. Over the last 30 years, the research field in the area of welding simulation has converged to three main areas with different requirements to the implemented mathematical and physical models. Radaj [3] classified these three domains in:

- Process simulation
- Material simulation
- Structure simulation

A representation of these domains with their respective interactions is shown in Fig. 2.1:

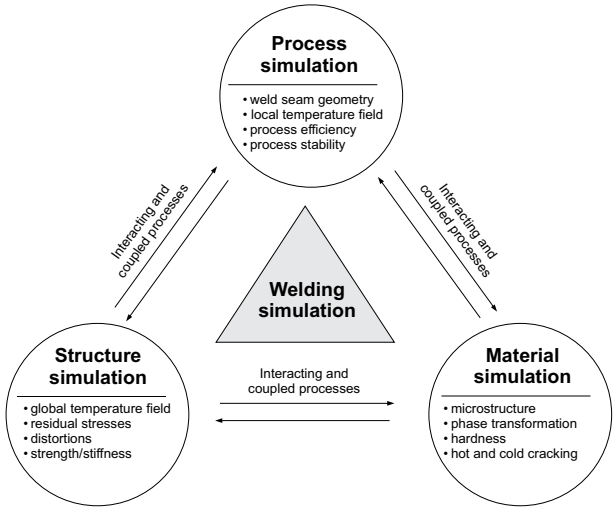

Fig. 2.1: Subdomains for the simulation of welding processes with their corresponding coupling factors, following Radaj [3]

The process simulation deals with the welding process itself. Radaj published a reference book about this topic [4]. In comparison to the structure simulation that describes the process effects on the surrounding structure, the goal of a process simulation is the description of the molten pool formation (and the fluid flow dynamics inside the weld pool)

as a function of the acting physical phenomena and the resulting local temperature field. Statements about the process stability and process efficiency are also focused on [5]. For laser beam welding for instance (this phenomenon occurs also in other welding processes), the Marangoni flow around the keyhole and other physical phenomena can be considered in the process models [6, 7]. For GMAW processes, the effects of various driving forces on heat and mass transfer have been published by Kim [8] and others [9-12]. There are only a few welding simulation software packages for process simulation. The software SimWeld® enables to simulate GMAW [13-15]. Electron and laser beam welding can be simulated with BeamSIM®. Both SimWeld® and BeamSim® are developped by ISF Welding and Joining Institute and are not commercially available. An application of SimWeld® in the ship building industry has been investigated by Rieger [16]. In this study, the process simulation results are transformed into an equivalent heat source for further thermomechanical simulations with the structure welding simulation software Sysweld®. A similar connection between a process and a structure simulation has also been investigated by Michailov in [17]. The SST (Schweißsimulationstool, in English, welding simulation tools) platform [18] also transfers the process simulation result from DC-LASIM [19, 20] into Ansys for further thermomechanical simulations. For spot welding, the commercial process simulation software SORPAS is widely used for industrial applications.

The material simulation deals with the microstructural evolution during and after the welding process in and around the weld seam on a micro- and macroscopic scale. The microstructural phase transformation, the hardness, the hot and cold cracking are the main topics of the material simulation. Many computational thermodynamic and kinetic models have been developed in the last decades to predict these phenomena. Babu summarised the actual state of research in this review paper [2]. The prediction of the thermal and mechanical material properties of alloys in dependence on their chemical composition also belongs to the material simulation. A few simulation tools for computational thermodynamics and kinetics are available. They are, however, still specialised for special study-cases and therefore not widely implemented in the industry [2]. For the solid phase transformation occurring with mild ferritic steels, the model of Leblond [21, 22] is actually the most widespread and is implemented in several FE-codes like Sysweld®. This model is based on the Johnson-Mehl-Avrami law [23], describing the microstructural kinetics, and on the Koistinen-Marburger's law [24], describing the martensitic transformation. This model can also be used to consider the softening effect in the HAZ of hardened aluminium alloys where precipitation particles come back into solution [25]. In Fig. 2.1, the phase transformation is classified under the material simulation. Many authors, however, also considered this phenomenological microstructure model in their structure welding simulation [26, 27].

The structure simulation deals with the heat effects of the welding process, which are the global temperature field and the resulting residual stresses and distortions of the welded assembly. This subdomain of welding simulation has been focused on in this Ph.D. thesis and is described in section 2.3.

2.2 Temperature field simulation

The simulation of the temperature field induced by a welding process is approximated by a heat conduction problem in a homogeneous solid. Based on the Fourier's law and on the first law of thermodynamics, the general nonlinear form of the partial differential equation to solve is:

$$\rho(T)c(T)\frac{\partial T}{\partial t} = div(\lambda(T)grad(T)) + q_{input} \tag{2.1}$$

where $c(T)$ is the temperature dependent specific heat capacity in $\mathrm{J \cdot kg^{-1} \cdot K^{-1}}$, $\lambda(T)$ is the temperature dependent heat conductivity in $\mathrm{W \cdot m^{-1} \cdot K^{-1}}$, $\rho(T)$ is the temperature dependent density in $\mathrm{kg \cdot m^{-3}}$. q_{input} is the volumetric energy input per time in $\mathrm{W \cdot m^{-3}}$.

According to Karkhin [28], the energy input can be composed as follows:

$$q_{input} = q_{net} + q_c + q_L \tag{2.2}$$

where q_{net}, q_c and q_L are function of time and space. q_{net} is the energy input per time and volume from the welding process, q_c describes the energy transport due to the weld pool convection and q_L the latent heat of fusion and solidification.

The boundary conditions at the outer surface Γ of the computational domain are defined as follows:

$$-\lambda(T)grad(T) \cdot \vec{n}\Big|_{\Gamma} = q_{lost} \tag{2.3}$$

where $\vec{n}$ corresponds to the surface normal vector pointing in outwards direction. q_{lost} corresponds to the energy lost to the environment in $\mathrm{W \cdot m^{-2}}$ by convection and radiation and is defined as:

$$q_{lost} = K_T(T - T_0) \text{ with } K_T = K_c + K_r \tag{2.4}$$

where $\mathrm{T_0}$ is the ambient temperature in °C, $\mathrm{K_T}$ the heat transfer coefficient in $\mathrm{W \cdot m^{-2} \cdot K^{-1}}$, $\mathrm{K_c}$ and $\mathrm{K_r}$ are the convective and the radiative term, respectively.

$$\begin{aligned} K_c &= \alpha \\ K_r &= \varepsilon\sigma\left(T^2 + T_0^2\right)(T + T_0) \end{aligned} \tag{2.5}$$

α is the convective heat transfer coefficient in $\mathrm{W \cdot m^{-2} \cdot K^{-1}}$, ε the emissivity coefficient (0< ε <1) and σ the Stefan-Boltzmann constant in $\mathrm{W \cdot m^{-2} \cdot K^{-4}}$.

The heat conduction problem (2.1) can be solved analytically and numerically. With analytical techniques, only the linearised expression of (2.1) can be solved for some simple geometries and boundary conditions as described in detail in section 2.2.2. The respective

solutions are nevertheless exact solutions of (2.1). Numerical techniques are contrarily approximate solutions and enable to solve (2.1) in a discrete manner as briefly described in the next section.

2.2.1 Numerical approach

The numerical techniques to solve the partial differential equation of heat conduction have not been focused on in this Ph.D. thesis. More information can be found in the following reference book about numerical analysis [29].

For the calculation of the temperature field induced by a welding process, the partial differential equation (2.1) can be solved with numerical techniques almost without restrictions regarding the geometry complexity, non-linearities (like temperature dependent material properties), the description of the welding heat source and the boundary conditions of the problem. This flexibily of the numerical approach makes this method very competitive in comparison to analytical solutions as shown by Moore in [30]. In the end of the 1970's, the first welding simulations with convective and radiative boundary conditions and with temperature dependent material properties were published [31-35]. In the same time, the restrictions of numerical techniques have also been recognised. In 1969, Pavelic already wrote that the high flexibility of numerical techniques is restrained by the resulting high computational demands [31]. Indeed, for an accurate temperature field simulation, the high gradient temperature occurring during the welding process around the weld seam must be well reproduced requiring a fine temporal and spatial discretisation of the simulation model in this area. Thus, a compromise must be made between the result's accuracy and the computational time. More information about this topic is described in section 2.3.1.

2.2.2 Analytical approach

All the fundamental theory of the heat distribution in welding has been developed during the late 1930's by Rosenthal [36-38] and later by Rykalin [39, 40]. In fact, they used the fundamental work of Carslaw and Jaeger about the heat conduction in solids [41] and applied it to the welding problem. The differential equation (2.1) could nevertheless not be solved in its complete form because of some restrictions of the analytical analysis. Therefore, the following assumptions and simplifications have been made in order to reach a solvable problem [42]:

- The material is solid at all times and at all temperatures, no phase transformations occur, and it is isotropic and homogeneous
- The thermal conductivity, density and specific heat capacity are temperature independent
- Adiabatic boundary conditions are assumed for all surfaces
- The heat source moves on an infinite plate
- The problem is in steady state. Transient state at the beginning and at the end of the welding process are neglected
- The heat source is considered to be a zero volume point or line source

These assumptions and simplifications enable to get the linear form of the general differential equation of the heat conduction:

$$c\rho\frac{\partial T}{\partial t} - \lambda\nabla^2 T - q_{input} = 0 \tag{2.6}$$

With c in $\mathrm{J}\cdot\mathrm{kg}^{-1}\cdot\mathrm{K}^{-1}$, ρ in $\mathrm{kg}\cdot\mathrm{m}^{-3}$ and λ in $\mathrm{W}\cdot\mathrm{m}^{-1}\cdot\mathrm{K}^{-1}$ the temperature independent specific heat capacity, density and heat conductivity respectively. Another widespread formulation of (2.6) is:

$$\frac{\partial T}{\partial t} = \kappa\nabla^2 T + \frac{q_{input}}{\rho c} \text{ with } \kappa = \frac{\lambda}{\rho c} \tag{2.7}$$

κ is the thermal diffusivity in $\mathrm{m}^2\cdot\mathrm{s}^{-1}$.

The solution of (2.7) is formulated by the use of Green's functions. A Green's function is regarded as the system response due to an excitation that has the shape of a Dirac function and acting instantaneously. The Green's function due to the action of an instantaneous point heat source of unity strength (equal to 1 Joule) is given by [40]:

$$G_{\mathrm{inf}} = \frac{1}{(4\pi\kappa t)^{\frac{3}{2}}}\exp\left(-\frac{R^2}{4\kappa t}\right) \tag{2.8}$$

With $R = \sqrt{x^2 + y^2 + z^2}$ is the position of the source at the time t. Based on the equations (2.8), the temperature distribution in an infinite body for any kind of heat source, e.g. point, line, surface or volumetric heat sources, can be calculated with an appropriate integral formulation [43].

$$T(x,y,z,t) = \frac{1}{\rho c}\int_t\int_V G_{\mathrm{inf}}(x,y,z,t)\, q_{input}(x,y,z,t)dtdV \tag{2.9}$$

In the mid 1950's, Rykalin and Rosenthal gave analytical solutions for 1D, 2D and 3D heat flow in infinite, finite, and other simple geometries in quasi-stationary state and they related it to welding procedures [36-40]. For a 2D heat flow, the analytical solution for a moving line source in a thin plate in quasi-stationary state is given by the following expression.

$$T(\xi,y) = \frac{q_{line}}{2\pi\lambda\delta}\exp\left(-\frac{v\xi}{2\kappa}\right)K_0\left(\frac{vR}{2\kappa}\right) \text{ with } R = \sqrt{\xi^2 + y^2} \tag{2.10}$$

For the 3D heat flow in a semi-infinite solid, the instantaneous and moving point source is expressed as:

$$T(\xi,y,z) = \frac{q_{point}}{4\pi\lambda R}\exp\left(-\frac{v(R+\xi)}{2\kappa}\right) \text{ with } R = \sqrt{\xi^2 + y^2 + z^2} \tag{2.11}$$

For both (2.10) and (2.11), the source is expressed in a moving coordinate system (ξ, y) and (ξ, y, z) for the 2D and 3D problem, respectively. $\xi = x - vt$ in the

global coordinate system (x, y, z), v is the welding speed in $\mathrm{m \cdot s^{-1}}$, q_{line} and q_{point} are the power of the line and the point source in W, δ is the thickness of the plate in m, κ is the thermal diffusivity in $\mathrm{m^2 \cdot s^{-1}}$ and $\mathrm{K_0}$ is the modified Bessel function of second kind and order zero.

These two analytical solutions have been widely implemented until today for diverse welding applications. Other formulations have been also developed; for instance, Rosenthal proposed two other solutions for the 2D thin plate in [36]. In the first one, the heat loss through convection at the upper and the bottom surface is taken into consideration and in the second one, the "linear source of variable strength", the heat source power q can vary along the thickness. These formulations have been used and extended in the end 1990s to characterise the temperature field induced by a pulsed laser process [44, 45].

The formulation for the point or the line source (2.10) and (2.11) are valid for an infinite solid and can only be used for thick plates. For a plate with finite thickness (thin plate), the reflection technique (also called the method of image) must be applied. Its principle is represented in Fig. 2.2:

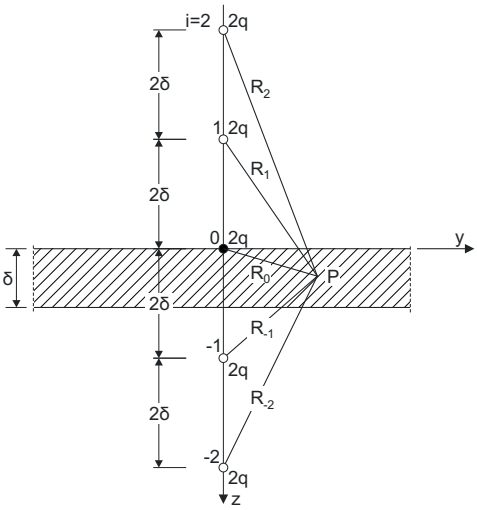

Fig. 2.2: Temperature field on a thin plate based on the analytical infinite point source solution with the reflexion technique, following Radaj [46]

In an infinite body, the heat resulting from a moving source can expand freely in the direction of the thickness. In a finite body with thickness δ, if we made the assumption that no heat is lost through the surface $z = 0$ and $z = \delta$, the heat flow through these surfaces is equal to zero. With the reflexion technique, fictive heat sources are added to the real one by means of a convergent series. These fictive sources are located at $\pm 2n\delta$ above and below the upper surface of the plate as shown in Fig. 2.2. Thus, the 3D temperature field for the moving point source in a plate with finite thickness δ is given by the series:

$$T(\xi,y,z)=\frac{q}{4\pi\lambda R}\exp\left(-\frac{v\xi}{2\kappa}\right)\left[\sum_{n=-\infty}^{n=+\infty}\frac{1}{R_n}\exp(\frac{vR_n}{2\kappa})\right] \tag{2.12}$$

With

$$R_n=\sqrt{\xi^2+y^2+\left(z-2n\delta\right)^2} \tag{2.13}$$

This reflexion technique can also be expressed by a Fourier-series expansion, also proposed by Rosenthal [36]. According to Karkhin [28], for small dimensionless time values of the Fourier number $\mathrm{F_o}=\kappa\cdot\mathrm{t}\,/\,\delta^2$, the series (2.12) converges faster than the Fourier-series expansion.

In the beginning of 1940s, Tanaka [47] proposed a general solution covering the moving point source in quasi-stationary state (a translation of this publication in English is available in [48]). This solution enables considering convective boundary conditions at the upper and the lower surface of the plate. Although this solution seems very interesting for welding problems of thin sheets, where the effect of convective and radiative boundary conditions cannot be neglected [49], it's application is rare in the literature.

In 1965 Christensen generalised the moving point source without reflexion (2.10) in a dimensionless form [50]. He used this formula to analyse single beads deposited on heavy pieces of mild steel and aluminium for GMAW and SAW processes. He then compared and discussed the simulation of the dimension and shape of the weld pool, the cooling time and the peak temperature with a high number of experimental data. In the same time, Myer summarised in [42] the existing analytical solutions in quasi-stationary state in 1D, 2D and 3D for welding simulation. He also drew many dimensionless graphs to enable a wide application of the simulation results. In addition to Christensen [50], he proposed some analytical formulations to simulate spot welding only based on a heat conduction problem. The simplification that the mechanical deformation during spot welding has no influence on the temperature is quite rough and these formulations have therefore rarely been used.

Since the development of computational techniques in the 1970s, the application of numerical integration techniques to solve non-linear differential equations is possible and enlarges the application of welding simulation. However, the high computational time of numerical techniques restrains the possibility of parameter studies. Analytical temperature field solutions have therefore been developed further in order to widen the application field of analytical solutions.

In 1975, Malmuth included the change of phase across the molten boundary to an analytical approximation technique, called the perturbation technique [51]. The model was in quasi-stationary state. A comparison of the analytical weld pool shape on the surface of the plate with a referenced numerical simulation matches well. However, no information about the shape of the fusion zone in the thickness and about the cooling behaviour is given. In 1983, Nunes extended the moving point source with the reflexion technique (2.12) to include effects of phase changes and circulations in the weld pool [52]. To achieve this goal, he used a "multipole weld model" comprising a monopole heat point source for the

welding power and several heat and sink point sources in the weld to represent the circulation flux in the weld pool. No comparison with numerical techniques or with experimental data has been made.

In the end of the 1980s, Steen combined the line source (2.10) with the reflected point moving source (2.12) in quasi-stationary state to simulate a laser beam welding process [45]. In order to match the typical fully penetrated fusion zone occurring by this process, he placed a moving point source at different positions in the thickness of the plate. This idea was extended by Akhter who replaces the simple line source of Steen by a line source whose strength varies with its position in the thickness [44]. As cited at the beginning of this section, this line source formulation was already published by Rosenthal [36] but without real applications. Akhter applied it to simulate a series of lap welds of galvanised steel plates. In the end of 1990s, Dowden extended this combination of point and line source techniques to a finite plate for transient state [53]. He developed this new analytical formulation to simulate pulsed laser welding, where the transient state cannot be neglected. However, he did not compare the simulation results to experimental data and no further publications with these analytical formulations are available. In 1999 Karkhin published a transient point and a line source model in order to simulate the HAZ during pulsed power welding [54]. In addition to Dowden, he proposed a method based on the Kirchhoff transformation in order to approximately take non-linearities in the model into consideration. With this method, Karkhin assumes that the thermal conductivity increases linearly with the temperature and that the thermal diffusivity is temperature independent. In 2004, Rogeon published an analytical dimensionless line source solution for electron beam welding to characterise the critical sample width [55]. Finally, Pittner used the analytical point and the line source solution in quasi-stationary state in combination with a neural network to simulate the temperature distribution occurring by laser beam and GMA-Laser-Hybrid Welding [56]. The virtual fusion zone in cross-sections and the temperature cycle matched the experimental data very well.

With new analytical solutions, Kasuya simulated a single pass submerged arc welding with three electrodes in tandem. This process is characterised by a high and large energy input. To achieve the simulation of this problem, he extended the moving point source solution of Tanaka further [47]. He took into consideration heat loss at the surface boundary through convection in a quasi-stationary state. This formulation was limited for a point heat source situated on the upper surface of the plate. Kasuka published the solution for a point situated at an arbitrary position in the thickness of the plate. As the differential equation for the analytical solution (2.7) is linear, he could superpose many point sources along the welding path on the surface and within the thickness of the plate to get the final temperature field. With this method, he could match the experimental data well. It can be noticed that the calibration of the temperature field with such a high number of heat sources was probably a time intensive task but the author did not mention this aspect. In these models, Kasuya also considered the preheating and cooling time of the temperature field by adding a transient analytical solution from Carslaw und Jaeger [41] for a constant preheating temperature [57, 58].

Some analytical applications for multipass welding have been published. Öberg simulated multipass welding on a pipe with the quasi-stationary line source model (2.10) [59]. He considered the pipe to be a plate and started several heat sources (corresponding to the

different passes) at the beginning of the plate with a time delay of $2\pi \mathrm{R} \mathrm{v}^{-1}$ where R is the radius of the pipe and v the welding speed. Using the same principle of superposition, Suzuki simulated multipass welding with analytical methods [60]. For this study, he extended the 2D line source model in quasi-stationary state (2.10) for temperature dependent material properties. He also extended the 3D analytical moving point source (2.11) by taking heat loss at the surface boundary into account while employing constant material properties. These applications of analytical solutions are interesting; however, the simulation of multi-pass welding can only be done with a transient analytical approach as already mentioned by Rykalin [39]. Without a transient formulation, the cooling behaviour of previous welding passes cannot be considered. A special technique has to be implemented with the transient solution to simulate the cooling of the plate when the heat source is not active anymore. When the heat source stops, two virtual heat sources are activated; the first one is the virtual continuity of the real one (with the same start point) and the second one is a virtual sink, which progressively switch off the influence of other virtual heat source. This technique is represented in the following Fig. 2.3:

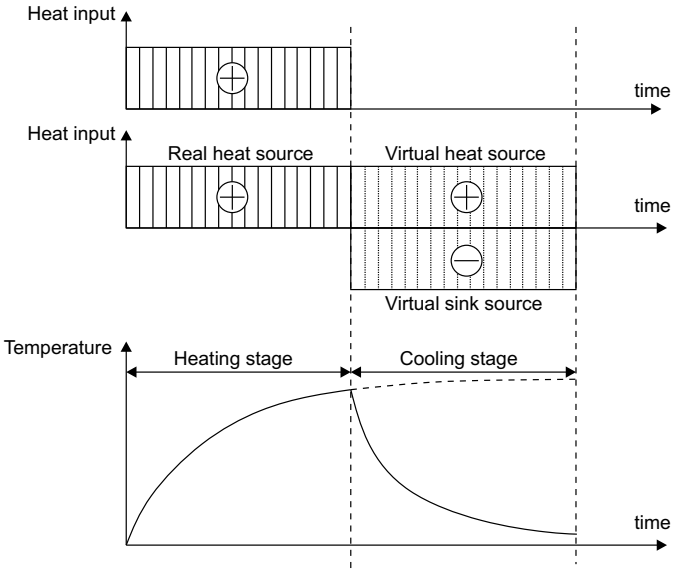

Fig. 2.3: Technique to simulate the cooling behaviour with a transient analytical solution based on the addition of a virtual sink at the end of the welding path, according to Rykalin [39]

This approach has been implemented by Cao in order to simulate the temperature field after multi-pass welding in a pipe and curved welds on complex structures [61]. For these examples, he proposed a new fast analytical closed form solution (which does not need any numerical integration techniques) of a transient point source moving in an infinite profile. In fact, this solution is not new and was already proposed by Rykalin in [39]. This analytical solution is described by the following expression:

$$T\left(\xi, y, z, t\right) = T_{st}\left(\xi, y, z\right) * T_{t}\left(\xi, y, z, t\right) \tag{2.14}$$

$\mathrm{T_{st}}\left(\xi,\mathrm{y},\mathrm{z}\right)$ corresponds to the analytical temperature field solution in steady state for a moving point source in an infinite solid, see equation (2.11) and $\mathrm{T_t}\left(\xi,\mathrm{y},\mathrm{z},\mathrm{t}\right)$ is the transient transform function which can be written as:

$$
\begin{aligned}
T_t\left(\xi,y,z,t\right) &= \frac{1}{2}\left(\exp\left(\frac{vR}{\kappa}\right) * A + B\right) \\
\text{with} \qquad A &= \left(1-\operatorname{erf}\left(\frac{vt+R}{2\sqrt{\kappa t}}\right)\right) \\
\text{and} \qquad B &= \left(1+\operatorname{erf}\left(\frac{vt-R}{2\sqrt{\kappa t}}\right)\right)
\end{aligned}
\tag{2.15}
$$

Here, it is worth to notice that the part A of (2.15) was wrong in the paper from [61] (a sign error) and has been corrected here. A combination of the analytical expression (2.14) with the reflexion technique enables obtaining a transient analytical temperature field solution for a moving point source on a thin plate.

The point and line source have been used to predict the size of the weld pool and other welding characteristics in plates of infinite and finite thickness in steady and in transient state. However, some authors have shown that for a plasma arc welding or a gas metal arc welding, a distributed heat source formulation would be more realistic than a point or a line source [62]. Therefore, in the 1980's, Cline [63] and Eagar [64] proposed a moving source with a surface Gaussian shape that moves on an infinite plate in quasi-stationary state. To solve the respective integral (2.9), the implementation of numerical integration techniques was required. Eagar [64] put the formulation in dimensionless form and plotted diverse weld characteristics, e.g. weld width or depth, fusion zone area, in function of the same dimensionless operating parameter n (Christensen's operating parameter) for different materials. He demonstrated that the Gaussian heat source formulation is more adapted to predict the weld pool shape than a point heat source formulation. Recently, Kwon simulated a double side arc weld [65] with analytical techniques. To achieve this task, he implemented two moving Gaussian heat sources in quasi stationary state (the same formulation as Eagar [64]) on the top and the bottom of the plate. In cross-section, the simulation results match the experimental ones quite well. However, no comparison of analytical and experimental temperature cycles is available.

In the mid 1980's, Goldak proposed a 3D distributed heat source model called the double ellipsoidal heat source [66, 67]. Its respective shape is represented in Fig. 2.4:

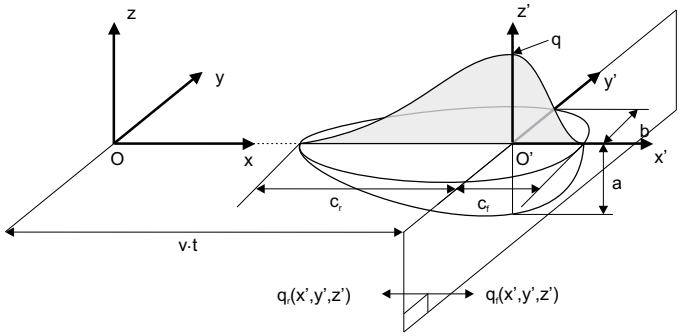

Fig. 2.4: Parameter shape of the double ellipsoid heat source, following Goldak [67]

The Goldak volumetric heat source contains two ellipsoids in front of and behind the plane (O',y',z') representing the power density of the heat source. Thus, an asymmetric amount of heat can be brought into the workpiece. These ellipsoids are mathematically described as follows:

$$\begin{cases} q_f = \dfrac{6\sqrt{3}f_f q}{abc_f\pi\sqrt{\pi}}\exp\left[-3\left(\dfrac{y'}{b}\right)^2 - 3\left(\dfrac{z'}{a}\right)^2 - 3\left(\dfrac{x'}{c_f}\right)^2\right] \forall x' \geq 0 \\ q_r = \dfrac{6\sqrt{3}f_r q}{abc_r\pi\sqrt{\pi}}\exp\left[-3\left(\dfrac{y'}{b}\right)^2 - 3\left(\dfrac{z'}{a}\right)^2 - 3\left(\dfrac{x'}{c_r}\right)^2\right] \forall x' \leq 0 \end{cases} \tag{2.16}$$

Where $\mathrm{a,b,c_f,c_r}$ are geometrical parameters of the ellipsoids; $\mathrm{x',y',z'}$ are the coordinates of an arbitrary point P in the moving coordinate system $\left(\mathrm{x',y',z'}\right)$; q represent the net energy input of the welding process in W. The continuity of the two ellipsoids in the plane $\left(\mathrm{O',y',z'}\right)$ is ensured by the following criterion [67, 68]:

$$\begin{cases} \dfrac{f_f}{c_{f\,r}} = \dfrac{f_r}{c_r} \\ f_f + f_r = 2 \end{cases} \tag{2.17}$$

Nguyen was the first to propose a transient analytical solution for a moving double ellipsoidal heat source in an infinite body [69]. He compared the resulting temperature distribution with the analytical moving point source from Rosenthal and the moving Gaussian source from Eagar. The resulting weld pool length and width fit the experimental data well; in the thickness however, the simulation does not match the experimental data well; this is due to the fact the analytical solution for an infinite solid is not appropriate for a plate with finite thickness. As the green's function for a moving point source in finite thickness is not trivial, Nguyen proposed an approximate approach to calculate the transient temperature field in finite plate based on the green's function in infinite body [68]. There still are no applications for this approximate solution. Recently, Fachinotti

demonstrated that the analytical solution of Nguyen is valid only for the case where $\mathrm{a} = \mathrm{b}$ and $\mathrm{c_f} = \mathrm{c_r}$, see Fig. 2.4, which is equivalent to an elliptic shape [70]. He then proposed a new transient analytical solution for the moving Goldak heat source in an infinite body and compared his solution and the solution from Nguyen with an FEM simulation considered in this case as reference. His solution is presented in the following equations (2.18):

$$T(x,y,z,t) = \frac{6\sqrt{3}q}{\rho c \pi \sqrt{\pi}} \int_0^t \frac{\exp\left[-3\dfrac{y^2}{12\kappa t + b^2} - 3\dfrac{z^2}{12\kappa t + a^2}\right]}{\sqrt{12\kappa t + b^2}\sqrt{12\kappa t + a^2}} \cdot \left[f_r A_r (1 - B_r) + f_f A_f (1 - B_f)\right] dt \tag{2.18}$$

With

$$A_i = A(x,t;c_i) = \frac{\exp\left[-3\dfrac{(x - vt)^2}{12\kappa t + c_i^2}\right]}{\sqrt{12\kappa t + c_i^2}}$$
$$B_i = B(x,t;c_i) = \operatorname{erf}\left[\frac{c_i}{2}\frac{x - vt}{\sqrt{\kappa t}\sqrt{12\kappa t + c_i^2}}\right] \tag{2.19}$$

Where κ is the thermal diffusivity in $\mathrm{m^2 \cdot s^{-1}}$. Karkhin also proposed several 3D heat source models with different heat distribution in the thickness, e.g. linear, exponential or normal with their respective transient analytical solutions in finite plate [28]. More recently, Pittner expanded these solutions for a solution to a parabolic shape in the thickness [71, 72]. This solution is particularly appropriate for the temperature distribution in full penetration laser beam welds.

In 1998, Ranatowski proposed the cylindrical-involution-normal C-I-N heat source model with its respective analytical solution [73]. This solution is transient and enables to take heat loss by convection into consideration. Later on, he proposed other volumetric heat sources and also a solution for the double ellipsoidal heat source from Goldak [74]. In comparison to Nguyen and others, Ranatowski can consider temperature dependent material properties by non-linear analytic-numerically computed calculations [74, 75]. This technique has not been implemented by other authors and according to Karkhin, it results in a discontinuous temperature field which violates the law of conservation of energy [28].

The development of transient analytical solutions of 3D heat source formulations for curved welding paths has recently been investigated. Thus, Winczek proposed a transient analytical solution for a Gaussian heat source with a linear heat repartition in the thickness direction for a curved weld in infinite body [76]. He did not compare his analytical results with any reference solution. Pittner implemented the Nguyen solution in combination with the reflexion technique and could simulate the temperature field of a double ellipsoidal heat

source on a small thin plate in transient state [77]. The comparison with referenced numerical results is excellent.

2.3 Workflow of a structure welding simulation

The structure simulation is focused on the simulation of the temperature field induced by the welding process and on the resulting distortions and residual stresses as highlighted by Radaj in Fig. 2.1 [3]. The typical workflow of a structural welding simulation is represented in Fig. 2.5:

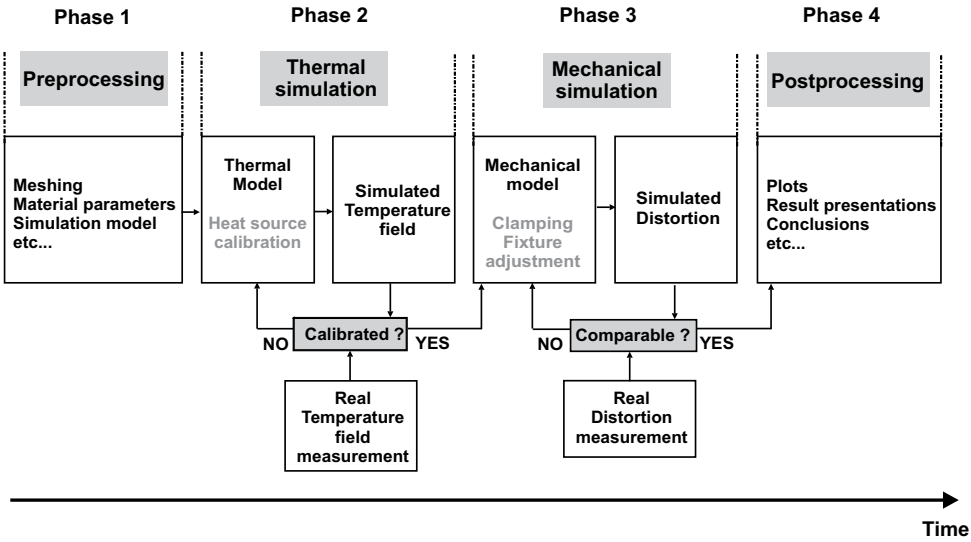

Fig. 2.5: Typical workflow of a structure welding simulation

An accurate definition of the expectations in a simulation by means of result accuracy and computational time should be done before starting any simulation project. For a structural welding simulation, several simplifications and assumptions are made as presented in the next section 2.3.1. The structure simulation itself is divided in a thermal and a mechanical simulation. For the thermal structure simulation, only a heat conduction problem is considered. The heat input is commonly replaced by a phenomenological heat source model, which has to be calibrated against experimental data. The resulting calibrated temperature field is used as thermal load in the mechanical simulation of distortion. Some iteration loops within the mechanical simulation, where the boundary conditions and clamps are adjusted, are also necessary in order get an optimal final simulation result.

2.3.1 Assumptions and simplifications

In this section, the assumptions and simplifications taken to run a structure welding simulation are presented. For the sake of clarity, they have been classified into two classes.

The first class is focused on the definition and the setups of the simulation model and the second class on the material properties.

First class of assumptions and simplifications:
The complete dynamics of a welding process governed by several highly non-linear and mostly coupled complex physical phenomena is simplified by a heat conduction problem in a solid medium. With this definition, the fluid dynamics in the weld pool are neglected or can be only indirectly considered by increasing the heat conductivity of the elements which have a temperature above the melting point [78-80]. The later technique is nevertheless difficult to control for the calibration of the thermal model.

In a structure welding simulation, the real welding heat source is replaced by a phenomenological formulation. Several expressions are commonly implemented in the literature as presented in section 2.2. If the 3D geometry of the fusion zone has been experimentally measured, the $T_{liquidus}$ can be directly prescribed in the simulation model at this boundary [81, 82]. With this technique, no phenomenological heat source formulation is required and the calibration step can be skipped. However, transient effects occurring at the beginning and at the end of the welding process cannot be taken into account. Furthermore, the later technique requires complex measurement techniques [83-85] and up to now the three dimensional measurement of the weld pool is not possible for complex geometries, seam shapes and welding processes.

For the construction of the welding simulation model, different techniques can be implemented depending on the accuracy levels and the maximum expected computational cost as discussed by Lindgren in [86]. The highest accuracy is reached with a model of 100% 3D-solid elements. Usually linear elements are used in a structure welding simulation. According to Faure [87], a higher degree of the finite element shape function does not yield significantly better results. As the high gradient temperature around the weld pool requires a very fine spatial and temporal resolution, it is a common approach to model an adequately fine mesh around the weld seam and a coarse mesh in the rest of the welded assembly in order to decrease the size of the simulation model [46]. According to Goldak, approximately four quadratic elements (two with cubic element) must be placed under the heat source implemented to guarantee a correct heat input formulation; the distance of the moving source between two time steps should not exceed half a weld pool length to ensure a continuous temperature field [66]. The time-step between two simulation results should also be fine enough to map the narrow peak temperature in the vicinity of the weld pool. During the cooling time, Radaj advises selecting time steps so that the temperature difference between two steps does not exceed 50°C [46].

For the structural thermomechanical simulation of distortions, a weak coupled analysis between the thermal and the mechanical simulation is used as represented in Fig. 2.6. According to Radaj [46], this simplified coupling can be done if the mechanical stress/strain field has no influence on the temperature field. In other words, the heat released by mechanical deformation is neglected.

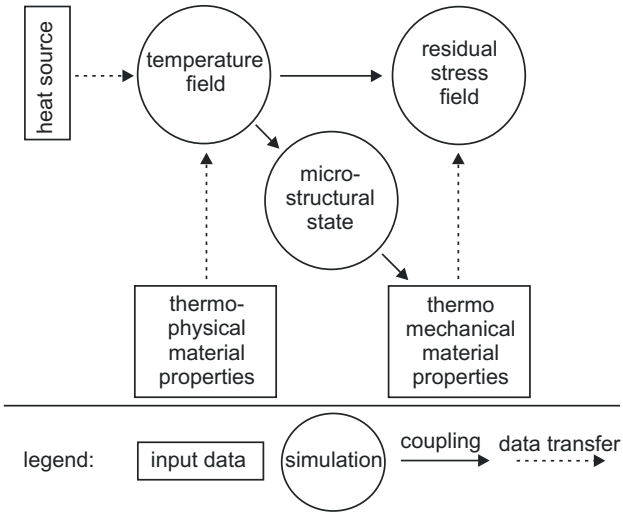

Fig. 2.6: Simplified structure welding simulation workflow – coupling between different simulation parts, following Radaj [46]

Second class of assumptions and simplifications:
Thermophysical material properties, e.g. the heat conductivity, the specific heat capacity and the density, are required for the thermal simulation and the thermomechanical material properties, e.g. Young's modulus, yield stress, flow curves, thermal expansion and Poisson's ratio, for the mechanical simulation. Since the material is heated up to its melting point and above during the welding process, the material properties of each material of the welded assembly should theoretically be given temperature dependent in the simulation model [46, 88]. Since the material properties for temperatures higher than the melting point are extremely expensive and difficult to obtain [89], they are often not considered in the simulation model by fixing them at the $T_{liquidus}$ (the "cut-off-temperature") [90, 91]. The best and the more reliable way to get temperature dependent material properties is by own measurements. If the necessary capacity by means of measurement devices and know-how is not available, the material data can be found in the literature, in material databases or can be simulated with sophisticated thermodynamic data bank systems like JMatPro® for instance. If no material properties can be found for the investigated alloy but for a similar alloy, the data may be carried over. For the thermophysical material properties, this approach can be used within a material class, where the chemical composition of corresponding alloys is almost equivalent. For the simulation of the distortions and residual stresses, the mechanical material properties are highly dependent on the production process and may therefore differ within a material class [89, 92].

As mentioned in section 2.1, many authors have implemented a phenomenological microstructure model in their structure simulation. According to Radaj, the consideration of phase transformations in a structure welding simulation model is recommended for the simulation of residual stresses [93]. For the mechanical simulation of the distortions only, Schwenk found that neglecting the phase transformation has less than 10 % influence on the final distortions [89].

2.3.2 Thermal simulation

In comparison to a process welding simulation, the input parameters of the phenomenological heat source formulation used in a structural welding simulation are not related to real process parameters and must therefore be calibrated against experimental data [94]. The shape and size of the real fusion zone and temperature distributions around the weld seam (measured with thermocouples) are commonly used as criterion for the calibration [95]. As the input parameters of the phenomenological heat input model are unknown, several simulations with a systematic variation of parameters are needed until the simulated and the measured fusion zone geometry and temperature distributions match well [94, 96]. Exemplarily, if the heat source model used for the simulation has three unknown input parameters, which can have ten different values, then 10^3 simulations would be needed to cover all the parameter space of the model. In other words, the calibration is very laborious, time consuming and highly dependent on the user expertise in welding simulation. The following three calibration techniques can be distinguished:

- Manual calibration technique
- Semi-automatic calibration technique
- Automatic calibration technique

In the manual calibration technique, the calibration of the temperature field is made manually. This technique is the most intuitive and is therefore the more popular. However, the influence of the variation of each single input parameter on the final simulation result is hard to control manually for a heat source with more than three input parameters. An expert user in welding simulation may find the optimal input parameter set of the heat source without scanning its entire parameter space. However, the typical industrial user may have less expertise in this field and the manual approach may be inappropriate to find the best heat source parameter configurations, especially if a single simulation takes more than 30 minutes.

With the semi-automatic and automatic calibration techniques, the model input parameters (parameters of the heat source model for instance) yielding the best agreement between the simulation results with the experimental validation data are automatically found by minimising an objective function.

The semi-automatic technique is based on a local optimisation algorithm. The particularity of this technique is the obligation to give an appropriate initial set of the model's parameters, which is often based on a priori knowledge [97, 98]. Moreover, only local minima can be found with this local technique, which is not optimal if the global parameter space has several minima. More information about semi-automatic optimisation algorithms can be found in [97, 98].

The automatic technique is based on a global optimisation algorithm, which enables to find a global minimum within an objective function containing several local minima. Such algorithms are in general more complex to implement and slower in convergence than those to calculate local minima due to their stochastic search algorithm [99]. Simulated annealing, genetic algorithms or neural networks are the most commonly known global optimisation techniques. Applications in welding simulations have for instance been published by Kumar [100, 101].

The potential of an optimisation tool (local or global) to automatically find the minimum of an objective function in a short calculation time is directly related to the calculation time of a single simulation; the use of fast analytical techniques can therefore become interesting. [56, 77, 94, 95, 102, 103] show for instance that a combination of a neural network algorithm with a fast analytical model allows the automatic calibration of the thermal model within a short time-frame and with an acceptable accuracy for laser and for gas-metal-arc welding. These results have nevertheless been simulated for a straight welding path in steady state on a simple plate with a point or a line source. An expansion of the implemented analytical solution to a curved welding path on complex geometry in transient state with a distributed heat source would therefore be of high interest for industrial applications.

2.3.3 Mechanical simulation

The mechanical simulation of the distortions is the main goal of the structure welding simulation. The thermal strains resulting from the temperature field simulation are used as input in the mechanical simulation in an uncoupled manner. This means that the effect the mechanical behaviour on the temperature field, i.e. the heat released by mechanical deformation, is neglected [89, 90, 104]. With this simplification, the calibration of the heat source model can be done in the thermal simulation in order to decrease the overall computation time.

Although there is a high number of publications about this topic, a general approach to deal with the mechanical simulation of a structure simulation has not been established yet [89]. The construction of a right simulation model may differ depending on the size, the form, the material of the welded assembly, the welding process and the boundary conditions of the system. Schenk finds for instance that a variation of the influence variables of a simulation model does not have the same effect on the distortions of a lap joint as of a T-joint [105].

In a structure welding simulation, the clamping boundary conditions are mostly simplified by fixing the degree of freedom of the nodes at the contact surface between the welded assembly and the clamp. This technique is fast to implement and enables saving computational time in comparison to a complex clamp definition [106, 107]. However, Roeren [108, 109] writes that this assumption is only true if the clamping devices are far away from the HAZ. Contrarily, for a clamping close to the HAZ, he shows that the mechanical influence of the clamps has a high importance for the prediction of the distortions and should be implemented in the simulation model as accurately as possible. Experimentally, Voss [110] observed that the final distortions become smaller the closer the clamps are located to the weld seam and the later they are released. Roeren [108] confirmed this experimental result by implementing the reaction forces caused by the clamping device in the simulation model. Schwenk [111] and Josserand [112] highlight that a clamp close to the weld seam has an influence on the thermal field by modifying the cooling rate around the weld. However, they did not relate these results to the problem of distortion; there are no publications on this topic. Complex clamping has been numerically investigated by Schenk [113, 114] with the goal to optimise the final distortions. He showed that the distortions could be decreased up to 60 % with a transient clamping close to the weld seam and a cold release for a T-joint.

According to Radaj [90], the residual stresses due to previous fabrication processes may have a high repercussion on the final distortions and should be implemented in the simulation model. The consideration of the forming process in a structure welding simulation has been investigated by Papadakis and Zaeh [115, 116]. The main difficulty of this approach is the transfer of the residual stresses calculated with 2D model from the forming simulation in a 3D welding simulation model. Actually, this virtual process chain method between the forming simulation and the structure welding simulation is still not state of the art in the automobile industry.

2.3.4 Experimental validation

As previously mentioned, experimental data is required in a structure welding simulation to calibrate and validate the thermal and mechanical models. An accurate simulated temperature field is a prerequisite for further mechanical simulations. Since the phenomenological heat source formulation is not directly related to the real welding process parameters, its distribution parameters need to be calibrated. The heat source model is considered calibrated when the resulting simulated shape and size of the fusion zone during the welding process match the real one [56, 102]. Since a complete three-dimensional measurement of the fusion zone is not possible, temperature cycles close to weld seam are also used to calibrate the thermal model. Furthermore, their transient behaviour enables also checking the boundary conditions of the system.

Thermocouples are used to measure temperature cycles. Even if this technique is well-known and well documented [117], a clear directive for a welding simulation application has not been established yet. Many different types of thermocouples with different diameters are available for diverse applications. For welding simulation, thermocouples types K with a diameter ranging from 0.1 mm to 1 mm are commonly used. They are robust, accurate for a temperature range from ambient temperature up to 1300°C. An alternative to thermocouples is a thermographic camera. The main advantage of the technique in comparison to thermocouples is its contact free application [118, 119]. Practically, the radiations occurring during the welding process falsify the temperature measurements and the use of special filter is therefore required. Even with an optimal application, the temperature cycle measurements with this technique are still not as accurate as with thermocouples today.

The measurement of the fusion zone shape is commonly made in 2D via a metallographic cross-section perpendicular to the weld seam. The width and the length of the weld-pool can also be measured during the welding process at the top surface with a CCD or with a high-speed camera.

For the validation of the mechanical simulation of distortions, displacement sensors can be used for a static and a transient measurement at single points. This solution is however inaccurate for large distortions; the start location of the investigated points can move out of the sensor position during the deformation process. For more accurate measurements, an optical 3D deformation analysis system enables getting transient and static results for a single point or a field. With this technique, the deformation of a fine pattern previously applied on the surface of the investigated part can be measured with a set of high-resolution cameras.

2.4 Welding simulation of complex structures

2.4.1 Industrial applications

The advantage of virtual tools has already been recognised in many industry sectors. For instance, computational fluid dynamics and computational solid dynamics models have been used in the industry for more than three decades [2]. The potential to reduce the cost and time consuming trial and error experimental procedures required to minimise the negative heat effect of welding with virtual methods is high. The advantage of welding simulation tools can be briefly summarised as follow [120]:

- Parameter sensitivity
- Decreasing the global development cost with a virtual pre-investigation
- Better understanding and interpretation of the experimental behaviour
- Extrapolation of the virtual results on other experimental test cases

Many simulation tools have been created to simulate the heat effects of welding. An overview of the existing welding simulation tools has been published in [121] in 1999. Since then, new welding simulation software packages have become available but an actual overview is not available. Even with this high number of software solutions, the industrial application of welding simulation for complex structures is not widely established yet. The few example applications available in the literature are presented in the following.

In the automotive industry, Rethmeier optimised the radial distortions during the laser welding of circumferential weld seams of three different automotive parts, a valve needle, a valve seat and a tube cup weld [122, 123]. The multi-purpose FE-software Ansys was used. The simulation results enabled optimising the global radial distortions from a laser welding process. A similar optimisation on circumferential weld seams has been made on a fuel injection unit by Shirai [124]. The optimal radial distortion was found for a twin laser beam with 90° separation in comparison with a single weld seam and a twin laser with 180° separation. Schwenk optimised also with Sysweld the radial distortions of a gearwheel welded with electron beam welding [125]. Saint-Germain showed the influence of viscoplasticity on a ferritic steel to simulate the residual distortions for a semi-industrial part [126, 127]. For the simulation, he combined the FE-code Abaqus with the software METAL7 to take into consideration the material behaviour. Saint-Germain later applied this model to simulate the welding of a rear axle of the Renault Mégane [126]. Unfortunately, no comparisons with experimental data for the thermal simulation and for mechanical simulation are available. A good appreciation of the simulation results can therefore not be done. With Sysweld, Häuser simulated the residual distortions of a Motorcycle rim [128, 129]. As in the previous example, no comparisons with experimental data have been made. Hackmair studied the influence of the welding sequences, welding direction, clamping conditions, and welding gap on the final distortions of a front axle carrier of a BMW series 7 with Sysweld [106, 130]. Grün also analysed the residual distortions of a rear axle carrier with Sysweld. He investigated the influence of the energy input on the final distortions; no comparison with experimental data is available [131]. Veneziano calculated the residual distortion of a B-pillar from the AUDI A2 with Sysweld and characterised the influence of the heat input, the clamping condition and the welding sequences on the residual distortions. He also investigated the residual distortions of an engine cradle [79]. With the welding

simulation software “Schweißplaner”, the residual distortions on a B-pillar from a VW Golf A5 could be simulated in 1.4 hours. To achieve this short simulation time, all the welds are heated up in on time step and the corresponding inherent thermal strains around the weld seam are calculated with simple formulations and used as input data in an elastic FEM model to simulate the global distortions of the structure [132]. It needs to be noted that only qualitative statements can be done with this technique. This software “Schweißplaner” has been developed from company INPRO and is commercially available since 2009 from the French company ESI under the name “WeldPlanner”.

In the literature of the aeronautic and shipbuilding industry, a few structure welding simulation examples can be found. In comparison to the previous automotive welded assemblies, their geometries are in general simpler but larger which makes their respective computational times an extremely critical point to take into consideration. Thus, the structure welding simulations of a large shipbuilding structure and a hat shaped structure have been carried out in [133-136]. The influences of different welding sequences and clamping boundary conditions have been focused on. In these publications, the simulation techniques were in the foreground and the simulation results are only briefly compared against experimental data. Rieger also simulated the welding distortions of a large panel for the shipbuilding industry [16]. For this simulation, he used the process simulation software SIMWELD [13, 15] to calculate the parameters of the phenomenological heat source model, and implemented them later as input data in a structure welding simulation model with Sysweld. With this technique, he could save some iteration loops for the calibration of the thermal model. Finally, Deng simulated a large ship structure with the inherent strain techniques [137]. He investigated the influence of the gap and misalignment defaults on the final distortions. For the aeronautic industry, Ploshikhin also implemented the inherent strain techniques in the CAE-Tool INSOFT. In [138], he showed the simulated distortions of a large panel with a calculation time lower than 30 min. The simulation results are nevertheless not compared to experimental data and only qualitative statements are possible. Finally, Darcourt ran a thermomechanical analysis of a laser beam welded Airbus A380 stiffened panel [139, 140]. As Rieger, she used a process model, DB-LASIM [19], to find the parameters of the phenomenological heat source model and then employed the finite element code MSC-Marc for the rest of the simulation. The simulation results are only briefly compared with experimental data.

All the industrial applications of welding simulation described in this section have been run with different software and simulation methods by expert users at the university or in research institutions. For a typical industrial user without welding simulation expertise, the choice of the right simulation model is a difficult task. The implementation of a welding simulation software without enough expert knowledge in this field can lead to wrong expectations of the simulation results and finally the potential error of an improper application is very high [141]. Thus, to guarantee an industrial application of welding simulation, standards regarding the procedure, the analysis and the post-processing of a transient 3D structure welding simulation should be established. This has been done recently by the German Institute for Standardization DIN and a standard for transient 3D structure welding simulation is available since 2011 [142].

2.4.2 Techniques to decrease time to solution

Despite a 3D welding simulation model with full complexity always guarantees the best quantitative and qualitative simulation results, the respective computational task can be high for large structures with long welds. Alternative techniques have been developed in order to decrease the global simulation time and are briefly presented in the following section.

The adaptive meshing technique is often used to decrease the number of degrees of freedom of the simulation model [143-145]. The technique consists of refining the mesh around the moving heat source to map the high gradient temperature occurring in this area. More information about this technique is available in [146-148]. With this technique, Lindgren [143] could apparently reduced the computational time by 60% without losing any accuracy in comparison with a traditional 3D fine meshing. Here, it should be noticed that this statement could not be properly verified with representation of the simulation results in the paper. Duranton [145] applied also this technique for multi-pass welding. In the literature, this technique is divided in dynamic and adaptive meshing techniques. For the dynamic technique [110], the mesh is refined around the moving heat source and is coarsened again after the heat source. This technique enables saving even more computational time but Roeren saw this re-coarsening after the moving heat source as a source of error for the calculation of residual stresses [108].

Another technique consists in modelling the structure only with 2D shell elements. This technique was already used in the 1980's for large geometries [149, 150]. On the computational time side, Faure could reduce his simulation time by four in comparison to a 3D analysis [87]. The implementation of this type of elements is nevertheless only adapted for 2D temperature field [151]. For a laser beam welding process on a thin plate for instance (characterised by a 2D temperature field), Papadakis [115] showed that he could reproduce the 3D welding simulation results of Schwenk [89] well with a simulation model containing 2D shell elements. For a 3D temperature field test case, Faure showed that even with a shell element formulation enabling a "quadratic through the thickness" variation temperature, the resulting temperature field could not match with a reference 3D temperature field simulation.

The hybrid meshing technique consists of a coupling of 3D solid elements with 2D shell elements. This technique is actually the most widespread for the simulation of thin structures. The weld seam and the HAZ are represented with 3D solid element and the rest of the structure is designed with 2D shell elements. Näsström and Gu [152, 153] already applied this technique for welding simulation in the beginning of the 1990's. Faure makes a combination of this technique with the adaptive mesh refinement technique [87, 154]. The connectivity of the 3D elements and the 2D elements has been improved by Duan in [155].

Souloumiac et al. [133, 134] proposed the local-global technique, which is another variant of the hybrid meshing technique. The method consists of only simulating the HAZ (thermo-elastic–plastic simulation) on a local 3D mesh with solid elements and then projecting the resulting plastic deformation as initial deformation on the 2D mesh with shell elements of the global structure. The distortions are then simulated with a simple elastic analysis. The definition of the dimension of the local model and the boundary conditions between the

local and the global model is a difficult aspect of this method and has been investigated by Duan [156, 157]. Hackmair [106] highlights that this method does not allow to consider the interaction between close weld seams and the reciprocal effect of the global structure on the local 3D mesh. The potential to decrease the welding simulation time with this technique is high. Its optimal implementation is nevertheless non trivial and still reserved for expert users in welding simulation. A wide implementation of this technique for industrial applications is therefore not possible yet [106].

Michaleris et al. [158, 159] and Ueda [160] proposed the inherent strain technique to accelerate the welding simulation of large structures. With this method, the deformations in the HAZ due to the welding process are replaced by elastic equivalent forces calculated with the inherent strain in the HAZ. This approach enables substituting a conventional thermomechanical 3D FEM analysis and requires less computational resources. These inherent strains are mostly calculated on a local 2D welding simulation model; the resulting welding loads (calculated with the elastic equivalent forces) are implemented in a coarsened 3D structure model. Simplified analytical models have been published to calculate the inherent strains from Murakawa et al. [161-163]. Recently, Deng [164] compared this method to a traditional thermomechanical FE-analysis for the distortion simulation of thin sheets. The results of the simplified inherent technique match the referenced thermomechanical FE-simulation well. The computational time of 1 min is very fast in comparison to the 12 hours required for the traditional technique. With this technique, he also investigated the influence of initial gap and misalignment before the welding process on welding distortions with the implementation of interface elements between the welded parts [137].

For all the simulation techniques presented in this section, the optimisation of the computational time only was in the foreground. It is nevertheless important to notice that the calibration of the thermal model, which is a prerequisite for an accurate welding induced distortion prediction, has not been taken into consideration. For large structure, however, the entire time to solution, e.g. calibration time, simulation time and postprocessing time, should be optimised to enable a possible implementation in an industrial environment.

3 Execution of experiments

3.1 Required data for welding simulation

In this section, the temperature dependent thermophysical and thermomechanical material properties of the investigated materials are presented. Furthermore, all the information required for the understanding of the experimental settings, i.e. welding processes, clamping conditions, measurement data, etc…, and later of the corresponding simulation models are also described.

3.1.1 Material properties

3.1.1.1 Steel DX 56 D+Z140

The steel DX 56 D+Z140 with the material number 1.0322 is an unalloyed cold rolled deep-drawing quality steel. The term Z140 corresponds to a $140\,g \cdot m^{-2}$ hot-dip galvanised coating with a thickness of approximately 9.8 µm, according to the standard DIN EN 10327 [165]. This steel has an excellent formability, is fairly resistant to aging and can be joined easily by spot welding or GMAW. Examples of application are in the automotive industry for complex body outer and inner panels, fenders, side panel frames. The maximum chemical composition in weight percent of this steel is given by the standard DIN EN 10327. In order to guarantee that the delivered material corresponds well with the corresponding standard, its chemical composition has been measured with spark emission spectrometry. Both standard and measured values are presented in Tab. 3.1:

Tab. 3.1: Maximal chemical composition (in weight %) of the steel DX 56 D+Z, according to DIN EN 10327

Material	Chemical composition in weight %						
	C	Si	Mn	P	S	Ti	Fe
DX 56 standard*	0.12	0.50	0.60	0.10	0.045	0.30	bal.
DX 56 delivered	<0.1	0.01	0.10	0.006	0.007	0.07	bal.

*Maximal values

The measured amount of each element of the delivered steel DX 56 D+Z is below the corresponding value given in Tab. 3.1. The requirement of the standard DIN EN 10327 is therefore fulfilled.

The mechanical properties of the steel DX 56 D+Z are given in Tab. 3.2:

Tab. 3.2: Mechanical properties of the steel DX 56 D+Z, according to DIN EN 10327

Material	$R_{p0.2}$ in MPa	R_m in MPa	$A_{80,\min}$ in %
DX 56 standard	120-180	260-350	39

The measurement of the temperature dependent thermo-physical material properties, specific heat capacity, heat conductivity and density, required for the temperature field simulation was not part of this Ph.D. thesis. In the literature, these values for the steel DX 56 D+Z are not available. For this study, they have been given by the steel producer ArcelorMittal Automotive Europe. The specific heat capacity and the heat conductivity have been calculated with the commercial software Thermocalc. The density has been measured at room temperature by pycnometry and its evolution in temperature has been derivated from the measurement of the thermal expansion using a dilatometer. All these temperature dependent thermo-physical material properties are available from 0°C up to 1500°C and plotted in Fig. 3.1:

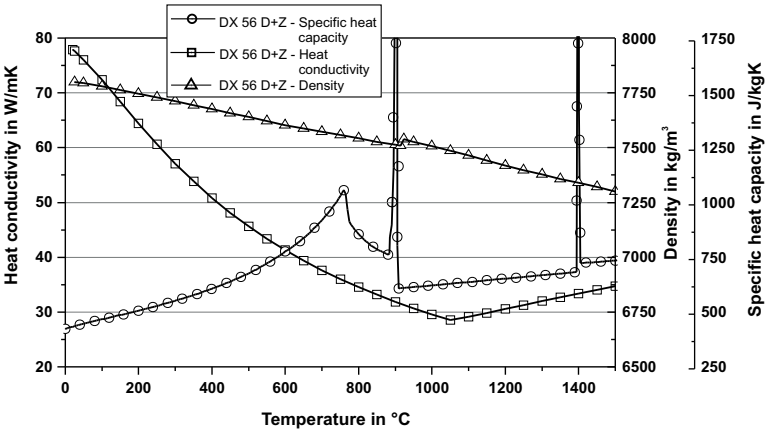

Fig. 3.1: Calculated temperature dependant thermo-physical material properties of the steel DX 56 D+Z140, data given by ArcelorMittal Automotive Europe

3.1.1.2 Steel HX 220 YD+Z140

The steel HX 220 YD+Z140 with the material number 1.0923 is a low alloyed cold rolled high-strength IF steel. The particularity of this steel is that interstitial carbon and nitrogen are removed (the term IF stands for “interstitial free”) from its ferritic matrix giving it a particularly good weldability and an excellent aging behaviour. Due to its relative good elongation $A_{80,min}$, see Tab. 3.4, this steel is also suitable for deep drawing operations. Its application field is similar to the steel DX 56 D+Z but it is used where a higher strength is required. The term Z140 corresponds to the same hot-dip galvanised coating as with the steel DX 56 D+Z described previously. The properties of this steel are defined in the standard DIN EN 10292 [166]. The validity of the delivered steel HX 220 YD has been done by comparing the maximal percentage by mass of its chemical composition given by the

standard DIN EN 10292 with the corresponding real values measured with spark emission spectrometry as shown in Tab. 3.3:

Tab. 3.3: Maximal chemical composition (in weight %) of the steel HX 220 YD, according to DIN EN 10292

Material	Maximal chemical composition in weight %								
	C	Si	Mn	P	S	Ti	Al	Nb	Fe
HX 220 standard*	0.01	0.2	0.90	0.080	0.025	0.12	0.10	0.09	bal.
HX 220 delivered	<0.01	0.01	0.40	0.061	0.008	0.02	0.04	0.02	bal.

*Maximal values

The quantity of each element of the steel HX 220 YD is below the corresponding maximum value of the standard DIN EN 10292 given in Tab. 3.3. Therefore, the investigated material corresponds with the standard.

The mechanical properties of the steel HX 220 YD are shown in Tab. 3.4:

Tab. 3.4: Mechanical properties of the steel HX 220 YD, according to DIN EN 10292

Material	$R_{p0.2}$ in MPa	R_m in MPa	$A_{80,\min}$ in %
HX 220 standard	220-280	340-410	32

As for the steel DX 56 D+Z, the temperature dependent material properties have been provided by the steel company ArcelorMittal Automotive Europe. The exact material properties from the steel HX 220 YD were not available. Instead, ArcelorMittal Automotive Europe supplied the value for two similar steels HX 180 and HX 260, also from room temperature up to 1500°C as plotted in Fig. 3.1:

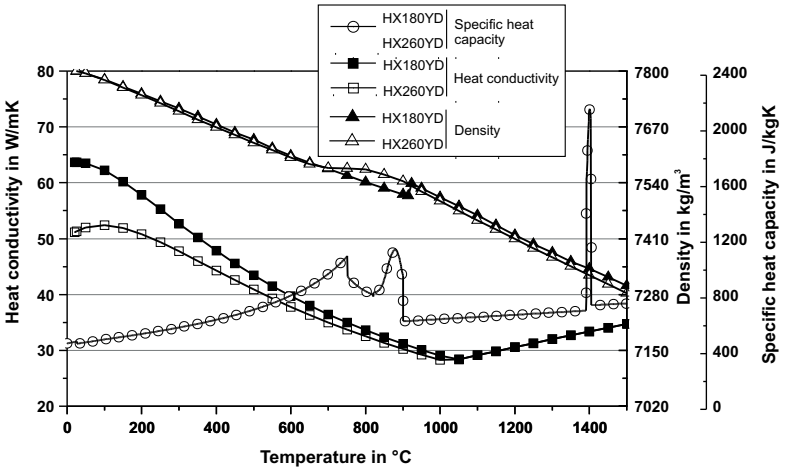

Fig. 3.2: Calculated temperature dependent thermo-physical material properties of the steels HX 180 YD and HX 260 YD, data given by ArcelorMittal Automotive Europe

3.1.1.3 Aluminium AW6106 – T6

The crossbeam welded assembly, see section 3.1.3.2, is made from a precipitation hardening aluminium alloy of the series 6xxx, precisely noted AW6106 – T6. This material has good mechanical properties in comparison to a standard aluminium alloy resulting from a tempering treatment indicated with the term "T6". During the fabrication process, β''-Mg_2Si particles are precipitated in the aluminium lattice and restrain dislocation movements. This results in an increase of the yield strength [167]. The requirements of this alloy and more generally of the aluminium of the series 6xxx in means of their extrusion characteristics and their mechanical properties can be found in the Volkswagen group standard TL 116 [168]. The chemical composition of all aluminium alloys of the series 6xxx can be found in the standard DIN EN 573-3 [169]. According to the standard DIN EN ISO 18273 [170], the AlSi12 filler material is well appropriate for the MIG welding process of this aluminium alloy. Here, the filler material from the company MIG WELD [171] has been used. The chemical composition of the aluminium AW 6106 and the filler material AlSi12 are presented in Tab. 3.5:

Tab. 3.5: Chemical composition (in weight %) of the aluminium alloy AW6106 and the filler material AlSi12, according to DIN EN 573-3 and MIG WELD material datasheet

Material	Chemical composition in weight %									
	Si	Fe	Cu	Mn	Mg	Cr	Zn	Be	Ti	Al
AW6106	0.3-0.6	<0.35	<0.25	0.005-0.2	0.4-0.8	<0.2	<0.1	-	-	bal.
AlSi12	11-13	<0.6	<0.3	<0.15	<0.1	-	<0.2	<0.0003	<0.15	bal.

In the Volkswagen group standard TL 116 [168], extruded profiles are divided into crash and non-crash relevant parts. In addition to all the requirements that the non-crash relevant parts have to fulfil, the crash relevant part must also pass a compression test. Therefore, their chemical composition may differ a little from non-crash relevant parts. In the welded assembly investigated in this study, both crash relevant and non-crash relevant aluminium parts are present. Their respective chemical compositions and also those from the filler material AlSi12 have been measured with spark emission spectrometry and are given in Tab. 3.6:

Tab. 3.6: Chemical composition (in weight %) of the aluminium AW6106 crash relevant and non-crash relevant and of the filler material AlSi12, measured with spark emission spectrometry

Material	Measured chemical composition in weight %									
	Si	Fe	Cu	Mn	Mg	Cr	Zn	Be	Ti	Al
AW6106 – CR*	0.56	0.16	0.13	0.11	0.41	-	0.01	-	-	bal.
AW6106 – NCR**	0.56	0.24	-	0.05	0.48	-	-	-	-	bal.
AlSi12	12.1	0.19	0.025	0.003	0.001	-	0.0015	-	0.0017	bal.

* CR: Crash relevant part; ** NCR: Non-crash relevant part

The mechanical properties of the crash and the non-crash relevant aluminium alloys are identical according to the Volkswagen group standard TL 116 and are presented in Tab. 3.7 with the mechanical properties of the filler material AlSi12:

Tab. 3.7: Mechanical properties of the aluminium AW6106 and of the filler material AlSi12, according to DIN EN 573-3 and MIG WELD material datasheet

Material	$R_{p0.2}$ in MPa	R_m in MPa	$A_{80,\min}$ in %
AW6106	200-245	≥ 220	≥ 11
AlSi12	60	130	5

For a precipitation hardening aluminium alloy, it is well-known that the welding process is responsible for a softening effect of the mechanical properties in the heat affected zone [25]. For this reason, the temperature dependent thermophysical material properties for the BM and for the HAZ have been used in the welding simulation model. Since the measurement of these data was not possible during this Ph.D. thesis, data from the literature have been enquired. A complete data set for welding simulation, e.g. the temperature dependent thermo-physical and thermomechanical data for the HAZ and the BM, could be found for a similar aluminium alloy AW6060 in [79, 172]. A comparison of the chemical composition of the aluminium AW6060 with the aluminium AW6106 is presented in Tab. 3.8:

Tab. 3.8: Comparison of the chemical composition of the investigated aluminium AW6106 with the aluminium AW6060 from [79]

Materials	Chemical composition in Mass -%							
	Si	Fe	Cu	Mn	Mg	Cr	Zn	Al
AW6106 – CR*	0.56	0.16	0.13	0.11	0.41	-	0.01	bal.
AW6106 – NCR**	0.56	0.24	-	0.05	0.48	-	-	bal.
AW6060 [79]	0.48	0.14	0.11	0.13	0.43	0.01	-	bal.

* CR: Crash relevant part; ** NCR: Non-crash relevant part

The chemical compositions of AW6106 and AW6060 correspond well. Furthermore, according to [173], the heat conductivity of AW6106 at room temperature is $160\,\mathrm{W}\cdot\mathrm{m}^{-1}\cdot\mathrm{K}^{-1}$ which suits AW6060 well. Therefore, the thermo-physical and thermomechanical material parameters of AW6060 have been used in this study.

For the welding simulation of the crossbeam assembly, the BM and the HAZ material properties have been implemented as explained in section 3.3.6. The thermo-physical material parameters for both BM and HAZ are identical and are plotted in Fig. 3.3:

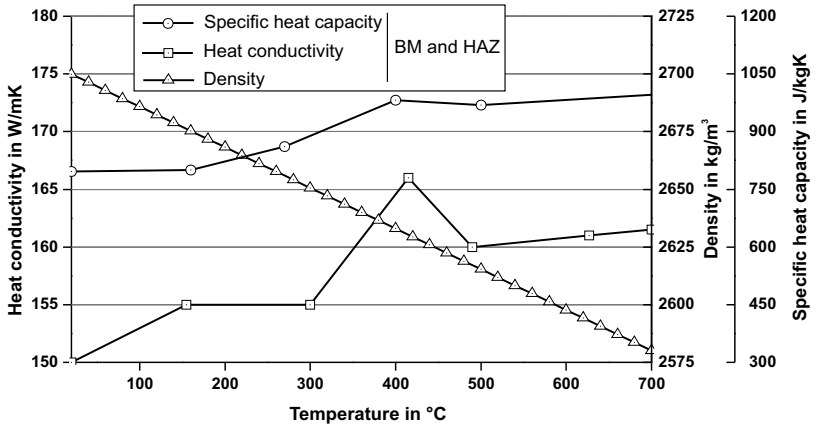

Fig. 3.3: Temperature dependent thermo-physical material properties of the aluminium alloy AW6060 for the BM and the HAZ, according to [79] and [172]

In addition to the wheelhouse welded assembly, a thermomechanical distortion analysis has been done for the crossbeam assembly. For this simulation, temperature dependent Young's modulus, thermal expansion and flow curves are required. These data have not been measured and have been found in the same literature source in [79] and [172]. For both BM and HAZ, the temperature dependent Young's modulus and thermal expansion are identical and are plotted in Fig. 3.4.

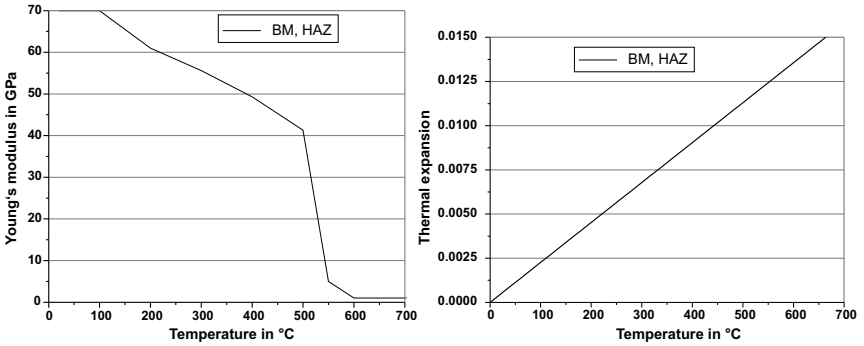

Fig. 3.4: Temperature dependent Young's modulus and thermal expansion of the aluminium alloy AW6060 in the BM and in the HAZ, according to [79] and [172]

The flow curves for the aluminium alloy AW6106 from 20°C up to 600°C have been published in [172] for the BM and the HAZ and are plotted in Fig. 3.5. The temperature dependent yield stresses (for the BM and the HAZ) of the aluminium alloy AW6106 can be derived from the start value of each flow curves (corresponding to the yield stress $R_{p0.2}$) as show in Fig. 3.5 illustrating therefore the drop of strength in the HAZ due to softening effect occurring during the welding process.

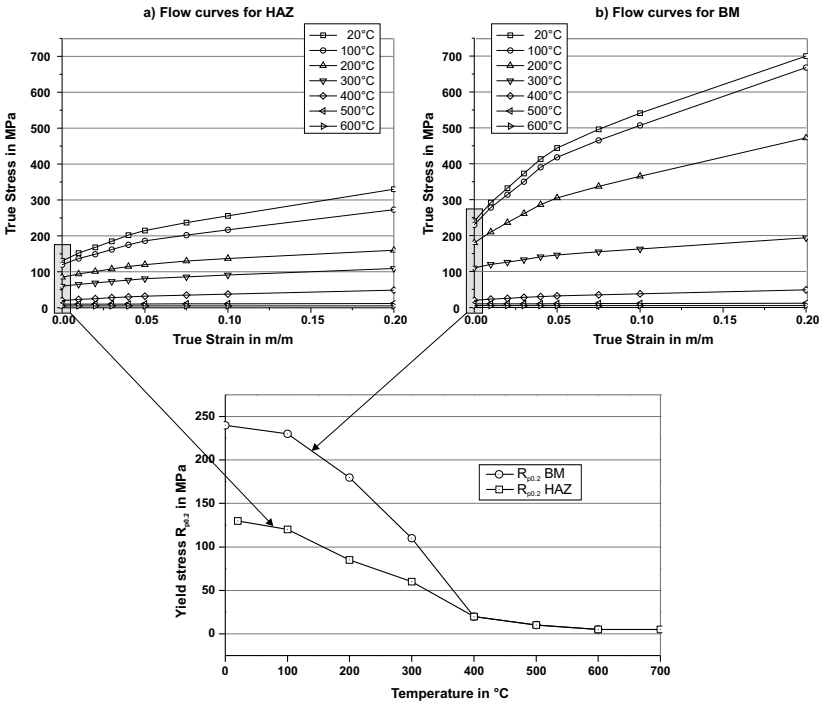

Fig. 3.5: Flow curves of the aluminium alloy AW6060 from 100°C up to 600°C and temperature dependent yield stress for the BM and the HAZ, according to [172]

3.1.2 Welding process parameters

The sheets and the two automotive welded assemblies investigated in this study have been welded with a laser beam welding process for the steel parts and with a MIG welding process for the aluminium parts. Both welding processes and the respective welding parameters are described in the following chapter.

3.1.2.1 Laser beam welding

All the steel parts investigated in this study have been joined with a 4.4 kW diode pumped Nd:YAG laser type DY 044 from the company Rofin Sinar.

A mixed shielding gas 82 % argon 18 % carbon dioxide has been used. All welds have been carried out with the same welding parameters. The welding sequences have been run automatically with a 6 axis robot – ROTROL 32 TM – from the company Cloos Schweißtechnik. The 1 mm thick sheets have been welded without filler metal.

Since the evaporation point of the galvanised zinc layer with 907°C is lower than the liquidus temperature of steel, a small gap of approximately 0.2 mm between the welded sheets is required so that the zinc vapour during the welding process can escape. The welding parameters used are presented in Tab. 3.9:

Tab. 3.9: Welding parameters, shielding gas and process characteristics for the laser beam welding of the steel sheets and the wheelhouse

Welding parameters		**Shielding gas**		**Process characteristics**			
Laser power	v_s*	Type	Flow rate	Focal distance	Focus position	Focus diameter	Gap (between sheets)
in kW	in cm/min		in l/min	in mm	in mm	in mm	in mm
3.3	300	82% Ar 18% CO_2	15	200	0 (at top surface)	0.6	0.1 – 0.2

*v_s is the welding speed

3.1.2.2 Pulsed GMAW

The crossbeam assembly has been welded with a pulsed GMAW (GMAW-P) MIG with the welding power supply PHOENIX 521 EXPERT from the company EWM. A 1.2 mm AlSi12 filler material has been used. In order to run all the welding tasks automatically, the welding torch system has been implemented on a industrial 6 axis robot – ROMAT® 400 – from the company Cloos Schweißtechnik [174]. The thickness of the welded parts is approximately 3 mm. All the welds have been carried out in an overlap-joint configuration with the same welding parameters summarised in Tab. 3.10:

Tab. 3.10: Implemented welding, shielding gas and robot parameters for the pulsed GMAW of the welded assembly made of aluminium

Welding parameter								
U_{ave}	I_{ave}	v_s*	v_{filler}*	I_b	I_p	t_b	t_p	F
in V	in A	in cm/min	in m/min	in A	in A	in s	in s	in Hz
22	162	100	7	120	240	0.003	0.002	200

*vs and vfiller are the welding speed and the filler material speed

Shielding gas		**Robot**	**Process characteristics**			
Type	Flow rate	Amplitude of weaving motion	Stick out	Angle of attack	Welding position	Nozzle orientation
	in l/min	in mm	in mm	in degree		in degree
Argon 5.0	25	4.5	13	25°	PA	Trailing 15°

The welding parameter U_{ave} and I_{ave} correspond to the average voltage and current. These values are useful to calculate the total energy input of the welding process required for the simulation later on. In order to characterise a GMAW-P process, several pulse parameters such as pulse current (I_p), base current (I_b), pulse time (t_p), base time (t_b) and pulse

frequency (F) at different arc voltages (automatically controlled by the welding power source) are required. These parameters and the process characteristics of the GMAW-P are illustrated in Fig. 3.6a.

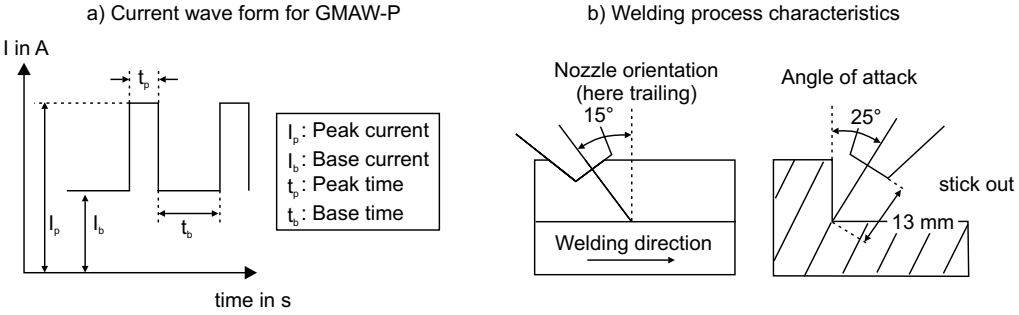

Fig. 3.6: a) Current wave form for GMAW-P - b) Representation of welding process characteristics

3.1.3 Welded assemblies

3.1.3.1 Wheelhouse and simplified geometries

The automotive steel welded assembly investigated in this work is a wheelhouse and belongs to the Audi A6 C6 car body as presented in Fig. 3.7. The two welded parts are both ferritic deep-drawing sheet metal parts with a thickness of 1 mm as described in section 3.1.1.1. The two parts are laser-beam welded with four parallel joints, from W1 up to W4 as represented in Fig. 3.7, with a total weld length of approximately 600 mm. The welding process takes approximately 20 seconds. No filler material is used. All the clamping units are simultaneously released after the welding process stops.

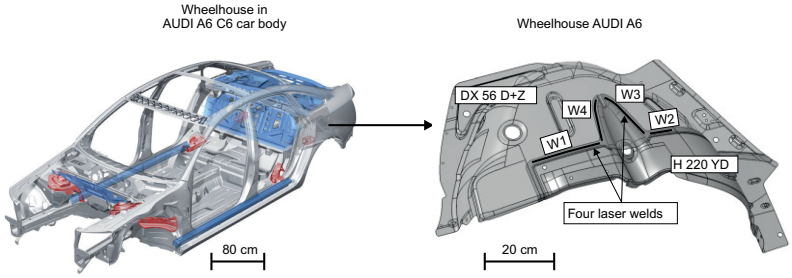

Fig. 3.7: Position of the wheelhouse in the AUDI A6 (type C6) car body - welding sequence from the weld W1 to the weld W4

The laser beam welding process introduced in section 3.1.2.1 has been used to join this automotive welded assembly. The welding parameters have been described in Tab. 3.1, see page 32. For the experimental part of this study, the measurements could not be made on the Audi production line and a clamping fixture has been designed as shown in Fig. 3.8:

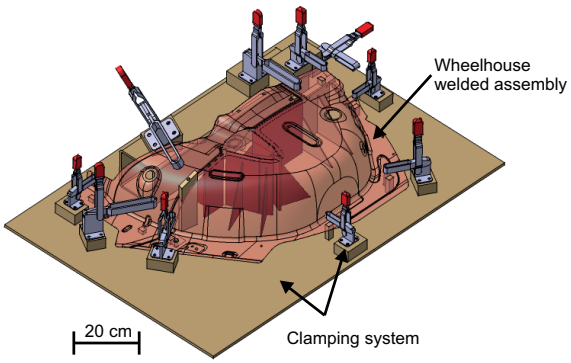

Fig. 3.8: Reproduction of the real clamping fixture for the wheelhouse welded assembly

In the vicinity of the parallel joints W1 to W4, where the curvature of the sheet metal is low, the geometry of the welds can be simplified with an overlap joint configuration as illustrated in Fig. 3.9a. Based on this observation, two simple geometries “overlap weld” and “parallel weld” have been investigated. Their respective dimension is shown in Fig. 3.9b und c. The welding of both simplified geometries has been carried out and all the experimental data required for the calibration of the thermal model, see section 3.1.4.1, have been measured. The same material as for the wheelhouse has been used. A gap of approximately 0.2 mm between the welded sheets has also been set to guarantee a good weld quality.

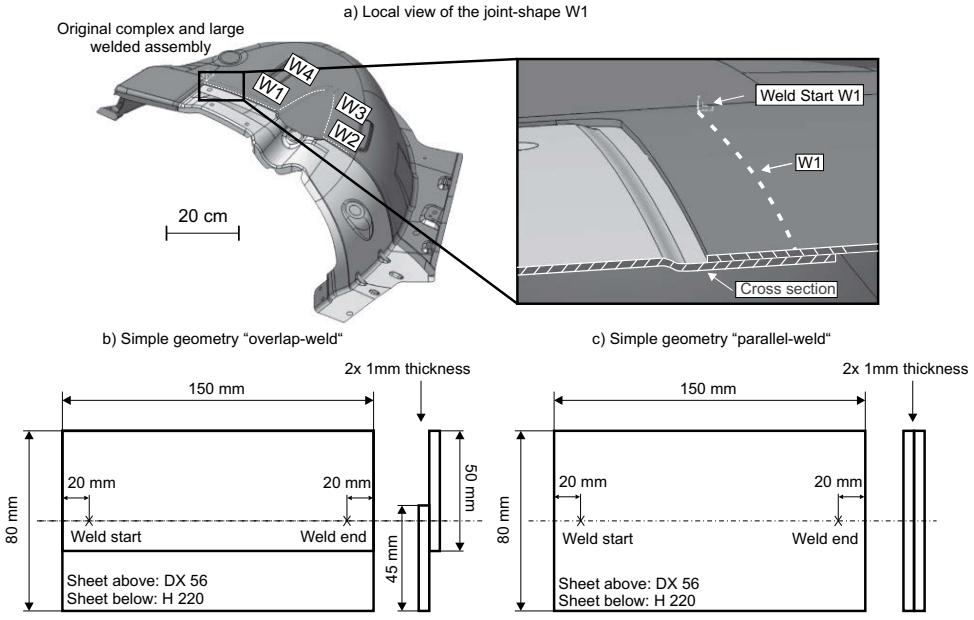

Fig. 3.9: a) Cross-section of the joint shape W1 - b) dimensions the simplified geometries “overlap-weld” – c) dimensions the simplified geometries “parallel-weld”

3.1.3.2 Crossbeam

The welded assembly investigated in this study, Fig. 3.10b), belongs to the rear part of an AUDI-Space-Frame (ASF®) of the Audi A8 D3. Its position in the car body is illustrated in Fig. 3.10a). It is composed of five aluminium extrusion profiles made of the AlMgSi alloy AW6106, see section 3.1.1.3. The four inserts are joined on the crossbeam with two MIG welds each, giving eight welds. The entire weld seam length is approximately 500 mm. The total welding time including robot movements is approximately 1.5 minutes. All the clamping units are simultaneously released after the last weld is finished. For more information about the welding process and welding parameters, see section 3.1.2.2.

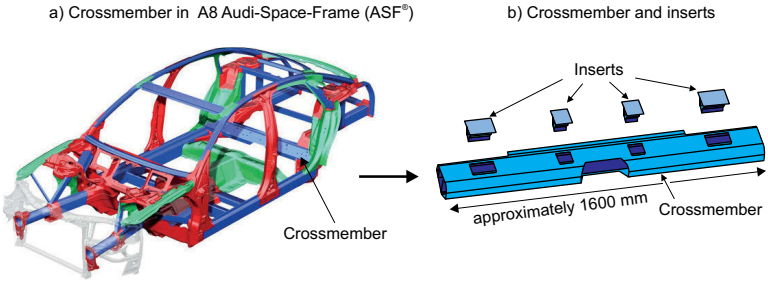

Fig. 3.10: Crossbeam and inserts, aluminium extrusions AlMgSi alloy, in the AUDI A8 (type D3) Audi-Space-Frame (ASF®)

The declaration of the four inserts, the welds and the welding direction are plotted in Fig. 3.11. The four inserts are named from I1 to I4, the welds are named Wxr and Wxl for the right and the left weld of the insert x, respectively. The entire welding process was done automatically from W1r to W4l. The welding parameters used in this study are comparable to those in the production line and are presented in Tab. 3.10.

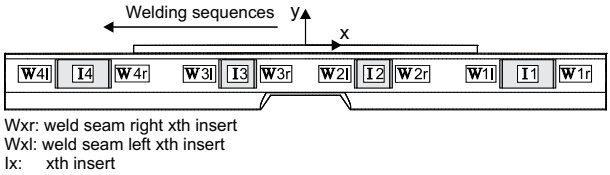

Fig. 3.11: Welds classification of the crossbeam welded assembly

For the experimental part of this study, the measurements could not be made on the Audi production line and a clamping fixture has been designed, Fig. 3.12. CC1 and CC2 are the clamping units of the crossbeam; CI1 to CI4 are the clamping units of the inserts. In the real production line, each clamping unit is released at the end of the welding process. For this study, one clamping unit must stay active to get a fixed reference point on the crossbeam, which is required for the measurements of the transient distortion distributions. Here, the clamping CC1 has been fixed during all the welding process and the cooling time.

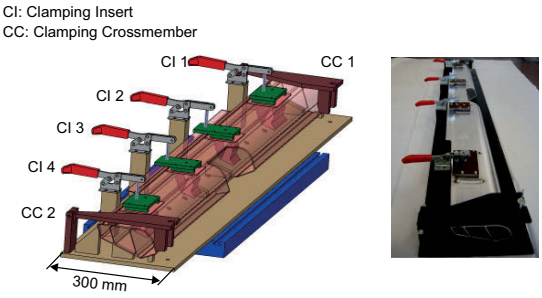

Fig. 3.12: Reproduction of the real clamping fixture for the crossbeam welded assembly

3.1.4 Experimental data

According to the standard DIN SPEC 32534-1 [142], the thermal model of a welding simulation must be partially or completely validated against temperature cycle measurements and against the real geometry of the fusion zone. This validation phase is a prerequisite for further mechanical simulation of distortion. In this section, the measurement settings used to validate the thermal and mechanical simulation models are presented. For each measurement data used for the validation of the simulation model, several experiments have been carried out in order to get an experimental scatter band.

3.1.4.1 Temperature measurements for the wheelhouse and simplified geometries

Since the wheelhouse was not a distortion relevant welded assembly by Audi, no distortion measurement (and also no distortion simulation) has been carried out. This welded assembly has been selected to investigate the application of analytical temperature field solutions on complex and large geometries. Therefore, all the data required to validate the thermal model, according to the standard DIN SPEC 32534-1 [142], have been measured.

For the transient temperature cycle measurements, six thermo-couples, T1 up to T6, have been spot-welded approximately to the middle of the weld W1 (four thermocouples) and W3 (two thermocouples) as represented in Fig. 3.13. For the simplified geometries “overlap-joint” and “parallel-joint”, four thermocouples T1 up to T4 have been spot welded in the same configuration as for the weld W1 of the wheelhouse in the middle of the weld trajectory.

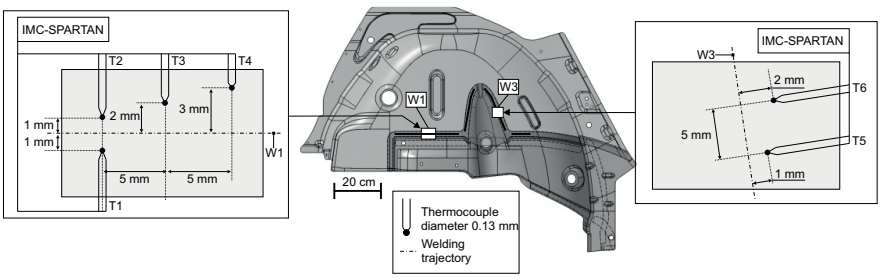

Fig. 3.13: Thermocouple positions on the wheelhouse

All the transient temperature cycle measurements have been carried out with the measurement system SPARTAN from the company IMC integrated measurement & control. Thermocouples of type K (Ni/CrNi) with a diameter of 0.13 mm have been used. A sampling rate of 200 Hz has been chosen in order to capture the high gradient temperatures around the welds. The position of the thermocouples has been determined from the centre line of the weld from a photograph of the weld.

The weld pool shape in the thickness of the welded assembly has been determined with a metallographic cross-section perpendicular to the weld's direction, according to [142]. In order to accentuate the visibility of the fusion line, a Nital etch has been used.

For the measurement of the weld pool length, the high-speed camera Photron Fast-cam-X 1024 PCI from the company VKT Video Kommunikation GmbH has been implemented with a sampling rate of 500 fps.

3.1.4.2 Temperature and distortion measurements of the crossbeam

In comparison to the wheelhouse, the crossbeam is much more rigid. In this case, the welding induced distortions cannot be compensated easily in further production steps and could handicap or even prevent further assembling operations. A virtual prediction of the welding induced distortion is therefore relevant and has been analysed in this work, see section 3.3.6. Thus, all the temperature data required to calibrate the thermal simulation model have been measured; static and transient distortion data have also been measured to validate the final simulation result. The experimental set-up for the transient temperature cycles and the distortion measurements is represented in Fig. 3.14:

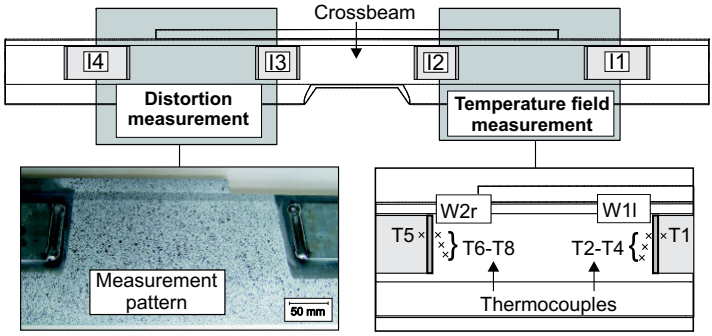

Fig. 3.14: Crossbeam measurement set-up: eight temperature cycles with thermocouples plus a transient distortion distribution of a defined pattern with an optical 3D deformation analysis system

The eight temperature cycles T1 to T8 have been measured with thermocouples type K (Ni/CrNi) with a diameter of 0.25 mm; T1 to T4 for the weld W1l and T5 to T8 for the weld W2r as shown in Fig. 3.14. As for the wheelhouse measurements, the same measurement system is used, here with a sampling rate of 50 fps. Due to the weaving motion of the welding torch, the centre line of the weld could not be determined clearly. In order to guarantee a correct positioning of the thermocouples in the simulation model, their real

positions have been measured not from the centre line of the weld but from the visible fusion line on the upper surface of the weld assembly.

For the determination of the fusion zone geometry in the thickness of the crossbeam, several metallographic cross-sections have been taken in the middle of the weld W1r, W2l and W4l. The etch solution used to accentuate the visibility of the fusion line was the Dix-Keller reagent (a mixture of nitric acid, hydrochloric acid and hydrofluoric acid). The weld-pool length has also been measured with the high-speed camera introduced previously in section 3.1.4.1 on the weld W1r.

For the transient distortion measurement, the optical 3D deformation analysis system, Aramis, from the company GOM GmbH has been used. A stochastic pattern must be applied onto the specimen's measurement surface, which is located between the insert I3, and I4 as shown in Fig. 3.14 before the welding process. The transient evolution of the pattern during and after the welding process is then recorded by photogrammetric procedures and 3D displacement fields or transient distortion distributions at single points can be measured. For the analysis of the transient distortion distributions of the crossbeam, a point A has been selected on the stochastic pattern as shown in Fig. 3.15.

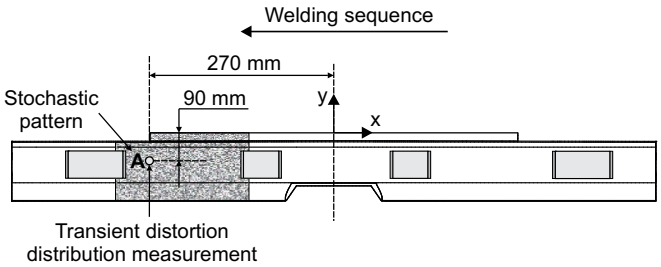

Fig. 3.15: Position of the point A for the transient distortion measurement during and after the welding process of the crossbeam

3.2 Analytical simulations

3.2.1 Computer and software

All the analytical simulations implemented have been run on a desktop PC (Intel® Core™ 2 CPU 6600 @ 2.4 GHz and 3 GB RAM) under Windows XP 32 bit. For the analytical temperature field solutions, which can be expressed in a closed form, the open source numerical computational software package Scilab has been implemented for the programming and the plot of the simulation results. For the analytical solutions which require numerical integration techniques, an adaptive Gauss integrator from the Gnu Scientific Library (GSL) [175] has been used. All the algorithms are implemented with in an in-house C++ code. The simulation results have also been plotted with Scilab.

3.2.2 Assumptions and simplifications

The application of the fundamental analytical temperature field solution for a point or a line source required the following assumptions and simplifications in the simulation model:

- The welding process is simplified to a heat conduction problem
- The material is solid at all times and at all temperatures, no phase transformations occur, and the material is isotropic and homogeneous
- The thermal conductivity, density and specific heat capacity are temperature independent
- Adiabatic boundary conditions are assumed for all surfaces
- The heat source moves on a straight welding path in an infinite plate
- The problem is in steady state. Transient states at the beginning and at the end of the welding process are neglected
- The heat source is considered to be a zero volume point or line source

With these assumptions and simplifications, the industrial application of analytical temperature field is restricted. Therefore, the extended analytical solutions applied in the following section enable considering also the following features:

- Transient state problem
- Thin samples
- Curved welding path
- Volumetrical heat source definition

3.2.3 Plates

The validation of the investigated analytical solutions presented in this section starts with the simplest analytical temperature field expression, which is the well-known point source in steady state moving in an infinite solid. Then, the degree of complexity of the physical problem is increased systematically until an analytical solution for volumetric heat source moving arbitrarily on a thin plate in transient state.

For all the simulations in this section, the following constant material properties were used. The heat conductivity is set to $21.45\,\mathrm{W}\cdot\mathrm{m}^{-1}\cdot\mathrm{K}^{-1}$, the specific heat to $565\,\mathrm{J}\cdot\mathrm{kg}^{-1}\cdot\mathrm{K}^{-1}$ and the density to $7735\,\mathrm{kg}\cdot\mathrm{m}^{-3}$. These values have been exemplarily taken from a steel at 400 °C. In this section 3.2.3, the simulation results are not related to experimental data and the implemented constant material properties could have been chosen for another steel at a different temperature.

3.2.3.1 Infinite solid – steady state – linear welding path – point heat source formulation

The first analytical simulation is done on an infinite solid. Since an infinite solid cannot be considered in a simulation model, a “quasi-infinite” solid with the dimension 200 x 200 x 100 mm^3 has been chosen to guarantee no influence of the transient effect at the beginning and at the end of the welding process. The experimental settings are shown in Fig. 3.16:

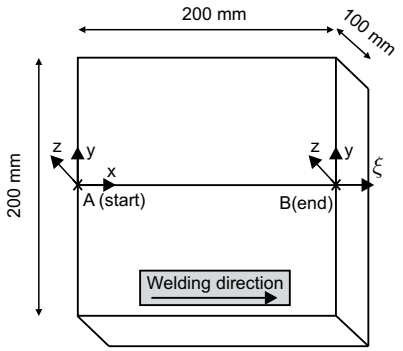

Fig. 3.16: Infinite solid 200 x 200 x 100 mm³ in steady state, linear welding path AB, analytical moving point source, q = 1.5 kW, and v_s = 10 mm/s

A moving point heat source moves from A to B with a welding speed of v_s = 10 mm/s and a net power of 1.5 kW. The analytical temperature field in the "quasi-infinite" plate in steady state for this moving point source is calculated with the analytical temperature field solution for an instantaneous moving point source in steady state given by the expression (2.11), see section 2.2.2. The temperature profile along the path AB is then calculated after the heat source reaches the point B (after 20 s). For the calculation, a step size of 0.5 mm along AB has been chosen making a total of 401 nodes for the temperature profile.

3.2.3.2 Infinite thin plate – steady state – linear welding path – point heat source formulation

For this test case, the plate is considered quasi-infinite in the plane (x,y) and has a finite thickness. For the validation of the presented method, two plates with the dimension 200 x 200 x 1.5 mm³ and 200 x 200 x 5 mm³ are investigated. Here it is worth to notice that the dimension 200 x 200 mm² is considered as infinite. A steady state is taken into account. The experimental settings are shown in Fig. 3.17

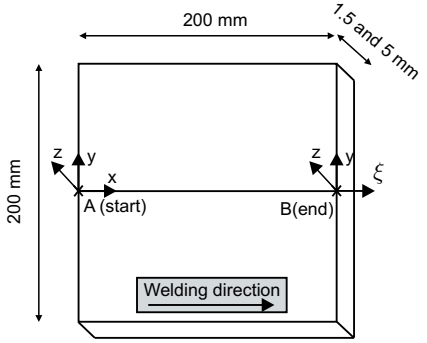

Fig. 3.17: Infinite thin plates 200 x 200 x 5 mm³ and 200 x 200 x 1.5 mm³ in steady state, linear welding path AB, analytical moving point source, q = 1.5 kW and v_s = 10 mm/s

The same configurations in means of welding characteristics and welding path as for the previous plate in section 3.2.3.1 have been used and the same temperature profile along

the path AB with 401 nodes is calculated after 20 s welding. In order to consider the finite thickness, the reflexion technique has been implemented. The same heat source as in the previous section plus a theoretically infinite number of virtual heat sources are acting simultaneously as described in detail in the state of research in section 2.2.2. The temperature field in steady state for a finite thickness is given by the expression (2.12) in section 2.2.2.

The infinite number of virtual heat sources cannot be considered in the simulation model. In practice, the equation (2.12) is a convergent series and the following two convergence criteria have been implemented in the analytical simulation model:

$$\frac{T_{n+1} - T_n}{T_n} \leq X\% \text{ and } T_{n+1} - T_n \leq T_c \tag{3.1}$$

With T_{n+1} and T_n the temperature for a point of the investigated plate at the n'th and the (n+1)'th reflexions, respectively. X% and T_c, which are the deviation in percent and the absolute deviation, respectively, have to be chosen by the user. Here and for the rest of this study, the following criteria have been set: X = 1 % and T_c = 1 K.

3.2.3.3 Finite thin plate – transient state – linear welding path – point heat source formulation

To guarantee a transient state, a finite (and small) thin plate 50 x 50 x 3 mm^3 is chosen and the welding path AB starts and ends 5 mm from the boundary of the plate. The welding characteristic, i.e. welding speed and power, are the same as in the two previous test cases. The experiment settings are plotted in Fig. 3.18.

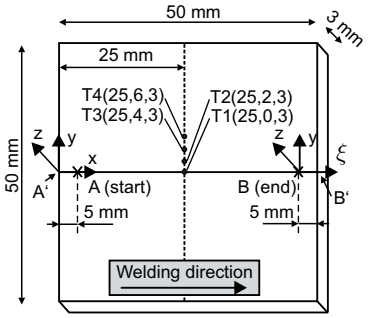

Fig. 3.18: Finite thin plate 50 x 50 x 3 mm^3 in transient state, linear welding path AB, analytical moving point source, q = 1.5 kW and v_s = 10 mm/s

A transient temperature field solution enables the calculation of the temperature at a single point in function of the time during the welding process and the cooling time. This technique is based on adding a virtual transient sink at the end of the welding process. More information is available in section 2.2.2. For this experiment, temperature cycles at four single points T1 to T4 and a temperature profile between A' and B', have been calculated. The temperature cycles have been calculated during the welding process plus 20 s cooling

with a time step of 0.05 s. For the temperature profile, a step size of 0.5 mm along A'B' has been chosen making a total number 101 nodes.

The transient analytical temperature field solution for a moving point source in an infinite body, see equation (2.14), has been implemented. In order to get the solution for a thin plate, the reflexion technique has been implemented in the thickness direction of the plate, see equation (2.12). For a finite thin plate, the heat transport is also limited before and after the moving heat source in the plane (xy) due to the small dimension of the plate. Consequently, the reflexion technique has also been implemented in the plane (xy) to guarantee a correct representation of the adiabatic boundary conditions for all boundaries of the finite thin plate.

3.2.3.4 Finite thin plate – transient state – linear welding path – double ellipsoidal heat source formulation

The experimental settings of this test case are exactly the same as in the previous section 3.2.3.3, see Fig. 3.18. The point heat source formulation is replaced by a volumetric double ellipsoidal source from Goldak [67]. The analytical formulation (2.18) has been used for this test case. In comparison with the previous analytical close form solutions, this analytical solution is in an integral form and can only be solved with numerical integration techniques. An adaptive Gauss integrator from the Gnu Scientific Library (GSL) [175] has been implemented for this task. The analytical solution (2.18) is only valid for an infinite solid. Since the finite thin plate investigated here is identical to the plate in the previous section, the reflexion technique has also been implemented in the thickness and in the plane (xy) to guarantee the adiabatic boundary condition.

As for the previous analytical solution, four transient temperature cycles at the points T1 up to T4 for two double ellipsoid heat sources have been simulated. The first one, called "the large ellipsoid", corresponds to an arc welding process with a wide energy distribution and the second one, called "the small ellipsoid" to a laser beam welding process with a high concentrated energy distribution. The respective geometrical parameters are a = 2 mm, b = 10 mm, c_f = 6 mm and c_r = 24 mm (large double ellipsoid) and a = 1.5 mm, b = 2.5 mm, c_f = 2.5 mm and c_r = 5 mm (small double ellipsoid). The net energy input q is set to 1.5 kW for both heat sources. For both test cases, the temperature cycles have been calculated for the entire welding process plus 20 s cooling time with a time step of 0.05 s. Since the temperature profile between A' and B' does not yield more relevant information as in the previous section, it has not been presented for this test case.

3.2.3.5 Finite thin plate – transient state – curved welding path – double ellipsoidal heat source formulation

The analytical solution of the double ellipsoid heat source for a curved welding path on a thin plate is investigated. The same small finite thin plate 50 x 50 x 3 mm^3 as previously investigated is considered. The analytical temperature field solution for a curved welding path does not exist and the analytical solution used is based on the analytical solution of the linear welding path presented in the previous section 3.2.3.4. The curvature of the path is obtained with a sum of linear segments. Every single segment has its own heat source defined in a local coordinate system and the global temperature field is obtained by adding

all the temperature fields of each single linear unit. The experiment settings are plotted in Fig. 3.19:

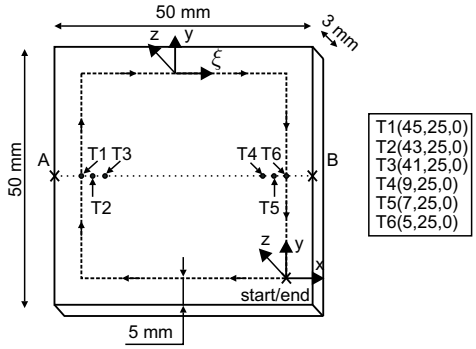

Fig. 3.19: Finite thin plate 50 x 50 x 3 mm³ in transient state, curved welding path, analytical moving point source, q = 1.5 kW and v_s = 10 mm/s

The curved welding path is composed of four linear units 5 mm from the boundary of the plate. An adiabatic boundary condition is considered at each outer surface. The welding speed is set to 10 mm/s and the power to 1.5 kW. The geometrical parameters of the double ellipsoidal heat source are a = 1.5 mm, b = 2.5 mm, c_f = 2.5 mm and c_r = 5 mm.

Six temperature cycles at the points T1 up to T6 are simulated during the welding process and cooling (for a total time of 30 s) with a time step of 0.05 s. Their positions are shown in Fig. 3.19. A temperature profile along the path AB is also calculated after the heat source run 16 s with the same step size of 0.5 mm as in the previous section 3.2.3.4.

3.2.4 Semi-industrial geometry

The validity of the analytical temperature field solution for a double ellipsoidal heat source moving on a curved welding path has been previously investigated on plates. In this section, the same analytical model as in the previous section is tested on a semi-industrial geometry with large dimension and several non-linear welds. Since the geometry of the wheelhouse around it's four welds is close to a plate and the curvature of the wheelhouse is low, the Semi-industrial geometry is derivated from this automotive demonstrator part as illustrated in Fig. 3.20a. The four welds of the wheelhouse are projected on a large plate, 500 x 250 x 2 mm³, giving two welds with a linear trajectory, weld 1 and weld 2, and two welds with a curved one, weld 3 and weld 4. The material parameters used for the simulation are the same as in the previous sections. Only the welding power and welding speed are set to 3.3 kW and 300 cm/min, which are the values used for the real welding of the wheelhouse, see section 3.1.2.1. In order to have a fusion zone geometry resembling a real one, two equal double ellipsoidal heat sources have been used, one on the top surface and one on the bottom surface as illustrated in Fig. 3.20b. The dimension of the two ellipsoids are a_{top} = a_{bottom} = 5 mm, b_{top} = b_{bottom} = 0.5 mm, $c_{f\text{-}top}$ = $c_{f\text{-}bottom}$ = 0.5 mm and $c_{r\text{-}top}$ = $c_{r\text{-}bottom}$ = 3 mm. For this test case, the industrial application of the presented analytical solution for a double ellipsoidal heat source moving on a curved welding trajectory is in focus. Therefore, the fusion lines in cross-section, the weld pool lengths and

widths of the weld 1 are also simulated in addition to the ten temperature cycles presented in Fig. 3.20a). A temperature field of the top surface is also calculated. For all the analytical simulation, a step size of 0.25 mm (the same as in the corresponding numerical model, see section 3.3.4) and a time step of 0.05 s has been implemented.

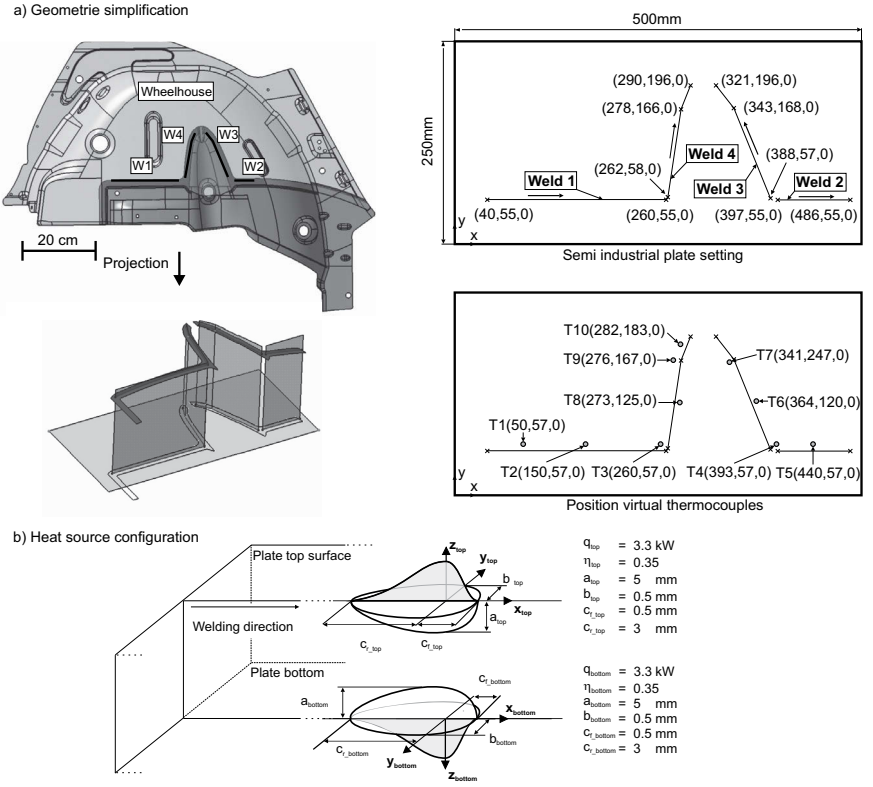

Fig. 3.20: Semi-industrial geometry with several independent curved welding paths – heat source configuration

3.2.5 Wheelhouse and simplified geometries

The analytical solutions introduced in the previous section are only valid for plates or sheets with a parallel joint configuration. For this reason, an “analytical” calibration of the thermal model of the wheelhouse could not be done directly and has been done with the simplified geometry “parallel weld”. Indeed, if the two sheets of the simplified geometry “parallel weld” are considered as one single thicker sheet metal, if adiabatic boundary condition and if the material properties of the investigated material are constant, then the simplified geometry “parallel weld” can be simulated with the analytical solutions previously presented. Therefore, the input parameters of the thermal model of the simplified geometry “parallel weld” have been calibrated with the fast analytical solutions previously presented. These analytical calibrated parameters are then implemented in the FE simulation model “parallel weld” as initial parameter set. The lack of knowledge of the analytical approach, i.e.

adiabatic boundary conditions, constant material parameters, etc., is then compensated by making a final “fine calibration” directly with the FE-model of “parallel weld”. The resulting calibrated heat source model is then used to simulate the geometry “overlap weld” and finally the entire wheelhouse. Here, it is important to notice that the thermal model is only calibrated for the geometry “parallel weld”; the geometry “overlap weld” is used only to validate the simplification made on the joint shape (from the overlap to parallel joint). Finally, the assumption that the temperature model of wheelhouse can be calibrated with the simple geometry “parallel weld” is analysed by comparing the simulation results of the wheelhouse (simulated with the calibrated heat source parameter of the geometry “parallel weld”) with its respective experimental data presented in section 4.1.1.1.

As briefly described in section 2.3.2, the calibration of the thermal model can be done manually or automatically by using an optimisation algorithm. For the geometry “parallel weld”, a global optimisation algorithm based on neural networks has been implemented. The goal of this global optimisation algorithm is to predict the unknown parameters of the heat source model so that the simulation results match the experimental data. During the automatic optimisation routine, multiple direct simulations are computed until the L2-norm between the simulated and given experimental simulation results reaches a convergence criterion. This L2-norm is defined as:

$$\left\| u_{\mathrm{sim},i} - u_{\mathrm{exp},i} \right\|_2 = \sqrt{\frac{1}{N}\sum_{i=1}^{N}\left[w_i (u_{\mathrm{sim},i} - u_{\mathrm{exp},i})^2 \right]} \leq C \tag{3.2}$$

Where $u_{sim,i}$ is the vector of the simulated characteristics (a temperature or the weld pool length of instance) of length N and $u_{exp,i}$ the corresponding experimental reference values. The weighting factor w_i is adjusted with respect to the quality of the experimental data [77]. The convergence criterion C is set to 1.0e-3. For more details, see the works of Pittner [56, 77] and Weiss [94, 103].

The vector of the experimental characteristics $u_{exp,i}$ used for the calculation of the L2-norm have been taken from the temperature field, fusion zone in cross-section and weld pool length measurements of the simplified geometry “parallel weld”. This input data have been classified from A_{exp} to H_{exp} giving the vector $u_{exp,i} = (A_{exp}, B_{exp}, C_{exp}, D_{exp}, E_{exp}, F_{exp}, G_{exp}, H_{exp})$. Their respective values are plotted in Fig. 3.21.

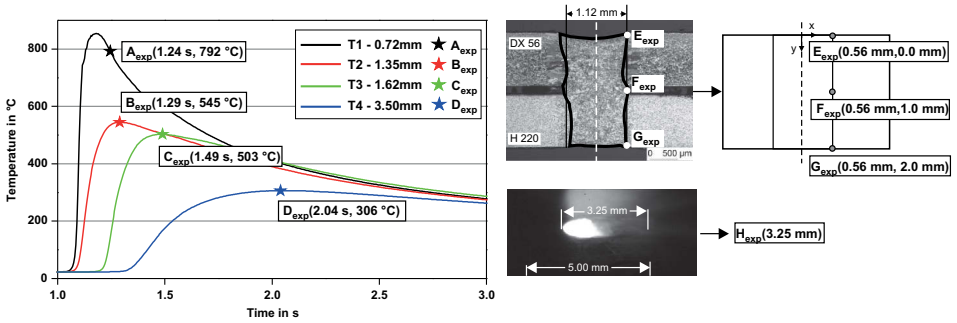

A_{exp}	(1.24 s, 792 °C)	E_{exp}	(0.56 mm, 0.0 mm)
B_{exp}	(129 s, 545 °C)	F_{exp}	(0.56 mm, 1.0 mm)
C_{exp}	(1.49 s, 503 °C)	G_{exp}	(0.56 mm, 2.0 mm)
D_{exp}	(2.04 s, 306 °C)	H_{exp}	3.25 mm

Fig. 3.21: Experimental input data $u_{exp,i}$ = (A_{exp}, B_{exp}, C_{exp}, D_{exp}, E_{exp} , F_{exp}, G_{exp}, H_{exp}) taken from characteristic temperature cycles T1, T2, T3 and T4, cross-section and weld pool length measurements

The data A_{exp} to D_{exp} are single temperatures from the thermocouples T1 to T4 (from simplified geometry “parallel weld”, see section 4.1.1.1), taken just after the respective peak temperatures. The measured position of the thermocouples shown in Fig. 3.21 and in Fig. 4.1 is exactly considered in the analytical simulation model. It is important to notice that only one single temperature per temperature cycle is given in the optimisation algorithm. Then, three points E_{exp}, F_{exp} and G_{exp} are taken to define the profile of the cross-section. Here, the fluctuation of the width of the real fusion line in the thickness cannot be simulated only with the implemented two heat sources. For this reason, an average fusion zone width of 1.12 mm has been chosen at the three investigated points E_{exp}, F_{exp} and G_{exp}. Finally, the information H_{exp} corresponds to the weld pool length.

For the simulation of the geometry “parallel weld”, two equivalent double ellipsoidal heat sources are running in parallel on the upper and lower part of the sheets as for the semi-infinite thin plate in section 3.2.4. Here, since the gap cannot be considered in the simulation model, a simple plate with 2 mm thickness has been used. In the analytical model, a step size of 0.25 mm and a time step of 0.05 s have been chosen. For the laser power and the welding speed, the same values as for the real welding experiments are used, see section 3.1.2.1. In the thermal model, the four parameters of the double ellipsoidal heat sources a, b, c_f and c_r and the efficiency η of the welding process are unknown making five unknown input parameters to calibrate. For each unknown parameters, a parameter range should be given in the optimisation algorithm to avoid some simulations with parameters out of realistic range. For the laser beam welding process of the geometry “parallel weld”, the following values are given, see Fig. 3.22:

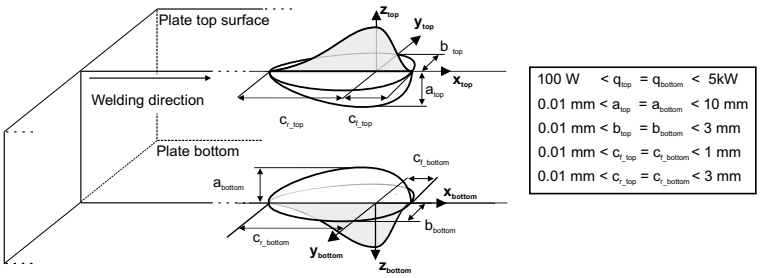

Fig. 3.22: Parameter ranges of the five unknown input parameters for the two double ellipsoidal heat source implemented for the geometry "parallel weld"

According to the assumptions of the analytical solutions given in section 3.2.2, the material properties implemented in the thermal model are temperature independent. Since the calibration of the thermal model is partially done against information about the shape and the size of the fusion zone, the temperature dependent material properties of the steel DX 56, presented in Fig. 3.1 in section 3.1.1.1, have been taken at $T_{solidus}$ = 1380°C for the geometry "parallel weld" and are summarised in Tab. 3.11:

Tab. 3.11: Material properties from the steel DX 56 at the solidus temperature $T_{solidus}$ = 1380°C for the analytical thermal model of the geometry "parallel weld"

Heat conductivity at $T_{solidus} = 1380°C$	$34\,W \cdot m^{-1} \cdot K^{-1}$
Specific heat capacity at $T_{solidus} = 1380°C$	$650\,J \cdot kg^{-1} \cdot K^{-1}$
Density at $T_{solidus} = 1380°C$	$7350\,kg \cdot m^{-3}$

Finally, an analytical simulation is run with the given calibrated parameter (from the optimisation algorithm) of the two double ellipsoidal heat sources. For the simulation, the four transient analytical temperature cycles T1 to T4, the fusion zone in cross-section and the weld pool length are plotted during all the welding process and cooling.

3.3 Numerical simulations

3.3.1 Computer and software

The simulation results presented in this paper have been run with a desktop PC (Intel Core i7 950@3 GHz and 12 GB RAM) under Windows XP 64 bit. The welding simulation software simufact.welding has been implemented for all the following numerical simulations. In this study, the *Weldsim-solver* from the Institute for Energy Technology IFE, Norway [176] has been used.

3.3.2 Assumptions and simplifications

For the temperature field simulation, the following assumptions and simplifications have been made:

- Material is isotropic and homogeneous
- Ideal geometries from the CAD drawing
- The welding process is simplified to a heat conduction problem
- Ideal thermal boundary conditions (heat transfer to the environment through convection and radiation)
- Phenomenological heat source model

The thermomechanical simulation of distortions has also been investigated for the industrial demonstrator part “crossbeam” and the following simplifications and assumptions have been used:

- Ideal mechanical boundary conditions (see section 3.3.6)
- The material history, i.e. residual stresses from previous production processes, is neglected
- The crossbeam, the inserts and the filler metal are considered into one geometry
- Non-coupled thermal and mechanical simulation

3.3.3 Plates

Usually in engineering, exact analytical solutions are used to validate the response of approximate numerical models. This approach has been used in this study with the exact analytical solution for a moving point source in infinite solid presented in section 3.2.3.1: a numerical model of the same “quasi-infinite” solid with the dimension 200 x 200 x 100 mm^3 has been built with the same welding and material parameters. The same data as in section 3.2.3.1 have also been simulated. Since all the other analytical solutions presented in section 3.2.3 are not exact but have been derivated from this first analytical solution in the infinite solid, they need to be also verified against a reference model. The validated numerical model (validated with the analytical solution for a moving point source in infinite solid) has been used for this task: all the analytical test cases presented from section 3.2.3.2 to 3.2.3.5 have been numerically simulated. The same plate geometries with the same welding and material parameters have been used.

All the numerical models of the investigated plates are built in the same way. The plates are meshed with 3D linear hexahedron elements. An automatic refinement tool enables to get an optimal fine mesh density only at the required positions by refining the initial coarse mesh systematically around the moving source according to a temperature gradient criterion ($\partial T/\partial x$, $\partial T/\partial y$ and $\partial T/\partial z$). Here, a temperature gradient criterion of 70°C is implemented. It means that if the temperature difference between two nodes exceeds 70°C, a Bi-section algorithm enables the corresponding element to be halved in all three dimensions. An overview of the numerical settings for all the investigated plates is given in Tab. 3.12:

Tab. 3.12: Mesh characteristics of the investigated plates

Plates	Element Type	Element edge length coarse mesh	Element edge length refined mesh	Number of nodes coarse mesh	Number of nodes refined mesh
1	3D linear hexa-hedron	3 mm	0.75 mm	154,904	205,567
2		3 mm	0.75 mm	9145	48,997
3		3 mm	0.75 mm	13,701	63,839
4		1.5 mm	0.75 mm	3859	14,677
5		1.5 mm	0.75 mm	3859	14,677
6		1.5 mm	0.75 mm	3859	14,677
7		1.5 mm	0.75 mm	3859	20,843

The plates 1 to 7 are the infinite solid 200 x 200 x 100 mm^3 in steady state (1), the infinite thin plate 200 x 200 x 1.5 mm^3 (2) and 200 x 200 x 5 mm^3 (3) in steady state, the transient linear moving point source on the plate 50 x 50 x 3 mm^3 (4), the transient moving small and large double ellipsoids on the plate 50 x 50 x 3 mm^3 (5 and 6) and the transient moving double ellipsoid on the plate 50 x 50 x 3 mm^3 (7) with a curved welding path, respectively.

For all the numerical simulations on plates, the same data as for the analytical test cases, i.e. temperature cycles and temperature profiles, have been simulated.

3.3.4 Semi-industrial geometry

A description of the semi-industrial geometry with its dimensions, welding paths and welding characteristics, i.e. welding speed, power, heat source implemented, etc. has been given in section 3.2.4. For sake of clarity, exactly the same model configurations, i.e. boundary conditions, material parameters, heat source models and simulated data, i.e. temperature cycles, fusion zone in cross-section and weld pool length as the corresponding analytical simulation, see section 3.2.4, have been implemented in the FE-model.

The plate has been meshed with the same 3D hexahedron elements with linear shape functions as in the previous section. An investigation of the mesh density is required for every new welding simulation to guarantee an accurate result quality and a minimal computational cost. This has been made for the heat source configuration of this test case and the optimal mesh density is found to be approximately 0.25 mm. In order to get this mesh density, a coarse mesh with element edge lengths from 1 mm to 20 mm has been manually generated giving a total number of nodes of approximately 53,000. The element edges with 1mm length are located around the four weld trajectories. The edge lengths of the rest of the elements are getting progressively larger when the distance from the welds increases. Finally, the automatic mesh refinement algorithm has been used during the

simulation to get the final element edge length of 0.25 mm in the required zones. After the refinement procedure, the plate consists of approximately 254,000 nodes.

3.3.5 Wheelhouse and simplified geometries

The same laser beam welding process with the same energy input per unit length has been used for the real experiment of the wheelhouse and the simplified geometries “parallel weld” and “overlap weld”. For this reason, an identical mesh density with an element edge length of 0.25 mm around the welding trajectories has been implemented in the respective simulation models. The mesh characteristics of the wheelhouse and the simplified geometries “parallel weld” and “overlap weld” are summarised in Tab. 3.13:

Tab. 3.13: Mesh characteristics of the simplified geometries “parallel weld” (1) and “overlap weld” (2) and of the wheelhouse (3)

Geometry	Element Type	Element edge length coarse mesh	Element edge length refined mesh	Number of nodes coarse mesh	Number of nodes refined mesh
1	3D linear hexa-hedron	1mm<X<20mm	0.25 mm	12,004	69,880
2				9,823	67,727
3				48,417	230,000

The geometries 1 to 3 are the “parallel weld” (1), the “overlap weld” (2) and the wheelhouse geometries (3), respectively. The mesh of the wheelhouse is exemplarily shown in Fig. 3.23.

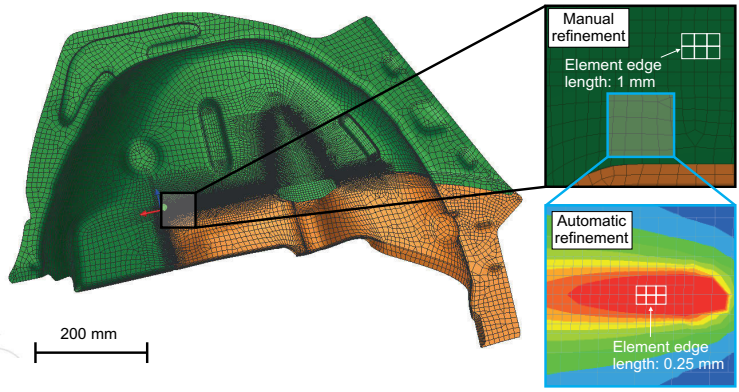

Fig. 3.23: Mesh of the wheelhouse with manual and automatic refinement techniques

For all geometries, the upper and the lower sheets are considered as one part. As explained in section 3.1.3.1, a gap of 0.2 mm is required between the welded sheets to allow the evaporated zinc to escape during welding. This gap has been taken into consideration during meshing the simple geometries “parallel weld” and “overlap weld”. For

the wheelhouse, no gap has been considered to keep the time for the construction of the simulation model in a reasonable frame.

Convective and radiative boundary conditions have been considered in the FE-model. The convective heat transfer coefficient α in $\mathrm{W \cdot m^{-2} \cdot K^{-1}}$ and the Stefan-Boltzmann-constant ε $(0 < \varepsilon < 1)$ are dependent on the material taken into consideration and have been taken from the literature [177]. For this study, $\alpha = 7\,\mathrm{W \cdot m^{-2} \cdot K^{-1}}$ and $\varepsilon = 0.25$. In the real welding experiment, the clamps have been positioned close to the weld. Since they may absorb some heat during the welding process, their influence have been quantified by running for each test case “parallel weld”, “overlap weld” and wheelhouse two simulations with and without clamps. For modelling the clamps, solid elements have been added in the simulation model at their respective real position, see Fig. 3.8.

To represent the laser beam welding process, two double ellipsoidal heat sources have been used on the top and bottom surface of the welded parts in the same way as for the semi-industrial welded assembly investigated in sections 3.2.4 and 3.3.4. Their distribution parameters have been set identical in order to minimise the number of unknown parameters.

For the calibration of the thermal model, the large size of the wheelhouse limits the number of simulation iterations required for the calibration of the heat source model. Therefore, the calibration of the heat source model is made on the simplest geometry “parallel weld”. The advantage of this simplification is that the input parameters of the two double ellipsoidal heat sources can be approximated automatically with the fast analytical model previously described in section 3.2.3 in combination with the global optimisation algorithm, see section 3.2.5. These analytical calibrated parameters are then implemented in the FE simulation model “parallel weld” as initial parameter set. The lack of knowledge of the analytical approach, i.e. adiabatic boundary conditions, constant material parameters, etc., is then compensated by making a final manual “fine calibration” directly within the FE-model of the simplified geometry “parallel weld”.

For the thermal simulation of the simple geometry “overlap weld” and the wheelhouse, the calibrated parameters of the simple geometry “parallel weld” are directly used.

For the simulations of the simplified geometries “parallel weld” and “overlap weld”, the four measured temperature cycles T1 to T4, see section 3.1.4.1, have been considered in the simulation model; their positions in the simulation models have been taken from the corresponding real experiments. For both test cases, the fusion zones in a cross-section and the weld pool lengths have also been simulated. For the wheelhouse, the six temperature cycles T1 to T6, see Fig. 3.13, have been simulated and their respective positions in the simulation model have been taken for the corresponding real measurements. Two fusion zones in cross-section and two weld pool lengths have been simulated for the weld 1 and 3.

3.3.6 Crossbeam

The crossbeam and the eight inserts are joined with eight overlap joints using a MIG welding process as described in section 3.1.2.2 and 3.1.3.2. The temperature field and

distortion simulations presented in this section have been simulated only with numerical techniques.

The mesh for the simulations is shown in Fig. 3.24. Here, it is worth to notice that the entire crossbeam welded assembly, the four inserts and the eight welds have been considered as one single part. The same element type as for the wheelhouse welded assembly – 3D hexahedron elements – has been used. Before the meshing operation, an investigation of the required element size in the weld metal has been done and an element size of approximately 2 mm in the high temperature gradient zones is found to be optimal by means of accuracy and computational costs. In order to minimise the final number of elements of the entire crossbeam welded assembly, a local mesh refinement strategy has been implemented around the welds. The entire structure is first coarsely meshed (element length = 8 mm), then the zone around the weld seam which corresponds to the HAZ is refined manually (element length = 3.5 mm). Finally, by applying the automatic refinement tool, the element edge length is halved in the weld area. Thus, the coarse mesh with the manual refinement around the eight welds has 66,000 nodes as illustrated in Fig. 3.24. After the automatic refinement technique, the FE-model has 118,000 nodes.

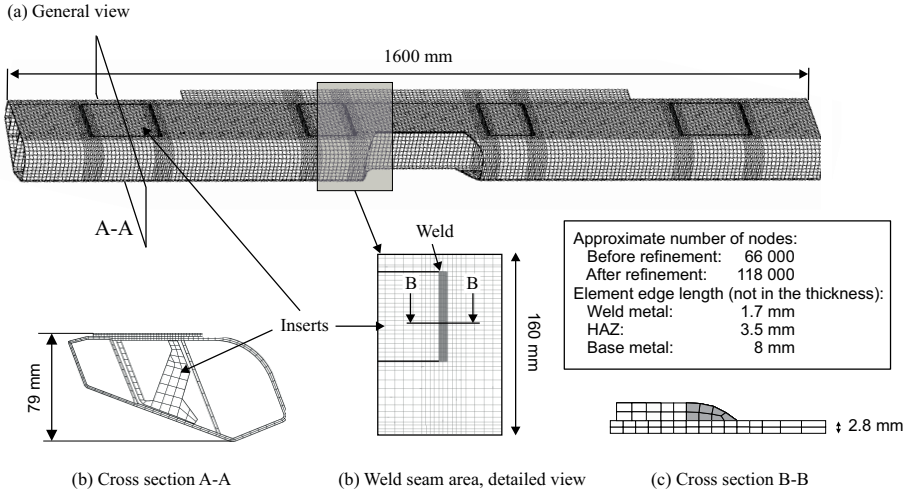

Fig. 3.24: Mesh of the crossbeam welded assembly

As explained in section 3.1.2.2, a weaving motion of the welding torch has been used during the real MIG welding process to guarantee good overlap joints. In order to reproduce this phenomenon, two Goldak heat sources with a distance of approximately the weaving motion amplitude (in the perpendicular direction to welding path) are running in parallel during the welding process as shown in Fig. 3.25:

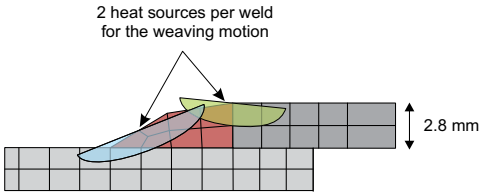

Fig. 3.25: Heat source configuration to simulate the weaving moving of the real welding process

Heat loss through convection and radiation has been considered in the simulation model for the thermal boundary conditions. For the convective heat transfer coefficient α in $\mathrm{W \cdot m^{-2} \cdot K^{-1}}$ and the emissivity coefficient ε ($0 < \varepsilon < 1$), the value of $20\ \mathrm{W \cdot m^{-2} \cdot K^{-1}}$ and $\varepsilon = 0.25$ have been used, respectively.

For the calibration of the thermal model of the crossbeam welded assembly, an initial set of input parameters (for the four parameters of the double ellipsoidal heat sources a, b, c_f and c_r and the efficiency η) has been calculated on a small part of the crossbeam in order to reduce the calibration time as shown in Fig. 3.26.

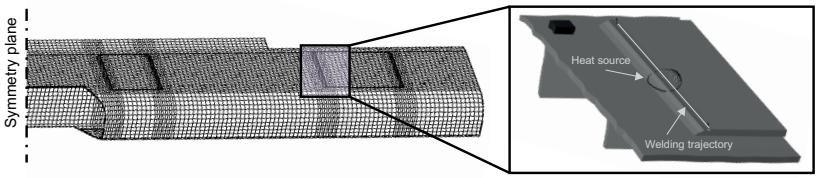

Fig. 3.26: Small part of the crossbeam welded assembly for a fast estimation of an initial parameter set for the thermal model

For this calibration, only the simulated fusion zones have been compared against the measured data. Since the respective calculation time for this small part is short, the manual calibration steps is done rapidly in comparison to a manual calibration of the entire crossbeam assembly. After the estimation of these initial input parameters, a final calibration on the entire crossbeam model is completed.

A correct consideration of the mechanical boundary conditions is a prerequisite for accurate simulation results. Two different clamping types are tested. In the first clamping type, all the degrees of freedom of the nodes in contact between the crossbeam and the clamps are fixed; this clamping is called the “rigid clamping”. In the second clamping type, the entire clamping device shown in section 3.1.3.2 is considered and implemented in the simulation model as an extra part; this clamping is called the “complete clamping”. With this method, the entire clamping device must be meshed; this increases the total number of nodes of the simulation model from 118,000 nodes to 122,000 nodes. For this test case, the clamping device is in contact with the crossbeam welded assembly. The heat transfer between two parts in contact is considered in the simulation model with a heat transfer coefficient of $\alpha_{\mathrm{cont}} = 100\,\mathrm{W \cdot m^{-2} \cdot K^{-1}}$.

After the calibration of the thermal model, two complete thermomechanical simulations with the BM and HAZ material properties, see section 3.1.1.3 are run to investigate the influence of the softening of the mechanical material properties in the HAZ.

The position of the real thermocouples T2, T4, T6 and T8 chosen in section 3.1.4.2 have been exactly considered in the simulation model and the respective four temperature cycles have been simulated. The fusion lines in cross-section as well as the weld pool length have been simulated in the middle of the welds W1r, W2l and W4l. For the mechanical simulation of the welding induced distortions, the same area between the inserts I3 and I4 investigated experimentally for the distortion field has been analysed in the numerical model. For the transient distortion field analysis, the position of the measurement-point D, see section 3.1.4.2, has also been reproduced in the simulation model.

4 Results

In the following section, all the experimental, analytical and numerical results of the experiments described in the previous section 3 are presented.

4.1 Experimental results

4.1.1 Temperature field measurement

4.1.1.1 Wheelhouse and simplified geometries

For the simplified geometry “parallel weld”, the four temperature cycles T1 to T4 are shown in Fig. 4.1a from 0 s to 200 s. The peak temperatures and the cooling behaviour can be seen. The positions of the four thermocouples have been plotted. A more detailed representation of the peak temperatures is given in Fig. 4.1b. Only the peak temperature of the thermocouple T1 is above 800 °C with a resulting $t_{8/5}$ cooling time of 0.46 s.

The experimental scatter band of the weld pool area in cross-section of the simplified geometry “parallel weld” has been also measured with four cross-sections. The results are plotted in Fig. 4.2. The average weld pool area is 2.13 mm^2 with a scatter band of $\pm$ 0.06 mm^2.

Finally, the results of the experimental scatter band of the weld pool length of the simplified geometry “parallel weld” are plotted in Fig. 4.3. Four samples have been analysed giving an average weld pool length of 3.2 mm with a scatter band of $\pm$ 0.18 mm.

For the simplified geometry “overlap weld”, the temperature fields T1 to T4 have been plotted in Fig. 4.4. In Fig. 4.4a, the four temperature cycles are shown for the entire measurement time of 200 s. The $t_{8/5}$ cooling time can only be determined for the temperature cycle T2, see Fig. 4.4b, and is approximated to 0.48 s. The temperature cycles are plotted from 1 s to 3 s in Fig. 4.4b.

A total of four metallographic cross-sections of the weld of the simplified geometry “overlap weld” have been analysed. Two of them are plotted in Fig. 4.5. The gap between the welded sheets is between 0.15 mm and 0.22 mm. The weld pool area in cross-section have been measured for the four analysed samples and the average value is found to be 2.07 mm^2 with a scatter band of $\pm$ 0.11 mm^2, see Fig. 4.5 below.

The weld pool length of the simplified geometry “overlap weld” has been analysed with six samples. It is found to be equal to 3.4 mm with a scatter band of $\pm$ 0.28 mm as plotted in Fig. 4.6.

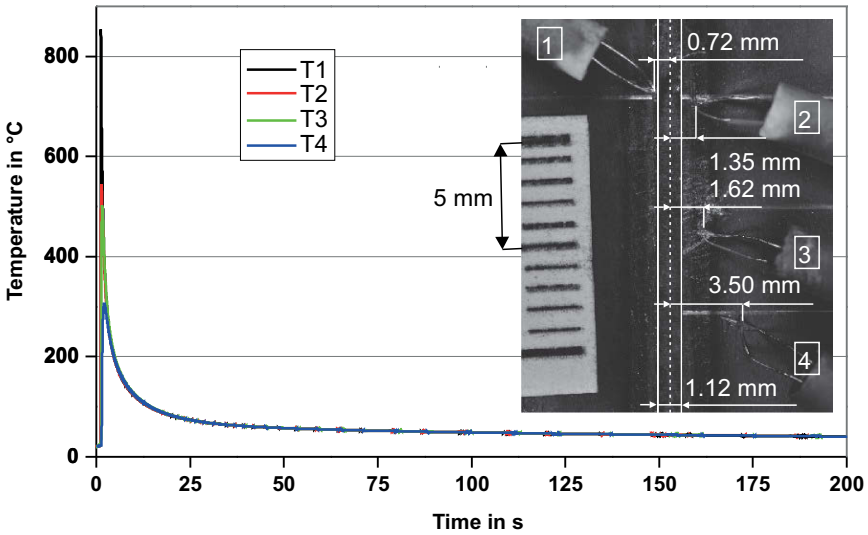

a) Temperature cycles T1-T4 from 0 s to 200 s - Position of all thermocouples from the centre line of the weld

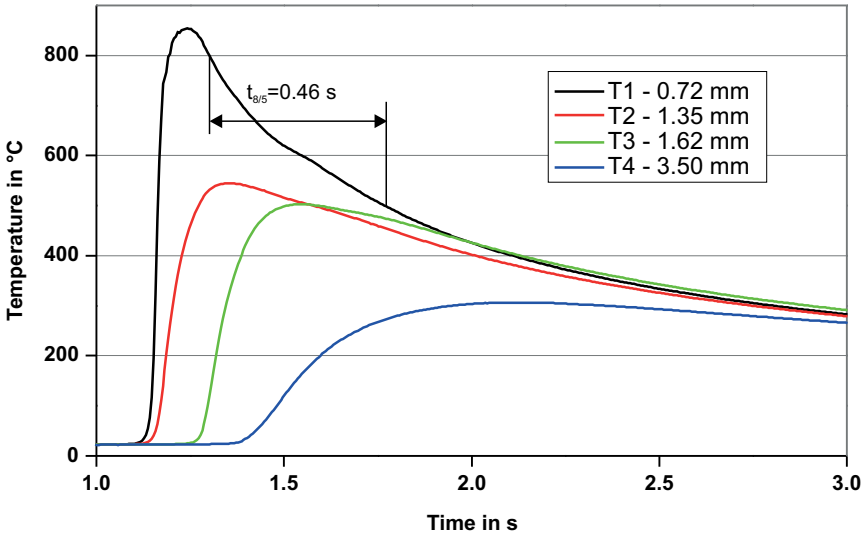

b) Temperature cycles T1-T4 from 1 s to 3 s

Fig. 4.1: Experimental four temperature cycles T1, T2, T3 and T4, simplified geometry "parallel weld", laser beam welding, sheet thickness 1 mm, q = 3.3 kW and v_s = 300 cm/min

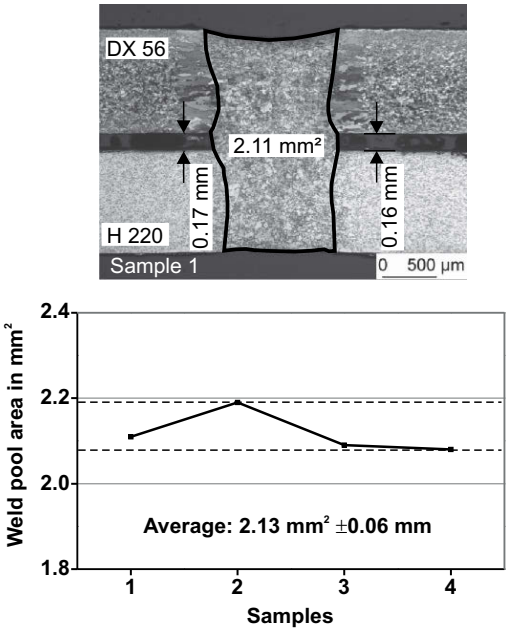

Fig. 4.2: Experimental scatter band of the fusion zone area in cross-section, simplified geometry "parallel weld", laser beam welding, sheet thickness 1 mm, q = 3.3 kW and v_s = 300 cm/min

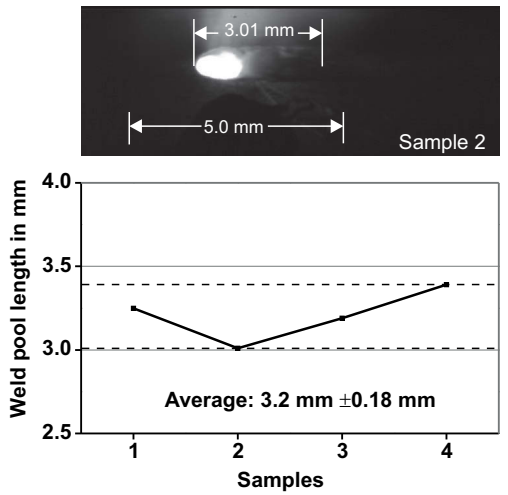

Fig. 4.3: Experimental scatter band of the weld pool length, simplified geometry "parallel weld", laser beam welding, sheet thickness 1 mm, q = 3.3 kW and v_s = 300 cm/min

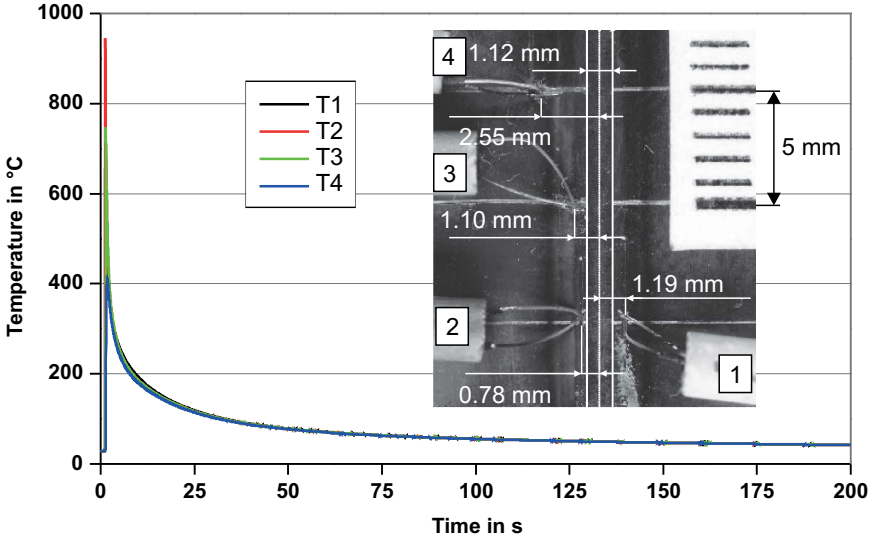

a) Temperature cycles T1-T4 from 0 s to 200 s - Position of all thermocouples from the center line of the weld

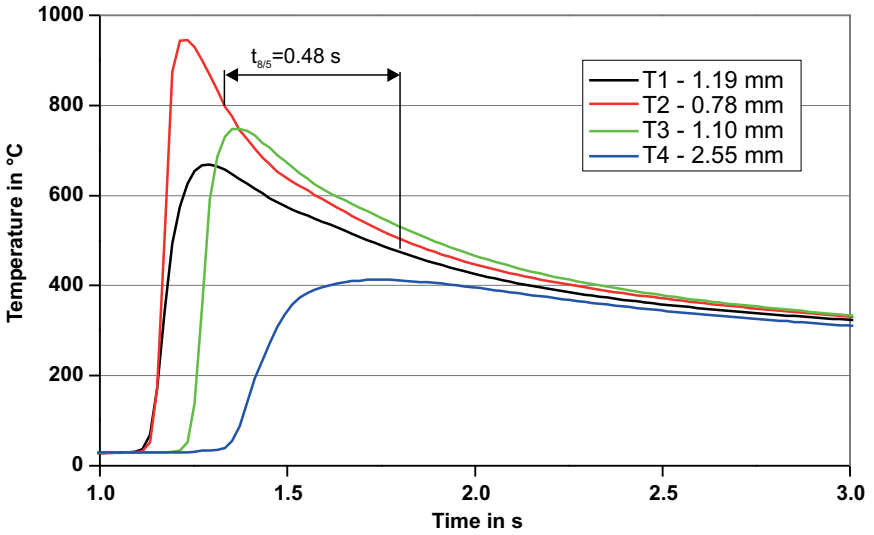

b) Temperature cycles T1-T4 from 1 s to 3 s

Fig. 4.4: Experimental four temperature cycles T1, T2, T3 and T4, simplified geometry "overlap weld", laser beam welding, sheet thickness 1 mm, q = 3.3 kW and v_s = 300 cm/min

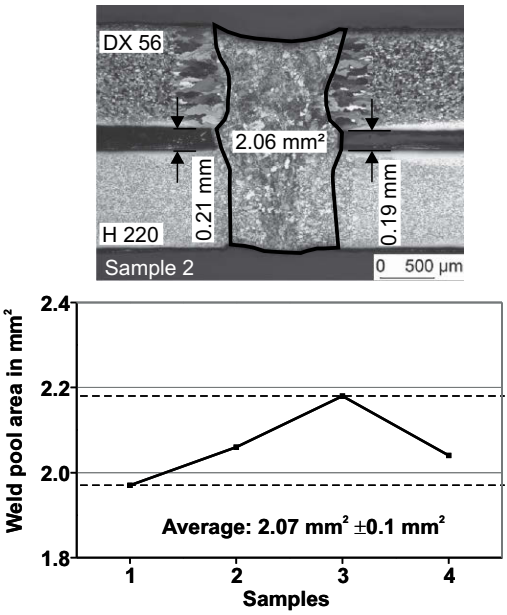

Fig. 4.5: Experimental scatter band of the fusion zone area in cross-section, simplified geometry "overlap weld", laser beam welding, sheet thickness 1 mm, q = 3.3 kW and v_s = 300 cm/min

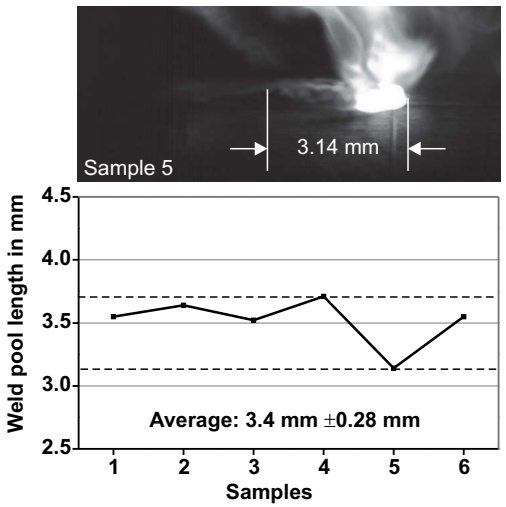

Fig. 4.6: Experimental scatter band of the weld pool length, simplified geometry "overlap weld", laser beam welding, sheet thickness 1 mm, q = 3.3 kW and v_s = 300 cm/min

The temperature cycles measured during the welding process of the wheelhouse assembly are shown in Fig. 4.7. The first peak temperatures correspond to the thermocouples T1 to T4 and the second to the thermocouples T5 to T6. The six transient temperature cycles T1 to T6 have been recorded for 200 s as shown in Fig. 4.7a. Even though the thermocouples have been spot-welded as closely as possible to the fusion line, the characteristic cooling time $t_{8/5}$ (which corresponds to the cooling time between 800°C and 500°C) could only be measured by the thermocouple T5 and is equal to 0.43 s. For the comparison with the simulation results, the temperature cycles of the thermocouples T1, T4, T5 and T6 have been chosen. In Fig. 4.7b, the respective temperature cycles are plotted from 0 s to 20 s in order to show the peak temperatures with more details.

The weld pool shape in the thickness of the wheelhouse has been determined with metallographic cross-sections along the welds W1 and W2 as shown in Fig. 4.8. Five samples have been measured along each weld in order to obtain an experimental scatter band. For the wheelhouse, the average weld pool area in the cross-section is 1.85 $mm^2 \pm 0.22$ mm^2. The gap between the two welded parts has been measured for each cross-section and is equal to 0.1 mm up to 0.2 mm.

For the wheelhouse test case, the weld pool length has been measured for weld W1. Several measurements have been done to obtain an experimental scatter as plotted in Fig. 4.9. The average weld pool length of the wheelhouse is found to be 3.3 mm ± 0.25 mm.

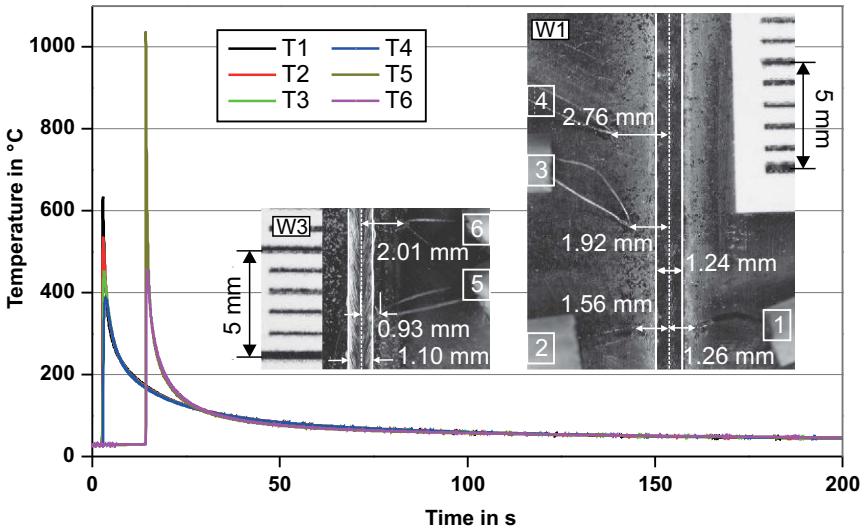

a) Temperature cycles T1-T6 from 0 s to 200 s - Position of all thermocouples from the center line of W1 and W3

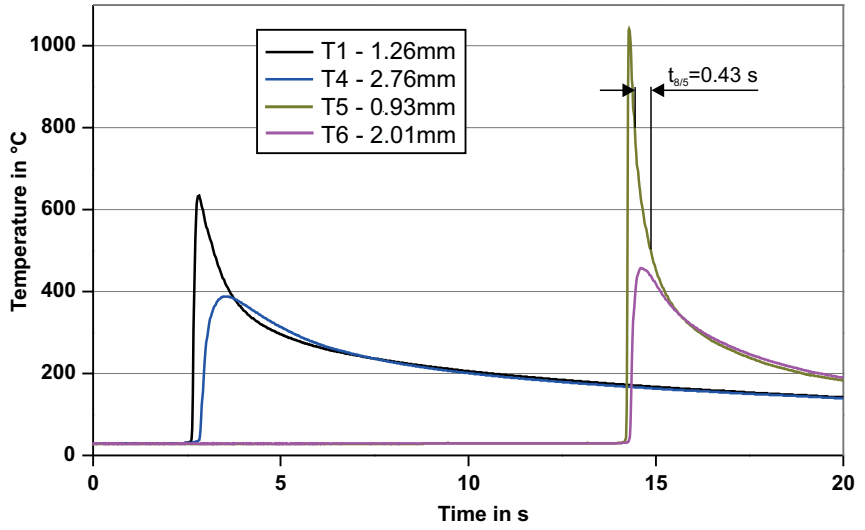

b) Temperature cycles T1, T4 and T6 chosen for the comparison with the simulation results - from 0 s to 20 s

Fig. 4.7: Experimental four temperature cycles T1, T4, T5 and T6, wheelhouse, laser beam welding, sheet thickness 1 mm, q = 3.3 kW and v_s = 300 cm/min

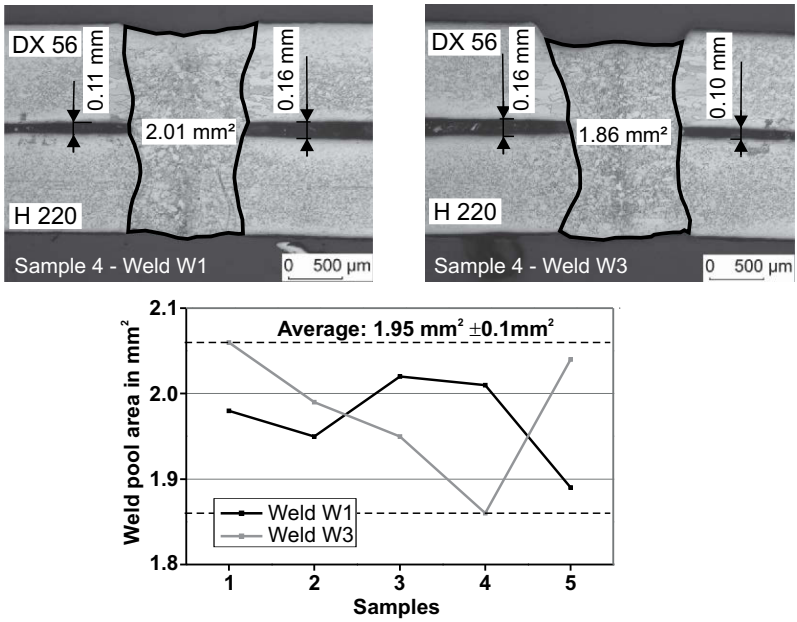

Fig. 4.8: Experimental scatter band of the fusion zone area in cross-section, wheelhouse welds W1 and W3, laser beam welding, sheet thickness 1 mm, q = 3.3 kW and v_s = 300 cm/min

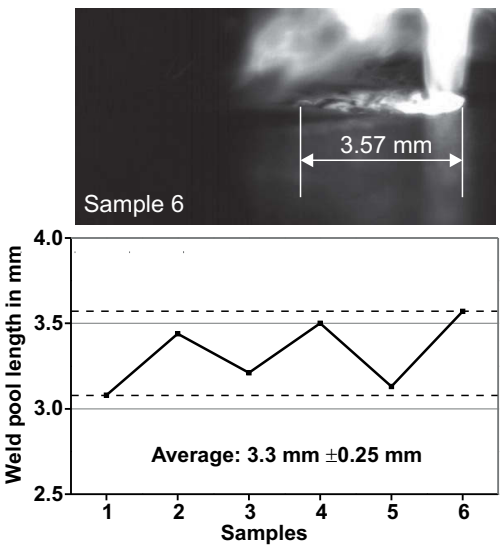

Fig. 4.9: Experimental scatter band of the weld pool length, wheelhouse, laser beam welding, sheet thickness 1 mm, q = 3.3 kW and v_s = 300 cm/min

4.1.1.2 Crossbeam

The temperature cycles measured by the eight thermocouples positioned along the welds W1r and W2l of the crossbeam are plotted in Fig. 4.10a) from 0 s to 200 s. The first peak temperatures correspond to the thermocouples T1 to T4 and the second to the thermocouples T5 to T8. This graph gives a good overview of the temperature gradients close to the weld and of the cooling behaviour of the welded assembly. The $t_{5/3}$ cooling time (equivalent to the $t_{8/5}$ cooling time for steel) could be measured only at the thermocouple T1 and is equal to 2.07 s. The position of the thermocouples, required for the simulation, is also displayed in Fig. 4.10a). The temperature cycles T2, T4, T6 and T8 have been chosen for the comparison with the simulation model. For a better comparison with the simulation results, they have been displayed from 0 s to 70 s in Fig. 4.10b).

The analysis of the fusion zone shape in cross-section is plotted in Fig. 4.11. In Fig. 4.11a), the metallographic cross-section of the three welds W1r, W2l and W4l are exemplarily plotted with their respective fusion zone area, width and depth for the crossbeam sample 2. The measurement data of all the six welded samples are gathered in Fig. 4.11b). The fusion zone area, width and depth are equal to 25 $mm^2 \pm 3$ mm^2, 9.6 mm $\pm$ 0.8 mm and 1.3 mm $\pm$ 0.6 mm, respectively.

The weld pool length is shown in Fig. 4.12a) (exemplarily for the crossbeam sample 2). All the measurement data are plotted in the graph in Fig. 4.12b). The weld pool length scatter band is found to be 16.6 mm $\pm$ 1.9 mm.

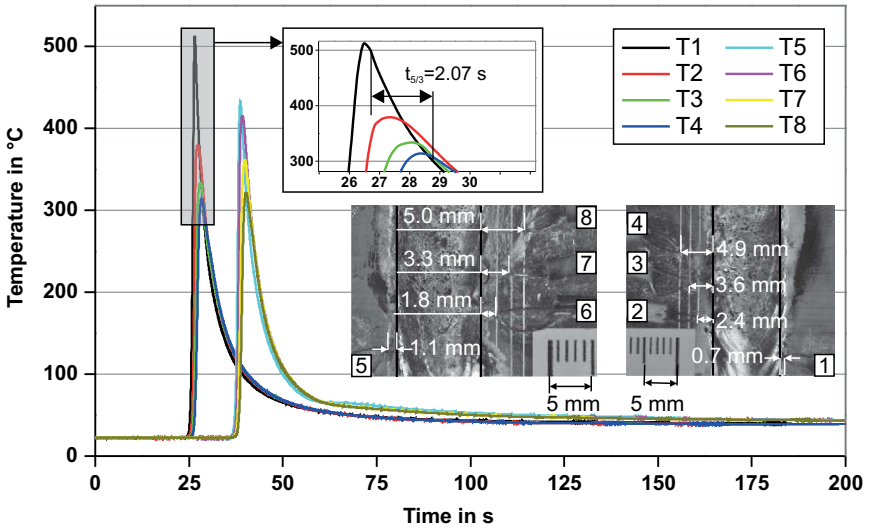

a) Temperature cycles T1-T8 from 0 s to 200 s - Position of all thermocouples from the closest edge of the molten zone

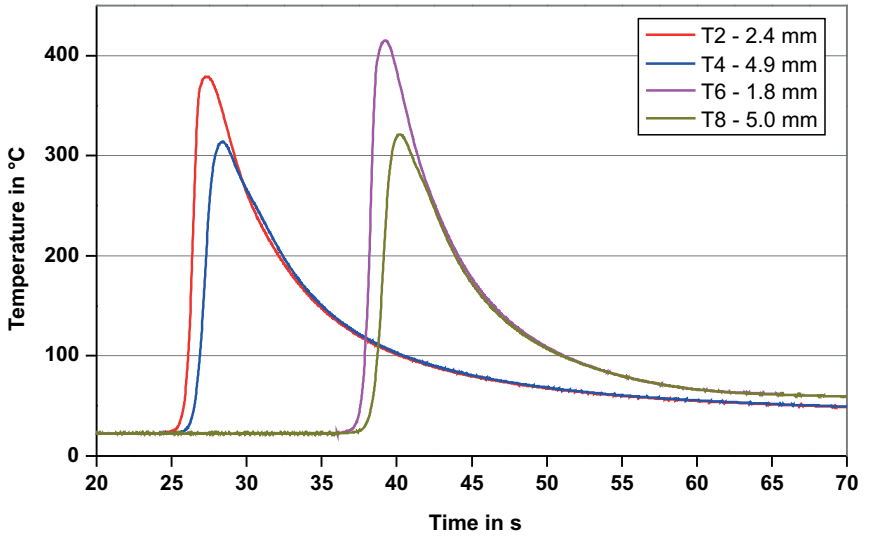

b) Temperature cycles T2, T4, T6 and T8 from 20 s to 70 s

Fig. 4.10: Experimental four temperature cycles T2, T4, T6 and T8, crossbeam, MIG welding overlap joint, material thickness 2.8 mm, U_{ave} = 162 V, I_{ave} = 22 A and v_s = 100 cm/min

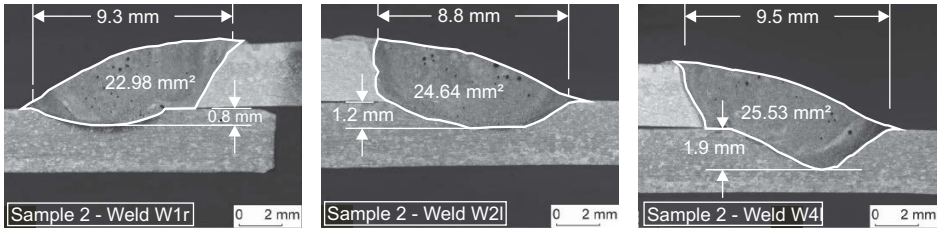

a) Dimension of the weld pool in cross-sections, crossmember, welds W1r, W2l and W4l

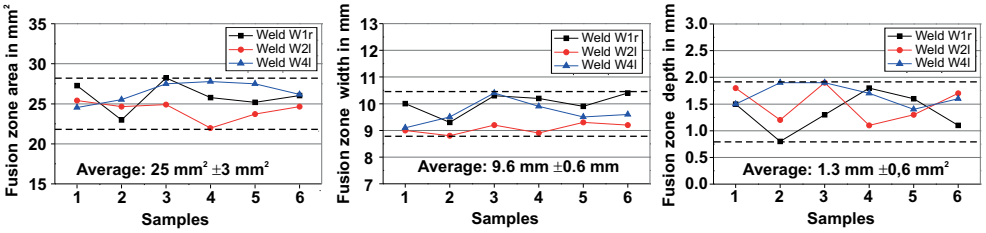

b) Scatter bands for the fusion zone area, width and depth, crossmember

Fig. 4.11: Experimental scatter bands of the fusion zone area, width and depth in cross-section, crossbeam welds W1r, W2l and W4l, MIG welding overlap joint, material thickness 2.8 mm, U_{ave} = 162 V, I_{ave} = 22 A and v_s = 100 cm/min

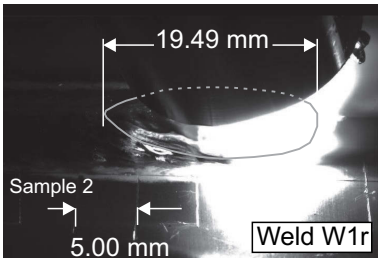

a) Weld pool length measurement with high speed camera

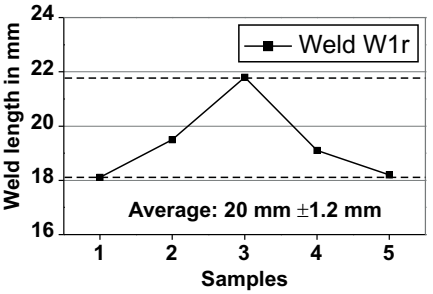

b) Experimental scatter band for the weld pool length

Fig. 4.12: Experimental scatter band of the weld pool length, crossbeam, MIG welding overlap joint, material thickness 2.8 mm, U_{ave} = 162 V, I_{ave} = 22 A and v_s = 100 cm/min

4.1.2 Distortion measurement

The experimental global distortion field measurement after 800 s (comprising the welding and the cooling time) of the crossbeam “sample 2” is shown in Fig. 4.13. For an accurate quantitative and qualitative validation of the simulation model, an analysis of the transient distortion behaviour during and after the welding process is compulsory. This has been made at the point A as shown in Fig. 4.13.

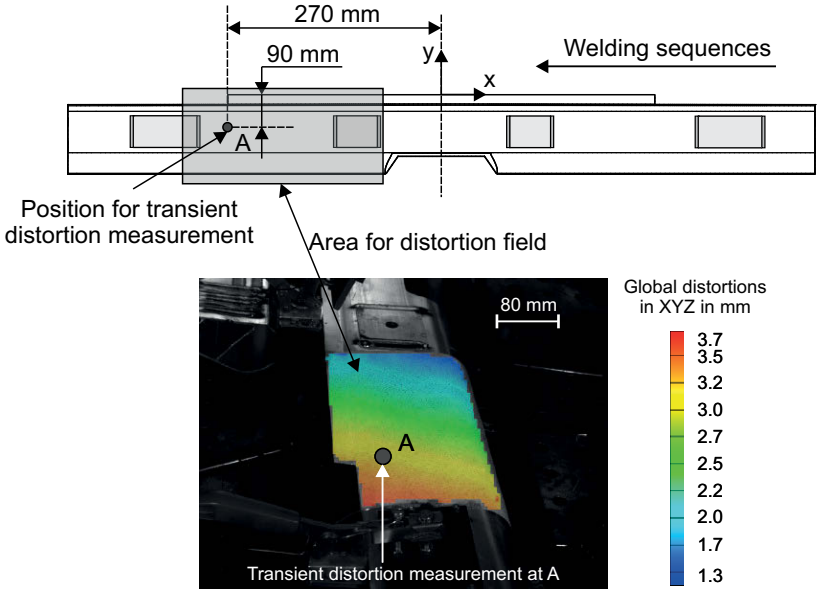

Fig. 4.13: Experimental global distortion field measurement after 800 s, crossbeam, optical 3D deformation analysis system Aramis

The transient distortions at the point A have been measured from 0 s to 800 s for each x, y and z-direction as shown in Fig. 4.16, Fig. 4.15 and Fig. 4.14, respectively. For each graph, the minimal and the maximal measurements have been plotted and set as scatter band for the simulation results. The clamping release at 108 s is apparent and is highlighted with a grey square in each graph.

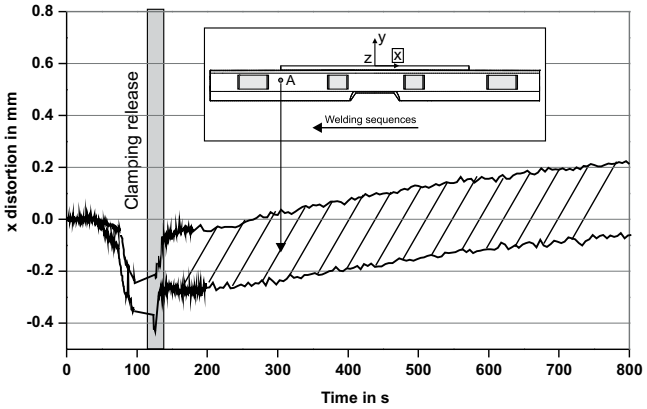

Fig. 4.14: Experimental transient distortion measurement at point A from 0 s to 800 s, x-direction, crossbeam, optical 3D deformation analysis system, Aramis

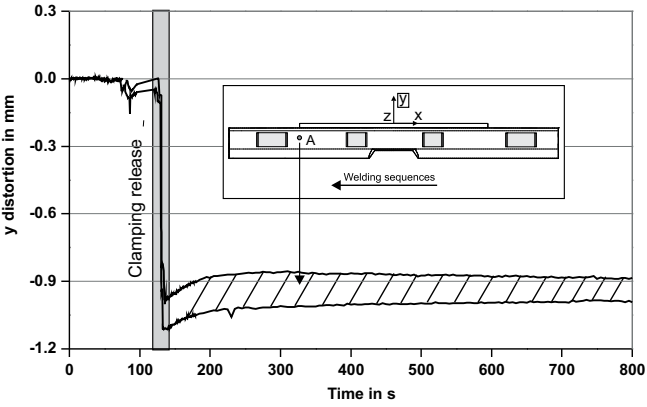

Fig. 4.15: Experimental transient distortion measurement at point A from 0 s to 800 s, y-direction, crossbeam, optical 3D deformation analysis system, Aramis

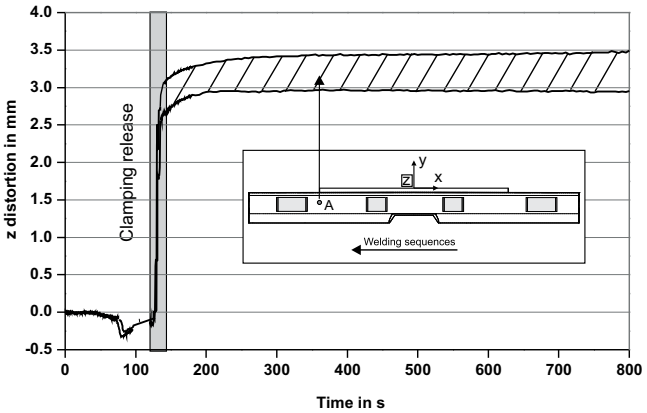

Fig. 4.16: Experimental transient distortion measurement at point A from 0 s to 800 s, z-direction, crossbeam, optical 3D deformation analysis system, Aramis

4.2 Analytical simulations

In the following sections, the analytical temperature field results for the plates and the semi-industrial plate are presented. The results of the application of this analytical approach to accelerate the temperature field simulation of a real industrial part are finally shown.

4.2.1 Plates

4.2.1.1 Infinite solid – steady state – linear welding path – point heat source formulation

The temperature profile between A and B for a point source in steady state moving on a plate with infinite thickness is presented in Fig. 4.17. In the corresponding analytical solution, the temperature at the position of the moving heat source (x=0,y=0,z=0) is singular and tends to infinite. For presentation reason, the temperature profile has therefore been "cut" for temperatures higher than 1500°C. The calculation time for this temperature profile is 0.1 s (see section 4.2.4). For a temperature field simulation of the top surface of the plate with approximately 16,000 nodes, the calculation time is 18 s.

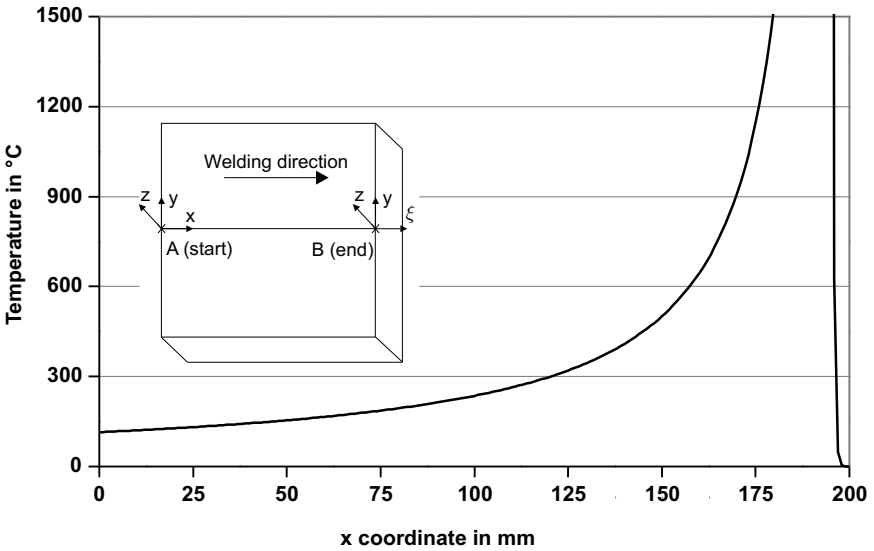

Fig. 4.17: Analytical temperature profile along AB at t = 20 s for a moving point heat source in steady state, infinite solid 200 x 200 x 100 mm³, q = 1.5 kW and v_s = 10 mm/s

4.2.1.2 Infinite thin plate – steady state – linear welding path – point heat source formulation

The temperature profiles between A and B for the point source in steady state moving on the finite plates with 1.5 mm and 5 mm, see section 3.2.3.2 are plotted in Fig. 4.18 and Fig. 4.19. For presentation reason, the temperature profiles of the thin plates with 1.5 mm and 5

mm thickness have been “cut” for temperatures higher than 5000 °C and 1500 °C, respectively.

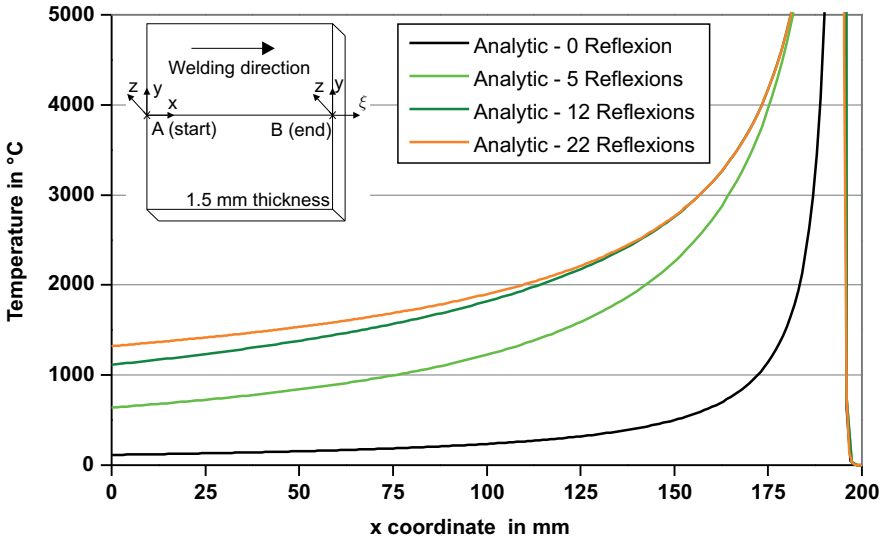

Fig. 4.18: Analytical temperature profiles with 0, 5, 12 and 22 reflexions along AB at t = 20 s for a moving point heat source in steady state, infinite thin plate 200 x 200 x 1.5 mm³, q = 1.5 kW and v_s = 10 mm/s

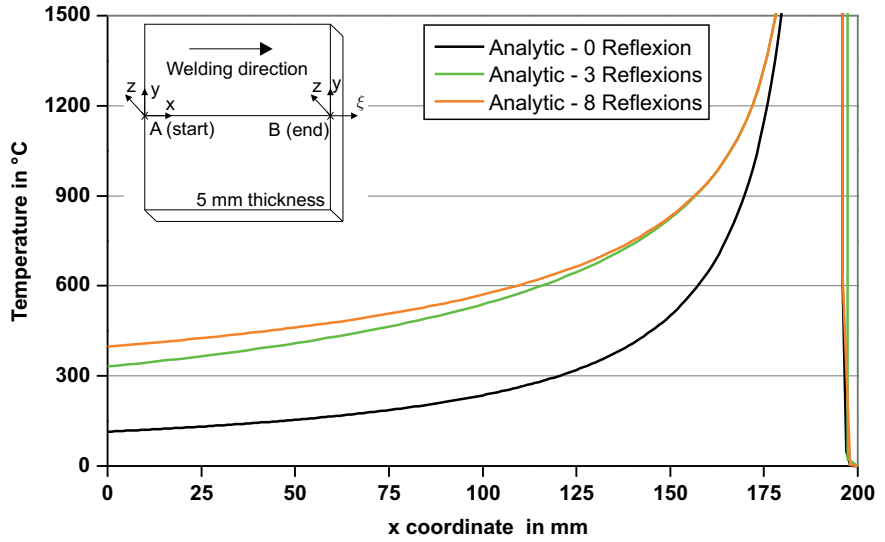

Fig. 4.19: Analytical temperature profiles with 0, 3, and 8 reflexions along AB at t = 20 s for a moving point heat source in steady state, infinite thin plate 200 x 200 x 5 mm³, q = 1.5 kW and v_s = 10 mm/s

The reflexion technique (see section 2.2.2 and 3.2.3.2) has been used to obtain the adiabatic boundary condition at the lower part of the infinite thin plate as shown in Fig. 4.20 a) for the infinite thin plate 200 x 200 x 1.5 mm^3.

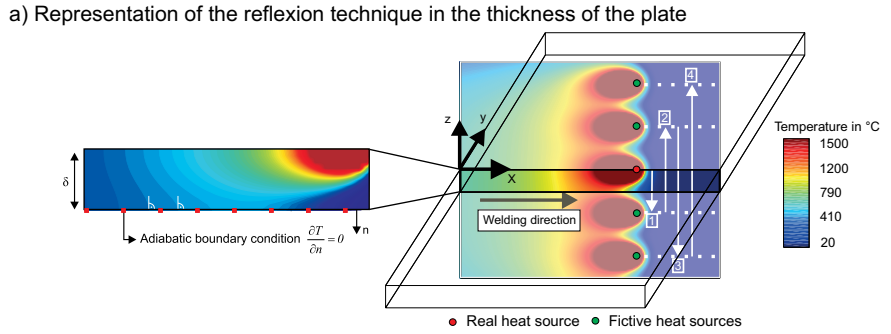

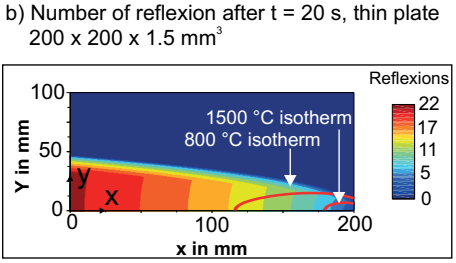

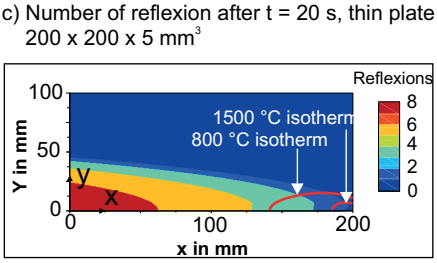

Fig. 4.20: a) Reflexion technique to obtain the adiabatic boundary condition at the lower side of the infinite thin plate 200 x 200 x 1.5 mm^3, q = 1.5 kW, v_s = 10 mm/s. b) and c) Number of reflexion according to the two convergence criteria defined in section 3.2.3.2 for a point source moving for t = 20 s, thin plate 200 x 200 x 1.5 mm^3 and 200 x 200 x 5 mm^3, q = 1.5 kW and v_s = 10 mm/s

The reflexion technique is a convergent series; for the infinite plate with 1.5 mm thickness in Fig. 4.18, the convergence has been reached for 22 reflexions; for the infinite thin plate with 5 mm thickness in Fig. 4.19, the temperature profile converges faster with 8 reflexions as plotted in Fig. 4.20 b) and c), respectively. The calculation times for the temperature profiles and a temperature field of the top surface of the both 1.5 mm and 5 mm infinite thin plates are 0.8 s – 98 s and 0.31 s – 39 s, respectively. For both 1.5 mm and 5 mm infinite thin plates, the number of nodes for the temperature field simulation is approximately 16,000.

4.2.1.3 Finite thin plate – transient state – linear welding path – point heat source formulation

The analytical solution of this moving point source in transient state is valid for an infinite plate with infinite thickness. The temperature field in the finite thin plate investigated here has been obtained by using the reflexion technique and the addition of virtual sinks as described in section 3.2.3.3. Since the investigated plate 50 x 50 x 3 mm^3 is relatively small in comparison with the previous test case, the moving heat source must also be reflected

against the boundary of the plate in the planes x-z and y-z in order to obtain an adiabatic boundary condition at these bounding planes. A representation of the main moving heat source and the virtual ones running simultaneously during and after the welding process is shown in Fig. 4.21:

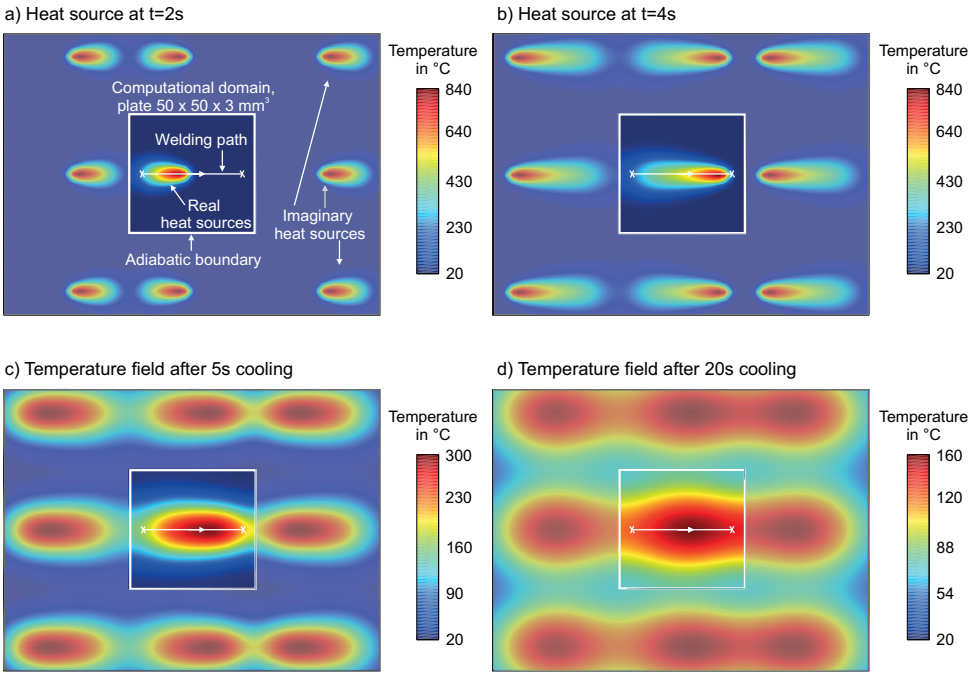

Fig. 4.21: Reflection technique to maintain the adiabatic boundary conditions at all boundaries of the finite thin plate 50 x 50 x 3 mm³, linear welding path, q = 1.5 kW and v_s = 10 mm/s

It is important to notice that in Fig. 4.21a), b), c) and d), all the moving real and virtual heat sources are also reflected in the thickness direction in the same manner as in the previous section. As the analytical solution implemented here is in transient state, the cooling behaviour is simulated by adding a virtual sink after the welding process as explained in section 3.2.3.3. This virtual sink is also running in addition to all the others in Fig. 4.21c) and d) and is also reflected like the real heat source.

For this test case, a temperature profile between A' and B' at t = 4 s and four transient temperature cycles at the four points T1 to T4 have been calculated and displayed in Fig. 4.22 and in Fig. 4.23. For the temperature cycles, the first 4 s correspond to the welding time, the other 16 s equal the cooling time. The calculation time for the simulation of the temperature profile A'B' and the four temperature cycles are 0.05 s and 0.2 s, respectively. For a temperature field simulation of the top surface of this plate, which contains approximately 10,000 nodes, the simulation lasts 37 s.

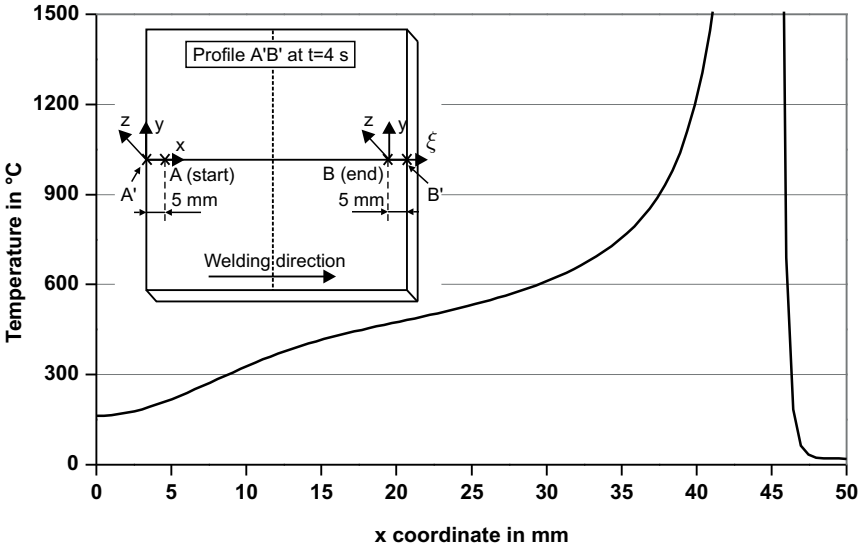

Fig. 4.22: Analytical temperature profile between A' and B' for a moving point heat source in transient state at t = 4 s, finite thin plate 50 x 50 x 3 mm³, q = 1.5 kW and v_s = 10 mm/s

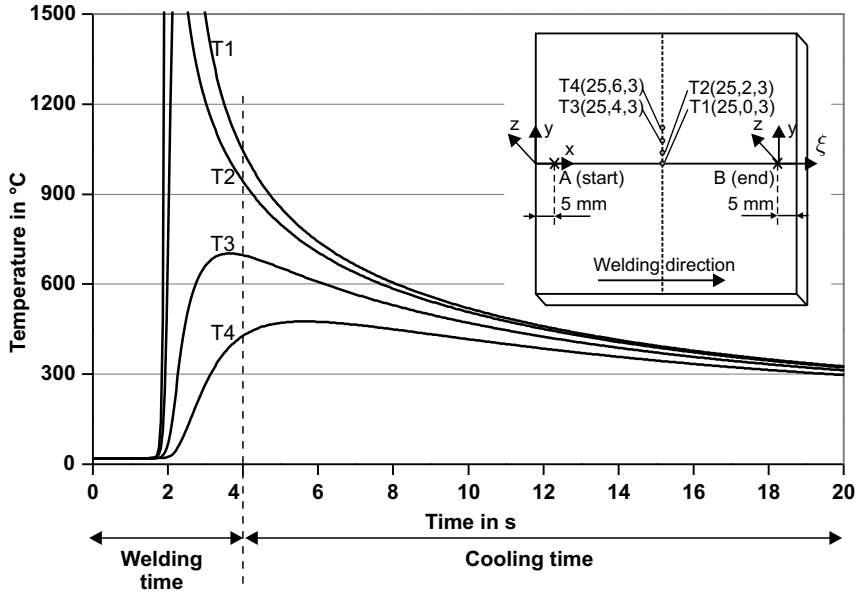

Fig. 4.23: Analytical temperature cycles for a moving point heat source in transient state, finite thin plate 50 x 50 x 3 mm³, q = 1.5 kW and v_s = 10 mm/s

4.2.1.4 Finite thin plate – transient state – linear welding path – double ellipsoidal heat source formulation

The experimental settings of this test case are identical to the previous section. Only the moving point source is extended to a distributed double ellipsoidal heat source formulation. The temperature cycles T1 to T4 for the investigated small and large double ellipsoids are plotted in Fig. 4.24. Even if the power of both double ellipsoids is equal, the respective temperature fields are different. For the large one, the energy distribution is spread on a larger surface on the plate resulting in a lower peak temperature. After 20s, all temperature cycles of both double ellipsoids are equal due to the same heat input.

The calculation times of the four temperature cycles T1 to T4 and for a temperature field are 2.4 s – 104 s and 2.6 s – 111 s for the large and small double ellipsoids, respectively.

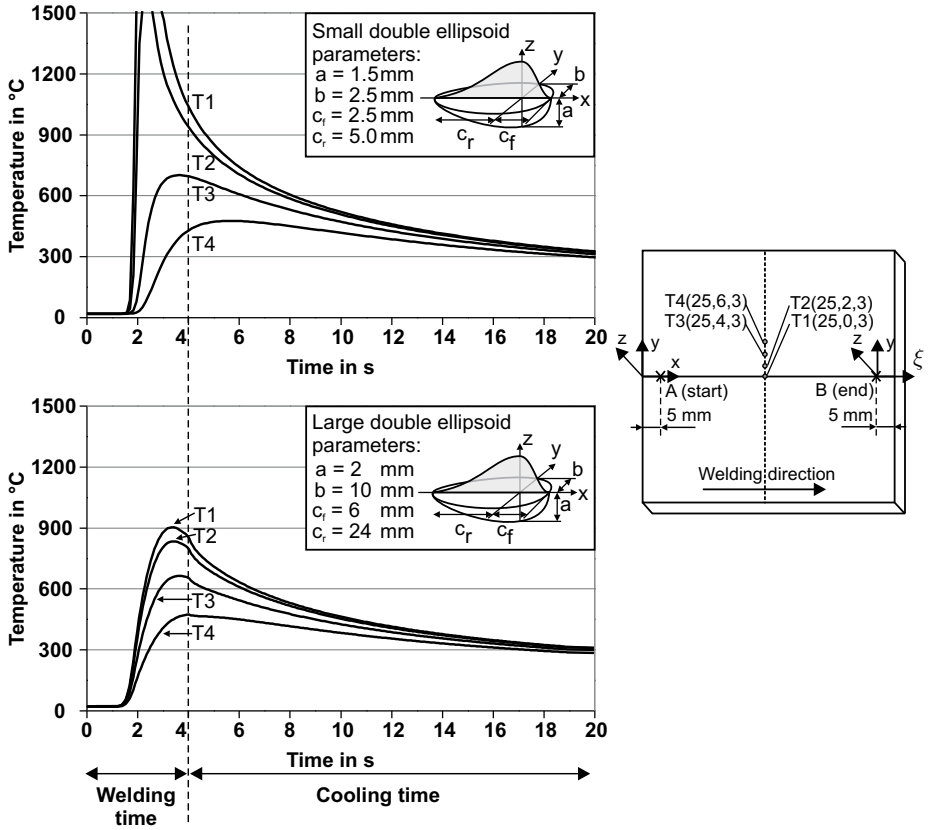

Fig. 4.24: Analytical temperature cycles for the moving small and large double ellipsoidal heat sources in transient state, finite thin plate 50 x 50 x 3 mm³, q = 1.5 kW and v_s = 10 mm/s

4.2.1.5 Finite thin plate – transient state – curved welding path – double ellipsoidal heat source formulation

The same plate and the same double ellipsoidal heat source as in the previous section 4.2.1.4 have been used in this test case. The linear welding path has been replaced by a curved one running 5 mm from the edge of the plate. The number of reflexions in the xy-plane after 16 s welding time is shown in Fig. 4.25. The square in the middle of the figure and zoomed on the right hand side of the figure corresponds to the real simulation domain and the rest to the virtual simulation domain. All the real and the virtual heat sources and sinks are also reflected in thickness direction (z-axis).

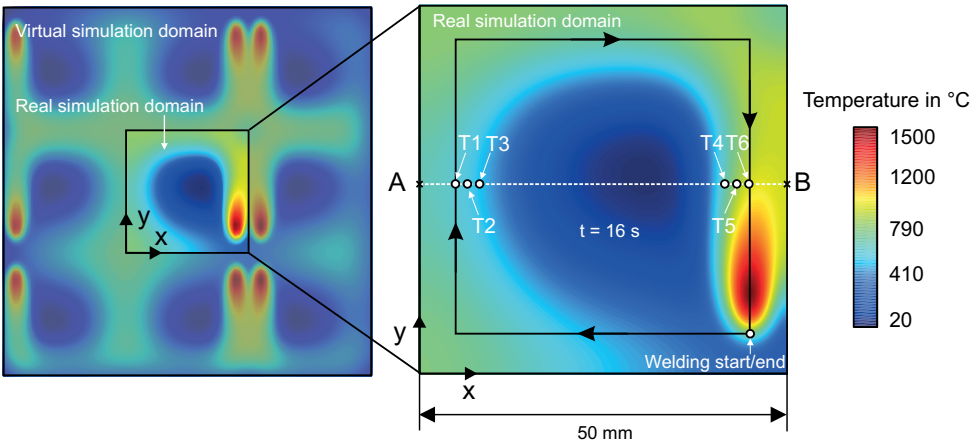

Fig. 4.25: Reflexion technique to reproduce the adiabatic boundary condition at all the boundaries of the finite thin plate 50 x 50 x 3 mm^3, curved welding path, q = 1.5 kW and v_s = 10 mm/s

For this test case, the six temperature cycles T1 to T6 and the temperature profile between A and B at t = 16 s (position remembered in Fig. 4.25) are displayed in Fig. 4.26a) and b), respectively. The 8 s time between the peaks of the temperature cycles T1 to T3 and T4 to T6 corresponds to the time the heat source needs to run from the point A to B with the speed of 10 mm/s. The calculation time for the six temperature cycles is 68 s, 6 s for the temperature profile between A and B and 1303 s for the temperature field of the top surface at t = 16 s.

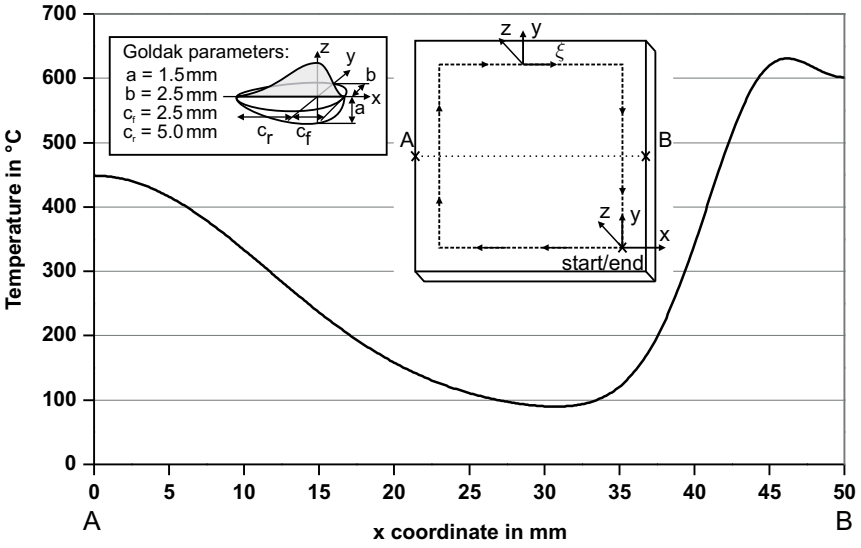

a) Analytical temperature profile between A and B at t = 16 s

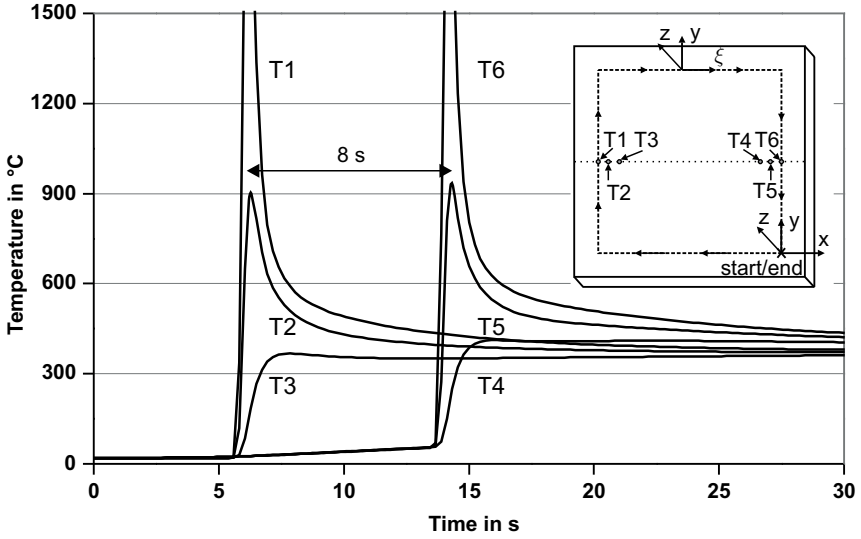

b) Analytical transient temperature cycles T1 to T6

Fig. 4.26: Analytical temperature profile between A and B and analytical temperature cycles for a double ellipsoidal heat source in transient state moving on a curved welding path, finite thin plate 50 x 50 x 3 mm³, q = 1.5 kW and v_s = 10 mm/s

4.2.2 Semi-industrial geometry

The ten temperature cycles investigated for this test case have been simulated for 30 s and are plotted in Fig. 4.27a). It is to notice that the four welds are completely independent with different start and end positions on the plate and with different lengths. Finally, the analytical simulation of the fusion line in a cross-section along the weld 1 is shown in Fig. 4.27b).

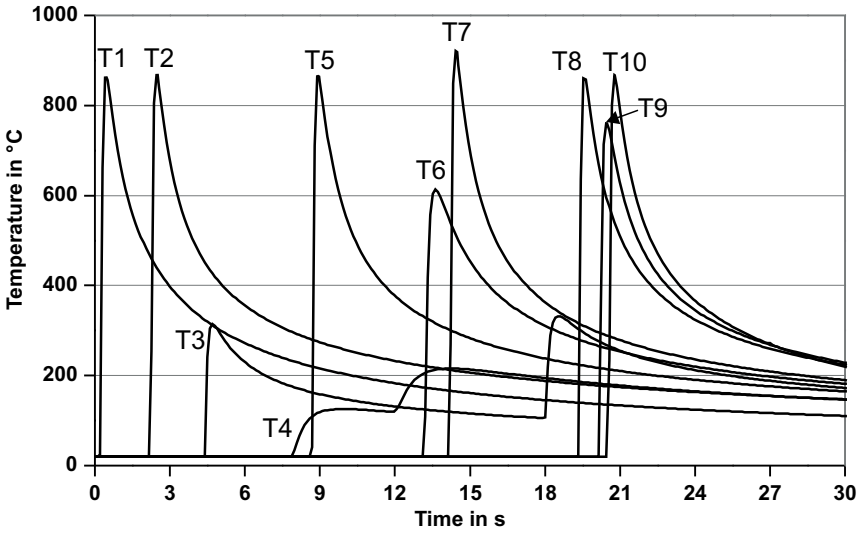

a) Analytical temperature cycles T1 to T10

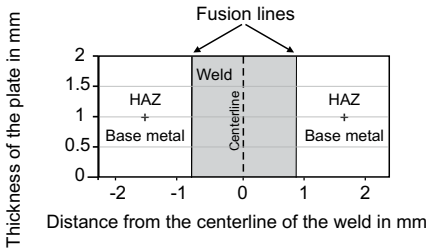

b) Fusion line in a cross-section along the weld 1

Fig. 4.27: Analytical temperature cycles for two double ellipsoidal heat sources in transient state moving on different and independent curved welding paths, semi-industrial plate 500 x 250 x 2 mm^3, q = 3.3 kW and v_s = 300 cm/min

The analytically calculated weld pool length and width are 5.3 mm and 1.65 mm, respectively. The calculation time of the analytical simulation results presented in Fig. 4.27 are summarised in section 4.2.4. The calculation time of the ten temperature cycles, the fusion line in cross-section, the weld pool length and the weld pool width take 120 s, 90 s, 0.1 s and 0.4 s, respectively. For the temperature field simulation on the top surface of the plate, 2,000,000 nodes have been required resulting in 22,500 s calculation time.

4.2.3 Wheelhouse and simplified geometries

As explained previously in section 3.2.5, the start values for the final calibration of the input parameter set of the wheelhouse's thermal model, i.e. the parameter distributions of the two double ellipsoidal heat sources $a_{top} = a_{bottom}$, $b_{top} = b_{bottom}$, $c_{f\text{-}top} = c_{f\text{-}bottom}$ and $c_{r\text{-}top} = c_{r\text{-}bottom}$ and the energy efficiency η of the welding process, have been calculated by solving the inverse heat conduction problem for the simple geometry "parallel weld" with the global optimisation algorithm presented in section 3.2.5.

After the convergence of the optimisation algorithm, the optimal parameter set for this 5D optimisation problem found to be, see Fig. 4.28:

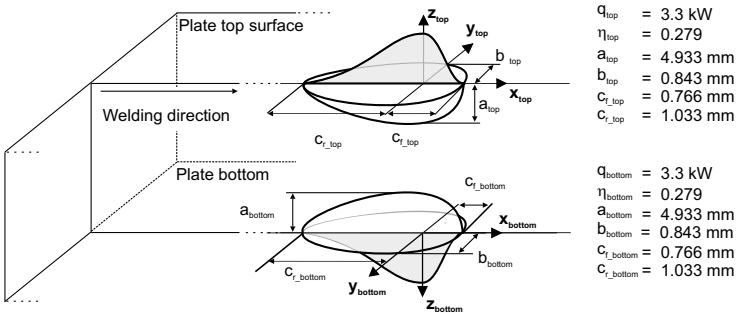

Fig. 4.28: Optimised parameter shape of the two double ellipsoidal heat sources used for the thermal simulation of the simplified geometry "parallel weld" given by the global optimisation algorithm

The welding power was given as input variable in the global optimisation algorithm, see section 3.2.5, and the welding efficiency has been subsequently calculated by comparing the response of the calibration with the real value of 3.3 kW. The calculation time of the automatic calibration was 1830 s, see Tab. 4.2 in section 4.2.4. Within this time, 3051 analytical simulations have been run within the 5D constrained parameter space, see Fig. 3.22 in section 3.2.5, until the L2-norm between the vectors of the simulated and experimental characteristics $u_{\mathrm{sim},i}$ and $u_{\mathrm{exp},i}$ has reached the convergence criterion C. The values of the vector of the simulated characteristics are plotted in Tab. 4.1:

Tab. 4.1: Vector of the simulated characteristics $u_{sim,i} = (A_{sim}, B_{sim}, C_{sim}, D_{sim}, E_{sim}, F_{sim}, G_{sim}, H_{sim})$ taken from characteristic temperature cycles T1, T2, T3 and T4, cross-section and weld pool length

A_{sim}	(1.24 s, 897 °C)	E_{sim}	(0.56 mm, 0.0 mm)
B_{sim}	(129 s, 652 °C)	F_{sim}	(0.56 mm, 1.0 mm)
C_{sim}	(1.49 s, 529 °C)	G_{sim}	(0.56 mm, 2.0 mm)
D_{sim}	(2.04 s, 272 °C)	H_{sim}	3.6 mm

The analytical temperature cycles T1 to T4, the shape of the fusion zone in cross-section and the weld pool length have been calculated with the respective calibrated input parameter set as shown in Fig. 4.29 and Fig. 4.30:

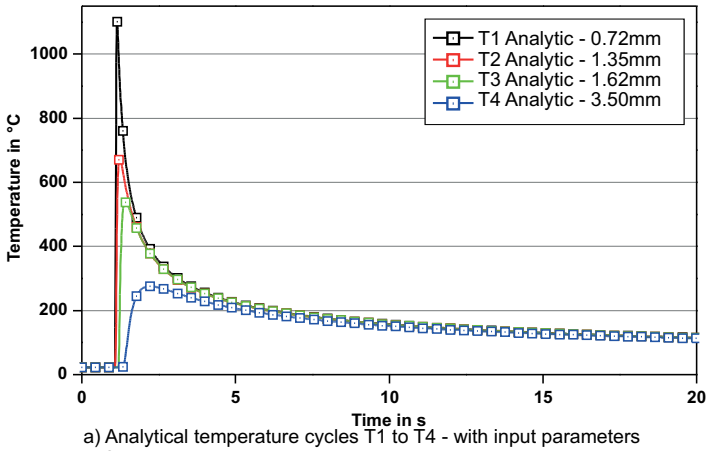

a) Analytical temperature cycles T1 to T4 - with input parameters from the optimisation algorithm - 0 s to 20 s

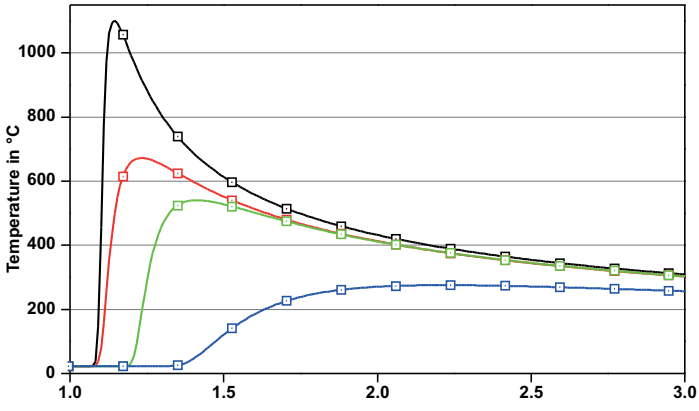

b) Analytical temperature cycles T1 to T4 - with input parameters from the optimisation algorithm - 1 s to 3 s

Fig. 4.29: Analytical temperature cycles T1 to T4 in transient state calibrated with the global optimisation algorithm, simplified geometry "parallel weld", q = 3.3 kW, η = 27.9 % and v_s = 300 cm/min

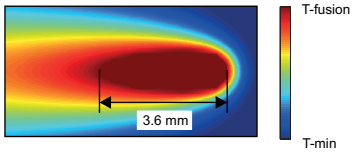

a) Weld pool length

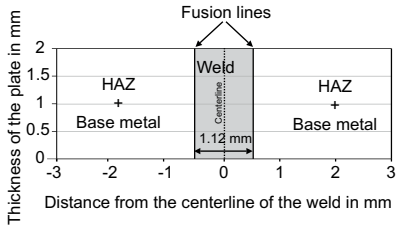

b) Fusion line in the cross-section

Fig. 4.30: Analytical weld pool length and fusion zone in cross-section for two double ellipsoidal heat sources in transient state calibrated with the global optimisation algorithm, simplified geometry "parallel weld", q = 3.3 kW, η = 27.9 % and v_s = 300 cm/min

4.2.4 Calculation time of analytical solutions

The calculation times of all the analytical simulation results presented in the section 4.2 are summarised in the following Tab. 4.2:

Tab. 4.2: Calculation time of all the analytical simulation results presented in section 4.2

Geometries	Test case	Software	Simulation time	
Plates	Linear trajectory - moving point source infinite solid 200x200x100 mm^3 steady state	Scilab	Temp. field	18 s
			Temp. profile	0.1 s
	Linear trajectory - moving point source infinite thin plate 200x200x1.5 mm^3 steady state		Temp. field	98 s
			Temp. profile	0,8 s
	Linear trajectory - moving point source infinite thin plate 200x200x5 mm^3 steady state		Temp. field	39 s
			Temp. profile	0.31 s
	Linear trajectory - transient moving point source 50x50x3 mm^3		Temp. field	37 s
			Temp. cycles	0.2 s
			Temp. profile	0.05 s
	Linear trajectory - transient small moving Goldak source 50x50x3 mm^3	In-house C++ code and Scilab	Temp. field	111 s
			Temp. cycles	2.6 s
	Linear trajectory - transient large moving Goldak source 50x50x3 mm^3		Temp. field	104 s
			Temp. cycles	2.4 s
	Curved trajectory -transient moving Goldak source 50x50x3 mm^3		Temp. field	1303 s
			Temp. cycles	68 s
			Temp. profile	6 s
Semi-industrial plate			Temp. field	22500 s
			Temp. cycles	120 s
			Fusion line	90 s
			Weld pool length	0.1 s
			Weld pool width	0.4 s
Automatic calibration of the simplified geometry „parallel weld“			Number of single analytical simulation	3051
			Time for one analytical simulation	0.6 s
			Optimised parameter for the two double ellipsoidal heat sources	1830 s

4.3 Numerical simulations

4.3.1 Plates

The same thermal simulations as in section 4.2.1 have been simulated with FEM techniques and are presented in the following sections.

4.3.1.1 Infinite solid – steady state – linear welding path – point heat source formulation

The result of the numerical temperature profile between A and B after the moving point source acts 20 s on the infinite solid is shown in Fig. 4.31:

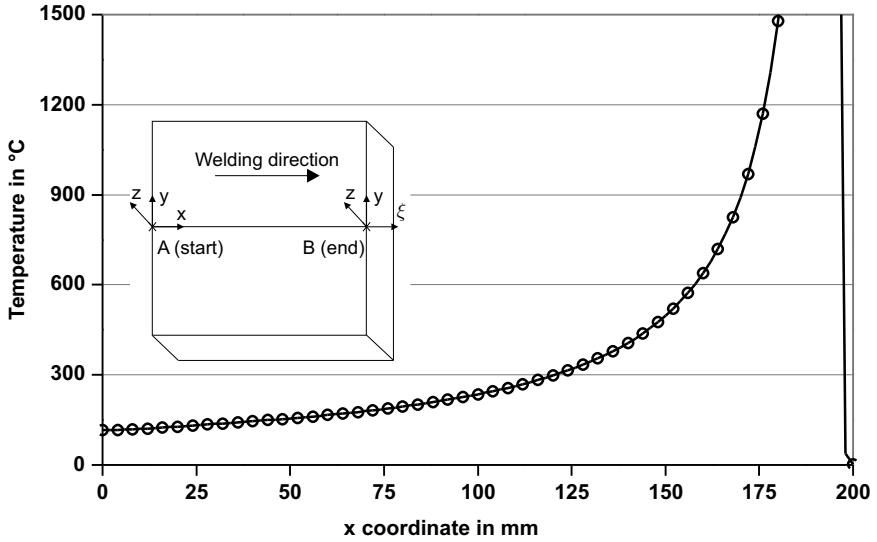

Fig. 4.31: Numerical temperature profile along AB at t = 20 s for a moving point heat source in steady state, infinite solid 200 x 200 x 100 mm³, q = 1.5 kW and v_s = 10 mm/s

In a FE-simulation, the simulation along a profile at a single time or the transient temperature cycles at different positions cannot be simulated separately from the simulation of the entire structure. Therefore, the calculation time of the profile AB and the 3D temperature field of this test case are identical and equal to 189,031 s.

4.3.1.2 Infinite thin plate – steady state – linear welding path – point heat source formulation

The temperature profile between A and B for the infinite thin plate with 1.5 mm and 5 mm thickness have been displayed in Fig. 4.32 and Fig. 4.33, respectively. As the for analytic results, the temperature has been cut above 5000°C and above 1500°C for the plates with 1.5 mm and 5 mm thickness, respectively. The calculation time to simulate the profile AB and the 3D temperature field is equal in a FE simulation. For the plate 200 x 200 x 1.5 mm³, it was 7,604 s and 11,175 s for the plate with 5 mm thickness.

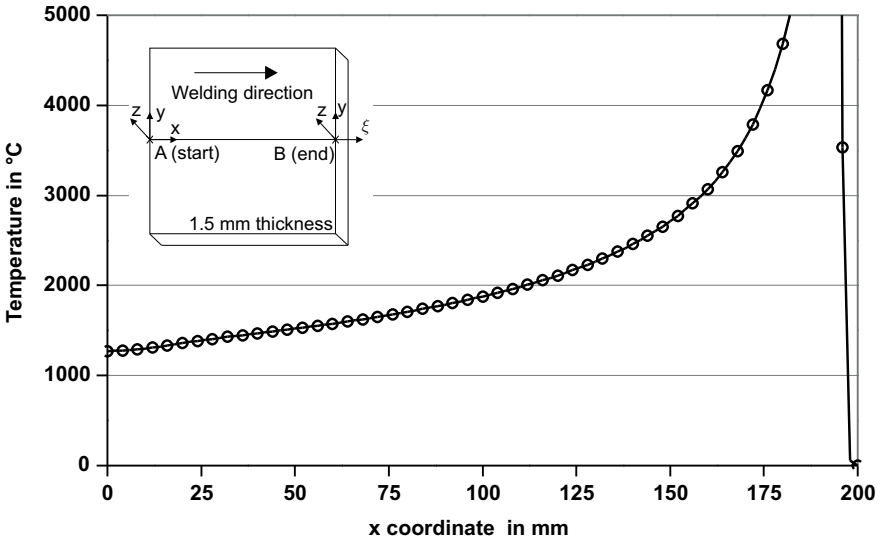

Fig. 4.32: Numerical temperature profile along AB at t = 20 s for a moving point heat source in steady state, infinite thin plate 200 x 200 x 1.5 mm^3, q = 1.5 kW and v_s = 10 mm/s

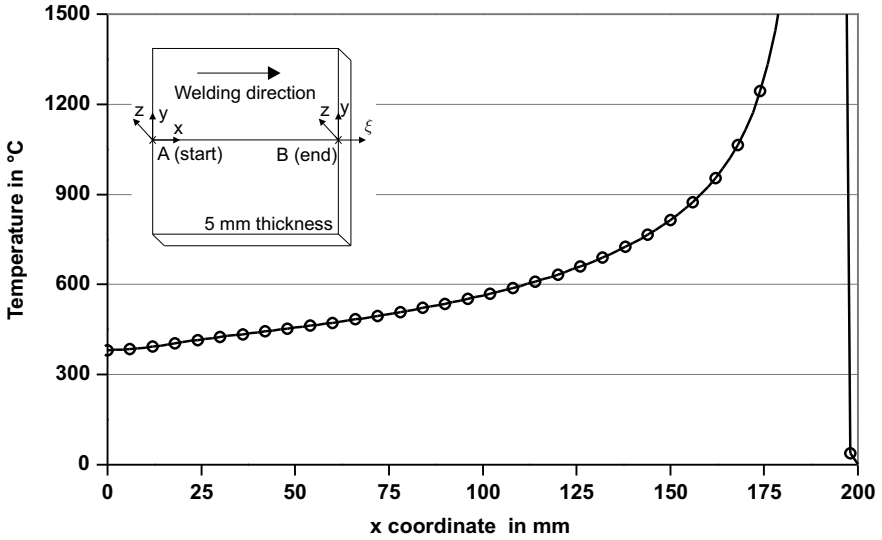

Fig. 4.33: Numerical temperature profile along AB at t = 20 s for a moving point heat source in steady state, infinite thin plate 200 x 200 x 5 mm^3, q = 1.5 kW and v_s = 10 mm/s

4.3.1.3 Finite thin plate – transient state – linear welding path – point heat source formulation

For this first test case in transient state, the same temperature profile between A' and B' and the same temperature cycles T1 to T4 as in section 4.2.1.3 have been calculated. The simulation result for the temperature profile is shown in Fig. 4.34. The four temperature

cycles T1 to T4 are shown in Fig. 4.35. The calculation time for the temperature profile and for the temperature cycles is 240 s.

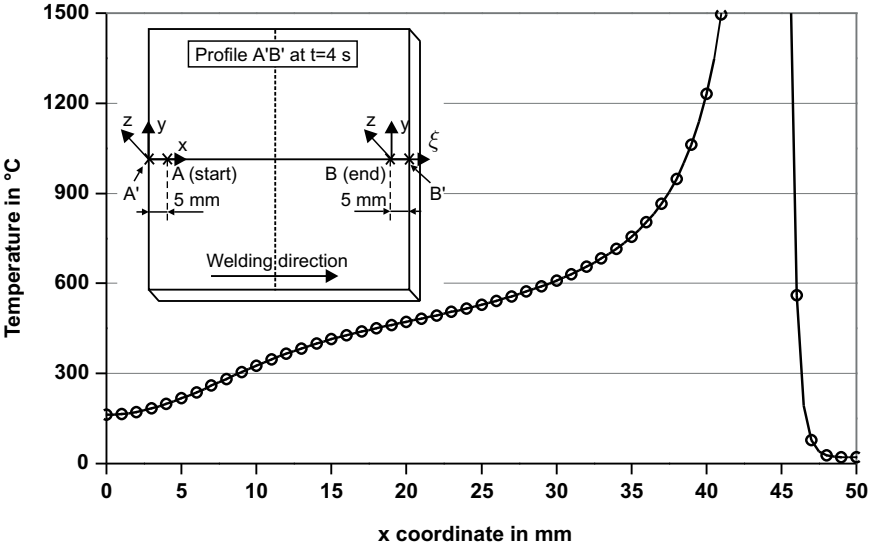

Fig. 4.34: Numerical temperature profile between A' and B' for a point heat source in transient state moving for 4 s, finite thin plate 50 x 50 x 3 mm³, q = 1.5 kW and v_s = 10 mm/s

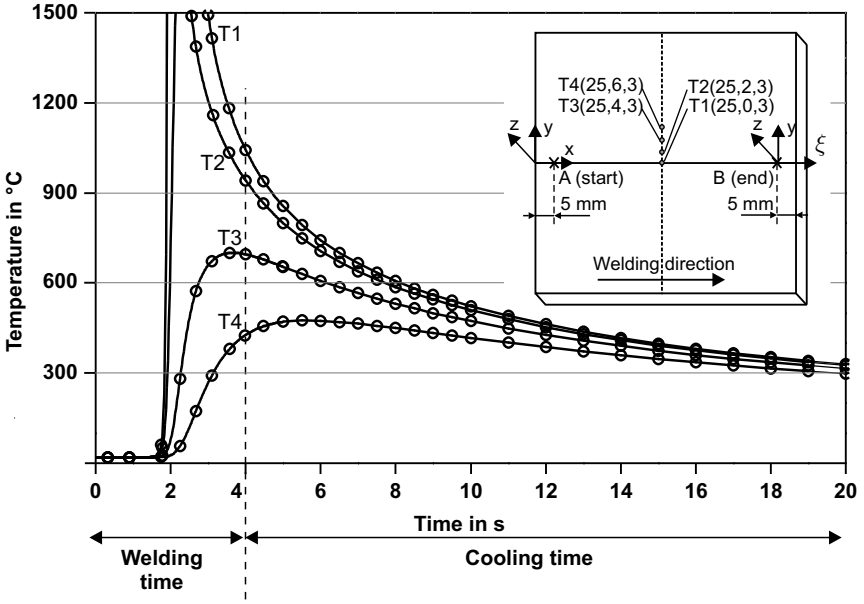

Fig. 4.35: Numerical temperature cycles for a moving point heat source in transient state, finite thin plate 50 x 50 x 3 mm³, q = 1.5 kW and v_s = 10 mm/s

4.3.1.4 Finite thin plate – transient state – linear welding path – double ellipsoidal heat source formulation

The numerical temperature cycles T1 to T4 for the simulation with the small and large double ellipsoid heat sources moving on the path AB are presented in Fig. 4.36. The respective calculation times are 240 s and 120 s.

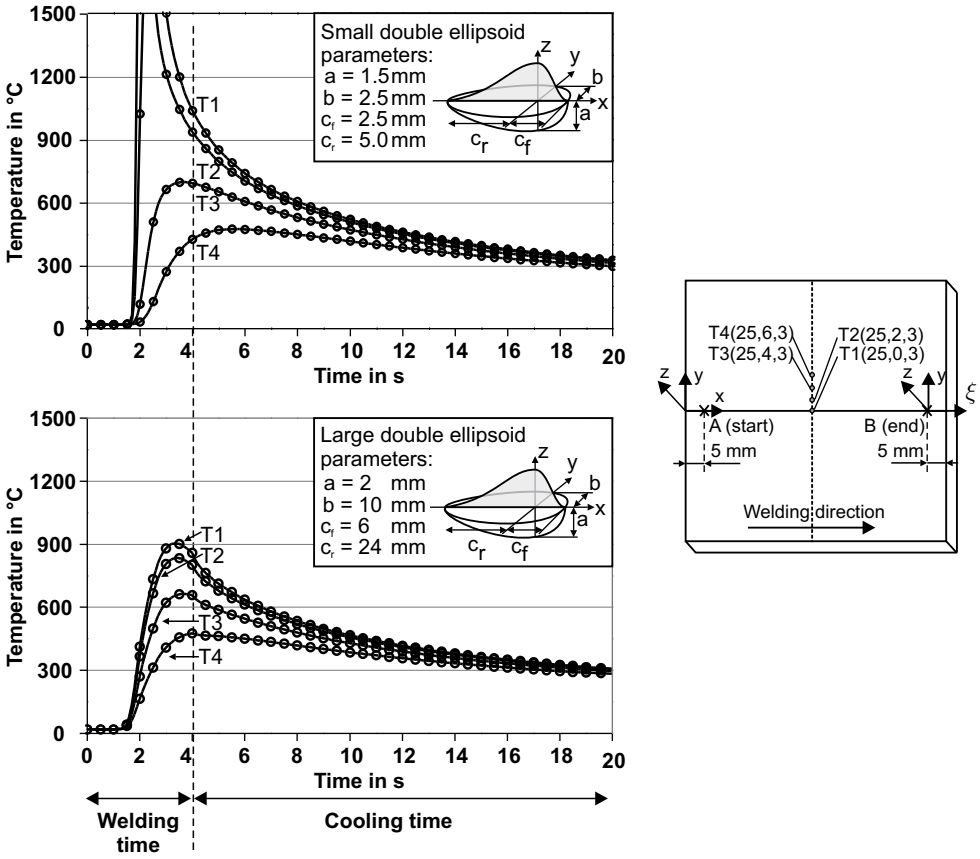

Fig. 4.36: Numerical temperature cycles for the moving small and large double ellipsoidal heat sources in transient state, finite thin plate 50 x 50 x 3 mm³, q = 1.5 kW and v_s = 10 mm/s

4.3.1.5 Finite thin plate – transient state – curved welding path – double ellipsoidal heat source formulation

The experimental setting of this test case is the same as previously. Only the welding path has been changed, from a linear one to a curved one. The numerical temperature profile between A and B at t = 16 s and the six temperature cycles T1 to T6 are plotted in Fig. 4.37a) and Fig. 4.37b. The calculation time for both numerical results is 1600 s.

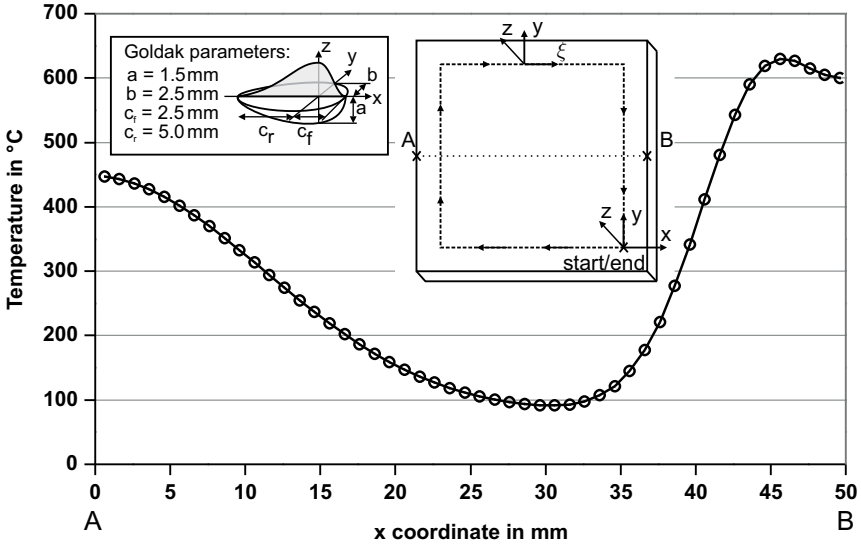

a) Numerical temperature profile between A and B at t = 16 s

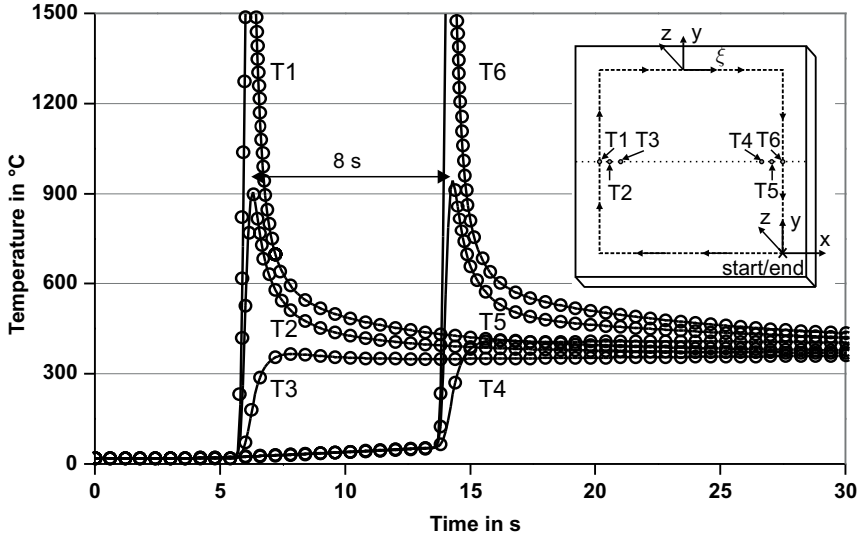

b) Numerical transient temperature cycles T1 to T6

Fig. 4.37: Numerical temperature profile between A and B and numerical temperature cycles for a double ellipsoidal heat source in transient state moving on a curved welding path, finite thin plate 50 x 50 x 3 mm³, q = 1.5 kW and v_s = 10 mm/s

4.3.2 Semi-industrial geometry

The numerical model for the semi-industrial geometry has been described in section 3.3.4. The ten temperature cycles T1 –T10 and the cross-section along the weld W1 are plotted in Fig. 4.38a) and b). The calculation for the numerical simulation is 8520 s.

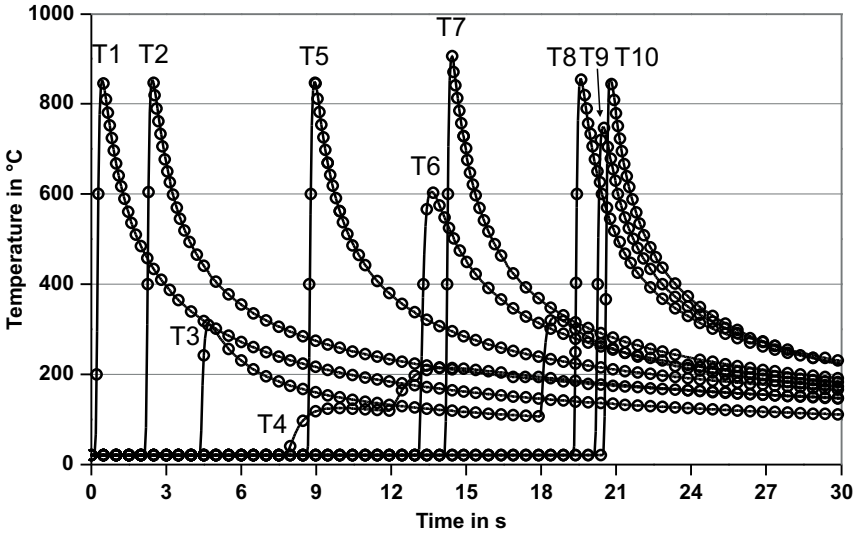

a) Analytical temperature cycles T1 to T10

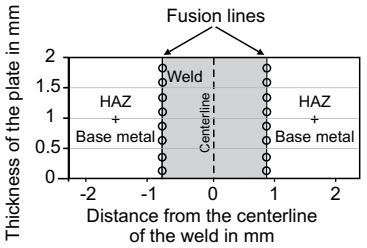

b) Fusion line in a cross-section along the weld 1

Fig. 4.38: Numerical temperature cycles for two double ellipsoidal heat sources in transient state moving on different and independent curved welding paths, semi-industrial plate 500 x 250 x 2 mm³, q = 3.3 kW and v_s = 300 cm/min

4.3.3 Wheelhouse and simplified geometries

As described in section 3.3.5, the calibration of the thermal model of the three cases investigated here is made only against the experimental data measured for the simplified geometry “parallel weld” and then used for the simulation of the simplified geometry “overlap weld” and the wheelhouse. The input parameters, i.e. the distribution parameters of the double ellipsoidal heat sources and the welding process efficiency, automatically calibrated analytically, see section 4.2.3, have been used as start values for a final calibration with numerical techniques. The final calibrated input parameters for the simplified geometries “parallel weld”, “overlap weld” and wheelhouse are presented in Fig. 4.39. In comparison to the analytical parameter prediction presented in section 4.2.3, only the welding efficiency parameter has been modified.

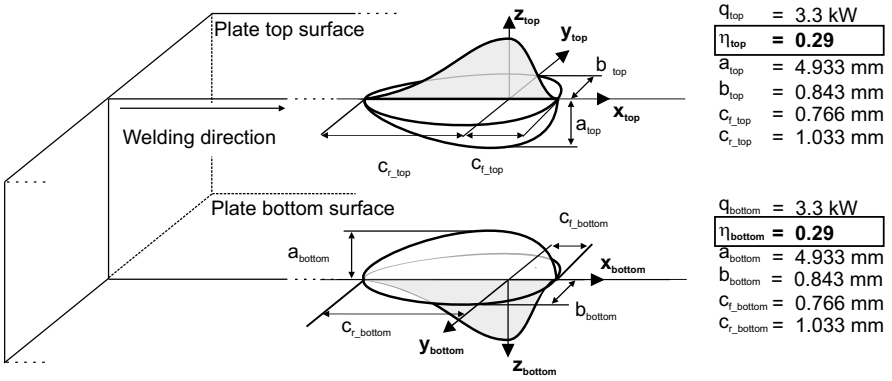

Fig. 4.39: Calibrated parameters for the two double ellipsoidal heat sources used for the thermal simulation of the simplified geometries "parallel weld" and "overlap weld" and the wheelhouse, 3.3 kW Nd:YAG laser beam welding, sheet thickness 1 mm and v_s = 300 cm/min

The simulation results for the four temperature cycles T1 to T4 of the simplified geometries "parallel weld" and "overlap weld" and the six temperature cycles T1 to T6 of the wheelhouse and have been plotted in Fig. 4.40, Fig. 4.41 and Fig. 4.42. In the three figures, the graph a) and the graph b) represent the transient temperature cycles during the entire welding process and a zoom around the peak temperatures, respectively. For each test case, a simulation with and without clamping has been run to see the influence of the clamping on the cooling behaviour. A zoom of the zone where the influence of the clamping is maximal has been plotted in the graph a) of each figure. The weld pool area and shape in cross-section in the middle of the weld of the simplified geometries "parallel weld" and "overlap weld" and in the middle of the welds W1 and W2 of the wheelhouse and the weld pool lengths have been simulated and plotted in Fig. 4.43a) and b), Fig. 4.44a) and b) and in Fig. 4.45a) and b), respectively. The calculation times of the thermal simulation of the simplified geometries "parallel weld" and "overlap weld" are 3030 s and 2900 s, respectively. For the wheelhouse, it takes approximately 5 times longer with a calculation time of 15,500 s.

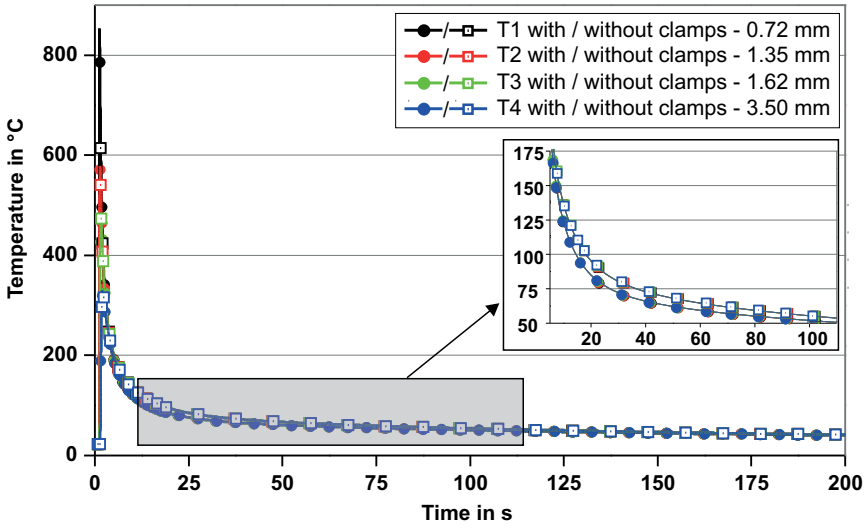

a) Simulated temperature cycles T1-T4 from 0 s to 200 s, with and without clamps

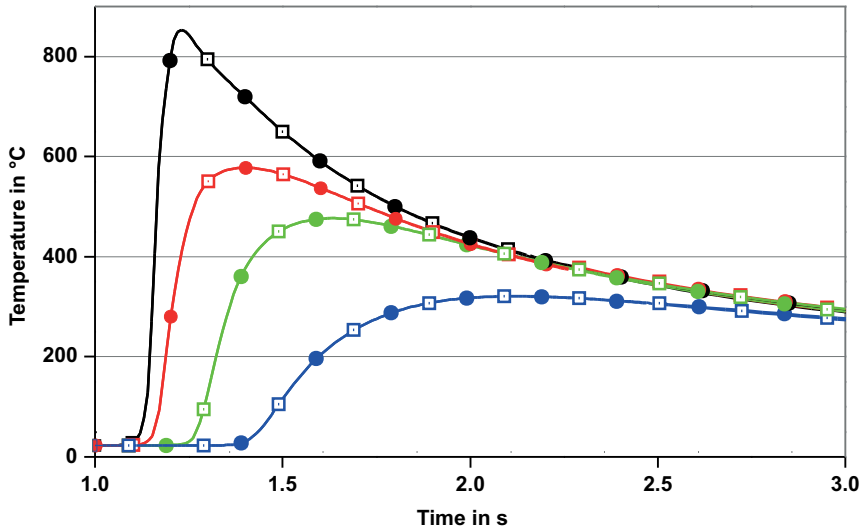

b) Simulated temperature cycles T1-T4 from 1 s to 3 s, with and without clamps

Fig. 4.40: Numerical temperature cycles T1 to T4, simplified geometry "parallel weld", $q = 3.3$ kW, $\eta = 29$ % and $v_s = 300$ cm/min

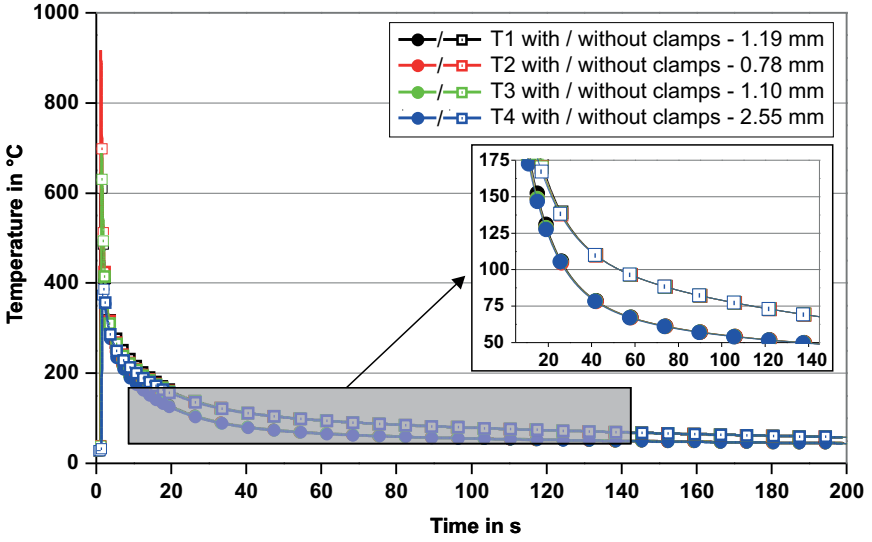

a) Simulated temperature cycles T1-T4 from 0 s to 200 s, with and without clamps

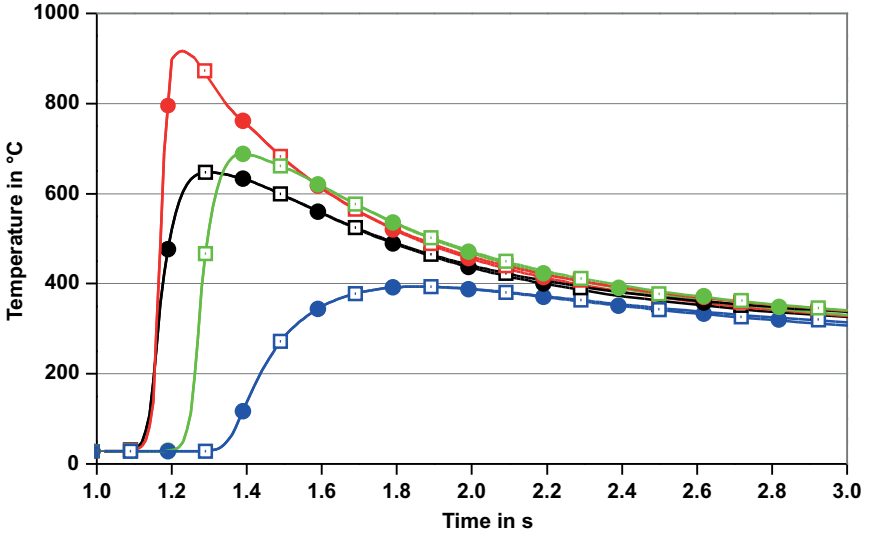

b) Simulated temperature cycles T1-T4 from 1 s to 3 s, with and without clamps

Fig. 4.41: Numerical temperature cycles T1 to T4, simplified geometry "overlap weld", q = 3.3 kW, η = 29 % and v_s = 300 cm/min

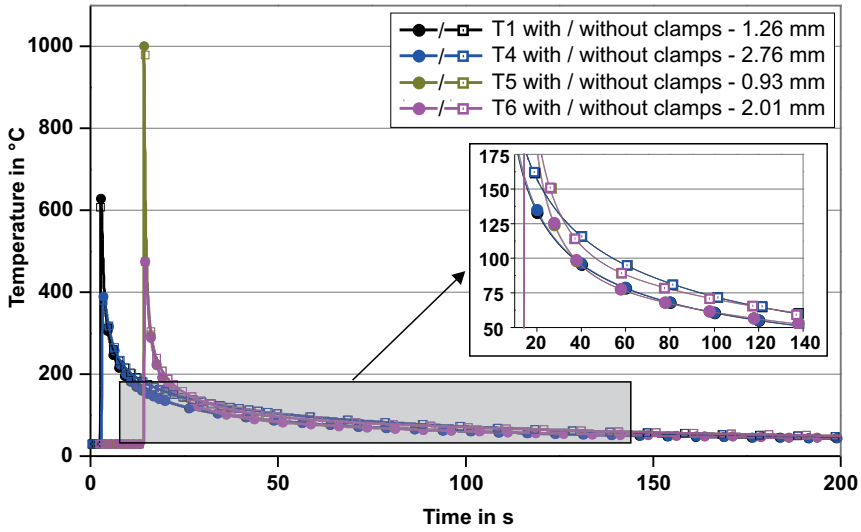

a) Simulated temperature cycles T1-T4 (weld W1) and T5-T6 (weld W3), from 0 s to 200 s, with and without clamps

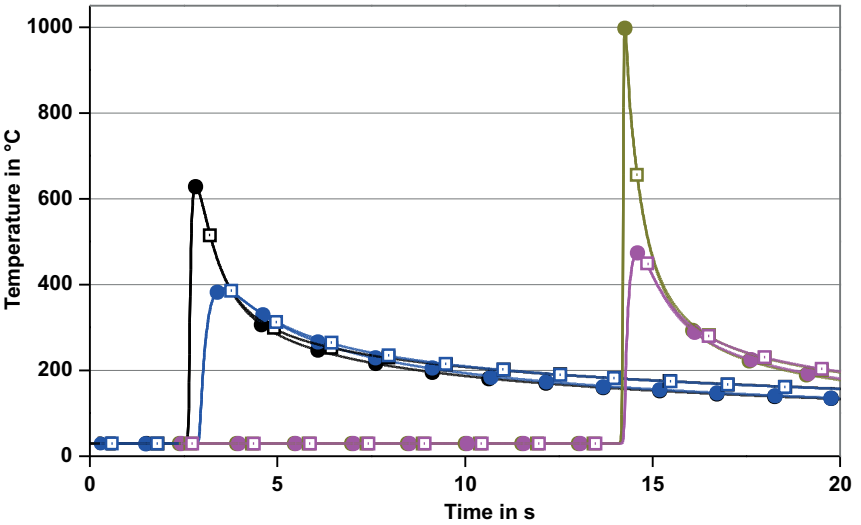

b) Simulated temperature cycles T1-T4 (weld W1) and T5-T6 (weld W3), from 0 s to 20 s, with and without clamps

Fig. 4.42: Numerical temperature cycles T1, T4, T5 and T6, wheelhouse, q = 3.3 kW, η = 29 % and v_s = 300 cm/min

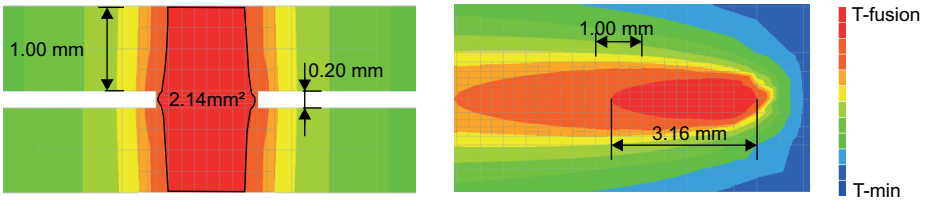

a) Simulated cross-section - simplified geometry "parallel weld"

b) Simulated weld pool length - simplified geometry "parallel weld"

Fig. 4.43: Numerical simulation of the weld pool area in a cross-section in the middle of the weld of the simplified geometry "parallel weld" and the weld pool length, q = 3.3 kW, η = 29 % and v_s = 300 cm/min

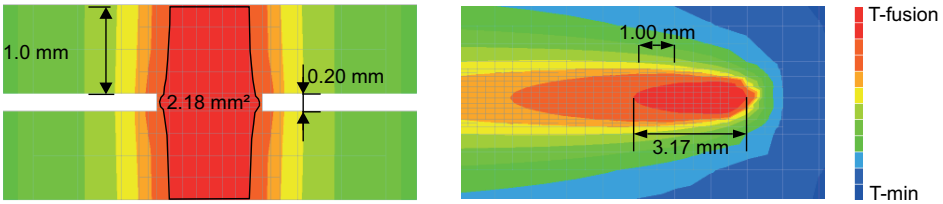

a) Simulated cross-section - simplified geometry "overlap weld"

b) Simulated weld pool length - simplified geometry "overlap weld"

Fig. 4.44: Numerical simulation of the weld pool area in a cross-section in the middle of the weld of the simplified geometry "overlap weld" and the weld pool length, q = 3.3 kW, η = 29 % and v_s = 300 cm/min

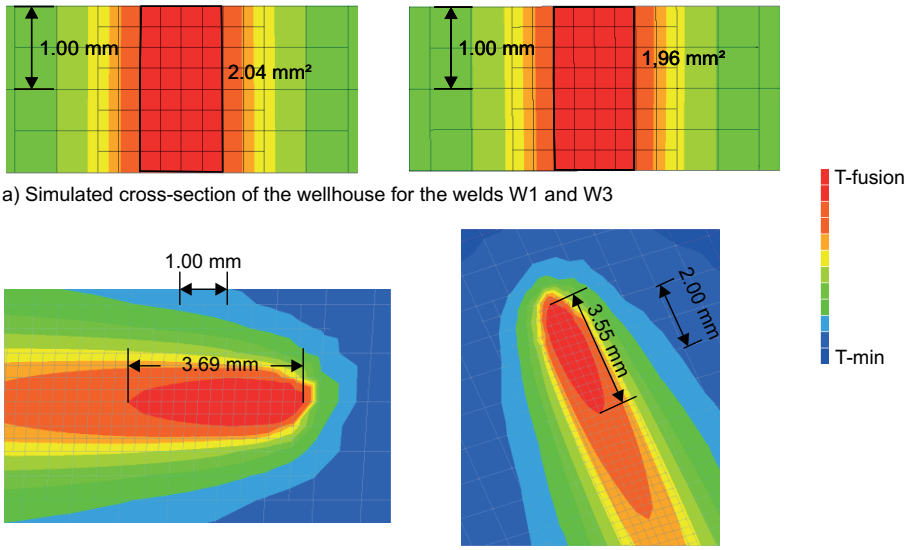

a) Simulated cross-section of the wellhouse for the welds W1 and W3

b) Simulated weld pool length of the wellhouse for the welds W1 and W3

Fig. 4.45: Numerical simulation of the weld pool area in cross-section in the middle of the welds W1 and W3 of the wheelhouse and the weld pool length for the welds W1 and W3, q = 3.3 kW, η = 29 % and v_s = 300 cm/min

4.3.4 Crossbeam

The numerical settings for the thermomechanical simulation of the crossbeam have been described in section 3.3.6. For the thermal simulation model, which is identical for all test cases investigated, the final calibrated parameters of the two implemented double ellipsoid heat sources are shown in Fig. 4.46.

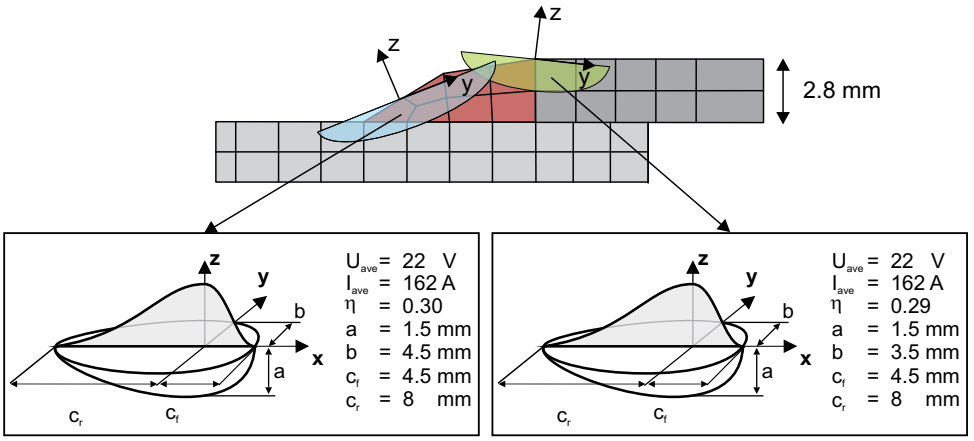

Fig. 4.46: Calibrated parameters for double ellipsoidal heat sources used for the thermal simulation of the crossbeam, U_{ave} = 162 V, I_{ave} = 22 A and v_s = 100 cm/min

The results of the thermal simulation with these two calibrated heat sources are shown Fig. 4.47 and Fig. 4.48.

In Fig. 4.47 the four temperature cycles T2, T4, T6 and T8 are plotted. As for the simplified geometries “parallel weld” and “overlap weld” and for the wheelhouse, they have been plotted in Fig. 4.47a) during the 200 s measurement time and plotted in Fig. 4.47b) around the peak temperatures.

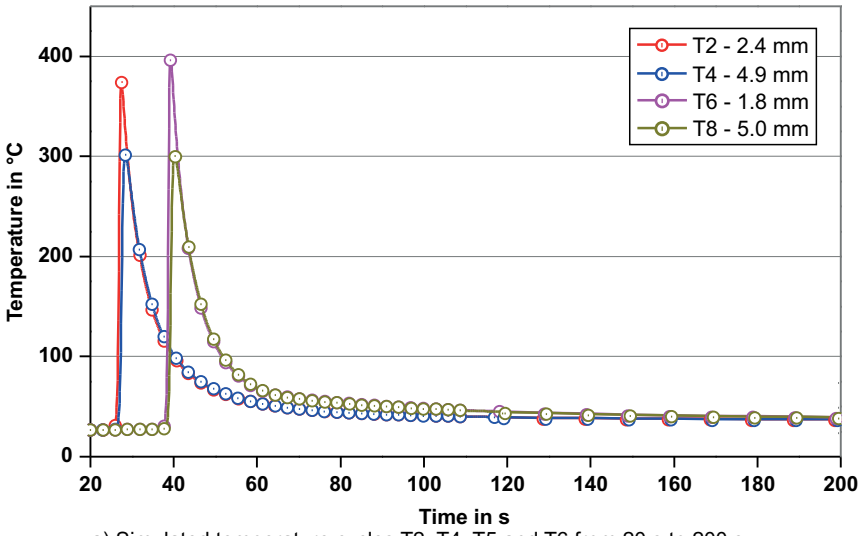

a) Simulated temperature cycles T2, T4, T5 and T6 from 20 s to 200 s

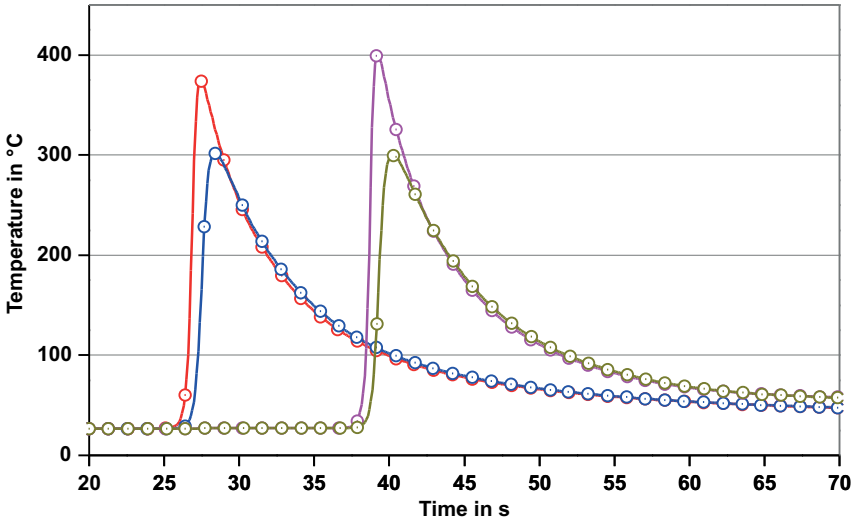

b) Simulated temperature cycles T2, T4, T5 and T6 from 20 s to 70 s

Fig. 4.47: Simulation of the four temperature cycles T2, T4, T5 and T6 for the crossbeam, U_{ave} = 162 V, I_{ave} = 22 A and v_s = 100 cm/min

The simulated weld pool area in a cross-section in the middle of the weld W1r, W2l and W4l is shown in Fig. 4.48a). The simulated weld lengths of the three welds W1r, W2l and W4l are plotted in Fig. 4.48b).

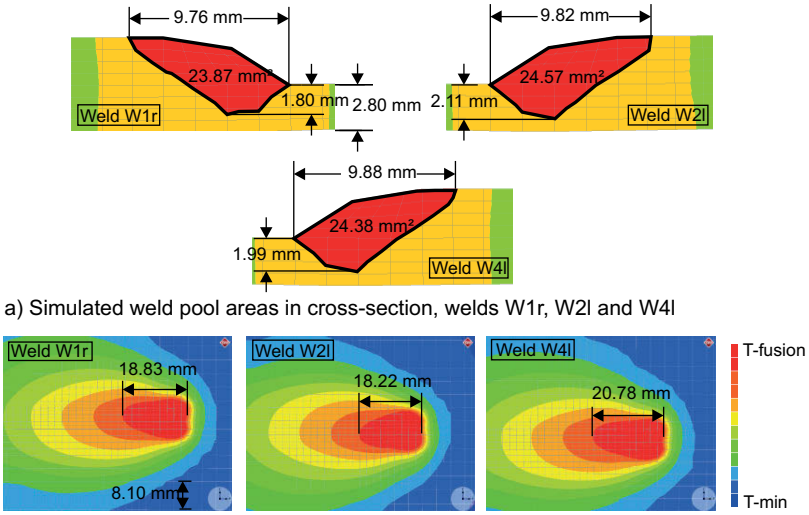

Fig. 4.48: Simulation of the weld pool area in a cross-section in the middle of the welds W1r, W2l and W4l and the weld pool length for each weld, U_{ave} = 162 V, I_{ave} = 22 A and v_s = 100 cm/min

The calculation of the thermal simulation with the rigid clamping is 10,656 s. For the simulation model, where the entire clamping device is integrated in the simulation model, the calculation time of the thermal simulation takes 11,322 s.

For the thermomechanical simulation of distortion, a simulation of a distortion field at t = 800 s for each clamping fixture definition has been carried out with the BM and with HAZ material properties as explained in section 3.3.6. No significant quantitative and qualitative differences can be observed between the simulated distortions with both different material properties. For this reason, the distortion field for the fixed and the real clamping fixture has been plotted in Fig. 4.49a) and b) only for the BM material properties.

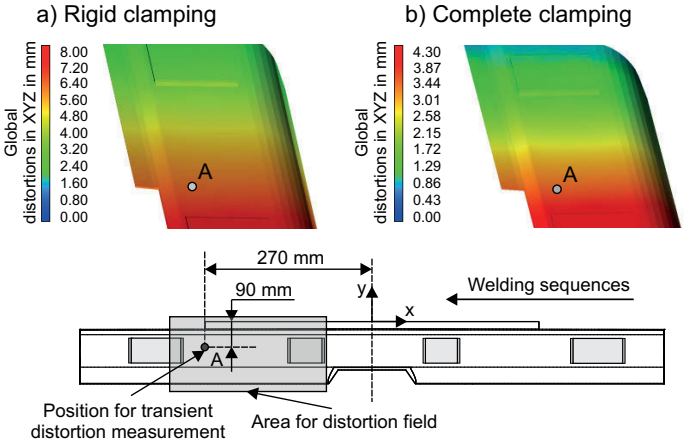

Fig. 4.49: Distortion field at t = 800 s for the three different clamping fixture definitions, crossbeam, BM material properties, U_{ave} = 162 V, I_{ave} = 22 A and v_s = 100 cm/min

The qualitative distortion behaviour for both investigated mechanical boundary conditions is quite similar for the investigated surface. Quantitatively, however, the distortions with the rigid clamping are higher than with the complete clamping.

For a more accurate analysis of the distortion behaviour of the crossbeam during the welding process and cooling time, a transient analysis at one or several points is required. Here, the point A has been chosen, see Fig. 4.49. The respective transient distortions in x-, y- and z-directions are shown in Fig. 4.50, Fig. 4.51 and Fig. 4.52 from 0 s to 800 s, respectively. In each figure, the distortions for the two clamping fixture types have been calculated with the BM (continuous line) and with HAZ (dashed line) material properties.

The calculation times of the thermomechanical simulation of the crossbeam with the rigid clamping and with complete clamping are 30,492 s and 57,900 s, respectively.

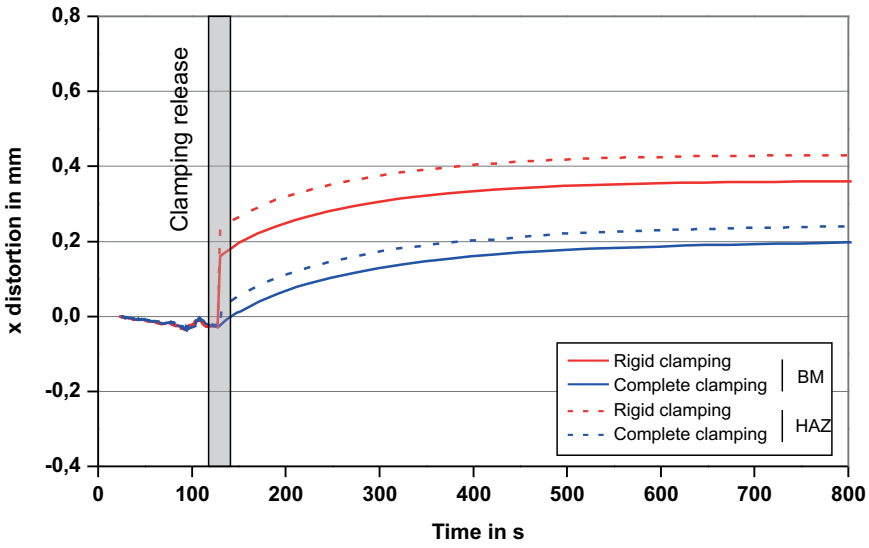

Fig. 4.50: Transient distortion from 0 s to 800 s at point A in x-direction, crossbeam, U_{ave} = 162 V, I_{ave} = 22 A and v_s = 100 cm/min

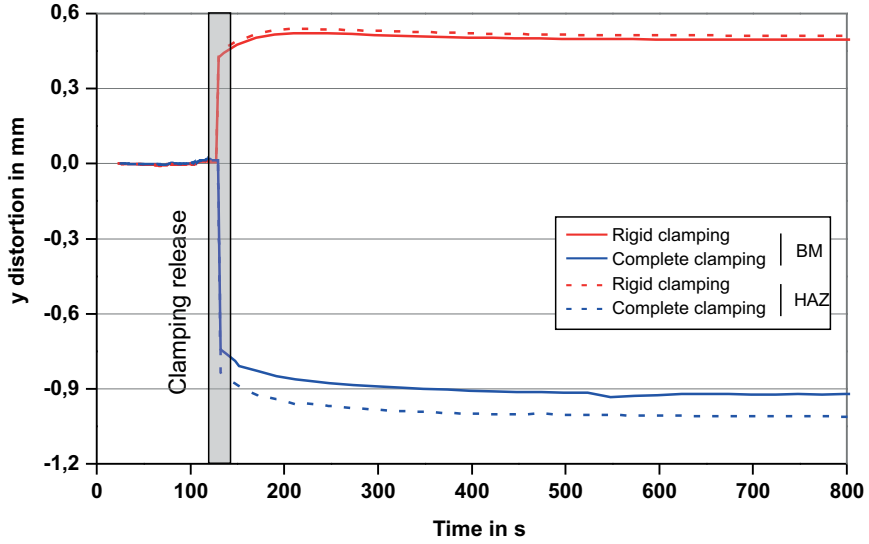

Fig. 4.51: Transient distortion from 0 s to 800 s at point A in y-direction, crossbeam, U_{ave} = 162 V, I_{ave} = 22 A and v_s = 100 cm/min

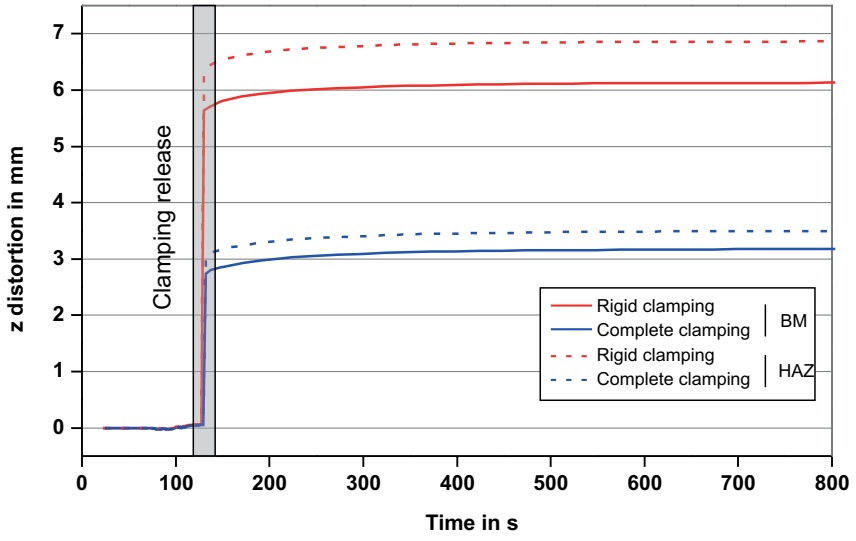

Fig. 4.52: Transient distortion from 0 s to 800 s at point A in z-direction, crossbeam, U_{ave} = 162 V, I_{ave} = 22 A and v_s = 100 cm/min

4.3.5 Calculation time of numerical solutions

The calculation times of all the numerical simulation results presented in the section 4.3 are summarised in the following Tab. 4.3:

Tab. 4.3: Calculation of the all the numerical simulation results presented in section 4.3

Geometries	Test case	Software	Simulation time	
Plates	Linear trajectory - moving point source infinite solid 200x200x100 mm^3 steady state	Simufact. welding	Temp. field	189031 s
			Temp. profile	
	Linear trajectory - moving point source infinite thin plate 200x200x1.5 mm^3 steady state		Temp. field	7604 s
			Temp. profile	
	Linear trajectory - moving point source infinite thin plate 200x200x5 mm^3 steady state		Temp. field	11775 s
			Temp. profile	
	Linear trajectory - transient moving point source 50x50x3 mm^3		Temp. field	240 s
			Temp. cycles	
			Temp. profile	
	Linear trajectory - transient small moving Goldak source 50x50x3 mm^3		Temp. field	240 s
			Temp. cycles	
	Linear trajectory - transient large moving Goldak source 50x50x3 mm^3		Temp. field	120 s
			Temp. cycles	
	Curved trajectory -transient moving Goldak source 50x50x3 mm^3		Temp. field	1600 s
			Temp. cycles	
			Temp. profile	
Semi-industrial plate			Temp. field	8520 s
			Temp. cycles	
			Fusion line	
			Weld pool length	
			Weld pool width	
Wheelhouse assembly	Simplified geometry “parallel weld“		Temp. field	3030 s
			Temperature cycles	
	Simplified geometry “overlap weld“		Temp. field	2900 s
			Temperature cycles	
	Wheelhouse		Temp. field	15500 s
			Temperature cycles	
Crossmember assembly	Rigid clamping		Temp. field	10656 s
			Distortions	30492 s
	Complete clamping		Temp. field	11322 s
			Distortions	57900 s

5 Discussion of the results

5.1 Validation of analytical temperature field solutions

The investigation of the possible application of fast analytical temperature field solutions to decrease the total computational time of a thermomechanical welding simulation for complex automotive structures has been in focus of this work. To achieve this, a combination between an analytical temperature field simulation with a conventional thermomechanical numerical simulation has been investigated. A prerequisite for this technique is that the fast analytical thermal solutions must lead to the same temperature field as if the simulation had been run numerically. For this reason, all the analytical temperature field solutions presented in this work have been compared systematically by increasing complexity with numerical counterparts.

5.1.1 Validation for plate geometries

5.1.1.1 Infinite solid – steady state – linear welding path – point heat source formulation

The analytical solution for this test case is an exact solution of the heat conduction problem (2.13). For this reason, this first test case has been used to validate the response of the numerical simulation. Since the same differential equation is solved by both analytical and numerical models, the thermal numerical simulation results should be almost identical to the analytical ones. Indeed, a theoretically perfect match between the analytical and the numerical temperature field is not possible due to the discretisation scheme of the numerical model. From a practical point of view, if the numerical model has been properly built with an optimal spatial and temporal discretisation to catch the investigated physical phenomena, then a “perfect matching” (perfect enough) of the simulation results against counterpart analytical model is expected. The optimal discretisation of a numerical model is found by making a mesh convergence study, where both temporal and spatial discretisations are refined systematically until the response of the simulation model reaches the previously defined convergence criterion. This mesh convergence study has been done for this and for all other test cases presented in this work.

The comparison of the analytical and the numerical temperature profile along AB for this point source in steady state moving on an infinite solid are plotted in Fig. 5.1. Both analytical and numerical temperature profiles match perfectly. At this point, it is important to notice that the numerical model has not been adapted or calibrated to match the analytical temperature profile but exactly the same welding and model parameters have been used in both models. This result enables to conclude that for this thermal analysis, the numerical model has been well implemented and can be considered as reference for the validation of the following analytical temperature field solutions.

This approach to validate a numerical model against an exact analytical solution with a comparable test case should always be done before any numerical analysis. In the literature, however, this approach is rarely described. Sometime even an analytical solution is incorrectly compared with a numerical model considering temperature dependent material properties and different boundary conditions not reproducible in the analytical solution. Moore, for instance compared in [30] the cooling time $t_{8/5}$ and $t_{15/1}$ calculated with conventional numerical techniques with different analytical solution for a thick and thin plate. A validation of the numerical model is not shown and the comparisons are not made on identical models making the understanding of the simulation results difficult. Rogeon compared in [55] his developed analytical solutions with a FE-simulation. Qualitatively, the temperature field matches well but quantitatively the analytical solution cools down faster. The author explained this phenomenon with a lower value of the heat conductivity in the austenitic phase in the analytical model. This conclusion is inaccurate and partially wrong. The 2D analytical model cools down faster mainly because the finite thickness of the plate is not considered; the lower heat conductivity may also have an influence. A systematic comparison with comparable analytical and numerical models would have been very interesting in this case.

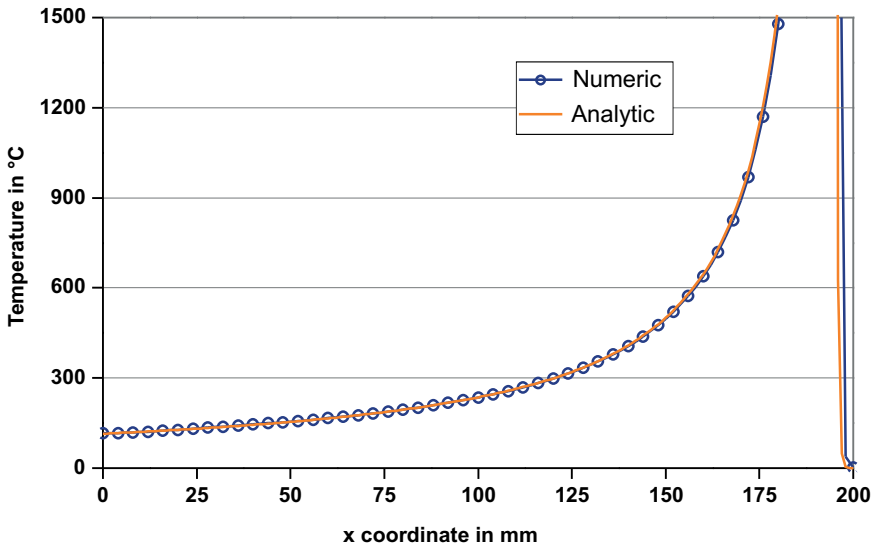

Fig. 5.1: Numerical and analytical temperature profile along AB at t = 20 s for a moving point heat source in steady state, infinite solid 200 x 200 x 100 mm³ q = 1.5 kW and v_s = 10 mm/s

The analytical and numerical calculation time for this test case are compared in Tab. 5.1:

Tab. 5.1: Analytical and numerical computational times for the point source in steady state moving on the infinite solid 200 x 200 x100 mm³

Test case	Simulation	Comp. time analytic	Comp. time numeric	Ratio (num / ana)
Linear trajectory - moving point source infinite solid 200x200x100 mm³ - steady state	Temperature field	18 s	189,031 s	10,500
	Temperature profile	0.1 s		1,890,310

For the temperature field and the temperature profile, the analytical solutions are 10,500 and 1,890,310 times faster than the numerical simulation, respectively. This result highlights the potential of fast analytical solutions in comparison to a conventional numerical approach. It is however to notice that the analytical calculation time for the temperature profile is 180 times faster than for the temperature field. This result shows that the real potential of the fast analytical solution relies much more on the possibility to calculate the temperature for single points at a single time step size independently of the rest of the structure.

5.1.1.2 Infinite thin plate – steady state – linear welding path – point heat source formulation

The solution for this problem is based on the analytical solution in infinite solid presented in the previous section; the adiabatic boundary conditions at the upper and lower surface of the thin plate are obtained by applying the reflexion technique described in section 2.2.2. In order to demonstrate the importance of managing the number of reflexions, two infinite thin plates with 1.5 mm and 5 mm thickness have been investigated. For each plate, the number of reflexions required to fulfil the convergence criteria have been plotted in Fig. 5.2:

a) Number of reflexion after t = 20 s, thin plate 200 x 200 x 1.5 mm³

b) Number of reflexion after t = 20 s, thin plate 200 x 200 x 5 mm³

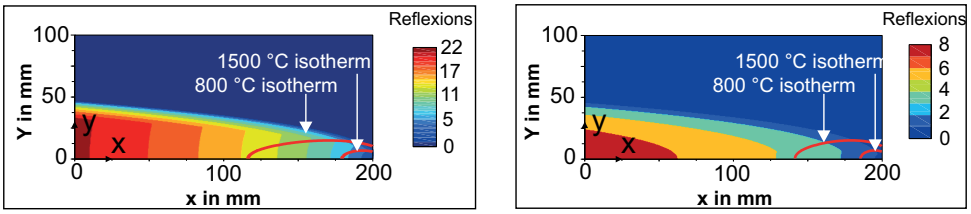

Fig. 5.2: Number of reflexions according to the two convergence criteria defined in section 3.2.3.2 for a point source moving for t = 20 s, thin plate 200 x 200 x 1.5 mm³ and 200 x 200 x 5 mm³, q = 1.5 kW and v_s = 10 mm/s

In both Fig. 5.2a) and b), the heat source moves along the x-axis at vt = 10 mm/s * 20 s = 200 mm and is represented by the 1500°C isotherm. It is interesting to see that the required number of reflexions is not constant over the plates and is also dependent on the thickness of the plates. For both plates, only the positions on the plate directly behind the heat source needs a low number of reflexions and the higher the distance behind the moving heat source, the higher the required number of reflexions. After t = 20 s, the maximal number of required reflexions for the thinner plate with 1.5 mm thickness is more than two times higher than the plate with 5 mm thickness. The statement of Cao [61], who wrote that approximately ten reflexions enable describing a thin plate is therefore not correct in a general manner. For an exact reproduction of the adiabatic boundary conditions at the upper and lower surface of the thin plate, the number of the reflexions must be calculated separately for each positions of the plate according to the convergence criteria defined in section 3.2.3.2. In addition, the major part of the investigated plate does not need any reflexions as illustrated in both Fig. 5.2a) and b) and using a fixed number of reflexions for all the plate would increase the total computational time.

The analytical and numerical temperature profiles for the infinite plate with 1.5 mm and 5 mm thickness are plotted in Fig. 5.3 and Fig. 5.4, respectively. In order to illustrate the influence of the number of reflexions on the simulation results, several analytical temperature profiles without and with a fixed number of reflexions are plotted in both Fig. 5.3 and Fig. 5.4 in addition to the temperature profiles with the optimal number of reflexions. A reference numerical temperature profile is also plotted in both figures. For the plate with 1.5 mm and 5 mm thickness, the temperature profiles without reflexion are identical and are also equal to the temperature profile for the infinite solid presented in the previous section. This result is logical and proves that the analytical expression implemented for this test case has been well derivated from the expression for an infinite solid in the previous section. For both plates, the convergent behaviour of the analytical series can be well illustrated: the closer the fixed number of reflexions used to the maximum required number of reflexion given in Fig. 5.2a) and Fig. 5.2b) (Simulation with 5 and 12 reflexions for the plate with 1.5 mm thickness in Fig. 5.3 and with 3 reflexions for the plate with 5 mm thickness in Fig. 5.4), the closer the resulting analytical temperature profile to the numerical reference one. This convergence behaviour has also been analysed by Cao [61] but he did not compare the final result with a reference model. In this case, the converged analytical temperature profiles match the numerical reference profiles very well for both plates except at the beginning of the welding trajectory where a temperature difference of 60K and 20K appears for the plate with 1.5 mm and 5 mm thickness, respectively. This behaviour was also observed by Fachinotti [70] and Rogeon [55] who compared an analytical temperature profile with a numerical reference simulation but they did not explain the deviation. This phenomenon is due to the fact that the infinite thin plate is not really infinite in the simulation model but finite with large dimensions. In the FE-model, an adiabatic boundary condition is considered for all bounding surfaces of the plate. In the analytical simulation model, only the surfaces in the thickness direction are set adiabatic by applying the reflexion technique. If the reflexion would be applied for all bounding surfaces, then these temperature differences would disappear as shown for the next test case. Here, it is negligible and would have increased the computational time considerably. In the next test case however, it has a significant influence on the simulation results and has therefore been analysed.

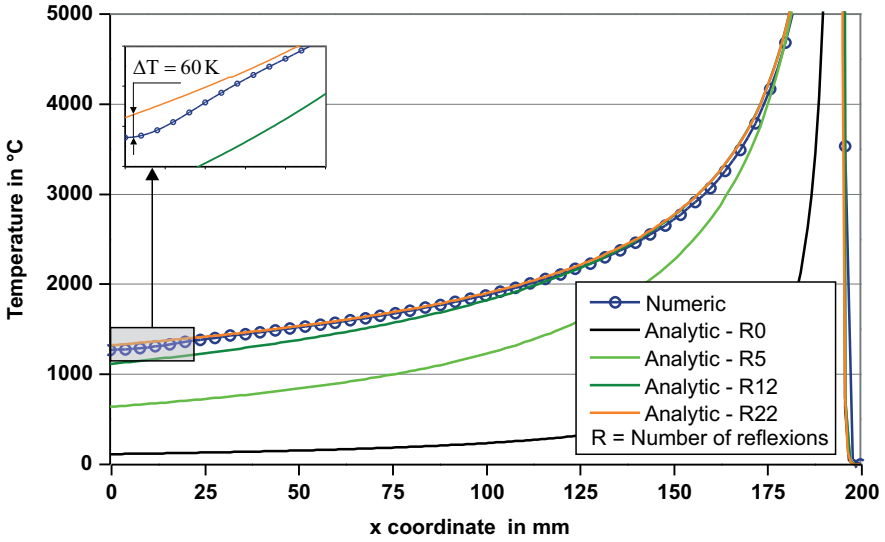

Fig. 5.3: Numerical and analytical temperature profiles with 0, 5, 12 and 22 reflexions along AB at t = 20 s for a moving point heat source in steady state, infinite thin plate 200 x 200 x 1.5 mm³, q = 1.5 kW and v_s = 10 mm/s

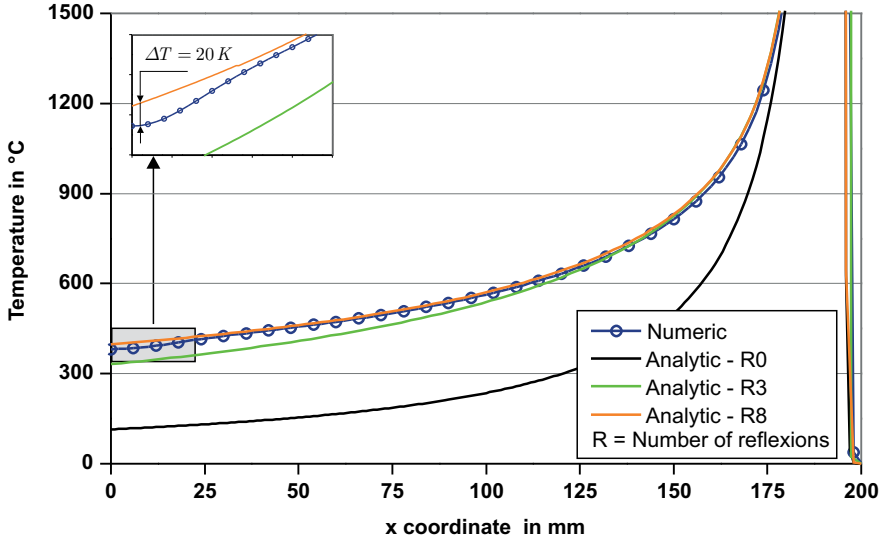

Fig. 5.4: Numerical and analytical temperature profiles with 0, 3, and 8 reflexions along AB at t = 20 s for a moving point heat source in steady state, infinite thin plate 200 x 200 x 5 mm³, q = 1.5 kW and v_s = 10 mm/s

The calculation time of the analytical and numerical simulations are compared in Tab. 5.2.

Tab. 5.2: Analytical and numerical computational times for the point source in steady state moving on the infinite thin plates 200 x 200 x 1.5 mm³ and 200 x 200 x 5 mm³

Test case	Simulation	Comp. time analytic	Comp. time numeric	Ratio (num/ana)
Linear trajectory - moving point source infinite thin plate 200x200x1.5 mm³ steady state	Temperature field	98 s	7604 s	77
	Temperature profile	0.8 s		9505
Linear trajectory - moving point source infinite thin plate 200x200x5 mm³ - steady state	Temperature field	39 s	11,775 s	301
	Temperature profile	0.31 s		37,983

On the numerical side, both plates with 1.5 mm and 5 mm thickness investigated in this section have 94% and 91% less elements than the previous “quasi-infinite” solid. This has a direct influence on the simulation time. With 7604 s and 11,775 s, the simulations of the plate with 1.5 mm and 5 mm thickness run 25 times and 16 times faster, respectively. On the analytical side, the opposite can be observed. With the implementation of the reflexion techniques, virtual heat sources are running simultaneously in addition to the real one and this has a direct influence on the simulation time. The more required reflexions, the higher the computational time. For the plate with 5 mm thickness, which required up to 8 reflexions, the simulation time for both temperature profile and temperature field is approximately 3 times slower than the corresponding simulations for the infinite body. For the plate with 1.5 mm thickness, which required up to 22 reflexions, the simulation is approximately 2.5 times slower than the simulation for the plate with 5 mm thickness. The number of required virtual reflected heat sources has therefore a significant influence on the analytical calculation time. The analytical calculation time for the temperature profiles is, with 0.8 s and 0.31 s for the plate with 5 mm and 1.5 mm thickness, still 9505 times and 37,983 times faster than the numerical simulations. For the temperature field, the analytical approach is only 77 times and 301 times faster than the numerical. This last result reinforces the statement made in the previous section that the advantage of the analytical solution is much more the possibility of an independent analysis of the temperature for a single point at a single time step than for a temperature field.

5.1.1.3 Finite thin plate – transient state – linear welding path – point heat source formulation

The analytical solution for this finite thin plate in transient state is based on the analytical solution for an infinite solid multiplied by a transient transform function in combination with the reflexion technique as described in section 2.2.2. For this reason, the validation of the analytical solutions for an infinite solid and in an infinite thin plate presented previously are a prerequisite for the validation of the analytical solution investigated in this section.

The comparison of the analytical and numerical temperature profiles along the welding trajectory A'B' is plotted in Fig. 5.5.

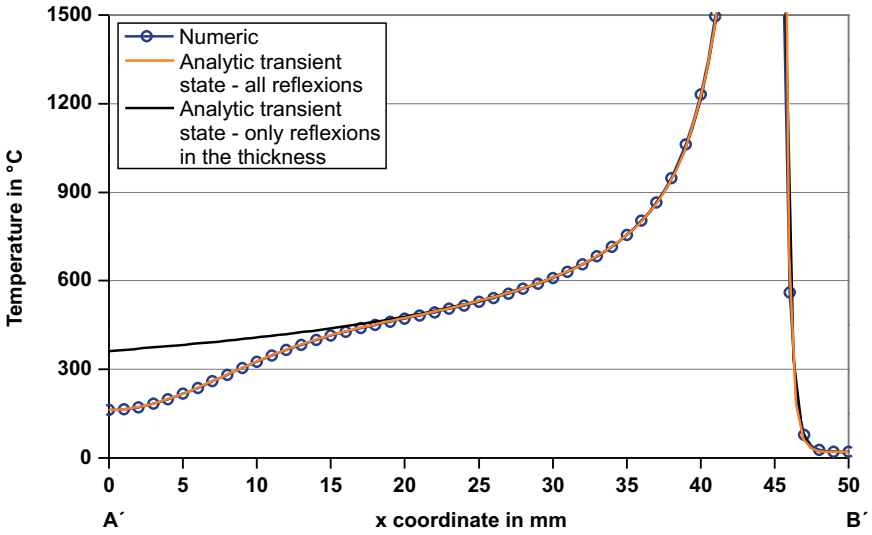

Fig. 5.5: Analytical and numerical temperature profile between A' and B' for a moving point heat source in transient state at t = 4 s, finite thin plate 50 x 50 x 3 mm³, q = 1.5 kW and v_s = 10 mm/s

It is interesting to see that the phenomenon observed in the previous section, i.e. the temperature drop at the beginning of the trajectory close to the boundary of the plate, is also present in this test case with higher amplitude due to the small dimension of the plate. If no reflections are implemented in the X-Y-plane, like in the previous section, the adiabatic boundary condition cannot be reproduced close to the welding start. This corresponds to the black curve in Fig. 5.5. With the addition of reflected heat sources in the X-Y-plane as shown in section 4.2.1.3 in the Fig. 4.21a) and b), the analytical and the numerical temperature profile agree.

For the calculation of the temperature profile between A' and B', however, the transient state at the beginning and at the end of the welding process can almost be neglected. It means that the matching of the analytical and numerical temperature profiles in Fig. 5.5 would have been given by the analytical solution in steady state implemented in the previous section with the reflexion technique applied for all boundaries of the plate. The advantage of a transient solution relies much more on the possibility to simulate temperature cycles at single positions during the welding and cooling time. The technique to get such temperature cycles is based on adding a virtual sink after the welding process as described in section 2.2.2 in Fig. 2.3. In order to get the temperature cycles for a thin plate, this virtual sink must be also reflected. For this test case, the comparison of the analytical and numerical temperature cycles at the position T1 to T4 is plotted in Fig. 5.6:

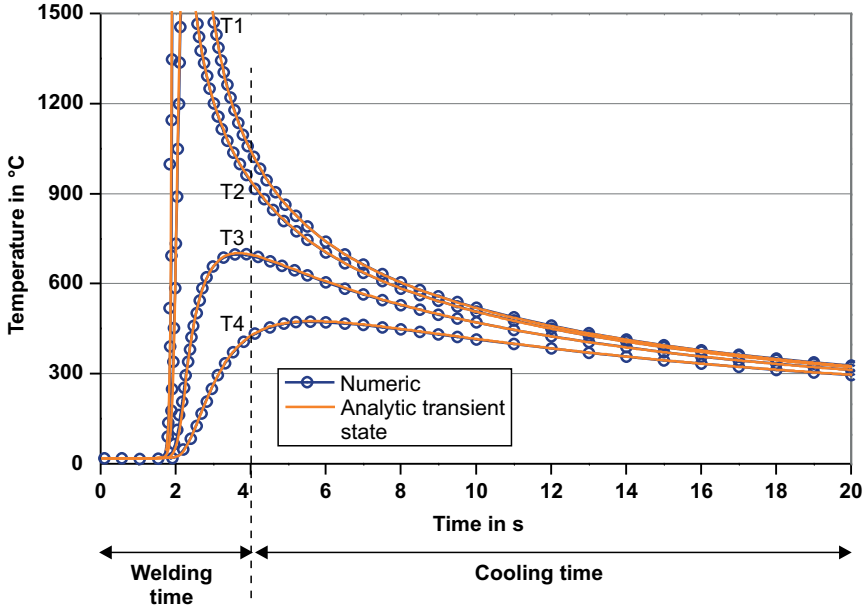

Fig. 5.6: Analytical and numerical temperature cycles for a moving point heat source in transient state, finite thin plate 50 x 50 x 3 mm^3, q = 1.5 kW and v_s = 10 mm/s

For the four temperature cycles T1 to T4, the analytical and the reference numerical simulations agree well during the welding and cooling time. This enables to conclude that the transient transform function has been well implemented as well as the virtual sink technique in combination with the reflexion technique.

The comparison of the analytical and the numerical calculation time for this test case are presented in Tab. 5.3:

Tab. 5.3: Analytical and numerical computational times for the point source in transient state moving on the finite thin plate 50 x 50 x 3 mm^3

Test case	Simulation	Comp. time analytic	Comp. time numeric	Ratio (num / ana)
Linear trajectory - transient moving point source 50x50x3 mm^3	Temperature field	37 s	240 s	6.5
	Temperature cycles	0.2 s		1200
	Temperature profile	0.05 s		4800

On the numerical side, the small plate investigated in this section has considerably fewer elements as the infinite solid and the infinite thin plates investigated previously, see Fig. 3.13 in section 3.3.3; the resulting computational time is therefore considerably lower. This trend is not followed by the analytical temperature field simulation. Even if the plate

50 x 50 x 3 mm^3 is approximately 25 times smaller (in volume) than the plate 200 x 200 x 5 mm^3, the respective computational times are almost identical. This is directly due to the higher number of required virtual heat sources and sinks plus their respective reflexions implemented to simulate this test case. In comparison to the numerical simulation, this analytical temperature field simulation is only 6.5 times faster. The same conclusion as in the previous section can be drawn: the potential of fast analytical temperature field solution does not rely on the calculation of field-problems but much more on the simulation of temperature cycles and profiles. Here, the analytical calculation times are 1200 and 4800 times faster than the numerical model for the simulation of the temperature cycles and profiles, respectively.

5.1.1.4 Finite thin plate – transient state – linear welding path – double ellipsoidal heat source formulation

In the literature, the double ellipsoidal heat source formulation is often implemented as shown in section 2.2.2. The validation of the analytical solution for this distributed heat source moving on a finite thin plate in transient state is therefore fundamental for the application of the combined method between the analytical and the numerical approach investigated in this work. The validation steps presented in the previous sections of the techniques to simulate an analytical temperature field in a finite thin plate in transient state are a prerequisite for the validation of this test case. The same methods have been implemented here, only the point heat source is replaced by a small and a large double ellipsoidal heat source as described in section 3.2.3.4. The analytical and numerical temperature cycles at the four points T1 to T4 for the large and small ellipsoidal heat sources are plotted in Fig. 5.7 and Fig. 5.8, respectively.

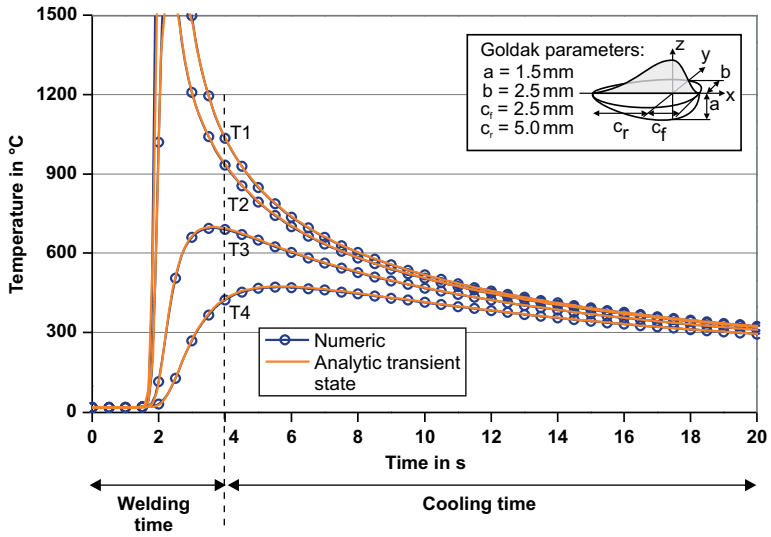

Fig. 5.7: Analytical and numerical temperature cycles for the moving small double ellipsoidal heat sources in transient state, finite thin plate 50 x 50 x 3 mm^3, q = 1.5 kW and v_s = 10 mm/s

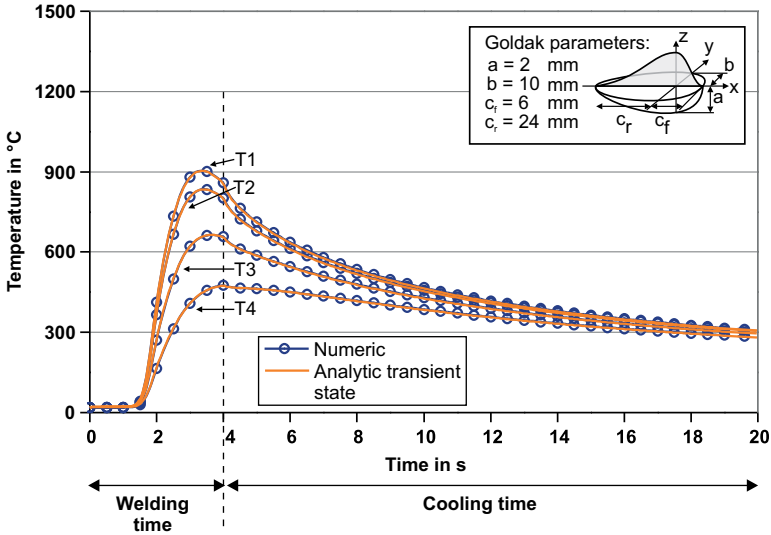

Fig. 5.8: Analytical and numerical temperature cycles for the moving large double ellipsoidal heat sources in transient state, finite thin plate 50 x 50 x 3 mm³, q = 1.5 kW and v_s = 10 mm/s

For each double ellipsoidal heat source, the analytical and the numerical temperature field are in agreement during welding and also during cooling. These results enable validating the presented analytical method to simulate a temperature field for a double ellipsoidal heat source moving linearly on a finite thin plate. Since the reflexion technique and the addition of the virtual sink method have been validated in the previous section, the implemented numerical integration technique required to solve the analytical solution in integral form, see equation (2.18) in section 2.2.2, is validated here. This result extends the work of Fachinotti [70], who has validated this analytical solution against a reference numerical model only for an infinite solid without considering the cooling behaviour after the welding process.

The comparison of the analytical and numerical calculation time is shown in Tab. 5.4. For the numerical simulation, the simulation of the finite thin plate for the small double ellipsoidal heat source takes two times longer than for the large one. This is due to the automatic refinement algorithm based on a temperature gradient criterion. With the small double ellipsoidal heat source, the energy density under the heat source is higher than for the large double ellipsoidal heat source resulting in a finer final mesh than the refined mesh for the large double ellipsoidal heat source. As explained in the previous section, the potential of analytical solutions is not in the simulation of temperature fields. Here, the analytical temperature fields are only 2.1 and 1.15 times faster than their numerical counterparts for the small and the large double ellipsoidal heat source, respectively. The potential of the analytical approach relies much more in the possibility to analyse independently to the rest of the structure the transient temperature distribution of single points required for the calibration of the double ellipsoidal heat source model. For this test case, the analytical temperature cycles T1 to T4 are 50 and 92 times faster than for the numerical simulations with the small and the large double ellipsoid heat source.

It is however interesting to notice that due to reflexion techniques and the addition of virtual heat sources (and sinks), the potential of the analytical solution decreases consequently as shown in the previous section. With the replacement of the point heat source by a double ellipsoidal heat source, which requires the use of numerical integration, the analytical calculation time is again multiplied by more than 10 times for the same plate and parameter settings.

Tab. 5.4: Analytical and numerical computational times for two double ellipsoidal heat source in transient state moving on the finite thin plate 50 x 50 x 3 mm^3

Test case	Simulation	Comp. time analytic	Comp. time numeric	Ratio (num/ana)
Linear trajectory - transient small moving Goldak source 50x50x3 mm^3	Temperature field	111 s	240 s	2.1
	Temperature cycles	2.6 s		92
Linear trajectory - transient large moving Goldak source 50x50x3 mm^3	Temperature field	104 s	120 s	1.15
	Temperature cycles	2.4 s		50

5.1.1.5 Finite thin plate – transient state – curved welding path – double ellipsoidal heat source formulation

For this test case, the same validated analytical solution and numerical integration techniques as in the previous section have been used to simulate this finite thin plate in transient state with a curved welding path. The following results enable to evaluate the method presented in section 3.2.3.5. For this validation, a temperature profile between A and B after the heat source has been active 16 s and six temperature cycles T1 to T6 have been simulated and compared with reference numerical simulations. The corresponding results are shown in Fig. 5.9.

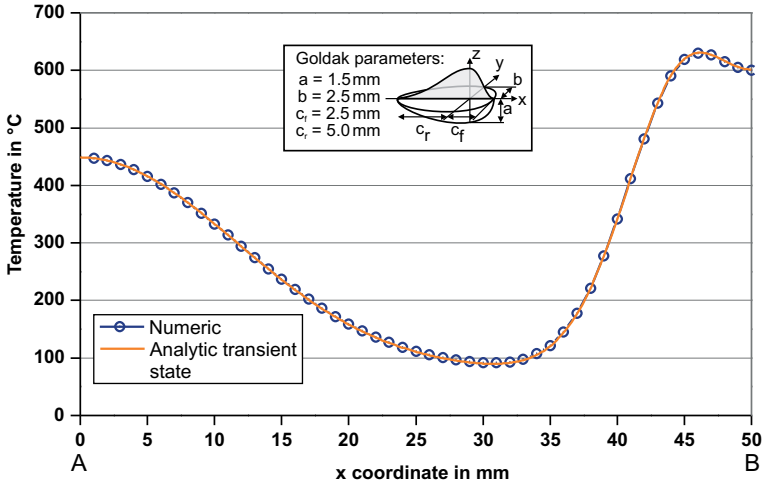

a) Analytical and numerical temperature profile between A and B at t = 16 s

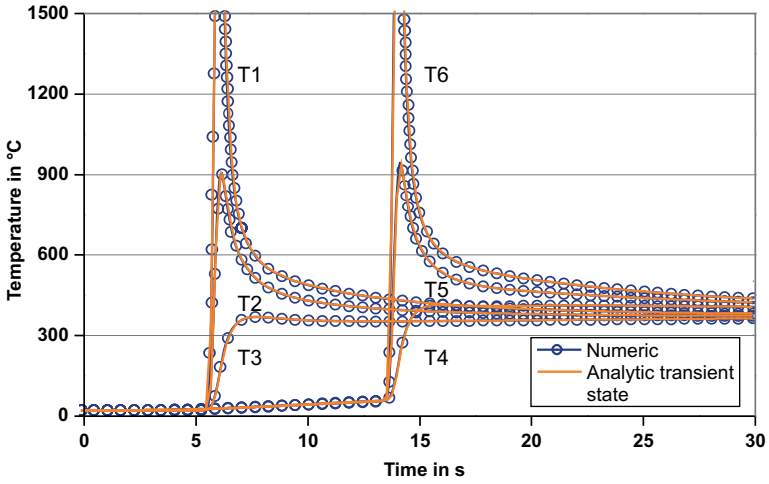

b) Analytical and numerical transient temperature cycles T1 to T6

Fig. 5.9: a) Numerical and analytical temperature profile between A and B, b) numerical and analytical temperature cycles for a double ellipsoidal heat source in transient state moving on a curved welding path, finite thin plate 50 x 50 x 3 mm³, q = 1.5 kW and v_s = 10 mm/s

For both the temperature profile AB and the six temperature cycles, the analytical results match the numerical ones as good as for previous test cases. Since the analytical solution with its respective techniques for a double ellipsoidal heat source moving on a finite thin plate has been validated for the previous test case, these results enable validating the techniques to consider a curved welding path. Here, it is interesting to mention that these results are close to those of Pittner [77]. However, he simplified the double heat source formulation by giving all the geometrical parameter a, b, c_f and c_r the same value of 1 mm resulting in a spherical heat source formulation, which is a simplified form of the double ellipsoidal heat source. Winczek, also published recently in [76] an analytical solution for another distributed heat source moving on a curved welding trajectory. In comparison to the

results presented in this section, he did not consider a finite thin plate in transient state but an infinite solid like in the first test case investigated in this work. Furthermore, the analytical simulation results are not validated against any referenced model making an appreciation of the quality of this analytical solution difficult.

The analytical and numerical simulation times for this test case are shown in Tab. 5.5. For the numerical simulation, the same plate with the same heat source configuration as for the previous test case has been used; however the calculation time takes 6.5 times longer. This is directly due to the four welding trajectories, which are responsible for a longer weld time and 42 % more elements. For this relative simple and small test case, it is noticeable that with 1600 s calculation time for the thermal simulation, a high number of iteration loops for a calibration of the input parameters of the model is restrained. With the corresponding analytical approach, for this test case, the number of real and virtual heat sources increases with the number of segments of the curved welding trajectory which results logically in an increase of the analytical calculation times. The advantage of the analytical approach by means of calculation time almost disappears for the temperature field simulation, which is only 1.2 times faster than the numerical simulation. For the analytical temperature cycle and profile simulations, which are respectively 23 and 266 times faster than the numerical simulation, the potential of the analytical approach is very interesting. However, due to a considerable increase of the number of virtual heat sources and sinks with each additional segment of a curved welding trajectory, the advantages of the fast analytical solutions decrease and may also disappear if a too high number of segments of the curved welding trajectory and a too long cooling time is used. Here for instance, the simulation for the analytical temperature cycles is still 23 times faster than the numerical counterpart but this simulation takes also approximately 25 times longer than in the previous section for the same plate 530 x 50 x 3 mm^3.

Tab. 5.5: Analytical and numerical computational times for a double ellipsoidal heat source in transient state moving with a curved trajectory on the finite thin plate 50 x 50 x 3 mm^3

Test case	Simulation	Comp. time analytic	Comp. time numeric	Ratio (num/ana)
Curved trajectory - transient moving Goldak source 50x50x3 mm^3	Temp. field	1303 s	1600 s	1.22
	Temp. cycles	68 s		23
	Temp. profile	6 s		266

5.1.2 Validation for the semi-industrial geometry

The analytical temperature field solution for an arbitrarily curved heat source moving on a finite thin plate has been validated for an academic small plate in the previous section. The advantage of this analytical approach in means of calculation time in comparison with a referenced numerical simulation is given. However, before applying this method for the industrial demonstrator, the wheelhouse, see section 5.2, a semi-industrial geometry with large dimension and with four curved welds is simulated and compared with a referenced

FE-model. The application of analytical solution for such a large and thin profile and with several non-linear welds has not been published in the literature yet.

The analytical and numerical model settings for this test case have been described in section 3.2.4 and 3.3.4. The comparison of the analytical and numerical simulation results is shown in Fig. 5.10.

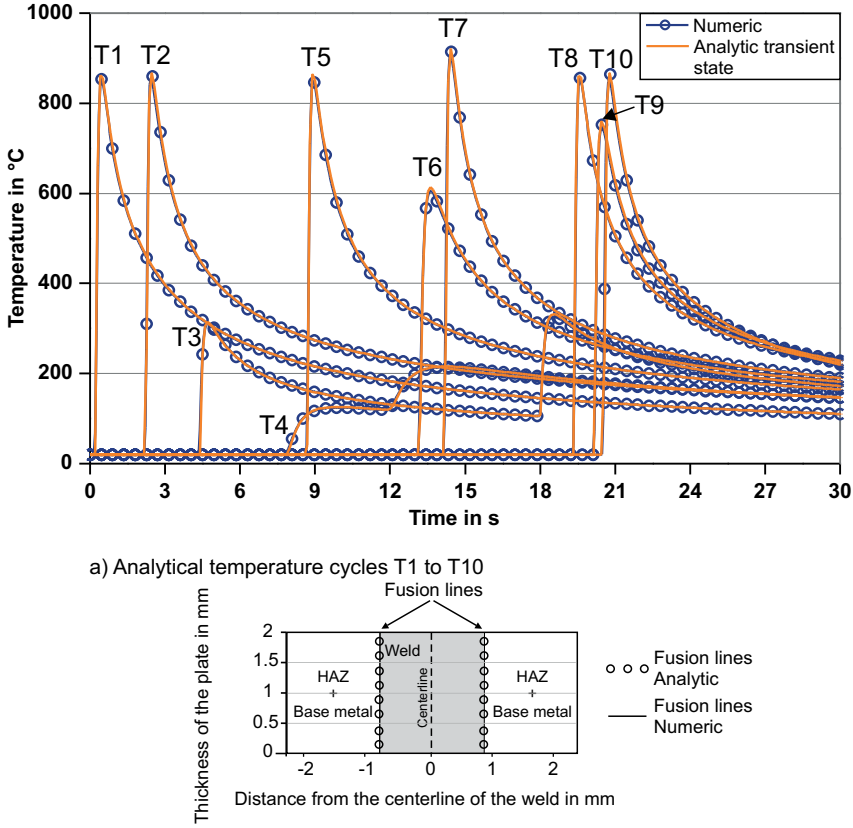

Fig. 5.10: Analytical and numerical temperature cycles for two double ellipsoidal heat sources in transient state moving on different and independent curved welding paths, semi-industrial plate 500 x 250 x 2 mm³, q = 3.3 kW and v_s = 300 cm/min

In the Fig. 5.10a), all the ten numerical and analytical temperature cycles match perfectly for the peak temperatures and the cooling behaviour. For the temperature cycles at the position T3 and T4, which are positioned close to the end and the beginning of two different welding trajectories, their reheating has been considered in the analytical model exactly in the same manner as in the numerical model. The analytical and numerical fusion lines in cross-section in Fig. 5.10b) match also very well. Finally, the analytical and numerical weld pool length and width, which are not represented in Fig. 5.10 (it is only a single value with the analytical model), match perfectly too.

These results enable validating the presented analytical method according to the assumptions and simplifications given in section 3.2.2. The temperature field induced by one or several arbitrary and independent double ellipsoidal heat sources moving on a large thin plate can be simulated analytically. As already mentioned, the potential of this analytical approach is the extremely competitive calculation time in comparison with a conventional discrete formulation scheme like FEM. For this semi-industrial demonstrator part, the calculation times can be found in Tab. 5.6.

Tab. 5.6: Analytical and numerical computational times for the two double ellipsoidal heat sources in transient state moving on different and independent curved welding paths, semi-industrial plate 500 x 250 x 2 mm³

Test case	Simulation	Comp. time analytic	Comp. time numeric	Ratio (num/ana)
Semi-industrial plate	Temp. field	22,500 s	8520 s	0.37
	Temp. cycles	120 s		71
	Fusion line in cross-section	90 s		95
	Weld pool length	0.1 s		85,200
	Weld pool width	0.4 s		21,300

The same remarks as for the previous academic plates can be given. The statement that the potential of the analytical method is not in the temperature field representation is confirmed. Here, the analytical one is even 2.7 times slower than the numerical one. However, for the calibration of the thermal model against experimental data, temperature cycles and information about the fusion zone are much more relevant. Here, the calculation time for the analytical temperature cycles and fusion zone are 71 and 95 times faster than with the numerical simulation. If the weld pool length and width have also been experimentally measured, the respective analytical simulations are 85,200 and 21,300 times faster than with numerical simulation. It is however to notice that a thermal model calibration requires several temperature cycles and information about the fusion zone characterised with the fusion line in cross-section and with the weld pool width and length. Therefore, the slowest analytical simulation result to calculate these data is relevant for the comparison of the analytical and numerical calibration time. Here, the simulation of the analytical temperature cycles is, with 120 s, the longest analytical simulation. Therefore, for this semi-industrial test case, the calculation time to get all the information for the calibration of the thermal model is 71 times faster with the presented analytical method than with the conventional numerical FE-simulation.

5.2 Application for simplified geometries

It is has been demonstrated in the previous section that the transient temperature field induced by one or several double ellipsoidal heat sources moving on a single or several arbitrarily curved welding trajectory on a large thin plate can be simulated with an analytical solution with the same result accuracy as with a reference numerical simulation. It has also been shown that the analytical calculation time required to get the data for the calibration of the phenomenological heat source model is much faster than for the numerical one.

The time for the calibration of the heat source model is directly connected to the calculation time of a direct simulation and with the expertise of the simulation user. It is also to be noticed that even with an advanced expertise in welding simulation, a manual calibration of the five input parameters of the double ellipsoidal heat source is an extremely difficult task. According to Karkhin [28], the lack of knowledge of the interdependency of all the input parameters of the heat source model can be compensated by automatically solving the inverse problem (e.g. the calibration) with measured weld characteristics by means of a multi variable global optimisation problem. Since solving one inverse problem requires many direct simulations, the application of a multi variable global optimisation algorithm makes sense only with fast direct simulations. In other words, the fast analytical temperature field solutions are well suited for solving an optimisation problem. As explained in section 3.2.5, the goal of this study is not focused on the development of an optimisation algorithm but on the application of analytical solutions for the welding simulation of complex automotive parts. Therefore, the global optimisation tool developed by Pittner and Weiss [77] has been used.

5.2.1 Simplified geometry “parallel weld”

As explained in section 3.3.5, the analytical temperature field simulation methods presented and validated in the previous sections have only been implemented for the simplified geometry “parallel weld”. Indeed, the potential of the analytical approach is not to replace the numerical thermal simulation, where more complex and realistic physical phenomena can be considered, but to accelerate the calibration time of the thermal model by giving an initial set of calibrated input parameters for the implemented distributed heat source. This statement is well illustrated by comparing the analytical and numerical simulation times of the thermal simulations of the simplified geometry “parallel weld” in Tab. 5.7.

Tab. 5.7: Comparison of the analytical and numerical computational time of the thermal simulation of the simplified geometry “parallel weld”

	Comp. time analytic	**Comp. time numeric**	**Ratio (num/ana)**
Simulation welding characteristics $u_{\mathrm{sim},i}$ - simplified geometry “parallel weld”	0.6 s	3030 s	5050
Time for calibration of thermal model	1830 s with 3051 simulations	t >> 3030 s dependent on user expertise in welding simulation	/

The computational time to calculate the eight weld-characteristics A_{sim} to H_{sim} with the presented analytical techniques takes 0.6 s and is 5050 times faster than the corresponding numerical simulation. The rapidity of the analytical model is due to the fact that only the eight weld-characteristics A_{sim} to H_{sim} have been simulated independently from the rest of the structure. Contrarily, in a discrete FEM formulation, the entire structure must be simulated before any post-processing analysis.

As previously explained in section 3.2.5, an important prerequisite for the implementation of a global optimisation algorithm (beside the "intelligence" of the implemented optimisation algorithm) to automatically solve an inverse problem is a short computational time of a single simulation. With 0.6 s for the simulation of the welding characteristics $u_{\mathrm{sim},i}$ for the calibration of the thermal model of the simplified geometry "parallel weld", this prerequisite is fulfilled. Thus, the convergence of the optimisation routine over the given constrained parameter space, see Fig. 3.22 in section 3.2.5, has been found after 3051 single simulations. With the analytical simulation time of 0.6 s, this corresponds to a calibration time of 1830 s. It is interesting to see that this time is 44 % faster than one single numerical simulation. Just to have a comparison, if 3051 numerical simulations are run, this would last 3030 * 3051 = 9244530 s or 2568 hours or 107 days!

The optimisation algorithm has converged after the best fit between the measured and the simulated eight weld-characteristics $A_{exp,sim}$ to $H_{exp,sim}$ was found as shown in Tab. 5.8:

Tab. 5.8: Comparison of the vectors of the experimental and simulated characteristics $u_{exp,i}$ = (A_{exp}, B_{epx}, C_{exp}, D_{exp}, E_{exp} , F_{exp}, G_{exp}, H_{exp}) and $u_{sim,i}$ = (A_{sim}, B_{sim}, C_{sim}, D_{sim}, E_{sim} , F_{sim}, G_{sim}, H_{sim}) taken from temperature cycles T1, T2, T3 and T4, cross-section and weld pool length

		$\frac{(\mathrm{sim}-\mathrm{exp})}{\mathrm{exp}} * 100$			$\frac{(\mathrm{sim}-\mathrm{exp})}{\mathrm{exp}} * 100$
A_{exp} A_{sim}	(1.24 s, 792 °C) (1.24 s, 897 °C)	+ 13 %	E_{exp} E_{sim}	(0.56 mm, 0.0 mm) (0.56 mm, 0.0 mm)	+ 0%
B_{exp} B_{sim}	(129 s, 545 °C) (129 s, 652 °C)	+ 20 %	F_{exp} F_{sim}	(0.56 mm, 1.0 mm) (0.56 mm, 1.0 mm)	+ 0 %
C_{exp} C_{sim}	(1.49 s, 503 °C) (129 s, 529 °C)	+ 5 %	G_{exp} G_{sim}	(0.56 mm, 2.0 mm) (0.56 mm, 2.0 mm)	+ 0 %
D_{exp} D_{sim}	(2.04 s, 306 °C) (129 s, 272 °C)	- 11 %	H_{exp} H_{sim}	3.25 mm 3.6 mm	+ 11 %

It is interesting to notice that the single values A_{sim} to H_{sim} of the vector of the simulated characteristics $u_{sim,i}$ differ to the single values A_{exp} to H_{exp} of the vector of the experimental characteristics $u_{sim,i}$ from -11 % to 20 %. A better fit could nevertheless not be achieved; this statement highlights the fact that the simplifications and assumptions made on the analytical models, see sections 3.2.2 and 3.2.5 do not enable reproducing a real temperature field distribution with high accuracy. The analytically calibrated input parameters for the two double ellipsoidal heat sources used to obtain the vector of the simulated characteristics $u_{sim,i}$ have been shown in Fig. 4.28 in section 4.2.3. A comparison of an analytical thermal simulation for the simplified geometry "parallel weld" simulated with

these calibrated heat source parameters against the corresponding real experimental data are plotted in the following Fig. 5.11 and Fig. 5.12.

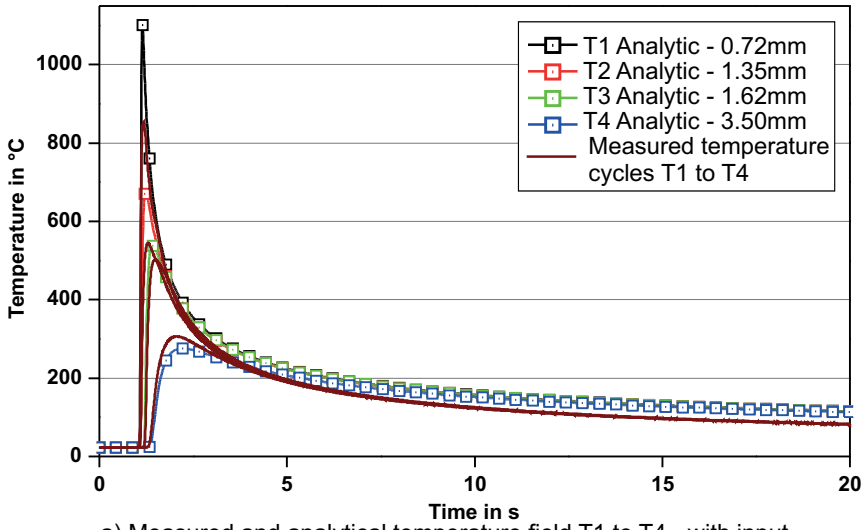

a) Measured and analytical temperature field T1 to T4 - with input parameters from the optimisation algorithm - 0 s to 20 s

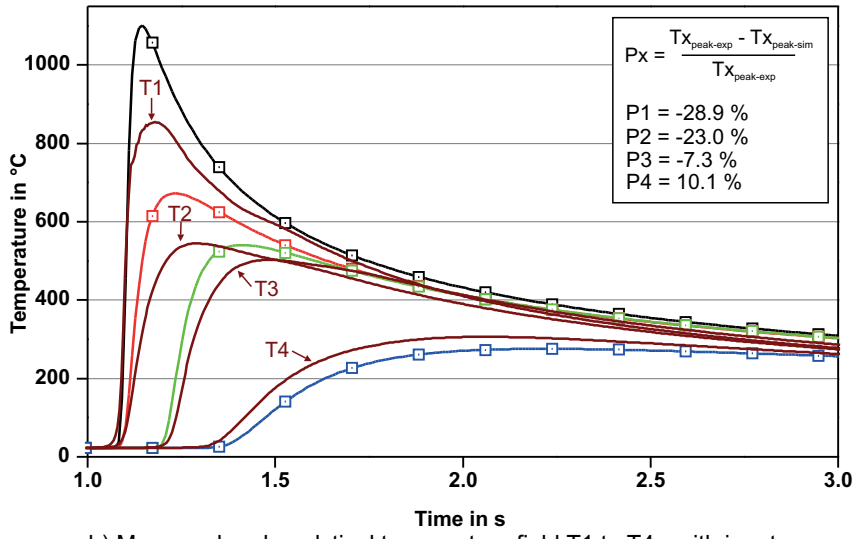

b) Measured and analytical temperature field T1 to T4 - with input parameters from the optimisation algorithm - 1 s to 3 s

Fig. 5.11: Comparison of the measured and the analytically simulated four temperature cycles T1-T4, simplified geometry "parallel weld", q = 3.3 kW, η = 27.9 % and v_s = 300 cm/min

For the four temperature cycles T1 to T4, the general overview from 0 s up to 20 s in Fig. 5.11a) shows a relative good agreement between the analytical and the measured temperature fields. A closer observation around the peak temperatures in the Fig. 5.11b) shows that the absolute deviations between the analytical and the numerical temperature

fields T3 and T4 are with 7.3 % and 10.1 % lower than those for the temperature fields T1 and T2 with 28.9 % and 23.0 %. At this point, an exact explanation of these phenomena is difficult to conclude due to the high number of assumptions and simplifications made in the analytical model. Surely, this is a combination of the constant material properties at $T_{solidus}$ = 1380 °C, the adiabatic boundary conditions and the non-consideration of the gap between the two sheets of the simplified geometry “parallel weld”.

Contrarily, for the temperatures below 200 °C, all the four measured temperature cycles show the same behaviour and cool faster than the simulated ones. This phenomenon can be related to two phenomena. Firstly, the constant value for the heat conduction taken at $T_{solidus}$ = 1380 °C of 34 $W \cdot m^{-1} \cdot K^{-1}$ is approximately two times smaller than the values for temperatures below 200 °C. With a lower heat conduction value, the heat from the welding process flows more slowly into the rest of the part, resulting in a slower cooling time. Secondly, the adiabatic boundary condition in the analytical model does not allow heat loss to the environment through convection and radiation, which results automatically in a higher temperature during the cooling of the thermocouples.

The comparison of the analytical and real fusion zone in cross-section and weld pool length for the simplified geometry “parallel weld” is shown in Fig. 5.12a) and b).

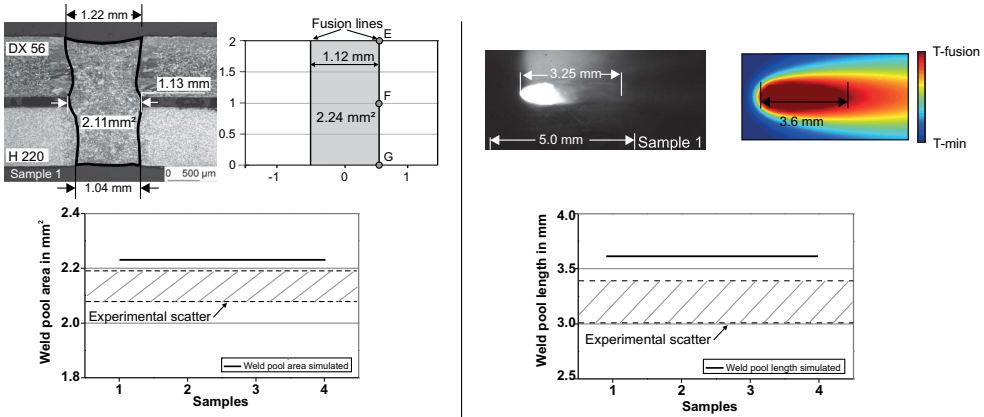

a) Measured and analytical fusion zone in cross section

b) Measured and analytical weld pool length

Fig. 5.12: Comparison of the measured and the analytically simulated fusion zone in cross-section and weld pool length, simplified geometry “parallel weld”, q = 3.3 kW, η = 27.9 % and v_s = 300 cm/min

The analytical simulated fusion zone in the thickness in Fig. 5.12a) has a “cylinder shape” with a constant width of 1.12 mm. This result differs from the real one, which fluctuates between 0.95 mm and 1.22 mm. At this point, it is important to notice that a representation of this complex variation of the real fusion zone width is not possible only with the two identical heat sources implemented in the simulation model at the upper and lower surface of the investigated plate as described in section 3.2.5. Furthermore, since no gap is considered in the analytical model, the heat accumulation zone observed in this area in the real experiment cannot be reproduced. These statements have been taken into consideration in the optimisation algorithm and an average value of 1.12 mm for the real width of the fusion zone in the thickness has been given for the three investigated points E,

F and G, see Fig. 3.21 in section 3.2.5. With a constant width of 1.12 mm, the analytical fusion zone matches the experimental values at those three points very well. This exact matching of the analytical fusion zone shape (at the point E, F and G) is directly due to the fact that the constant material properties at $T_{solidus}$ = 1380°C has been used in the simulation model. Finally, the area of the analytical fusion zone in cross-section is, with 2.24 mm^2, 1.3 % higher than the upper limit of the experimental scatter band. This result is also related to the simplification made in the analytical simulation model.

For the weld pool length, the analytical simulation result is, with 3.6 mm, 6 % higher than the upper limit of the experimental scatter band. Here also, an exact explanation of this phenomenon is hard to conclude due to the assumptions and simplifications made in the analytical simulation model.

Finally, the weld pool shape (characterised with the fusion zone in cross-section and the weld pool length) could be simulated analytically with a deviation to the experimental data less than 10 %. For the temperature cycles T1 to T4, the deviation is less than 30 %. The focus of this study, however, is not to calibrate the analytical model until the corresponding results match the experimental data perfectly. The presented analytical methods in combination with the optimisation algorithm should give an accurate initial set of input parameters for the numerical model with full complexity in as little time as possible. For this reason, the analytical results previously presented are treated as acceptable. The corresponding calibrated input parameters of the implemented two double ellipsoidal heat sources and efficiency of the welding process are therefore implemented in the numerical model as explained in section 3.2.5. The same temperature cycles T1 to T4 as in Fig. 5.11 have been simulated in the numerical model and compared to the respective experimental data in Fig. 5.13.

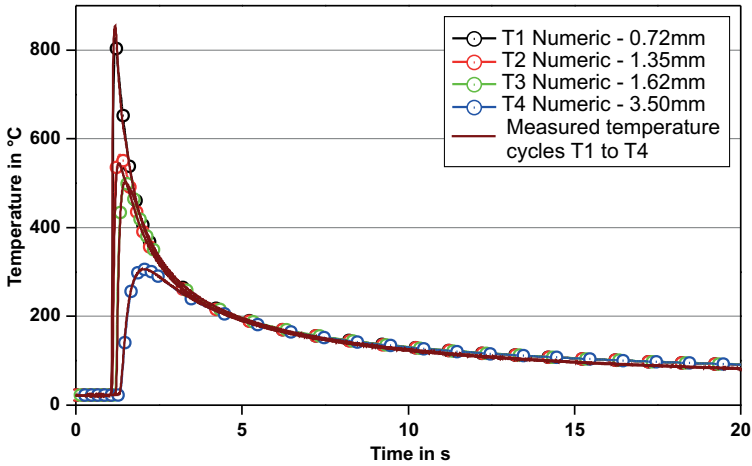

a) Measured and numerical temperature field T1 to T4 - with input parameters from the optimisation algorithm - 0 s to 20 s

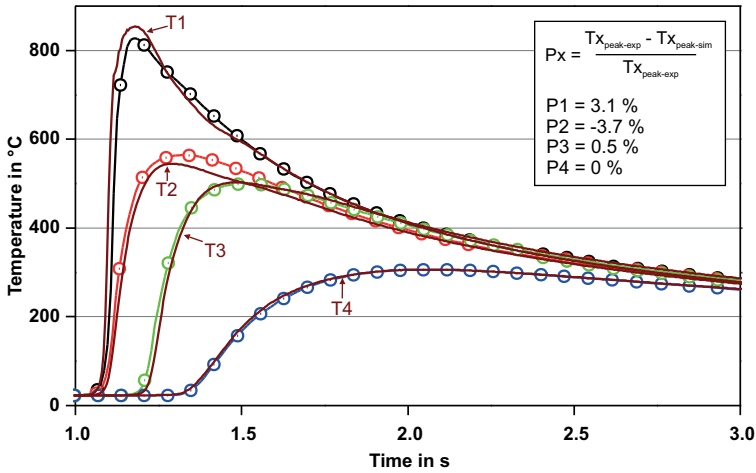

b) Measured and numerical temperature field T1 to T4 - with input parameters from the optimisation algorithm - 1 s to 3 s

Fig. 5.13: Comparison of the measured and the simulated (with FEM) four temperature cycles T1-T4, simplified geometry "parallel weld" with the initial heat source input parameters provided by the global optimisation routine, q = 3.3 kW, η = 27.9 % and v_s = 300 cm/min

For all the four simulated temperature cycles T1 to T4, the overall behaviour from 0 s to 20 s plotted in Fig. 5.13a) match the experimental data very well. For the peak temperatures shown in Fig. 5.13b), the absolute deviation of the numerical results to the experimental ones does not exceed 4 %. It is here interesting to notice that almost all the divergences between the analytical temperature cycles and the experimental data observed previously have been erased. The four peak temperatures have been well reproduced as well as the cooling behaviour below 200 °C. These results demonstrate that the deviations between the analytical and experimental results presented previously were really related to the assumptions and simplifications of the analytical model. These results enable also to

conclude that the assumption to use the constant material properties at $T_{solidus}$ = 1380 °C in the analytical model to calibrate the fusion zone of the weld is correct.

The potential of the analytical methods combined with the optimisation algorithm to reduce the calibration time of the thermal model of the simplified geometry “parallel weld” is given. The time for the simulation of the analytical initial set of input parameters lasts 40 % faster than one single numerical simulation and the corresponding “first” numerical simulation match the experimental temperature field data with an absolute deviation less than 4%. Finally, after this first numerical simulation, only a few numerical simulation iterations have been required to find the final calibrated parameters of the simplified geometry “parallel weld”. The parameter shapes of the two double ellipsoidal heat sources have not been changed. Only the efficiency of the welding process has been slightly increased from 27.9 % to 29 % and the influence of the clamping close to the welds has been considered.

The final calibrated thermal model of the simplified geometry “parallel weld” with and without clamps is shown in the following Fig. 5.14 to Fig. 5.16.

The measured and the simulated temperature cycles T1 to T4 are compared in Fig. 5.14. In Fig. 5.14a), the comparison is shown for the whole measurement time of 200 s. In this representation, the cooling behaviour of the thermocouples can be investigated. Here, after 100 s until the end of the measurement, the simulated and measured temperatures are identical for the four thermocouples T1 to T4; this enables to conclude that the quantity of energy brought into the system and the boundary conditions are correct. A zoom of the temperature distributions between 10 s and 105 s in Fig. 5.14a) shows that the simulations without clamps cool more slowly than the experimental ones. After considering the clamps in the numerical model, see section 3.3.5, the respective four temperature cycles match the experimental data very well.

The peak temperatures of the four thermocouples T1 to T4 are shown in Fig. 5.14b). In this small time interval around the peak temperatures, the clamps do not have any influences on the peak temperatures. This effect is comprehensible; the clamps are positioned behind the four thermocouples and the respective peak temperatures appear consequently before the heat reaches the clamps. For the amplitude of the peak temperatures, as expected, the simulation results are almost equivalent to those presented in Fig. 5.13b). With 1.1 % higher welding process efficiency (from η = 27.9 % to η = 29 %), the absolute deviation between the simulated and measured thermocouple T1, T3 and T4 is below 2.5 %. For the thermocouple T2, it is 6 %. At this point, it is important to remember that there is always an experimental scatter band. According to Schwenk [89], a thermal model for a welding simulation can be considered calibrated when the difference between the measured and simulated temperature cycles does not exceed ±10 %. Since experimental scatter bands for the temperature cycles have not been measured, this value has been considered for the validation of the thermal model. Thus, for the temperature cycles, the simulation results lie within the experimental scatter band.

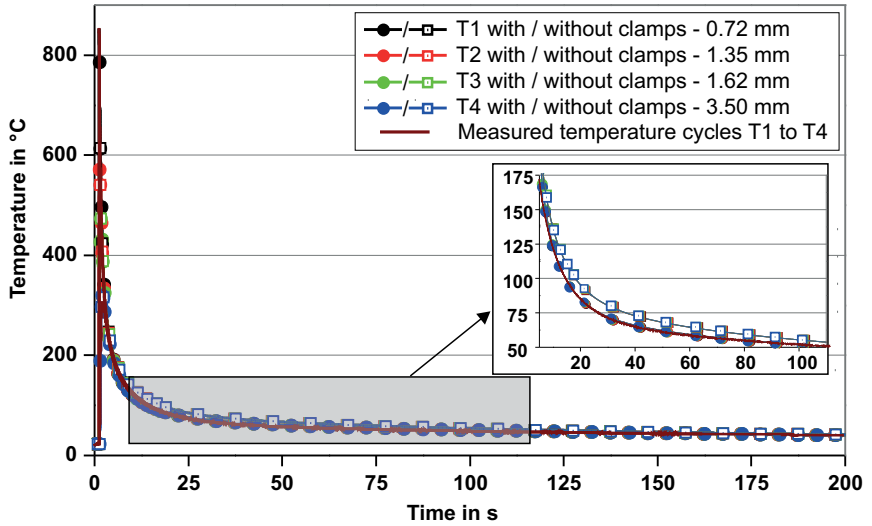

a) Measured and simulated temperature cycles T1-T4 from 0 s to 200 s

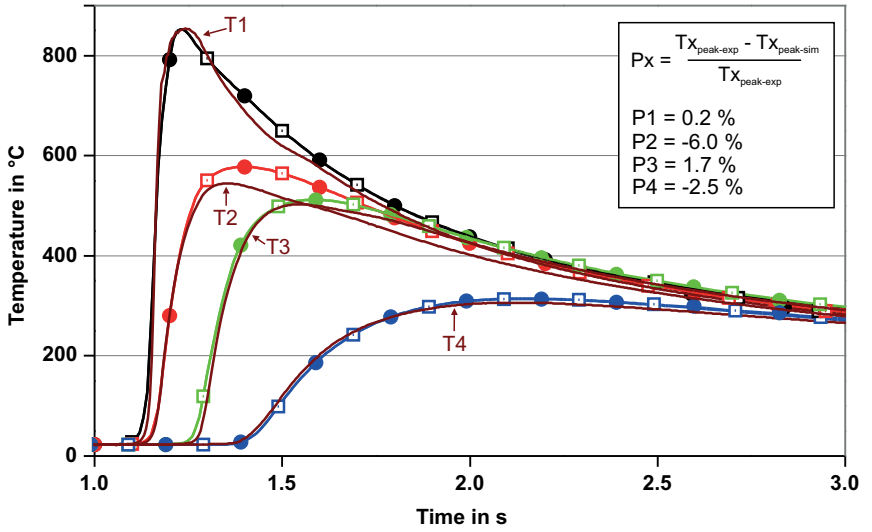

b) Measured and simulated temperature cycles T1-T4 from 1 s to 3 s

Fig. 5.14: Comparison of the measured and simulated (with FEM) four temperature cycles T1-T4, simplified geometry "parallel weld" with the final calibrated heat source input parameters, $q = 3.3$ kW, $\eta = 29$ % and $v_s = 300$ cm/min

The fusion zone in cross-section has been simulated and compared with the real experimental data in Fig. 5.15. In comparison to the analytical model previously presented, the 0.2 mm gap between the joined sheet metals and realistic boundary conditions could be considered in the numerical simulation model. As expected, the resulting simulation results are closer the real experimental data than with the analytical model. The simulated weld pool area is within the experimental scatter band as shown in Fig. 5.15. The fluctuation of

the fusion zone width in the thickness could also be represented in the simulation model. In the middle of the weld at the interface between both sheet metals, the accumulation of heat due to the interruption of solid material can be well reproduced in the simulation model. The rest of the fusion zone width also matches the experimental data relatively good. Only at the upper and lower surface of the joined sheet metals, the fusion zone width becomes slightly larger for the real measurements. This phenomenon is probably related to the Marangoni convection flow (due to the temperature dependent gradient of surface tension) in the weld pool responsible in a general manner for a larger and longer weld pool. With the assumptions and simplifications assumed in this work, such a phenomenon cannot be considered. In a phenomenological way, however, it could have been reproduced by adding two small heat sources at the upper and lower surfaces. In practice, it would have considerably increased the number of input parameters to calibrate and has consequently been neglected.

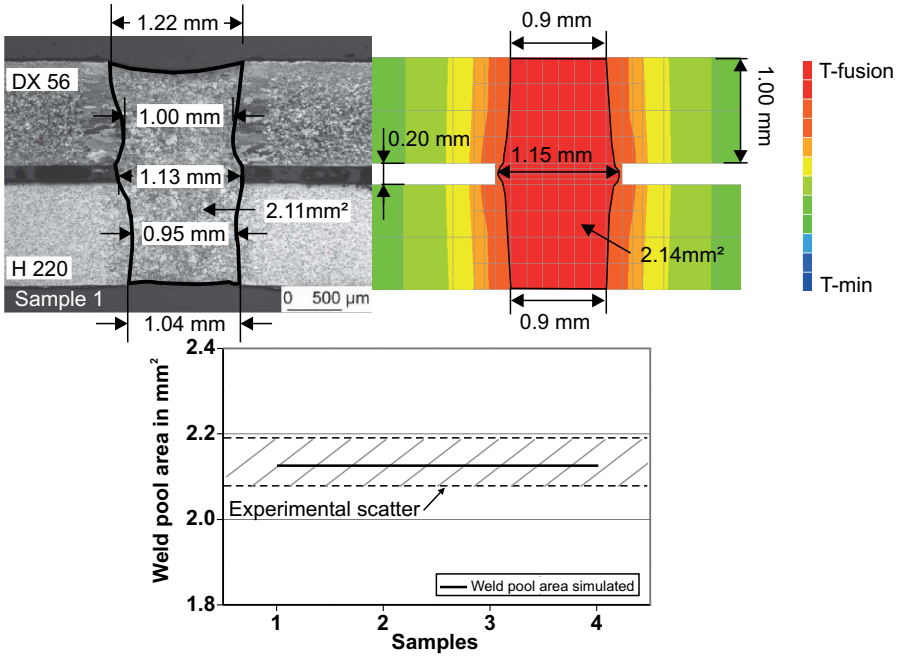

Fig. 5.15: Comparison of the measured and simulated (with FEM) weld pool area in cross-section, simplified geometry "parallel weld" with the final calibrated heat source input parameters, $q = 3.3$ kW, $\eta = 29$ % and $v_s = 300$ cm/min

For the weld pool length, the comparison of the simulated and the measured results are plotted in Fig. 5.16. In comparison to the analytical simulation results, the weld pool length simulation with the numerical model with full complexity lay, with 3.16 mm, within the experimental scatter band.

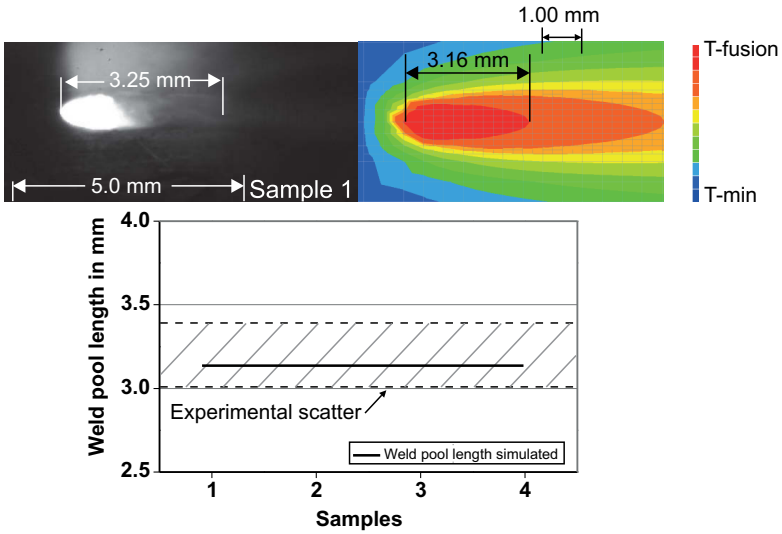

Fig. 5.16: Comparison of the measured and simulated (with FEM) weld pool length, simplified geometry "parallel weld" with the final calibrated heat source input parameters, q = 3.3 kW, η = 29 % and v_s = 300 cm/min

Finally, even with the assumptions and simplifications made in the numerical simulation model, see section 3.3.2, the calibrated thermal model for this simplified geometry "parallel weld" enables to obtain a virtual temperature field with an absolute deviation between the simulated and the experimental data of less than 6 % for the temperature distributions and a fusion zone geometry (fusion zone in cross-section and weld pool length) within the experimental scatter band. The combination of the fast analytical temperature solutions with an accurate FE-model enables to obtain this result within a very short time in comparison with a conventional 100 % numerical approach. These results, i.e. the calibrated parameters of the two implemented double ellipsoidal heat source, are used as basis for the next simplified geometry "overlap weld" and finally for the demonstrator part wheelhouse.

5.2.2 Simplified geometry "overlap weld"

The simplified geometry "overlap weld" is a transition step between the simplified geometry "parallel weld" and the wheelhouse assembly as shown in section 3.1.3.1. At this point, it is important to remember that no calibration of the thermal model of this simplified geometry is done. Exactly the same calibrated input parameters of the implemented two double ellipsoidal heat sources as for the simplified geometry "parallel weld", see section 4.3.3, have been used for the respective thermal simulation.

The comparisons between the simulated and measured thermal results, i.e. temperature cycles, fusion lines in cross-sections and weld pool lengths, are shown in the following Fig. 5.17 to Fig. 5.19. For the simulated and measured temperatures cycles T1 to T4, the comparison is plotted for all the welding process and cooling time from 0 s to 200 s in Fig. 5.17a) and locally around the peak temperatures between 1 s and 3 a in Fig. 5.17b).

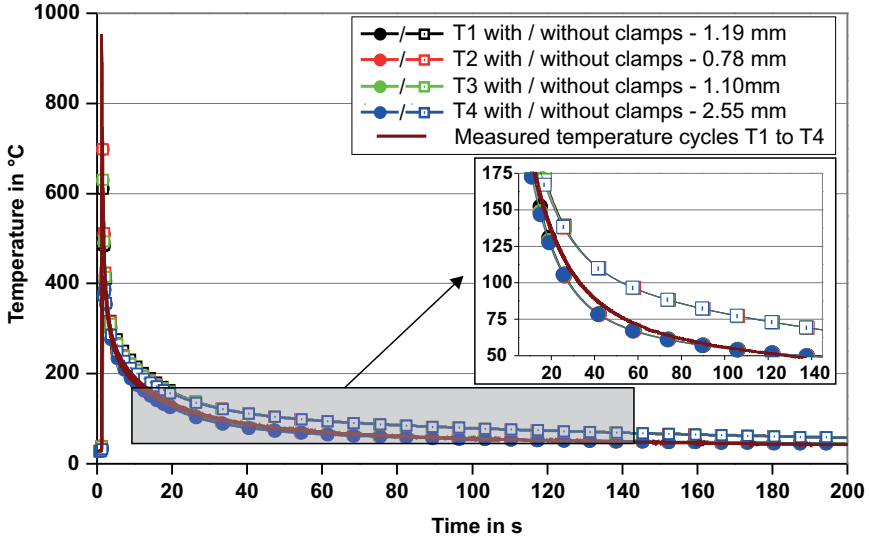

a) Measured and simulated temperature cycles T1-T4 from 0 s to 200 s

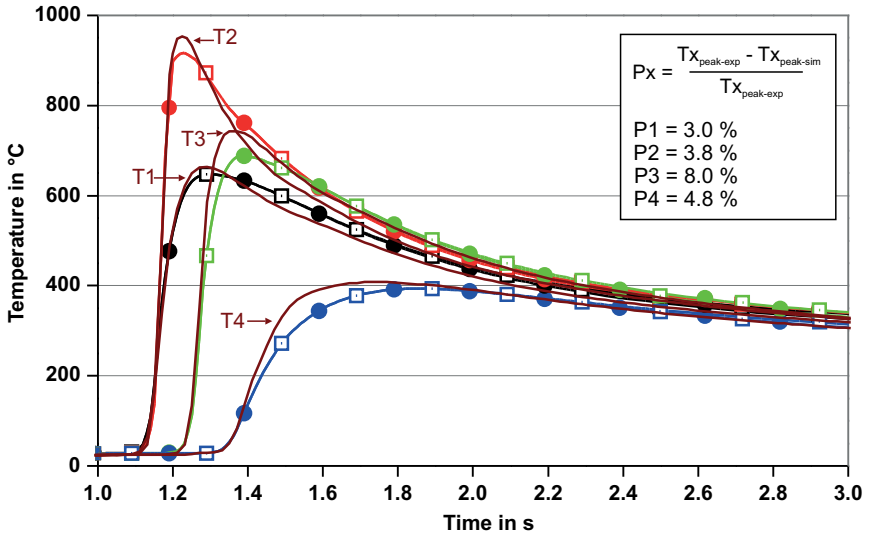

b) Measured and simulated temperature cycles T1-T4 from 1 s to 3 s

Fig. 5.17: Comparison of the measured and simulated (with FEM) four temperature cycles T1-T4, simplified geometry "overlap weld" simulated with the final calibrated heat source input parameters from the simplified geometry "parallel weld", q = 3.3 kW, η = 29 % and v_s = 300 cm/min

In Fig. 5.17a), the simulation without clamps cools slower than the measured ones. The same trend has been observed for the simplified geometry "parallel weld"; however with smaller amplitude. This observation is related to the different clamping conditions for both models, which have automatically different heat absorption capacities. In this case, after considering the clamps in the simulation models, the cooling behaviour of the simulated

temperature cycles match the real ones very well as shown in the zoomed view in Fig. 5.17a). This enables to conclude that the clamping device for the simplified geometry “overlap weld” absorbs more heat energy than those from the simplified geometry “parallel weld”.

For the peak temperatures of the temperature cycles T1 to T4, the same observation as for the simplified geometry “parallel weld” can be made: the influence of the clamping conditions on the cooling behaviour begins after the heat reached the thermocouples and have therefore no significant influence of the peak temperatures within the time interval plotted in Fig. 5.17b). The difference of the peak temperature amplitudes between the measured and simulated four temperature cycles T1 to T4 does not exceed 8 %. The maximal value of 8 % have been measured for the thermocouple T3 and is only 2 % higher than the maximum value of the simplified geometry “parallel weld”, see Fig. 5.14, but stays within the maximum ±10 % boundary taken for the simplified geometry “parallel weld” in the previous section. Thus, from the point of view of the temperature cycles, the calibrated parameters of the simplified geometry “parallel weld” enable simulating the simplified geometry “overlap weld” directly without any readjustments.

The comparison of the measured and simulated fusion line in cross-section and weld pool length for the simplified geometry “overlap weld” are plotted in the following Fig. 5.18 and Fig. 5.19:

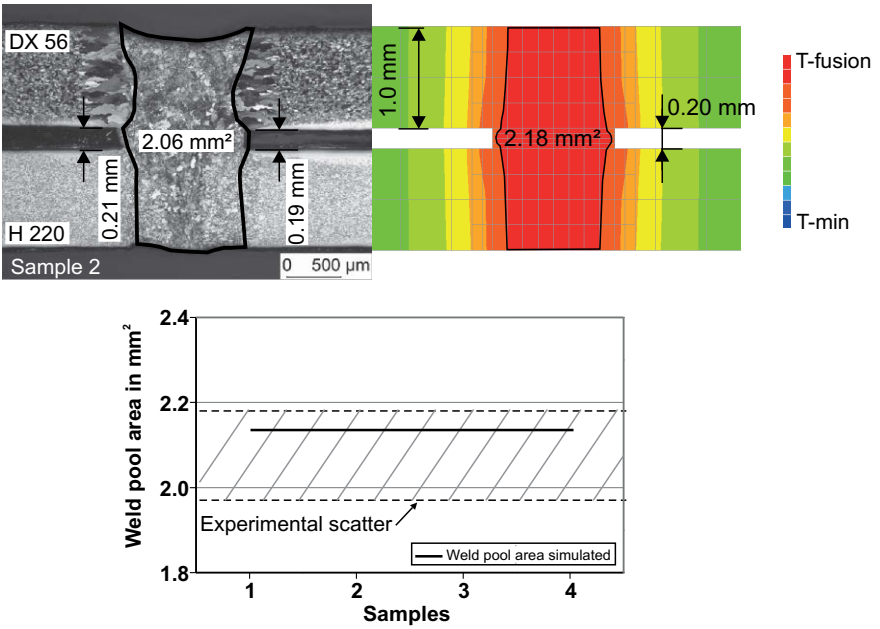

Fig. 5.18: Comparison of the measured and simulated (with FEM) weld pool area in cross-section, simplified geometry “overlap weld” simulated with the final calibrated heat source input parameters from the simplified geometry “parallel weld”, $q = 3.3$ kW, $\eta = 29$ % and $v_s = 300$ cm/min

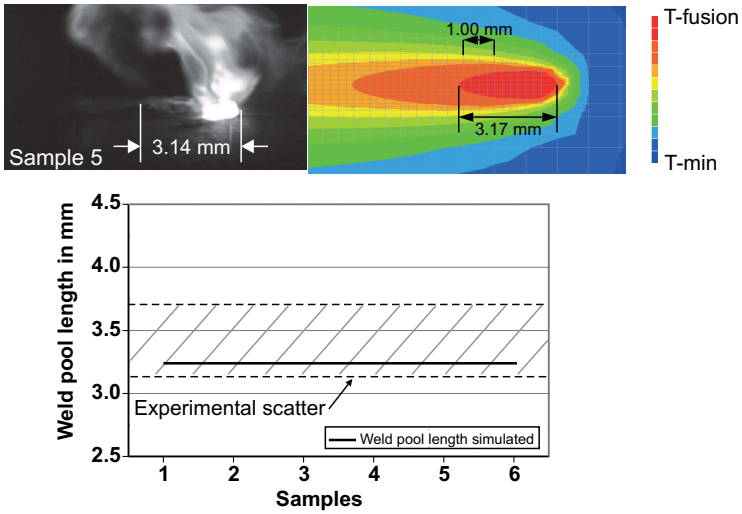

Fig. 5.19: Comparison of the measured and simulated (with FEM) weld pool length, simplified geometry "overlap weld" simulated with the final calibrated heat source input parameters from the simplified geometry "parallel weld", q = 3.3 kW, η = 29 % and v_s = 300 cm/min

The simulation results are almost identical to those for the simplified geometry "parallel wed" in the previous section and both also lie within the respective experimental scatter bands. After the validation of the thermal model for the temperature cycles, these results were expected and confirm the statement that the calibrated parameters for the thermal model of the simplified geometry "overlap weld" could be exactly overtaken from those of the simplified geometry "parallel weld".

Finally, the results in this section demonstrate that the initial input parameters for the thermal model of the simplified geometry "parallel weld" given by the optimisation algorithm presented in section 3.2.5 can also be used also as initial input parameters for the simplified geometry "overlap weld". In other words, it means that the presented fast analytical temperature solutions can be used with a global optimisation routine to automatically calibrate an initial set of input parameters for the thermal model of the simplified geometry "overlap weld".

5.3 Application for the industrial welded assemblies

The combined method presented in the previous sections between the fast analytical temperature field solutions with a conventional numerical approach has been succefully implemented for the calibration and the simulation of the thermal model of the simplified geometries “parallel weld” and “overlap weld”. The possible implementation of this approach has been analysed for the two complex industrial demonstrator’s wheelhouse and crossbeam. The results of these analyses are presented and discussed in the following sections 5.3.1 and 5.3.2. Finally, the thermomechanical simulation results of the welding induced distortions of the crossbeam welded assembly are compared to the experimental data in section 5.3.3.

5.3.1 Temperature field simulation of the wheelhouse

As described in section 3.1.4, the wheelhouse is not a distortion relevant part and only the welding induced temperature field has been simulated and compared to experimental data. The combination of the extreme high gradient temperature around the welds due to the high energy density of the laser beam welding process with the large dimension of the wheelhouse are responsible for a large numerical simulation model with approximately 230,000 nodes. The respective numerical temperature field simulation takes more than four hours (15,500 s). For such a large structure, this calculation time for a full transient temperature field simulation is competitive in comparison to the calculation time of equivalent structures in the literature [126]. This is directly related to the mesh refinement algorithm, which enables to start the simulation with a coarse numerical model with less than 50,000 nodes. For the calibration of the thermal model against experimental data, however, this time still restrains a high number of direct simulations. For this reason, the same approach as for the simplified geometry “overlap weld” has also been tested for the wheelhouse. In the previous section, the calibration of the thermal model of the simplified geometry “overlap weld” has been succefully skipped by taking the calibrated parameters of the simplified geometry “parallel weld”. Since the weld configuration of the wheelhouse is locally identical to the simplified geometry “overlap weld”, the same calibrated parameters from the simplified geometry “parallel weld” have been used for the temperature field simulation of the wheelhouse. The comparison of the measured and simulated four temperature cycles T1, T4, T5 and T6 of the wheelhouse are plotted in Fig. 5.20.

In Fig. 5.20a), the numerical temperature fields match the experimental ones during the welding process and cooling time very well for both welds W1 and W3. As for the simplified geometries “parallel weld” and “overlap weld”, the consideration of the clamps has no effect on the peak temperatures and on the final temperature after 200°C. This statement is due to the fact that if the peak temperatures are measured, the heat has not diffused into the clamps yet. Below approximately 200°C, however, the influence of the clamps is perceivable; the temperature cycles simulated with clamps cool faster than those simulated without clamps and are closer to the corresponding real measurement. This phenomenon has already been observed with the geometries “parallel weld” and “overlap weld” but with different magnitudes. These differences can be explained by looking at the clamping fixtures. For the wheelhouse for instance, the contact areas with the clamps are much smaller than those for the simplified geometry “overlap weld” resulting in a lower heat

transfer between both parts. A zoomed view of the peak temperatures and high gradient temperatures close to the welds W1 and W3 is plotted in the Fig. 5.20b). The simulated peak temperatures of the four plotted temperature cycles T1, T4, T5 and T6 for both welds W1 and W3 match the experimental ones well with an absolute deviation between both simulated and experimental results lower than 4 %. These results are in the same order of magnitude as those from the simplified geometry “overlap weld”.

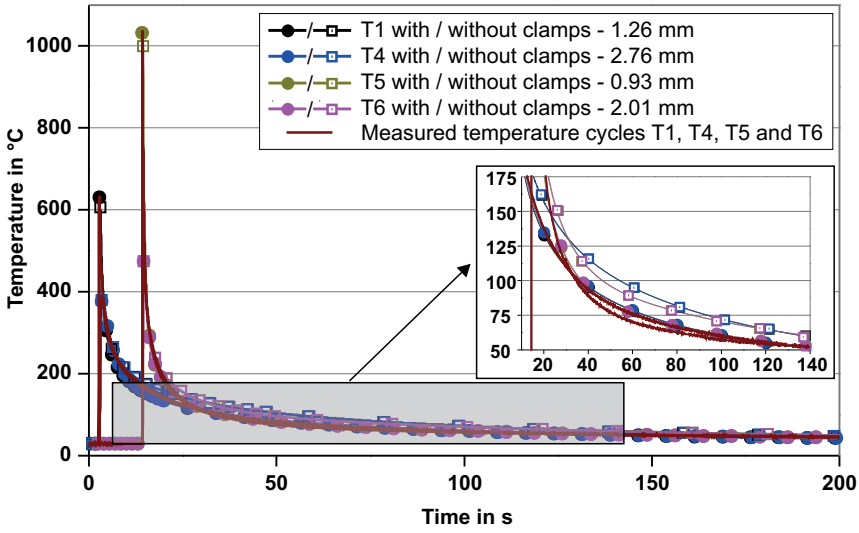

a) Measured and simulated temperature cycles T1-T4 (weld W1) and T5-T6 (weld W3), from 0 s to 200 s

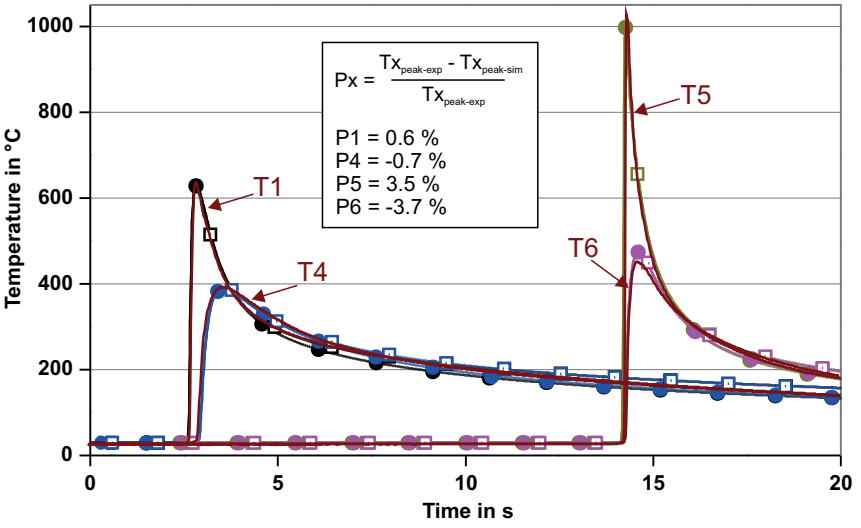

b) Measured and simulated temperature cycles T1-T4 (weld W1) and T5-T6 (weld W3), from 0 s to 20 s

Fig. 5.20: Comparison of the measured and simulated (with FEM) four temperature cycles T1, T4, T5 and T6, wheelhouse simulated with the final calibrated heat source input parameters from the simplified geometry “parallel weld”, q = 3.3 kW, η = 29 % and v_s = 300 cm/min

The comparison of the simulated and measured fusion zones in a cross-section perpendicular to the welds W1 and W3 is plotted in Fig. 5.21.

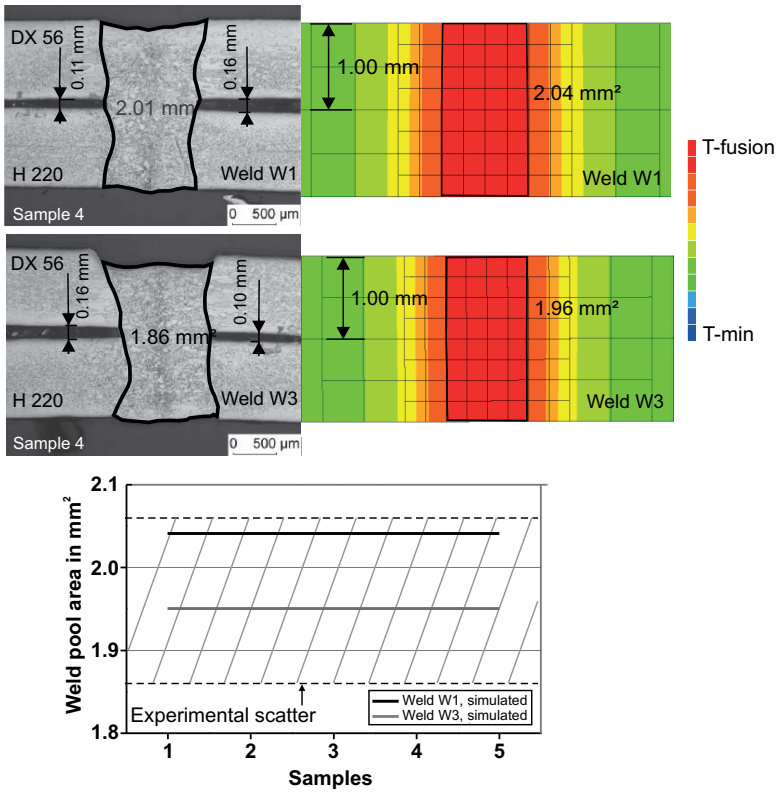

Fig. 5.21: Comparison of the measured and simulated (with FEM) weld pool area in cross-section, wheelhouse simulated with the final calibrated heat source input parameters from the simplified geometry "parallel weld", q = 3.3 kW, η = 29 % and v_s = 300 cm/min

It is important to remember that the gap between the two welded parts of the wheelhouse assembly has not been considered in the simulation model as explained in section 3.3.5. For this reason, the accumulation of heat in the middle of the joint (due to the gap), observable in the experimental cross-sections in Fig. 5.21, cannot be reproduced in the simulation model. With neglecting the local fluctuations of the real fusion zone geometries, however, the fusion zone geometries of the weld W1 and W3 have been well considered in the simulation model; the corresponding simulated fusion zone areas are within the experimental scatter band.

Finally, the comparison of the simulated weld pool lengths of the weld W1 and W3 against the experimental data is shown in Fig. 5.22.

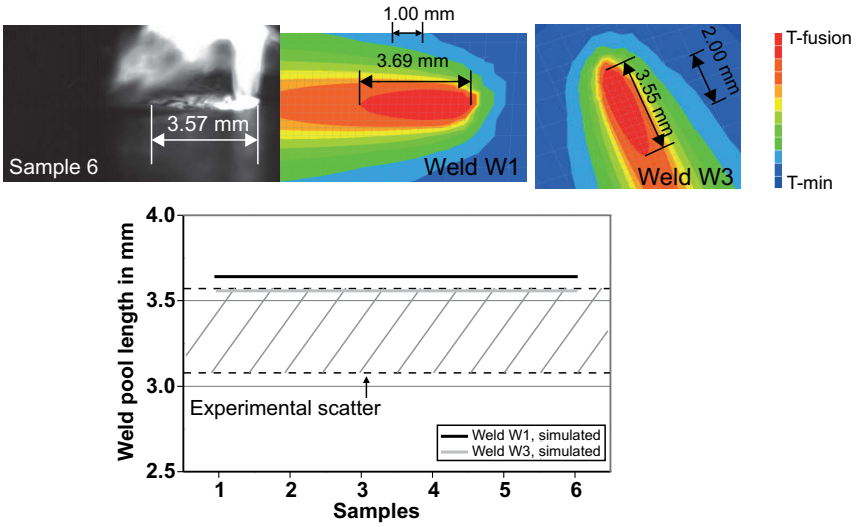

Fig. 5.22: Comparison of the measured and simulated (with FEM) weld pool length, wheelhouse simulated with the final calibrated heat source input parameters from the simplified geometry "parallel weld", q = 3.3 kW, η = 29 % and v_s = 300 cm/min

Both simulated weld pool lengths from the welds W1 and W2 are situated in the upper part of the experimental scatter band. For the simplified geometry "overlap weld", whose joint shape is identical to the wheelhouse, the experimental weld pool length scatter band is almost the same as for the wheelhouse as shown in section 5.2.2. This observation is logical and was expected. In the simulation models, however, the simulated weld pool length of the simplified geometry "overlap weld" is situated in the lower part of the experimental scatter band. This difference between the simplified geometry "overlap weld" and the wheelhouse is related to the 0.2 mm gap considered in the simplified geometry "overlap weld". Fig. 5.23 illustrates this statement. The geometry with gap has a larger joint-volume (V1+V2+V3) than the geometry without gap (V4). The energy required to melt the supplement gap volume (V2) for the geometry with gap is also used in the geometry without gap and is therefore responsible for the longer weld length. This statement has been verified with the simplified geometry "overlap weld"; a simulation has been run without gap and the resulting weld pool length was also situated in the upper part of the experimental scatter band like for the wheelhouse.

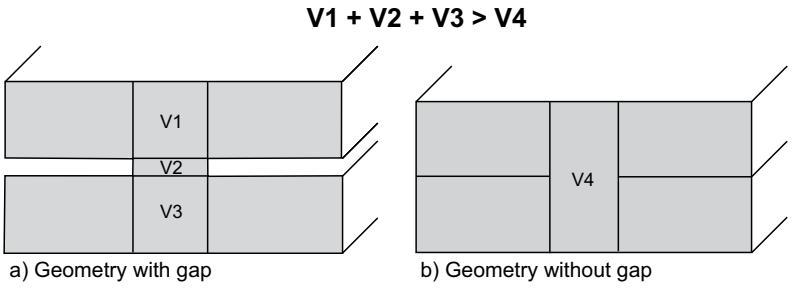

Fig. 5.23: Joint-volume for geometries with and without gap

Finally, the calibrated parameters of the simplified geometry “parallel weld” could be directly implemented without any readjustment for the temperature field simulation of the wheelhouse. The respective simulated temperature cycles, fusion zones in cross-section and weld pool lengths are within the corresponding experimental scatter bands. The normally extremely time-intensive calibration procedure for such a large industrial welded assembly could be skipped out. With the application of the analytical temperature field solutions with the global optimisation algorithm, good initial parameters for the thermal model of the wheelhouse could be obtained automatically in 1830 s which is approximately 8 times faster than a respective single temperature field simulation. With this test case, the potential of fast analytical temperature field solutions to accelerate the calibration of the thermal model for the welding simulation of complex and large industrial structure is given.

It is however important to notice that this combined method between the analytical and the numerical approach is only possible for a parallel joint configuration. For an overlap joint configuration like for the crossbeam welded assembly presented in the next section, the analytical temperature field solutions are not valid and the combined method can therefore not be implemented. Up to now, no analytical temperature solutions for an overlap joint have been published yet and research work in this field is still required.

5.3.2 Temperature field simulation of the crossbeam

As previously mentioned in the section 5.3.1, the analytical temperature field solutions previously presented are only valid for parallel joints. They can therefore not be implemented to simulate the overlap joints of the crossbeam welded assembly. Thus, the entire welding simulation, i.e. thermal model calibration plus thermomechanical welding simulation, has been completely run with FEM. The simulation for the temperature field simulation takes approximately 11000 s or 3 hours. The same remarks as for the wheelhouse can be done: This full transient temperature field simulation for a FE-model containing more than 100,000 nodes is competitive but still restrains the high number of required iterations for the calibration of the thermal model. For this reason, an initial set of input parameters for the thermal model of the crossbeam has been iteratively estimated on a small part as explained in section 3.3.6. For this first calibration, only the fusion line in cross-section has been taken as criterion. Finally, after this first fast initial calibration, a final fine manual calibration is done for the entire crossbeam. The comparison of the simulated and measured temperature cycles is shown in Fig. 5.24.

The representation of the temperature cycles is equivalent as for the wheelhouse in the previous sections. Firstly, the entire welding process and cooling is observed; in this view, the overall behaviour of the temperature cycles and the boundary conditions of the system can be proved. Accurate quantitative statements can then be formulated with the second view concentred around the peak temperatures. In Fig. 5.24a), the temperature cycles T2, T4, T5 and T6 are plotted from 20 s to 200 s. The overall behaviour of the simulated four temperature cycles matches the corresponding experimental data very well. The final temperatures after 200 s have been well reproduced which enables to conclude that the boundary conditions of the system are correct. Quantitative statements concerning the peak temperatures can be made in Fig. 5.24b). The respective maximum deviation between the simulated and the measured values is 6.2 % for the temperature cycles T8. The cooling

behaviour in the high temperature gradient zones (just before and after the peak temperatures) is well reproduced by the simulation for all the four temperatures cycles. In conclusion, the thermal model is well calibrated according to the temperature cycle measurements.

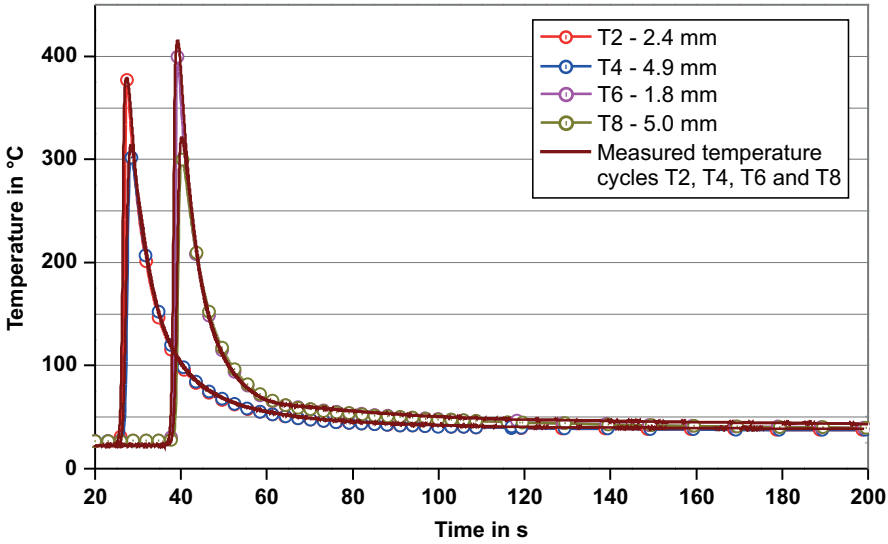

a) Measured and simulated temperature cycles T2, T4, T5 and T6 from 20 s to 200 s

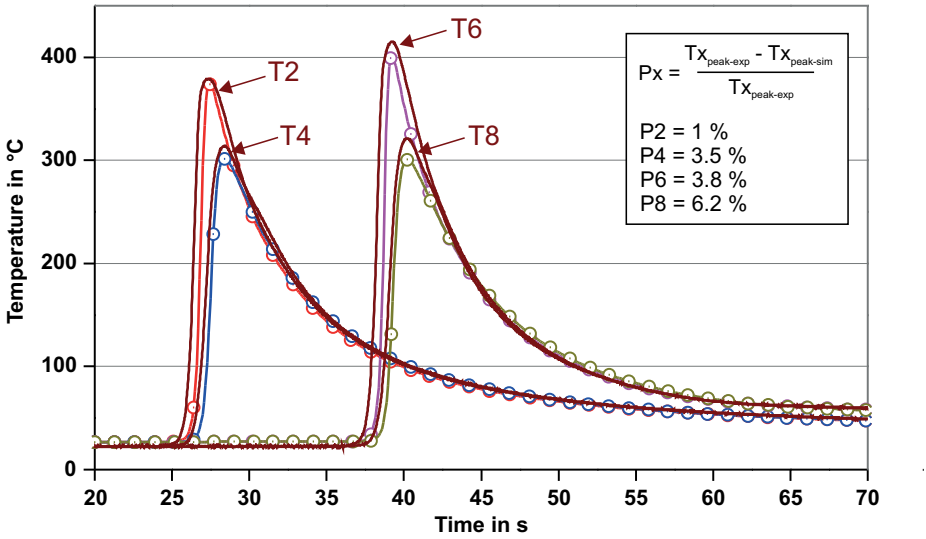

b) Measured and simulated temperature cycles T2, T4, T5 and T6 from 20 s to 70 s

Fig. 5.24: Comparison of the measured and simulated (with FEM) four temperature cycles T2, T4, T5 and T6, crossbeam, MIG welding overlap joint, material thickness 2.8 mm, U_{ave} = 162 V, I_{ave} = 22 A and v_s = 100 cm/min

For the final validation of the thermal model, however, the simulated weld pool shape must also be compared to experimental data. For this task, the fusion zone in cross-section and the weld pool length are taken as criterion as explained in section 3.1.4.2. The comparison of the simulated and measured fusion zone in cross-section for three welds W1r, W2l and W4l is plotted in Fig. 5.25.

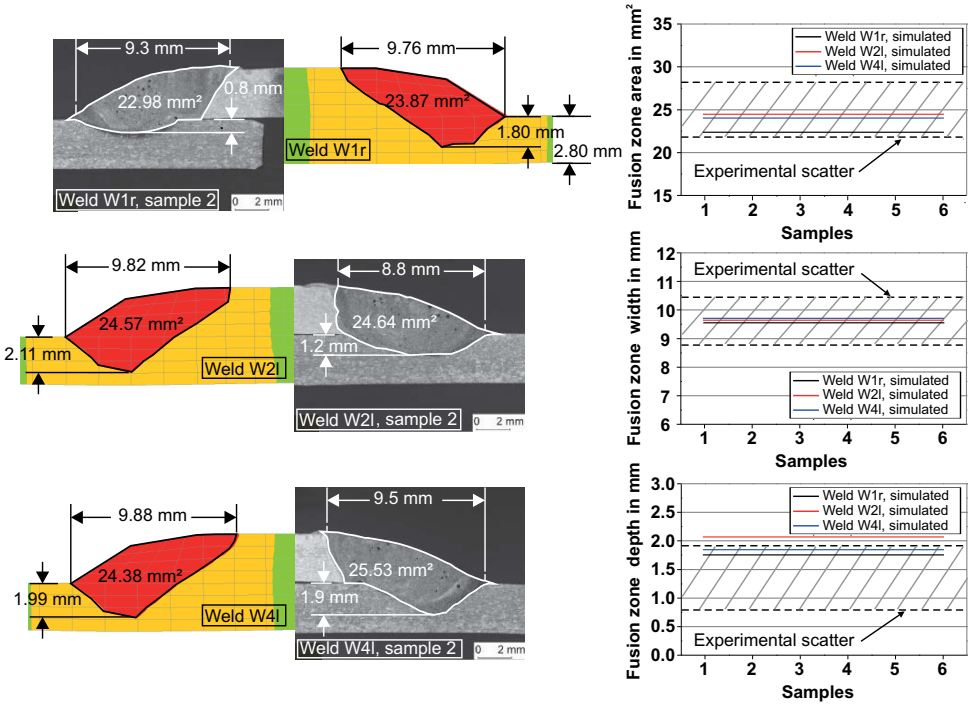

Fig. 5.25: Comparison of the measured and simulated (with FEM) welds W1r, W2l and W4l in cross-section, crossbeam, MIG welding overlap joint, material thickness 2.8 mm, U_{ave} = 162 V, I_{ave} = 22 A and v_s = 100 cm/min

For the three welds W1r, W2l and W4l the simulated fusion zones in cross-section match the experimental data qualitatively very well. Quantitatively, the simulated fusion zone areas and fusion zone widths are within the experimental scatter band. For the simulated fusion zone depths, the values of the welds W1r and W4l are situated in the upper part of the respective experimental scatter band and only the value of the weld W2l is, with 2.11 mm, 10 % higher than the upper limit of the scatter band. At this position, this 10 % deviation only for one single value has been judged acceptable and the thermal model is also considered calibrated according to the fusion zone shape in cross-section.

The comparison of the simulated and measured weld pool length is shown in Fig. 5.26. All the three simulated weld pool lengths for the welds W1r, W2l and W4l are situated with the corresponding experimental scatter band and the thermal model is therefore considered calibrated.

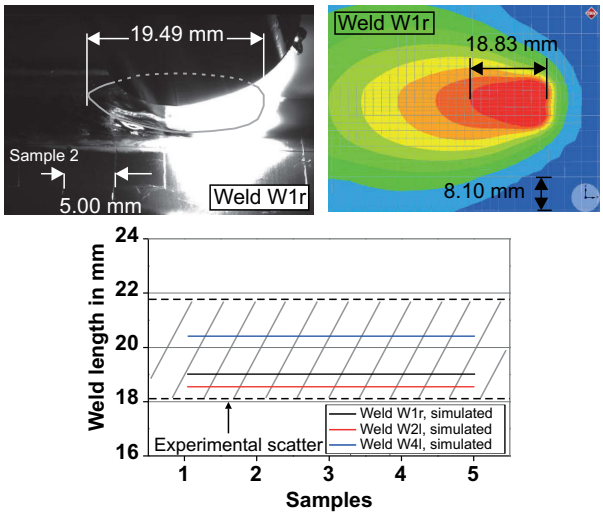

Fig. 5.26: Comparison of the measured and simulated (with FEM) weld pool length, crossbeam, MIG welding overlap joint, material thickness 2.8 mm, U_{ave} = 162 V, I_{ave} = 22 A and v_s = 100 cm/min

Finally, for the calibration of the thermal model of the crossbeam, the difference between the experimental and the simulation data is less than 7 % for the peak temperatures and high temperature gradients and the simulated fusion zones in cross-sections and weld-pool-length are within the experimental scatter bands. The calibrated thermal model is therefore validated and a thermomechanical simulation of the distortion can be started. No further calibration of the heat source model is done within the validation of the thermomechanical simulation of distortion presented in the next section.

5.3.3 Distortion simulation of the crossbeam

The results discussed in the previous section are used as thermal load for the thermomechanical simulation of the distortions. According to the simplifications and assumptions made in section 3.3.2, a non-coupled relationship is considered between the thermal and the mechanical simulation. Surely, the consideration of a more complex simulation model may lead to more accurate results as in [126] for instance. The corresponding expert knowledge's in welding simulation and the computational cost are nevertheless still too high for a wide application in the industry. Furthermore, a full transient non-coupled thermomechanical simulation based on a heat conduction problem in solid medium has often been used and validated to simulate the welding induced distortions [89, 122, 130] making this assumption suitable.

In the mechanical model used for the simulation of the distortions, no mechanism for the softening effect occurring during the welding process of the aluminium alloy from the 6xxx series described in section 3.1.1.3 has been implemented. In order to quantify the influence of this simplification, two simulations have been run, one with the BM and one with the HAZ material properties as described in section 3.3.6. Since the plastic deformation zone around

the weld pool, which is responsible for distortions, is composed of a mixture between the BM and the HAZ materials, the resulting two simulation results form a bandwidth around this softening mechanism.

The comparison of the simulated and measured distortion fields and distributions are plotted in the next four figures, Fig. 5.27 to Fig. 5.31. The experimental global distortion field measured with the optical distortion measurement system, see section 3.1.4.2, is compared to the corresponding two simulation fields calculated for the two investigated clamping types in Fig. 5.27.

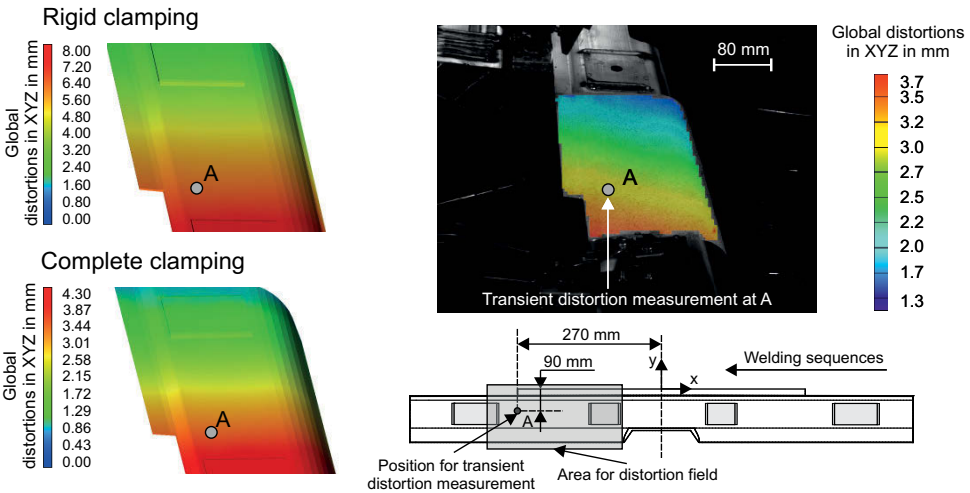

Fig. 5.27: Comparison of the simulated (with BM material properties) and experimental global distortion field measurement after 800 s, crossbeam, measured with optical 3D deformation analysis system Aramis, simulated for two different mechanical boundary conditions

Here, it is worth to notice that a field representation enables to give a global appreciation of the investigated phenomenon. For this reason, the influence of the BM and the HAZ material properties on the simulated distortions cannot be analysed well in this form and only the simulation results for the BM material properties are plotted in Fig. 5.27. Qualitatively, the two simulations match the measured field well; this means that the implemented physical model is adequate. Quantitatively, the global distortions simulated with the model with the complete clamping are in the same order of magnitude as the measured ones. The global distortions predicted by the simulation model with the rigid clamping are, however, approximately twice as large compared with the experimental data. This phenomenon can be explained by analysing the clamps during the distortion measurements. As explained in section 3.1.3.2, the clamp CC1 has not been released after the welding process in order to have a reference fixed point for the distortion measurements. This configuration is represented in Fig. 5.28a).

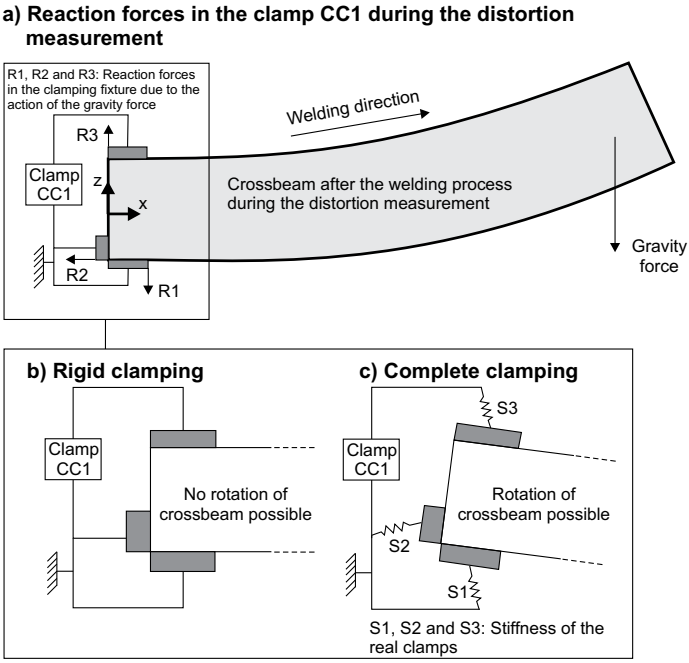

Fig. 5.28: Influence of the clamping definition in the simulation model on the final simulated distortions

Due to the welding induced distortions, the crossbeam bends itself in z-direction. If the crossbeam is clamped in the clamp CC1 as shown in Fig. 5.28a), the resulting lever arm at the other extremity of the crossbeam in combination with the gravity force is responsible for the three reaction forces R1, R2 and R3 in the clamp CC1. In the simulation model with the rigid clamping, represented in Fig. 5.28b), the degree of freedom of the nodes at the contact surface between the clamps and the crossbeam are fixed to zero and prevent therefore any displacements and rotations of the crossbeam. In the simulation model containing the complete clamping as independent part, represented in Fig. 5.28c), the stiffness's S1, S2 and S3 of the clamp CC1 at the contact surfaces with the crossbeam are therefore automatically considered by the FE- model. In this configuration, the small rotations and displacements of the crossbeam due to reaction forces R1, R2 and R3 on the clamp CC1 are responsible for a small subsidence of the crossbeam in the clamp and therefore for global lower distortion amplitude.

For an accurate quantitative and qualitative validation of the simulation model, however, an analysis of the transient distortion distributions at a single position during all the measurement process, i.e. welding and cooling, is more appropriate. Thus, the transient distortion distribution in x-, y- and z-directions have been measured and simulated at the position A, see Fig. 5.27. The comparisons of the respective simulated and the experimental results are plotted in the following Fig. 5.29, Fig. 5.30 and Fig. 5.31:

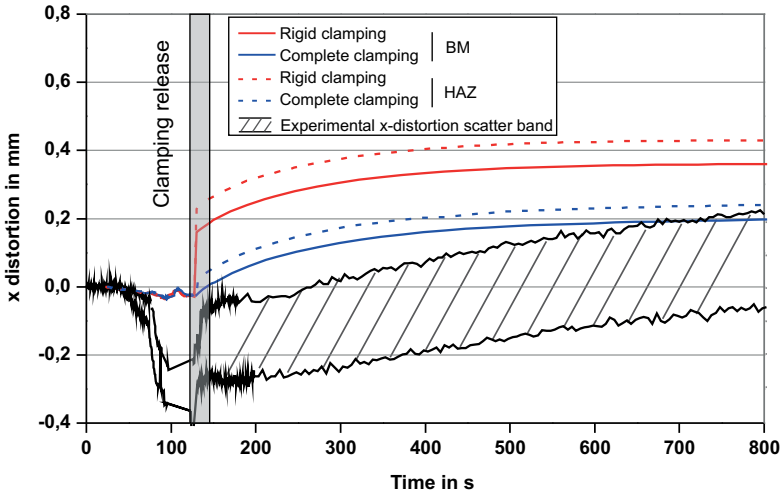

Fig. 5.29: Comparison of the measured and simulated transient distortion at point A in x-direction, crossbeam, MIG welding overlap joint, material thickness 2.8 mm, U_{ave} = 162 V, I_{ave} = 22 A and v_s = 100 cm/min

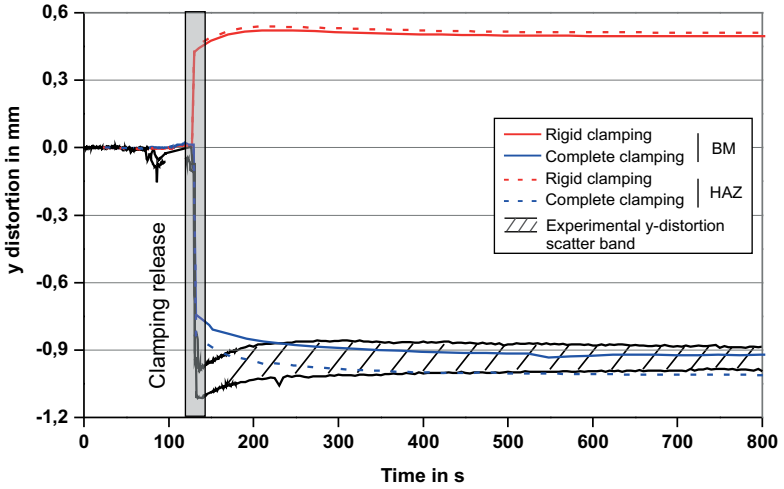

Fig. 5.30: Comparison of the measured and simulated transient distortion at point A in y-direction, crossbeam, MIG welding overlap joint, material thickness 2.8 mm, U_{ave} = 162 V, I_{ave} = 22 A and v_s = 100 cm/min

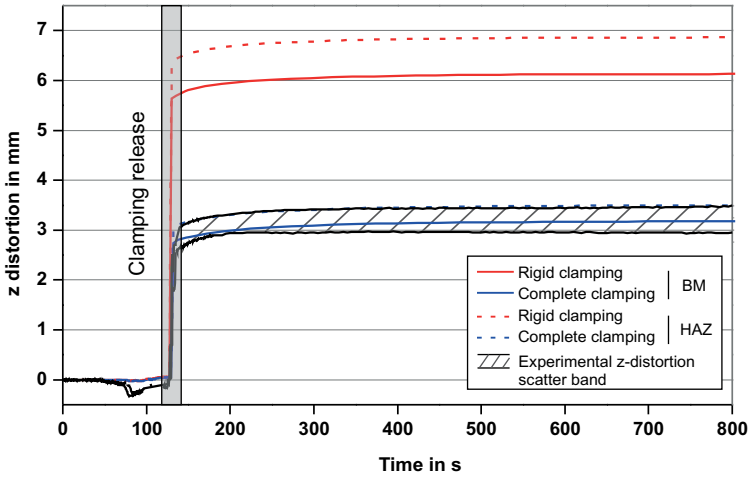

Fig. 5.31: Comparison of the measured and simulated transient distortion at point A in z-direction, crossbeam, MIG welding overlap joint, material thickness 2.8 mm, U_{ave} = 162 V, I_{ave} = 22 A and v_s = 100 cm/min

The value of the global distortion field at the point A plotted at t = 800 s in Fig. 5.27 is close to the value of the distortion in z-direction (also at t = 800 s) in Fig. 5.31. This is due to the fact that the distortions in z-direction are approximately 3 and 17 times higher than the distortions in the y- and x-directions, respectively. The statement made previously with the distortion field analysis is therefore confirmed: the global distortions (mainly governed by the distortion in z-direction) simulated with the complete clamping are approximately two times lower than the simulation with the rigid clamping at t = 800 s. The transient distortion distributions enable analysing the evolution of the distortion with time. Here, the distortions in z-direction are within the experimental scatter band during all the measurement process. In the x-direction in Fig. 5.29, the distortion distributions for both clamping models have only been qualitatively well reproduced during all the cooling process. Quantitatively, both simulation models with the real and with the fixed clamps are slightly above the experimental scatter band; the simulation with the complete clamping gives the more accurate simulation results. For the distortion in y-direction in Fig. 5.30, the simulation results of the model with rigid clamping are quantitatively and qualitatively wrong; this phenomenon can be directly related to the ideal rigid clamping definition in the simulation model, which does not alloy in this case to reproduce the measured distortion distribution in the y-direction. Contrarily, with the complete clamping definition, the corresponding simulation results are within the experimental scatter band almost during all the welding and cooling time. Only between 100 s and 200 s, the simulation results are out of the experimental scatter band. Here, it is important to notice that the rigid clamping definition is not a wrong assumption in a general manner; an analysis of its possible application to reproduce the investigated real clamping system is nevertheless required in order to avoid wrong simulation results.

This result highlight the importance of the concordance between the real clamping system and its virtual definition in the simulation model

As previously mentioned the influence of the softening effect occurring during the welding of the aluminium alloy of the crossbeam has been indirectly investigated by running two thermomechanical simulations with the BM and with HAZ material properties. In each figure Fig. 5.29, Fig. 5.30 and Fig. 5.31, the dashed lines represent the simulations with the HAZ material properties and the full lines with the BM material properties. Qualitatively, all the distortion distributions in x-, y- and z-directions with the BM and HAZ material properties are equivalent. Quantitatively, for all simulations, the distortion amplitudes calculated with the HAZ material properties are higher than those calculated with the BM material. This is due to the fact that the yield stress of the HAZ material is lower than the yield stress of the BM, see section 3.1.1.3. Therefore the material with the lower yield stress develops a higher plastic deformation for an equivalent load resulting in a higher degree of plastification and consequently in higher distortions. Here, the different amplitudes between these dashed lines and solid lines for all the distortions in x-, y- and z-directions do not exceed 10 %. According to the simplifications and assumptions made in the simulation model, an absolute deviation between the simulated and the experimental results of 10 % is considered appropriate. For this reason, in this test case and more generally for a large welded assembly with this aluminium alloy, the consequent effort required to consider the softening effect in the simulation model would not bring a relevant improvement of the simulation result.

Finally, a correct definition of the mechanical boundary conditions of the crossbeam welded assembly is found to be essential to guarantee a qualitatively and quantitatively good distortion prediction. In this test case, it has been shown that the simulation model containing the complete clamping as single part enables to obtain the more accurate simulation results in comparison with the simulation model with rigid clamping. This statement is in accordance with the conclusions given by Roeren [108, 109].Here, however, the real clamping device used to weld the crossbeam assembly was relatively simple in comparison to the real one in the automotive production line and could be therefore quickly implemented in the simulation model. For more complex clamping devices, this approach may not be possible. In fact, the choice of the clamping type in the simulation model is dependent on the expected degree of accuracy of the simulation results. For only a qualitative distortion analysis, the simulation model with the rigid clamping is appropriate; for the crossbeam, the main distortions in z-direction have been qualitatively well calculated. For more accurate results, the consideration of the complete clamping devices in the simulation model is optimal but increased the complexity of the simulation model and therefore the global time to solution. A third clamping type in the simulation model could be a good alternative between the rigid and the complete clamping model as shown by Roeren [108, 109]. With this clamping type, elements with a predefined stiffness characteristic are implemented at the contact surface between the welded assembly and the clamps in the same manner as for the rigid clamping. The advantage of this clamping definition is its relative simple implementation and the corresponding computational time, equivalent to the rigid clamping model. The main handicap of this technique is the determination of the corresponding stiffness of the clamps. This can be done experimentally as shown by Lutzman in [107], but the corresponding techniques and required experimental equipment are highly time and cost intensive. For this reason, this approach has been judged not easily adaptable in an industrial context and has been not taken into account.

6 Summary and outlook

This Ph.D. thesis has been focused on the possibilities and limits of the application of fast analytical temperature field solutions to simulate the welding induced distortion of complex automotive welded assemblies. A structure welding simulation approach has been implemented: in a first simulation step, the temperature field induced by the welding process is calculated and then transferred in a second simulation step as input data for the mechanical simulation of the welding distortions. For the temperature field simulation, the energy of the welding process has been simplified with a phenomenological heat source model. This approach is relatively easy to implement but the respective heat source model is not related to the physical properties of the investigated welding process and needs therefore to be calibrated iteratively against experimental data. The high number of direct simulations required to obtain a calibrated thermal model in combination with the extremely time-consuming transient welding simulation with conventional numerical methods has restrained the wide application of welding simulation in the automotive industry. In comparison to a conventional numerical approach, the calculation time of analytical solutions is extremely fast but restricted, so far, to ideally simple geometries. The idea followed in this study is to extend the application of analytical solutions for realistic geometries and to combine both analytical and numerical approaches to accelerate the calibration of the thermal model and finally improve the global welding simulation workflow. The application of this combined method is possible only if the analytical temperature results are comparable to an equivalent numerical simulation. For this reason, the first investigation is done for a point heat source moving along a straight welding trajectory on an infinite solid in steady state. In this configuration, the analytical temperature field is exact and allows validating the result of the numerical model. In the next steps, this analytical solution is taken as basis and is extended and validated with increasing complexity until an analytical solution for a double ellipsoidal heat source moving along an arbitrarily curved welding trajectory on a finite thin plate in transient state is reached. All these analytical temperature field solutions are validated on small, simple geometries. In order to highlight the potential of the last validated analytical solution in means of result accuracy and computational time, the temperature field on a semi-industrial thin plate with four long curved welds is simulated analytically and numerically. The results accuracy of both methods is comparable and, for instance, the analytical simulations are up to 85,000 times faster for the estimation of the weld pool length.

The application of the presented analytical temperature field solutions is then tested on two large and complex automotive welded assemblies. The first one is a wheelhouse composed of two ferritic deep-drawing sheet metal parts with 1 mm thickness joined with a laser beam welding process with approximately 600 mm weld seam length. The second one is crossbeam composed of five aluminium extrusion parts with 2.8 mm thickness in a 6xxx series aluminium alloy joined with a MIG welding process with approximately 500 mm weld seam length. For both test cases, transient temperature field measurements, metallographic cross-sections perpendicular to the weld seams and weld pool length measurements have been carried out to have reference data for the calibration of the respective thermal models.

Distortion field and transient distortion distribution measurements are also done to validate the thermomechanical simulation results.

The analytical solution for the double ellipsoidal heat source moving along an arbitrarily curved welding trajectory on a finite thin plate in transient state is up to now the most complex application of analytical temperature field solutions for welding simulation. However, for the simulation of real welding problems, the consideration of temperature dependent material properties and realistic boundary conditions is of major importance and can only be considered in the thermomechanical numerical simulation model. For this reason, the replacement of a slow but accurate numerical temperature field simulation with a fast simplified analytical temperature field simulation is not investigated. Since the effort required to calibrate the numerical thermal model is more time consuming than the time for a single numerical simulation. A reduction of these iteration loops could decrease the global simulation time considerably. Therefore, it has been investigated if the fast analytical temperature field models can give an initial set of calibrated heat input parameters to the numerical model. The simplifications and assumptions made in the simplified analytical model are then compensated with a final calibration only carried out within the numerical model with full complexity. Furthermore, the short computational efforts of the analytical solutions enables the implementation of a global calibration algorithm based on neural networks so that unknown input parameters of the phenomenological simulation model are automatically evaluated by calibration against the experimental data.

This method has been implemented for the welding simulation of the wheelhouse. With a calculation time of 15,500 s for a single thermal simulation of the entire geometry, the calibration of the numerical thermal model would have not been possible in a realistic industrial time frame. Locally around the weld seams, the parallel joints in overlap configuration can be simplified with parallel joints. With this simplification, the analytical approach could be used. Thus, welding experiments have been carried out for two small sheets welded in a parallel joint configuration; the same welding parameters as for the wheelhouse are used. A simplified analytical model with linear material properties and adiabatic boundary conditions and a numerical model with full complexity are used for this simple test case. The phenomenological heat source model is then automatically calibrated with the analytical approach combined with the global optimisation algorithm. The potential of the fast analytical methods to decrease the calibration time of the phenomenological heat source model could be well demonstrated within this example. Indeed, the calculation time of the 3051 direct simulations run during the automatic calibration is shorter than one equivalent FE-simulation. The respective analytically calibrated heat source parameters are finally used in the counterpart FE-model as an initial set of parameters. The resulting numerical simulation results are close to the corresponding experimental data with an absolute deviation of the peak temperatures to the experimental data below 4%. Only a few calibration loops are then necessary within the numerical model to obtain the final calibrated thermal model.

The possibilities to use the calibrated heat source parameters of the simplified geometry “parallel weld” as input parameters for the parallel joints in overlap configuration of the wheelhouse is not directly tested on the complete wheelhouse geometry but on a second simplified test case composed of two small steel sheets positioned exactly in the same overlap joint configuration than the wheelhouse. The resulting simulation results match the

experimental data with a maximum deviation between the simulated and measured peak temperatures of 8 % validating the geometry simplification of the joint. With the same logic, the thermal model of the wheelhouse is not directly calibrated; the entire welded assembly is directly simulated with the heat source parameters of the simplified geometry “parallel weld”. The simulation results match also the respective experimental data well with a maximum deviation between the simulated and measured peak temperatures of 4 %. Finally, the calibration of thermal model of the complex and large wheelhouse demonstrator part could be significantly accelerated with the implementation of the combined analytical-numerical method on an optimum simplified test case.

For the simulation of the crossmember welded assembly, the overlap joint geometry could not be simplified with the analytical approach presented in this work; the entire simulation workflow has been done consequently only with FEM. In order to accelerate the calibration of the thermal model, a small part of the crossbeam around one weld is cut apart from the rest of the structure and a first calibration is made on this small part. The advantage of this method is the extremely short calculation time in comparison to the thermal simulation of the entire crossmember. Similarly to the wheelhouse, the calibrated heat source parameters on its small test case are used as initial set of parameters for the final calibration on the entire crossbeam structure. After the calibration, the maximum deviation between the real and the simulated peak temperature does not exceed 6%. With this method, the global calibration time of the thermal model is not as fast as with the analytical approach implemented for the wheelhouse welded assembly. However, it is much faster than a conventional calibration on the entire structure and could enable to calibrate the thermal model of the crossbeam welded assembly within an acceptable industrial time frame. After the calibration of the thermal model, a thermomechanical simulation is carried out for the estimation of the distortions. Two types of the clamping boundary conditions have been investigated. In the first clamping fixture, all the degrees of freedom of the nodes in contact between the crossmember and the clamps are fixed. This method is easy to implement but can lead to wrong distortion distributions as shown for the crossbeam welded assembly with the distortion in y-direction. For the second clamping fixture, the entire clamping geometry is implemented in the simulation model. This technique leads to the best qualitative and quantitative distortion results but also to the higher computational times.

The results presented and discussed in this Ph.D. have shown that an application of welding simulation in the automotive industry is connected with an optimisation of the time required for an industrial user to carry out the entire workflow of a welding simulation. The extensions of the analytical temperature field solutions proposed in this work have a high potential to reduce the calibration time of the thermal model. For large and complex industrial structures, this analytical approach can however only be implemented in an indirect manner for parallel weld joint geometry limiting therefore its universal applicability. Some research work is still required to develop new analytical solutions for other joint geometries.

Nomenclature

Abbreviations

Abbreviation	Meaning
AWS	American Welding Society
BAM	Bundesanstalt für Materialforschung und -prüfung, Federal Institute for Materials Research and Testing
BEM	Boundary Element Method
BMBF	Bundesministerium für Bildung und Forschung
BM	Base Metal
CAD	Computed Aided Design
CAE	Computed Aided Engineering
CCD camera	Charged-coupled-device camera
1D, 2D, 3D	One, two, three dimensions
DIN	Deutsches Institut für Normung e.V.
EBW	Electron Beam Welding
LBW	Laser Beam Welding
FDM	Finite Differences Method
FE	Finite Element
FEM	Finite Element Method
FVM	Finite Volume Method
GMAW	Gas Metal Arc Welding
GMA Laser-Hybrid Welding	Gas Metal Arc Laser-Hybrid Welding
GMAW-P	Pulsed Gas Metal Arc Welding
HAZ	Heat-Affected Zone
Hz	Hertz
IHCP	Inverse Heat Conduction Problem
IIW	International Institute of Welding
K	Kelvin
Nd:YAG-Laser	Neodymium-doped Yttrium Aluminium Granet-Laser
MIG	Metal Inert Gas

MAG	Metal Active gas
OEM	Original Equipment Manufacturer
PEP	product engineering process
RAM	Random Access Memory
SAW	Submerged Arc Welding
SST	Schweißsimulationstool (in German) in English welding simulation tool

Symbols

Symbol	Dimension	Meaning
ρ	$\left[kg \cdot m^{-3}\right]$	Density
λ	$\left[W \cdot m^{-1} \cdot K^{-1}\right]$	Heat conductivity
c	$\left[J \cdot kg^{-1} \cdot K^{-1}\right]$	Specific heat capacity
κ	$\left[m^2 \cdot s^{-1}\right]$	Thermal diffusivity
ε	$\left[-\right]$	Emissivity coefficient
K_T	$\left[W \cdot m^{-2} \cdot K^{-1}\right]$	Heat transfer coefficient
K_0	$\left[-\right]$	Modified Bessel function of second kind and order zero
erf	$\left[-\right]$	Error Function
σ	$[W \cdot m^{-2} \cdot K^{-4}]$	Stefan-Boltzmann constant
F_o	$\left[-\right]$	Fourier number
Ω	$\left[-\right]$	Computational domain
Γ	$\left[-\right]$	Outer surface of computational Domain
∇^2	$\left[-\right]$	Nabla operator
div	$\left[-\right]$	Divergence
$grad$	$\left[-\right]$	Gradient
α	$[W \cdot m^{-2} \cdot K^{-1}]$	Convective heat transfer coefficient
δ	$[m]$	Thickness of plate
t	$\left[s\right]$	Time
t_p	$\left[s\right]$	Pulse time by GMWA-P process
t_b	$\left[s\right]$	Base time by GMWA-P process
$t_{8/5}$	$\left[s\right]$	Cooling time from 800°C to 500°C
$t_{5/3}$	$\left[s\right]$	Cooling time from 500°C to 300°C
E	$\left[GPa\right]$	Young's Modulus
υ	$\left[-\right]$	Poisson's ratio
$R_{p0.2}$	$\left[MPa\right]$	0.2% Yield stress
R_m	$\left[MPa\right]$	Ultimate stress
A_{80}	$\left[\%\right]$	80 % of ultimate elongation

T	$[°C]$	Temperature
T_0	$[°C]$	Ambient Temperature
$T_{Liquidus}$	$[°C]$	Liquidus Temperature
$T_{Solidus}$	$[°C]$	Solidus Temperature
q_{input}	$[W \cdot m^{-3}]$	Energy input per time
q_{net}	$[W \cdot m^{-3}]$	Energy per time from the welding process
q_c	$[W \cdot m^{-3}]$	Convective energy per time in the weld pool
q_L	$[W \cdot m^{-3}]$	Latent heat of fusion and solidification
q_{lost}	$[W \cdot m^{-2}]$	Energy per time lost to the environment
q_{line}	$[W]$	Energy per time of the line source
q_{point}	$[W]$	Energy per time of the point source
v	$[m \cdot s^{-1}]$	Welding speed
(x, y, z)	$[-]$	Global coordinate system
ξ	$[m]$	Position of the moving point source on the axis
I	$[A]$	Electric current
I_p	$[A]$	Pulse current by GMWA-P process
I_b	$[A]$	Base current by GMWA-P process
U	$[V]$	Electric voltage

List of figures

List of tables

Literature

[1] BUNDESMINISTERIUM FÜR BILDUNG UND FORSCHUNG BMBF - FEDERAL MINISTRY OF EDUCATION AND RESEARCH, Abschlussbericht zum Leitprojekt integrierte Virtuelle Produktentstehung iViP - Final report about the integrated virtual product development iViP, 2002 (in German).

[2] BABU S. S., SONNENBERG G., SCHWENK C., GOLDAK J., PORZNER H., KHURANA S. P., ZHANG W. AND GAYLER J. L., How Can Computational Weld Mechanics Help Industry?, *Welding Journal,* vol. 89 (1), pp. 40s-45s, 2010.

[3] RADAJ D., Heat Effects of Welding: Temperature Field, Residual Stress, Distortion: Springer-Verlag, 1992.

[4] RADAJ D., Schweißprozesssimulation: Grundlagen und Anwendungen - Welding process simulation: Basics and utilisations: DVS-Verlag, 1999 (in German).

[5] BONIFAZ E., Finite Element Analysis of Heat Flow in Single-Pass Arc Welds, *Welding Journal,* vol. 79, pp. 121s-125s, 2000.

[6] MAHRLE A. AND SCHMIDT J., The influence of fluid flow phenomena on the laser beam welding process, *International Journal of Heat and Fluid Flow,* vol. 23, pp. 288-297, 2002.

[7] MACKWOOD A. P. AND CRAFER R. C., Thermal modelling of laser welding and related processes: a literature review, *Optics and Laser Technology,* vol. 37, pp. 99-115, 2005.

[8] KIM W.-H., FAN F. G. AND NA S.-J., Effect of Various Driving Forces on Heat and Mass Transfer in Arc Welding, *Numerical Heat Transfer, Part A: Applications,* pp. 633-652, 1997.

[9] HU AND TSAI H. L., Heat and mass transfer in gas metal arc welding. Part I, *International Journal of Heat and Mass Transfer,* vol. 50, pp. 833-846, 2007.

[10] HU AND TSAI H. L., Heat and mass transfer in gas metal arc welding. Part II, *International Journal of Heat and Mass Transfer,* vol. 50, pp. 808-820, 2007.

[11] LIN M. L. AND EAGAR T. W., Influence of Arc Pressure on Weld pool Geometry, *Welding Journal,* vol. 64, pp. 163s-169s, 1984.

[12] LIN M. L. AND EAGAR T. W., Pressure Produced by Gas Tungsten Arcs, *Metallurgical Transactions B,* vol. 17B, pp. 601-607, 1986.

[13] DILTHEY U., MOKROV O. AND PAVLYK V., Modeling of Consumable-Electrode Gas-Shielded Multi-Pass Welding of Carbon Steel With Preheating, *The Paton Welding Journal,* vol. 4, pp. 2-6, 2005.

[14] DILTHEY U., DIKSHEV I., MOKROV O. AND PAVLYK V., Software Package Simweld for Simulation of Gas-Metal-Arc-Welding processes of Steels and Aluminium Alloys, *H. Cerjak, H.K.D.H. Bhadeshia, E. Kozeschnik (Eds.): Mathematical Modelling of Weld Phenomena,* vol. 7, pp. 1057-1079, 2005.

[15] MOKROV O., PAVLYK V. AND DILTHEY U., Analysis of Thermo-electrical Processes and Electrode Metal transfer During Gas-Metal-Arc-Welding With the Aid of Numerical Modelling, *Math. Mod. Inf. Techn. Weld. Relat. Pro, Paton Electric Welding Institute,* pp. 250-257, Kiev 2006.

[16] RIEGER T., GAZDAG S., PRAHL U., MOKROV O., ROSSITER E. AND REISGEN U., Simulation of Welding and Distortion in Ship Building, *Advanced Engineering Materials,* vol. 12 No. 3, pp. 153-157, 2010.

[17] DOYNOV N., OSSENBRINK R., SCHMIDT J. AND MICHAILOV V. G., Utilization of Weld Pool Models in Thermal-Mechanical Simulations, *H. Cerjak, H.K.D.H. Bhadeshia, E. Kozeschnik (Eds.): Mathematical Modelling of Weld Phenomena,* vol. 8, pp. 925-938, 2007.

[18] MICHAILOV V. G., Schweißsimulationstools: Antworten eines Entwicklers (Bericht aus dem BMBF-Projekt SST Schweißsimulationstool) - Welding Simulation tools: Developer's answers (Report from the BMBF-Project SST welding simulation tool), *DVS-Forschungsseminar Fügeprozesssimulation - Innovative Anwendungen der Informatik - Materialprüfungsanstalt der Universität Stuttgart,* 2004 (in German).

[19] SUDNIK W., Simulation von Schweißprozessen - simulation of welding processes, *DVS Berichte Band 214,* pp. 14-31, 2001 (in German).

[20] SUDNIK W., RADAJ D. AND EROFEEW W., Validation of computerised simulation of welding processes, *H. Cerjak, H.K.D.H. Bhadeshia (Eds.): Mathematical Modelling of Weld Phenomena,* vol. 4, pp. 477-493, 1998.

[21] LEBLOND J. B. AND DEVAUX J., A New Kinetic Model for Anisothermal Metallurgical Transformations in Steel Including Effect of Austenite Grain Size, *Acta Met,* vol. 32, pp. 137-146, 1984.

[22] LEBLOND J. B., Mathematical Modelling of Transformation Plasticity in Steels. I: Case of Ideal-Plastic Phases, *International Journal of Plasticity,* vol. 5, pp. 551-572, 1989.

[23] JONHSON A. W. AND MEHL F., Reaction Kinetics in Process of Nucleation and Growth, *Trans. Metal. Soc.,* vol. 135, 1939.

[24] KOISTINEN D. P. AND MARBURGER R. E., A General Equation prescribing the Extent of a Austenite-Martensite Transformation in Pure Iron-Carbon Alloys and Plain Carbon Steels, *Acta Metallurgica 7,* vol. 7, pp. 59-60, 1959.

[25] GRONG O., Metallurgical Modelling of welding: Material Modelling Series, The Institution of Materials, 1997.

[26] CARON J., HEINZE C., SCHWENK C., RETHMEIER M., BABU S. S. AND LIPPOLD J., Effect of Continuous Cooling Variations on Numerical Calculation of Welding-Induced Residual Stresses, *Welding Journal,* vol. 89, pp. 151s-160s, 2010.

[27] CARON J., HEINZE C., SCHWENK C., RETHMEIER M., BABU S. S. AND LIPPOLD J., Sensitivity Analysis of Martensite Transformation Temperatures with Respect to Numerical Calculation of Welding-Induced Residual Stresses, *H. Cerjak, N. Enzinger (Eds.): Mathematical Modelling of Weld Phenomena,* vol. 9, pp. 215-238, 2010.

[28] KARKHIN V. A., HOMICH P. N. AND MICHAILOV V. G., Models for volume heat sources and functional-analytical technique for calculating the temperature field in butt welding, *H. Cerjak, H.K.D.H. Bhadeshia, E. Kozeschnik (Eds.): Mathematical Modelling of Weld Phenomena,* vol. 8, pp. 819-834, 2007.

[29] BATHE K. J., Finite Element Procedures: Prentice-Hall, 1996.

[30] GOLDAK J., MOORE J. E. AND BIBBY M. J., A Comparison of the Point source and Finite Element Schemes for Computing Weld Cooling, *ASM Material Week 85,* pp. 1-8, 1985.

[31] PAVELIC V., TANBAKUCHI R., UYEHARA O. A. AND MYERS P. S., Experimental and Computed Temperature Histories in Gas Tungsten-Arc Welding of Thin Plates, *Welding Journal,* vol. 48, pp. 295s-305s, 1969.

[32] FRIEDMAN E., Thermomechanical Analysis of the Welding Process Using The Finite Element Method, *Transactions of the ASME,* pp. 206-213, 1975.

[33] KRUTZ G. W. AND SEGERLIND L. J., Finite Element Analysis of Welded Structures, *Welding Journal,* vol. 57, pp. 211s-216s, 1978.

[34] TEKRIWAL P. AND MAZUMDER J., Finite Element Analysis of three-Dimensional Transient Heat Transfer in GMA Welding, *Welding Journal,* vol. 67, pp. 150-156, 1988.

[35] TEKRIWAL P. AND MAZUMDER J., Finite Element Modeling of Arc Welding Processes, *Advances in Welding Science and Technology,* pp. 71-80, 1986.

[36] ROSENTHAL D., The Theory of Moving Sources of Heat and Its Application to Metal Treatments, *Transactions of the ASME,* vol. 43, pp. 849-866, 1946.

[37] ROSENTHAL D., Mathematical Theory of Heat Distribution During Welding and Cutting, *Welding Journal,* vol. 20, pp. 220s-234s, 1941.

[38] ROSENTHAL D. AND SCHMERBER R., Thermal Study of Arc Welding, Experimental Verification of Theoretical Formulas, *Welding Journal,* vol. 17, pp. 2-8, 1938.

[39] RYKALIN N. N., Berechnung der Wärmevorgänge beim Schweißen - calculation of the heat mechanisms during welding: Berlin, Verlag Technik, 1957 (in German).

[40] RYKALIN N. N., Die Wärmegrundlagen des Schweissvorganges - Heat foundations of welding process: Berlin, Verlag Technik, 1952 (in German).

[41] CARSLAW H. S. AND JAEGER J. C., Conduction of Heat in Solids, Second Edition: Clarendon Press Oxford, 2001.

[42] MYERS P. S., UYEHARA O. A. AND BORMAN G. L., Fundamentals of Heat Flow in Welding, *Welding Research Council Bulletin 123,* pp. 1-46, 1967.

[43] BECK J. V., COLE K. D., HAJI-SHEIKH A. AND LITKOUHI B., Heat Conduction Using Green's Functions: Hemisphere publishing Corporation, 1992.

[44] AKHTER R., DAVIS M., DOWDEN J., KAPADIA P., LEY M. AND STEEN W. M., A method for calculating the fused zone profile of laser keyhole welds, *J. Phys. D: Appl. Phys.,* vol. 21, pp. 23-28, 1989.

[45] STEEN W. M., DOWDEN J., DAVIS M. AND KAPADIA P., A point and line source model of laser keyhole welding, *J. Phys. D: Appl. Phys.,* vol. 21, pp. 1255-1260, 1988.

[46] RADAJ D., Welding Residual Stresses and Distortion: Calculation and Measurement: DVS-Verlag, Düsseldorf, 2003.

[47] TANAKA S., *Journal of Japan Welding Society,* vol. 13, pp. 347-359, 1943.

[48] KAZUMARA K., TAKASHI Y. AND NOBUKATA Y., A Numerical Analysis of the Diffusion and Trapping of Hydrogen in Steels and Steel Weldments, *IIW. Doc. IX-951-76,* vol. 43, pp. 921-930, 1974.

[49] BOO K. S. AND CHO H. S., Transient temperature distribution in arc welding of finite thickness plates, *Proceedings of the Institution of Mechanical Engineers, Part B: Journal of Engineering Manufacture,* vol. 204, pp. 175-183, 1990.

[50] CHRISTENSEN N., DAVIES V. D. L. AND GJERMUNDSEN K., Distribution of Temperatures in Arc Welding, *British Welding Journal,* pp. 54-75, 1965.

[51] MALMUTH N. D., Temperature Field of a Moving point Source with Change of State, *International Journal of Heat and Mass Transfer,* vol. 19, pp. 349-354, 1976.

[52] NUNES A. C., An Extended Rosenthal Weld Model, *Welding Journal,* vol. 62, pp. 165s-170s, 1983.

[53] DOWDEN J., DUCHARME R. AND KAPADIA P., Time-dependent Line and Point Sources: A Simple Model for Time-Dependent welding Processes, *Lasers in Engineering,* vol. 7, pp. 215-228, 1998.

[54] KARKHIN V. A., MICHAILOV V. G. AND AKATSEVICH V. D., Modelling the Thermal Behaviour of Weld and Heat-Affected Zone during Pulsed Power Welding, *H. Cerjak, H.K.D.H. Bhadeshia (Eds.): Mathematical Modelling of Weld Phenomena,* vol. 4, pp. 411-426, 1998.

[55] ROGEON P., COUEDEL D., LE MASSON P., CARRON D. AND QUEMENER J. J., Determination of Critical Sample Width for Electron Beam Welding Process Using Analytical Modeling, *Heat Transfer Engineering,* vol. 25, pp. 52-62, 2004.

[56] PITTNER A., WEISS D., SCHWENK C. AND RETHMEIER M., Methodology to Improve Applicability of Welding Simulation, *Science and Technology of Welding and Joining,* vol. 13, No 6, pp. 496-508, 2008.

[57] KASUYA T. AND YURIOKA N., Prediction of welding thermal history by a comprehensive solution, *Welding Journal,* vol. 72, pp. 107s-115s, 1993.

[58] KASUYA T. AND YURIOKA N., Analysis of three dimensional heat conduction in welding by dispersed point heat sources, *IIW Doc.IX-1554-89,* pp. 1554-1589, 1989.

[59] ÖBERG T. T., Computation of Temperature Distribution due to Welding in Piping Systems, *Mechanical effects of welding – IUTAM Symposium,* 1991.

[60] SUZUKI R. N., TREVISAN R. E. AND TREVISAN O. V., Analytical solutions for heat flow in multiple pass welding, *Science and Technology of Welding and Joining,* vol. 5, pp. 63-70, 2000.

[61] CAO Z., DONG P. AND BRUST F., Report No. 2 A Fast Thermal Procedure for Analyzing 3D Multi- Pass Welded Structures, *Progress in Analysis of Welding Residual Stresses,* vol. WRC Bulletin 455, pp. 12-21, 2000.

[62] LU M. AND KOU S., Power and Current Distributions in Gas Tungsten Arcs, *Welding Journal,* vol. 67, pp. 29s-34s, 1988.

[63] CLINE H. E. AND ANTHONY T. R., Heat treating and melting material with a scanning laser or electron beam, *Journal of Applied Physics,* vol. 48, No. 9, pp. 3895-3900, 1977.

[64] EAGAR T. W. AND TSAI N.-S., Temperature Fields Produced by Traveling Distributed Heat Sources, *Welding Journal,* vol. 62, pp. 346s-355s, 1983.

[65] KWON Y. AND WECKMAN D. C., Analytical thermal model of conduction mode double sided arc welding, *Science and Technology of Welding and Joining,* vol. 13, pp. 539-547, 2008.

[66] GOLDAK J., BIBBY M., MOORE J., HOUSE R. AND PATEL B., Computer Modelling of Heat Flow in Welds, *Metallurgical Transactions B,* vol. 17B, pp. 587-600, 1986.

[67] GOLDAK J., CHAKRAVARTI A. P. AND BIBBY M., A New Finite Element Model for Welding Heat Sources, *Metallurgical Transactions B,* vol. 15B, pp. 299-305, 1984.

[68] NGUYEN N. T., MAI Y.-W., SIMPSON S. AND OHTA A., Analytical Approximation Solution for Double Ellipsoidal Heat Source in Finite Thick Plate, *Welding Journal,* vol. 83, pp. 82s-92s, 2004.

[69] NGUYEN N. T., OHTA A., MATSUOKA K., SUZUKI N. AND MAEDA Y., Analytical Solution for Transient Temperature of Semi-Infinite Body Subjected to 3-D Moving Heat Sources, *Welding Journal,* vol. 78, pp. 265s-274s, 1999.

[70] FACHINOTTI V. D. AND CARDONA A., Semi-analytical solution of the thermal field induced by a moving double-ellipsoidal welding heat source in a semi infinite body, *Mecánica Computacional,* vol. 18, pp. 1519-1530, 2008.

[71] KARKHIN V. A., PITTNER A., SCHWENK C. AND RETHMEIER M., Heat Source Models in Simulation of Heat Flow in Fusion Welding, *in conference proceedings, The Fifth International Conference "Mathematical Modelling and Information, Technologies in Welding and Related Processes",* pp. 56-60, 2010.

[72] PITTNER A., A Contribution to the Solution of the Inverse Heat Conduction Problem in Welding Simulation , Ph.D. Thesis, Fakultät V - Verkehrs- und Maschinensysteme der Technischen Universität Berlin, 2012.

[73] RANATOWSKI E. AND POCWIARDOWSKI A., An analytical-numerical evaluation of thermal cycle in the HAZ during welding, *H. Cerjak, H.K.D.H. Bhadeshia (Eds.): Mathematical Modelling of Weld Phenomena,* vol. 4, pp. 379-395, 1998.

[74] RANATOWSKI E. AND POCWIARDOWSKI A., An analytical-numerical estimation of the thermal cycle during welding with various heat source models application, *H. Cerjak, H.K.D.H. Bhadeshia (Eds.): Mathematical Modelling of Weld Phenomena,* vol. 5, pp. 725-742, 2001.

[75] RANATOWSKI E. AND POCWIARDOWSKI A., An Analytic-Numerical Assesment of the Thermal Cycle in HAZ with Three Dimensional Heat Source Models and Pulsed Power Welding, *H. Cerjak, H.K.D.H. Bhadeshia, E. Kozeschnik (Eds.): Mathematical Modelling of Weld Phenomena,* vol. 7, pp. 1111-1128, 2005.

[76] WINCZEK J., Analytical solution to transient temperature field in a half-infinite body caused by moving volumetric heat source, *International Journal of Heat and Mass Transfer,* vol. 53, pp. 5574-5781, 2010.

[77] PITTNER A., SCHWENK C., WEISS D. AND RETHMEIER M., An efficient solution of the inverse heat conduction problem for welding simulation, *H. Cerjak, N. Enzinger (Eds.): Mathematical Modelling of Weld Phenomena,* vol. 9, pp. 761-792, 2010.

[78] ANDERSON B. A. B., Thermal Stresses in a Submerged-Arc Welded Joint Considering Phase Transformations, *Transactions of the ASME,* vol. 100, pp. 356-362, 1978.

[79] VENEZIANO C., BRAND M., BURDACK M., SGUAIZER Y., PFEIFFER W., ULRICH B. AND SIEGELE D., Numerische Simulation von Verzug und Eigenspannung geschweißter Komponenten aus Al-Guss und Strangpressprofilen - numerical simulation of distortion and residual stresses of welded Aluminium-cast and extruded parts, *Fraunhofer Institut Werkstoffmechanik,* 2006 (in German).

[80] LEUNG K. C. AND PICK R. J., The Use Of Generalized Plane Strain Elements in the Prediction of Residual Stresses in Welded Flat Plates, *Computer Modelling of Fabrication Process and Constitutive Behaviour of Metals,* pp. 563-585, 1986.

[81] JONES B. K., EMERY A. F. AND MARBURGER S. J., An analytical and Experimental Study of the Effetcs of Welding Parameters on Fusion Welds, *Welding Journal,* vol. 72, pp. 51s-59s, 1993.

[82] ROELENS J. B., MALTRUD F. AND LU J., Determination of residual stresses in submerged arc multi-pass welds by means of numerical simulation and comparison with experimental measurements, *Welding in the World,* vol. 33, pp. 152-159, 1994.

[83] SAVAGE W. F., NIPPES E. F. AND ZANNER F. J., Determination of GTA Weld-Puddle Configurations by Impulse Decanting, *Welding Journal,* vol. 57, pp. 201s-210s, 1978.

[84] WAHAB M. A. AND PAINTER M. J., Numerical models of gas metal arc welds using experimentally determined weld pool shapes as the representation of the welding heat source, *International journal of pressure vessels and piping,* vol. 73, pp. 153-159, 1997.

[85] WAHAB M. A., PAINTER M. J. AND DAVIES M. H., The prediction of the temperature distribution and weld pool geometry in the gas metal arc welding process, *Journal of Materials Processing Technology,* vol. 77, pp. 233-239, 1998.

[86] LINDGREN L. E., Numerical modelling of welding, *Computer Methods in Applied Mechanics and Engineering,* vol. 195, pp. 6710-6736, 2006.

[87] FAURE F., BERGHEAU J. M., LEBLOND J. B. AND SOULOUMIAC B., Prediction of Distortions of Large Thin Structures During Welding Using shell Elements and Multiscale Approaches, *H. Cerjak, H.K.D.H. Bhadeshia, E. Kozeschnik (Eds.): Mathematical Modelling of Weld Phenomena,* vol. 7, pp. 605-620, 2005.

[88] LINDGREN L. E., Finite Element Modeling and Simulation of Welding. Part 2: Improved Material Modeling, *Journal of Thermal Stresses,* vol. 24, pp. 195-231, 2001.

[89] SCHWENK C., FE-Simulation des Schweissverzugs laserstrahlgeschweisster dünner Bleche - FE-Simulation of welding distortions in laser welded thin plates, Ph.D. Thesis, Fakultät V - Verkehrs- und Maschinensysteme der Technischen Universität Berlin, 2007 (in German).

[90] RADAJ D., Eigenspannungen und Verzug beim Schweißen - Residual Stresses and Distortions in Welding: DVS-Verlag, Düsseldorf, 2002 (in German).

[91] JONES B. K., EMERY A. F. AND MARBURGER S. J., Design and analysis of test coupon for fusion welding, *ASME J. Press. Vess. Technol.,* vol. 115, pp. 38-46, 1993.

[92] SCHWENK C., RETHMEIER M., DILGER K. AND MICHAILOV V. G., Sensitivity analysis of welding simulation depending on material properties value variation, *H. Cerjak, H.K.D.H. Bhadeshia, E. Kozeschnik (Eds.): Mathematical Modelling of Weld Phenomena,* vol. 8, pp. 1007-1129, 2007.

[93] RADAJ D., Simulation von Temperaturfeld, Eigenspannungen und Verzug beim Schweißen - Simulation of temperature field, residual stresses and distortions during welding: DVS-Verlag, Düsseldorf, 2001 (in German).

[94] WEISS D., CHRISTENSEN K. H. AND KRISTENSEN L. K., Computerised calibration of thermal welding models, *H. Cerjak, H.K.D.H. Bhadeshia, E. Kozeschnik (Eds.): Mathematical Modelling of Weld Phenomena,* vol. 8, pp. 469-484, 2007.

[95] PITTNER A., SCHWENK C., RETHMEIER M. AND WEISS D., A New Methodology for the Fast Temperature Field Generation for Welding Simulation, *17th International Conference on Computer Technology in Welding and Manufacturing Compcon,* pp. 1-12, 2008.

[96] RADAJ D. AND LINDGREN L. E., Verification and Validation in Computational Welding Mechanics, *H. Cerjak, H.K.D.H. Bhadeshia, E. Kozeschnik (Eds.): Mathematical Modelling of Weld Phenomena,* vol. 8, pp. 1039-1051, 2007.

[97] KARKHIN V. A., PLOCHIKHINE V. V. AND BERGMANN H. W., Solution of Inverse Heat Conduction Problem for Determining Heat Input, Weld Shape and Grain Structure

During Laser Welding, *Science and Technology of Welding and Joining,* vol. 7, No. 4, pp. 224-231, 2001.

[98] JEBERG P., Automatic Process Optimised Weld Planning of Full Penetration I-joint GMA Welding, Ph.D. Thesis, Aalborg University, 2005.

[99] SEN M. AND STOFFA P. L., Global Optimisation Methods in Geophysical Inversion, *Elsevier,* 1995.

[100] KUMAR A. AND DEBROY T., Tailoring Fillet Weld Geometry Using Genetic Algorithm and a Neural Network Trained With Convective Heat Flow Calculations, *Welding Journal,* vol. 86, pp. 26-33, 2007.

[101] KUMAR A. AND DEBROY T., Guaranteed Fillet Weld Geometry From Heat Transfer Model and Multivariable Optimization, *International Journal of Heat and Mass Transfer,* pp. 5793-5806, 2004.

[102] PITTNER A., WEISS D., SCHWENK C. AND RETHMEIER M., Fast Generation and Prediction of Welding Temperature Fields for Multiple Experiments, *Proceedings of the Fourth international Conference "Mathematical Modelling and Information Technologies in Welding and Related Processes",* pp. 134-140, Katsiveli, Ukraine, 2009.

[103] WEISS D., CHRISTENSEN K. H. AND KRISTENSEN L. K., Acceleration of numerical solution of inverse problems in gas metal arc welding, *in 14th International Conference on Computer Technology in Welding and Manufacturing,* pp. 1-10, 2004, Sheffield Hallam University, UK, 16 - 17 June 2004.

[104] RADAJ D., Simulation von Temperaturfeld, Eigenspannungen und Verzug beim Schweißen - Simulation of temperature field, residual stresses and distortions during welding, *DVS Berichte Band 214,* pp. 32-59, 2001 (in German).

[105] SCHENK T., RICHARDSON I. M., KRASKA M. AND OHNIMUS S., Non-isothermal thermomechanical metallurgical model and its application to welding simulations, *Science and Technology of Welding and Joining,* vol. 14, pp. 152-160, 2009.

[106] HACKMAIR C., Messung und numerische Simulation der Schweißverzüge an Aluminium-Fahrwerkskomponenten - Measurement and welding simulation of the distortions of an aluminium chassis component, Ph.D. Thesis, Technische Univerisität München, 2003 (in German).

[107] LUTZMANN S., PAPADAKIS L. AND SCHOBER A., Simulationsgestützte, bauteilbezogene Analyse industriell relevanter Einspannsituationen beim Schweißen - Simulation-aided, component-focused analysis of industry-relevant clamping situations during welding, *AiF-Mitgliedsvereinigung: Forschungsvereinigung Schweißen und verwandte Verfahren e. V. des DVS,* 2010 (in German).

[108] ROEREN S., Komplexitätsvariable Einflussgrößen für die bauteilbezogene Struktursimulation thermischer Fertigungsprozesse - Influence of complex variables to the structure simulation of the thermal manufacturing processes of welded assemblies, Ph.D. Thesis, Technische Univerisität München, 2006 (in German).

[109] ROEREN S., SCHWENK C. AND RETHMEIER M., Different Approaches to Model Clamping Conditions with welding Simulation, *H. Cerjak, H.K.D.H. Bhadeshia, E. Kozeschnik (Eds.): Mathematical Modelling of Weld Phenomena,* vol. 8, pp. 1093-1106, 2007.

[110] VOSS O., Untersuchung relevanter Einflußgrößen auf die numerische Schweißsimulation - Investigation of the influence of relevant parameters on the

numerical welding simulation, Ph.D. Thesis, Technische Universität Braunschweig, 2000 (in German).

[111] SCHWENK C., RETHMEIER M., DILGER K. AND MICHAILOV V. G., Schweißsimulation im Fahrzeugbau – Möglichkeiten, Grenzen und Herausforderungen - Welding simulation in automotive construction - possibilities, boundaries and challenges, *DVS Berichte Band 237,* pp. 353-358, 2005 (in German).

[112] JOSSERAND E., JULLIEN J.-F., NELLAS D., BOITOUT F. AND DELOISON D., Numerical simulation of welding-induced distortions taking into account industrial clamping conditions, *H. Cerjak, H.K.D.H. Bhadeshia, E. Kozeschnik (Eds.): Mathematical Modelling of Weld Phenomena,* vol. 8, pp. 1073–1092, 2007.

[113] SCHENK T., RICHARDSON I. M., KRASKA M. AND OHNIMUS S., A study on the influence of clamping on welding distortion, *Computational Materials Science,* vol. 45, pp. 999-1005, 2009.

[114] SCHENK T., RICHARDSON I. M., KRASKA M. AND OHNIMUS S., Influence of clamping on distortion of welded S355 T-joints, *Science and Technology of Welding and Joining,* vol. 4, pp. 369-375, 2009.

[115] PAPADAKIS L., Simulation of the Structural Effects of Welded Frame Assemblies in Manufacturing Process Chains, Ph.D. Thesis, Lehrstuhl für Werkzeugmaschinen und Fertigungstechnik der Technischen Universität München, 2008.

[116] ZAEH M. F., PAPADAKIS L. AND RAUH W., Realisation of the virtual prozess chain forming-welding on whole assembled automotive body components by means of shell elements, *H. Cerjak, H.K.D.H. Bhadeshia, E. Kozeschnik (Eds.): Mathematical Modelling of Weld Phenomena,* vol. 8, pp. 537-554, 2007.

[117] IRRGANG K. AND MICHALOWSKY L., Temperaturmesspraxis mit Widerstandsthermometern und Thermoelementen: Vulkan Verlag, 2004.

[118] CAMILLERI D., GRAY T. AND COMLEKCI T., Use of Thermography to Calibrate Fusion Welding Procedures in Virtual Fabrication Applications, *InfraMation 2004 Proceedings (27.04.2004),* 2004.

[119] MATTEÏ S., GREVEY D., MATHIEU A. AND KIRCHNER L., Using infrared thermography in order to compare laser and hybrid (laser+MIG) welding processes, *Optics and Laser Technology,* vol. 41, pp. 665-670, 2009.

[120] STADTAUS M., WELTERS T. AND DILGER K., Fügeprozesssimulation – Innovative Anwendung der Informatik - Joining process simulation - innovative appliance of informatics, *Schweißen und Schneiden,* vol. 57, pp. 32-34, 2005 (in German).

[121] SEYFFARTH P. AND SCHARFF A., Schweißtechnische Software - Versuch einer Übersicht - Welding technology software - Attempt of an overview, *DVS Berichte Band 198,* vol. 198, pp. 1-29, 1999 (in German).

[122] RETHMEIER M., STADTAUS M., MICHAILOV V. G. AND WOHLFAHRT H., Numerical Calculation of Temperature Load and Distortion During Welding of Circumferential Weld Seams, *H. Cerjak, H.K.D.H. Bhadeshia (Eds.): Mathematical Modelling of Weld Phenomena,* vol. 6, pp. 685-701, 2002.

[123] RETHMEIER M., VOSS O., WOHLFAHRT H., DECKER I. AND KOCIK R., Minimierung der Temperaturbelastung und des Verzugs an Einspritzventilen mit Hilfe der Methode der Finiten Elemente - Minimisation of thermal strain and distortion on injection valves by using the method of finite elements, *Schweißen und Schneiden,* vol. 52, pp. 466-471, 2000 (in German).

[124] SHIRAI H., MOCHIZUKI M. AND TOYODA M., Reduction of welding Deformation by Split Laser Beams in Automobile Parts, *IIW Doc.X-1618-07* pp. 1-11, 2007.

[125] SCHWENK C., RETHMEIER M. AND DILGER K., Analysis of the transient deformation behaviour and numerical optimisation of an electron beam welded gearwheel, *H. Cerjak, H.K.D.H. Bhadeshia, E. Kozeschnik (Eds.): Mathematical Modelling of Weld Phenomena,* vol. 8, pp. 1155-1166, 2007.

[126] SAINT-GERMAIN B., Étude expérimentale et numérique des distorsions de structures mécano-soudées - Experimental and numerical study of the distortions of welded structures, Ph.D. Thesis, École Centrale Paris, 2006 (in French).

[127] SAINT-GERMAIN B., OTT S., GABRIEL F. AND PILVIN P., Simulation des distorsions induites par soudage MAG d'un assemblage bras-plaque en acier ferritique - Simulation of the distortions induced by a MAG welding process on a arm-sheet metal assembly in a ferritic steel, 2006 (in French).

[128] PORZNER H., Possibilities of Numerical Simulation for Evaluation and optimisation of Welded Designs. Principles, *H. Cerjak, H.K.D.H. Bhadeshia (Eds.): Mathematical Modelling of Weld Phenomena,* vol. 5, pp. 701-724, 2000.

[129] HÄUSER H., BRAUN S. AND REITSAM R., Finite-Element-Simulation von Schweißprozessen mit AlMg- und AlMgSi Legierungen unter Berücksichtigung von Rekristallisation, Ausscheidungsrückbildung und natürlichem Altern - Finite-element-simulation of welding processes with AlMg- and AlMgSi-alloys in regard of recristallization, precipitation-regression and natural aging, *DVS Berichte Band 194,* pp. 47-51, 1998 (in German).

[130] HACKMAIR C., WERNER E. AND PÖNISCH M., Application of welding simulation for chassis components within the development of manufacturing methods, *Computational Materials Science,* vol. 28, pp. 540-547, 2003.

[131] GRÜN A., HECKELER G. AND HÜGEL M., Analyse von Verzug und Eigenspannungen für das geschweißte Seitenteil eines Hinterachsträgers - Analysis of distortions and residual stresses for the welded side panel of a rear wheel carrier, *DVS Berichte Band 194,* vol. 241, pp. 118-121, 2001 (in German).

[132] TIKHOMIROV D., RIETMAN B., FRANZ T. AND SCHWENK C., Methoden der Schweißverzugssimulation für die Anwendung in der Automobilindustrie - Methods for welding-distortion simulation for application in the automotive industry, *Schweißen und Schneiden,* vol. 59 Heft 12, pp. 678-680, 2007 (in German).

[133] MOURGUE P., GOOROOCHURN Y., BERGHEAU J. M., BOITOUT F., PORZNER H. AND NIEDENZU P., Modeling welding sequence on industrial parts, *Proceedings of EUROPAM 2000,* pp. 1-9, 2000.

[134] SOULOUMIAC B., BOITOUT F. AND BERGHEAU J. M., A New Local-Global Approach for the Modelling of Welded Steel Components Distortions, *H. Cerjak, H.K.D.H. Bhadeshia (Eds.): Mathematical Modelling of Weld Phenomena,* vol. 6, pp. 573-590, 2002.

[135] BERGHEAU J. M., Modélisation numerique des procedés de soudage - Numerical modelisation of welding processes, *Techniques de l'ingénieur,* vol. BM 7 758, pp. 1-15, 2004 (in French).

[136] TSIRKAS S. A., PAPANIKOS P., PERICLEAOUS K., STRUSEVICH N., BOITOUT F. AND BERGHEAU J. M., Evaluation of distortions in laser welded shipbuilding parts using local -

global finite element approach, *Science and Technology of Welding and Joining,* vol. 8, pp. 79-88, 2003.

[137] DENG D., MURAKAWA H. AND LIANG W., Numerical simulation of welding distortion in large structures, *Computer Methods in Applied Mechanics and Engineering,* vol. 196, pp. 4613–4627, 2007.

[138] PLOSHIKHIN V., PRIKHODOVSKY A., FRANK T., ILIN A., BÄCHLE D., KRAFT P. AND HEIMERDINGER C., Schweißverzüge bei Großbauteilen verstehen und beherrschen - understanding and controlling welding-distortions in large components, *DVS Berichte Band 250,* pp. 338-340, 2008 (in German).

[139] DARCOURT C., ROELANDT J. M., RACHIK M., DELOISON D. AND JOURNET B., Simulation du soudage laser de structures aéronautiques - Welding simulation of laser welded Aeronautical structures, vol. 2, pp. 401-406, 2005 (in French).

[140] DARCOURT C., ROELANDT J. M., RACHIK M., DELOISON D. AND JOURNET B., Thermomechanical analysis applied to the laser beam welding simulation of aeronautical structures, *J. Phys. IV France 120,* pp. 785-792, 2004.

[141] SCHWENK C. AND RETHMEIER M., Structured Approach for a Transient 3D Numerical Welding Simulation, *H. Cerjak, N. Enzinger (Eds.): Mathematical Modelling of Weld Phenomena,* vol. 9, pp. 901-917, 2010.

[142] DIN DEUTSCHES INSTITUT FÜR NORMUNG E. V., DIN SPEC 32534-1 - Numerical welding simulation - Execution and documentation - Part 1: Overview, ed, 2011.

[143] LINDGREN L. E., HÄGGBLAD H.-A., MCDILL J. M. J. AND ODDY A. S., Automatic remeshing for three-dimensional finite element simulation of welding, *Computer Methods in Applied Mechanics and Engineering,* vol. 147, pp. 401-409, 1997.

[144] RUNNEMALM H. AND HYUN S., Three-dimensional welding analysis using an adaptive mesh scheme, *Computer Methods in Applied Mechanics and Engineering,* vol. 189, pp. 515–523, 2000.

[145] DURANTON P., DEVAUX J., ROBIN V., GILLES P. AND BERGHEAU J. M., 3D modelling of multipass welding of a 316L stainless steel pipe, *Journal of Materials Processing Technology,* pp. 457–463, 2004.

[146] MCDILL J. M. J., JOHNSTON M. A. AND ODDY A. S., A generic error estimate for three-dimensional h-adaptive finite element analysis, *Mathematical Modelling and Scientific Computing,* vol. 9, 1997.

[147] MCDILL J. M. J. AND ODDY A. S., Arbitrary coarsening for adaptive mesh management in automatic finite element analysis, *J.Math. Modelling Sci. Comput. 2B,* pp. 1072-1077, 1993.

[148] MCDILL J. M. J., ODDY A. S. AND GOLDAK J., An adaptive mesh-management algorithm for three-dimensional automatic finite element analysis, *Trans. CSME 15,* pp. 57-70, 1991.

[149] BROWN S. AND SONG H., Finite Element Simulation of welding of Large Structures, *Journal of Engineering for Industry,* vol. 114, n°4, pp. 441-451, 1992.

[150] KARLSSON L. AND LINDGREN L. E., Combined Heat and Stress-Strain Calculation, *Modeling of Casting, Welding and Advanced Solidification Processes V,* pp. 187-202, 1991.

[151] LINDGREN L. E., Modelling for Residual Stresses and Deformations due to Welding - Knowing what isn't necessary to know, *H. Cerjak, H.K.D.H. Bhadeshia (Eds.): Mathematical Modelling of Weld Phenomena,* vol. 6, pp. 491-518, 2002.

[152] GOLDAK J., NÄSSTRÖM M., WIKANDER L., KARLSSON L. AND LINDGREN L., Combined 3-D and shell modelling of welding, *Mechanical effects of welding – IUTAM Symposium,* pp. 197-206, 1991.

[153] GU M. AND GOLDAK J., Mixing thermal shell and brick elements in FEA of welds, *Materials Engineering ASME,* vol. 3-A, 1991.

[154] FAURE F., BERGHEAU J. M., LEBLOND J. B. AND SOULOUMIAC B., New methods for numerical simulation of welding of large thin structures, *Revue Européenne des Eléments Finis, numéro special Numerical Simulation of Welding,* vol. 13, N°2/3, pp. 289-311, 2004.

[155] DUAN Y., FAURE F., BERGHEAU J. M. AND LEBLOND J. B., Prediction of welding distortions using an adaptive 3D/shell approach, *Modelling of Casting, Welding and Advanced Solidification Processes XI,* pp. 887-894, 2006.

[156] DUAN Y., BOITOUT F., DELOISON D., LEBLOND J. B. AND BERGHEAU J. M., Une approche local/globale pour déterminer les distorsions résiduelles de soudage - A local/global appraoch to obtain welding induced residual stresses, 2006 (in French).

[157] DUAN Y., BOITOUT F., LEBLOND J. B. AND BERGHEAU J. M., Simulation numérique du soudage de grandes structures par une approche locale/globale - Numerical welding simulation of large structures with a local/global approach, *Mécanique and Industries 9,* pp. 97-102, 2008 (in French).

[158] DEO M. V., MICHALERIS P. AND SUN J., Prediction of Buckling Distortion of Welded Structures, *Science and Technology of Welding and Joining,* pp. 55-61, 2003.

[159] MICHALERIS P. AND DEBICCARI A., Prediction of welding distortion, *Welding Journal,* vol. 76, pp. 172s-179s, 1997.

[160] UEDA Y. AND YUAN M., Prediction of residual stresses in butt-welded plates using inherent strain, *ASME J. Engrg. Mater. Technol.,* vol. 115, pp. 417–423, 1993.

[161] LUO Y., MURAKAWA H. AND UEDA Y., Prediction of welding deformation and residual stress by elastic FEM based on inherent strain. Third report: Deformation and residual stress in narrow gap welding, *Journal of the Society of Naval Architects of Japan,* vol. 183, pp. 323 - 333, 1998.

[162] LUO Y., MURAKAWA H. AND UEDA Y., Prediction of welding deformation and residual stress by elastic FEM based on inherent strain. Second report: Deformation and residual stress under multiple thermal cycles, *Journal of the Society of Naval Architects of Japan,* vol. 182, pp. 783 - 793, 1997.

[163] MURAKAWA H., LUO Y. AND UEDA Y., Prediction of welding deformation and residual stress by elastic FEM based on inherent strain. First report: mechanism of inherent strain production, *Journal of the Society of Naval Architects of Japan,* vol. 180, pp. 739-751, 1996.

[164] DENG D. AND MURAKAWA H., Prediction of welding distortion and residual stress in a thin plate butt-welded joint, *Computational Materials Science,* vol. 4, pp. 353–365, 2008.

[165] DIN DEUTSCHES INSTITUT FÜR NORMUNG E. V., DIN EN 10327 - Continuously hot-dip coated strip and sheet of low carbon steels for cold forming - Technical delivery conditions, ed, 2004.

[166] DIN DEUTSCHES INSTITUT FÜR NORMUNG E. V., DIN EN 10292 - Continuously hot-dip coated strip and sheet of steels with higher yield strength for cold forming - Technical delivery conditions, ed, 2005.
[167] KAMMER C., Aluminium-Taschenbuch Bd. 1: Grundlagen und Werkstoffe - Aluminium-pocket-book vol. 1: Basics and Materials: Aluminium Verlag, 1995 (in German).
[168] VOLKSWAGEN GROUP STANDARD, TL 116 - Extruded Profiles of Al Alloy 6xxx, ed, 2005.
[169] DIN DEUTSCHES INSTITUT FÜR NORMUNG E. V., DIN EN 573-3 - Aluminium und Aluminiumlegierung - Chemische Zusammensetzung und Form von Halbzeug - Teil 3: Chemische Zusammensetzung und Erzeugnisformen; Deutsche Fassung EN 573-3:2007, ed, 2007.
[170] DIN DEUTSCHES INSTITUT FÜR NORMUNG E. V., DIN EN ISO 18273 - Schweißzusätze - Massivdrähte und -stäbe zum Schmelzschweißen von Aluminium und Aluminiumlegierungen, ed, 2004.
[171] MIG WELD GMBH, http://www.migweld.de, Datasheet ML 4047: AlSi12, Mars 2012.
[172] ESI GROUP, SYSWELD 2007-Werkstoffdatenbank, ed, 2007.
[173] RIO TINTO, http://sales.riotintoaluminium.com/freedom.aspx?pid=525, ed, 2011.
[174] CARL CLOOS SCHWEIßTECHNIK GMBH, http://www.cloos.de/cloos/de, ed, 2011.
[175] GNU LIBRARY, http://www.gnu.org, ed, 2011.
[176] WELDSIM AND WELDSIMS, Reference Manual, 2008.
[177] VDI-Gesellschaft Verfahrenstechnik und Chemieingenieurwesen (Ed.): VDI Wämeatlas: Springer-Verlag, 2006 (in German).

Own Publications

[1] PERRET W., THATER R., SCHWENK C., ALBER U. AND RETHMEIER M., Case study for welding simulation in the automotive industry, *Welding in the World,* vol. 55, 2011.

[2] PERRET W., THATER R., ALBER U., SCHWENK C. AND RETHMEIER M., Approach to assess a fast welding simulation in an industrial environment - Application for an automotive welded part, *International Journal of Automotive Technology,* vol. 12, pp. 895-901, 2011.

[3] PERRET W., SCHWENK C. AND RETHMEIER M., Comparison of analytical and numerical welding temperature field calculation, *Computational Materials Science,* vol. 47, pp. 1005-1015, 2010.

[4] THATER R., PERRET W., SCHWENK C., ALBER U. AND RETHMEIER M., Industrial Application of Welding Temperature Field and Distortion Visualization using FEA, *Transaction of the JWRI,* vol. 39, pp. 232-234, 2010.

[5] PERRET W., THATER R., ALBER U., SCHWENK C. AND RETHMEIER M., Efficient Welding Simulation of an Automotive Sheet Metal Assembly, in *Proceedings of Steels in Cars & Trucks*, June 05th–09th, Salzburg, Austria, 2011.

[6] PERRET W., SCHWENK C., ALBER U. AND RETHMEIER M., Anwendung der numerischen Schweißsimulation im Karosseriebau - Möglichkeiten und Grenzen - Application of Numerical Welding Simulation of Car Body Construction - Possibilities and Limitations, in *Proceedings of the Automotive Circle International Conference*, April 12th-14th, Bad Nauheim, Germany, 2011 (in German).

[7] THATER R., PERRET W., SCHWENK C., ALBER U. AND RETHMEIER M., Industrial Application of Welding Temperature Field and Distortion Visualization using FEA, in *Proceedings of the International Symposium "Visualization in Joining & Welding Science through Advanced Measurements and Simulation*, November 11th-12th, Osaka, Japan, 2010.

[8] THATER R., PERRET W., SCHWENK C., ALBER U. AND RETHMEIER M., Different modelling approaches for efficient distortion calculation of an automotive assembly, in *Proceedings of the 3rd International Workshop on Thermal Forming and Welding Distortion IWOTE*, April 06th-07th, Bremer Institut für angewandte Strahltechnik BIAS, Bremen, Germany, 2011, pp. 279-291.